This is to certify that the
dissertation entitled

THE EFFECT OF MOLYBDENDUM ON THE PHYSICAL AND MECHANICAL METALLURGY OF ADVANCED TITANIUM-ALUMINIDE ALLOYS AND METAL MATRIX COMPOSITES

presented by

JEFFREY PAUL QUAST

has been accepted towards fulfillment
of the requirements for the

Doctoral degree in Materials Science Engineering

Mark C. Hardy Co Carl Boehlert
Major Professor's Signature

12/11/08
Date

THE EFFECT OF MOLYBI
METALLURGY OF ADV
ME T

in part

D

M

THE EFFECT OF MOLYBDENDUM ON THE PHYSICAL AND MECHANICAL METALLURGY OF ADVANCED TITANIUM-ALUMINIDE ALLOYS AND METAL MATRIX COMPOSITES

By

Jeffrey Paul Quast

A DISSERTATION

Submitted to
Michigan State University
in partial fulfillment of the requirements
for the degree of

DOCTOR OF PHILOSOPHY

Materials Science Engineering

2008

THE EFFECT
METALLUR

ABSTRACT

THE EFFECT OF MOLYBDENDUM ON THE PHYSICAL AND MECHANICAL METALLURGY OF ADVANCED TITANIUM-ALUMINIDE ALLOYS AND METAL MATRIX COMPOSITES

By

Jeffrey Paul Quast

This dissertation represents a systematic study of microstructure-mechanical property relationships of titanium-aluminum-niobium-molybdenum (Ti-Al-Nb-Mo) alloys and metal matrix composites (MMCs). The aspects investigated were the microstructures, elevated-temperature creep behavior, room-temperature and elevated-temperature tensile behavior, and the out-of-phase thermomechanical fatigue behavior. The specific alloy compositions investigated were: Ti-24Al-17Nb-0.66Mo (at.%) and Ti-24Al-17Nb-2.3Mo (at.%). The MMCs were reinforced with Ultra SCS-6 fibers and the specific compositions of the matrices were: Ti-24Al-17Nb-0.66Mo (at.%), Ti-24Al-17Nb-1.1Mo (at.%), and Ti-24Al-17Nb-2.3Mo (at.%). All of the materials were fabricated using a powder-metallurgy, tape casting technique. A subtransus heat-treatment produced microstructures containing a hexagonal close-packed α_2 phase, orthorhombic (O) phase, and a body-centered cubic (BCC) phase. The higher Mo contents were shown to stabilize the BCC phase and result in an increase the O+BCC phase volume percent and a subsequent decrease in the α_2 phase volume percent. The creep deformation behavior of the alloys and MMCs was the main focus of this dissertation. Creep experimentation was performed to understand the deformation mechanisms as a function of stress, temperature, and strain rate. Higher Mo contents significantly increased the creep resistance of the alloys, which was attributed to the decrease in the number of α_2/α_2 grain

...ures increased O-BCC

...e of the major findings

...n boundaries were the

...ocated MMC creep ex

...rallel to the loading dir

...ased the creep resistance o

...ificantly less than tha

...ould model the creep behavi

...the matrix bond strength

...Mises for a condition ass

...dicts that the MMC

...ere the applied creep st

...ain transition was observe

...ation modeling revealed tha

...e was indeed very small,

...ater than the matrix alloy

...ented in this dissertation h

...chanical metallurgy effe

boundaries, increased O+BCC colony size, and Mo solid solution strengthening. This was one of the major findings of the work. *In-situ* tensile-creep experiments indicated that grain boundaries were the locus of deformation and cracking in each of the alloys investigated. MMC creep experimentation was performed with the fibers aligned perpendicular to the loading direction. Similar to alloy creep results, higher Mo contents increased the creep resistance of the MMCs. However, the creep resistance of the MMCs was significantly less than that of their respective alloy compositions. An effort was made to model the creep behavior of the MMCs based on the creep behavior of the alloys and fiber/matrix bond strength. The model predicted the secondary creep rates of the MMCs well for a condition assuming no bond strength between the fiber and matrix. The model predicts that the MMC will exhibit a secondary creep rate lower than that for the alloy when the applied creep stress is less than the fiber/matrix bond strength. However, no such transition was observed in the experimental data. Experimental testing and finite element modeling revealed that the interfacial bond strength between the matrix and the fiber was indeed very small, suggesting that the MMC creep resistance would not be greater than the matrix alloy under practical loading applications. Overall, the work performed in this dissertation helped fill the knowledge gap which exists for the physical and mechanical metallurgy effects of varying Mo additions in titanium aluminides.

This dissertation is dedic
research to furthering
whatever thoughts

Dedication

This dissertation is dedicated to my father, whose teaching, guidance, persistence, and commitment to furthering my education motivated and challenged me to achieve more than I had ever thought possible.

First and foremost
provided me with the opp
graduate students at
assist me in the
questions and provided
annual conferences. In
obtain a research p
always been a great adv
I express grati
Jeanine and Dr. Patrick
and Dr. Michael Step
Speech Applications. I
Petty Dr. Petta for her
Oak Ridge Nation
I am appreciative o
Davis. I especially than
reaching my goals, and I th
Petta. I also thank my
completion of my dissert
privilege to have worked w
Gerdom, and Sara Lon
at Michigan State U

Acknowledgements

First and foremost I would like to thank my advisor, Dr. Carl Boehlert, who provided me with the opportunity to perform this work. I was fortunate to be one of his first graduate students at Michigan State University. I will always remember his dedication to assist me in the completion my degree. He made himself available to answer my questions and provided me opportunities to present my work in publications and at technical conferences. In particular, I am very appreciative of his assistance in helping me obtain a research position for two summers at Wright-Patterson Air Force Base. He has truly been a great advisor and friend and for that I cannot thank him enough.

I express gratitude to my thesis committee of Dr. Marty Crimp, Dr. David Grummon, and Dr. Patrick Kwon for their guidance in the completion of my degree. I thank Dr. Michael Shephard (Air Force Research Laboratory) and Mr. Paul Smith (Research Applications, Inc.) for providing the materials in this work. I also thank Tiffany Di Petta for her assistance with the finite element modeling and Mr. Larry Walker (Oak Ridge National Lab) for performing the microprobe work.

I am appreciative of all the love and support that I received from my family and friends. I especially thank my mother Linda and father Timothy for pushing me to expand my goals, and I thank my brothers, Robert and Matthew, for always being there for me. I also thank my wife Stacie for her love and encouragement throughout the completion of my dissertation. Without her I would not be where I am now. Lastly, I am grateful to have worked with fellow graduate students and friends, Christopher Cowen, Kebin Low, and Sara Longanbach, who were there to share ideas with and make my time spent at Michigan State University more enjoyable.

TABLE OF CONTENTS

LIST

LIST OF TABLES

LIST OF FIGURES

Images in this thesis/dissertation are presented in color.

igure 4.22 Creep strain
ample at 20 MPa during

igure 4.23 Creep strain
Ti-24Al-1Nb-1Mo (M
nd (0005) alloy at T =

igure 4.24 Creep strain
Nb-1Mo alloy sampl
ts greater creep resistanc

igure 4.25 A log-log plo
Nb-1Mo and Ti-24
ep rate n values were de

igure 4.26 In of the mini
Mo alloy at (a) 30 MP
ues determined from the

igure 4.27 ln of the mini
Mo alloy at 150 MPa.
om the linear curve fits o

igure 4.28 A plot of cree
ested at 593°C and 172 M

igure 4.29 Displacement
ens tested at 150 MPa a

igure 4.30 BSE SEM mic
ested at 593°C showing
ntained in all images an

igure 4.31 BSE SEM mic
ering cracking pred
ntained in all images an

igure 4.32 BSE SEM pi
cking indicated by arr
Nb-1Mo alloy
ed under the stress rup
e main mechanism

igure 4.44 Carbon layer
nsile-tested cruciform
ove the fiber and (b) be

igure 4.45 Carbon layer
nsile-tested cruciform s
e side of the fiber and (

igure 4.46 Carbon layer
nsile-tested cruciform s

igure 4.47 BSE SEM m
ber. The radial cracks

igure 4.48 Room-temper

igure 4.49 Secondary el
d (a) and (b) HT Ti-24Al-1

igure 4.50 Secondary el
d (a) and (b) HT Ti-24Al-1

igure 4.51 Room temper

igure 4.52 Secondary el
d (a) and (b) HT Ultra S
rface cracking exhibited

igure 4.53 Secondary el
d (a) and (b) HT Ultra S
rface cracking exhibited

igure 4.54 650°C tensile
24Al-Nb-2Mo alloy sa

igure 4.55 Secondary elec
Ti-24Al-1Nb-0.66Mo

igure 4.56 650°C tensile
ed and Ultra SCS-6 T

igure 4.57 Secondary elec
Ultra SCS-6 Ti-24Al-
MCs. Note the gr

igure 5.10 A contour s
ample to 850°C. The l
his suggests that debo
pplied tensile stress wa

igure 5.11 A plot of
ocusing at various ang
gainst tangential stress

igure 5.12 Fracture surf
2Mo and (b) Ti-24Al-

at%	Atomic pe
Al	Aluminum
AP	As-proces
ATS	Applied T
b	Burger's v
BCC	Body-cent
BSE	Backscatte
BZ	Ordered b
c	Disordered
C	Carbon
CTE	Coefficien
d	Average g
D_l	Lattice di
D_{gb}	Coefficien
DTA	Differenti
E	Grain bou
E	Young's m
EDM	Electron d
EDS	Energy di
ε	Elongatio
$\dot{\varepsilon}$	Steady-st
FCP	Bonding
FEG	Hexagonal
FIT	Hot isost
γ	Heat treat
γ_{APB}	Boltzmann
γ_{SF}	Stress co
HCOT	Linear th
HIPC	Metal ma
HP	Molybden
HT	Creep exp
I	Niobium
IN	Nickel
κ	Orthorhom
L	Quasi-cry
LCF	Volume c
M	Activatio

LIST OF SYMBOLS

at.%	Atomic percent
Al	Aluminum
AP	As-processed
ATS	Applied Test Systems, Inc.
b	Burger's vector
BCC	Body-centered cubic
BSE	Backscattered electron
B2	Ordered body-centered cubic
β	Disordered body-centered cubic
C	Carbon
CTE	Coefficient of thermal expansion
d	Average grain diameter
D_L	Lattice diffusion coefficient
D_{SD}	Coefficient of lattice self diffusion
DTA	Differential thermal analysis
δ	Grain boundary spacing
E	Young's modulus
EDM	Electron discharge machining
EDS	Energy dispersive spectroscopy
ε_f	Elongation-to-failure
$\dot{\varepsilon}_s$	Steady-state creep rate
η	Bonding factor
HCP	Hexagonal close packed
HIP	Hot isostatic press
HT	Heat treated
k	Boltzmann's constant
K	Stress concentration factor
LVDT	Linear variable differential transformer
MMC	Metal matrix composite
Mo	Molybdenum
n	Creep exponent
Nb	Niobium
Ni	Nickel
O	Orthorhombic
OOP	Out-of-phase
Ω	Volume of a vacancy
Q	Activation energy

Q_{ap}	Apparent
R	Universal
RT	Room ter
SiC	Silicon c
SEM	Scanning
σ	Applied s
T	Temperat
T_m	Melting te
Ti	Titanium
TMF	Thermom
UTS	Ultimate te
V_f, V_f	Fiber vol
V_f	Volume pe
V_ϕ	Phase vol
$V_{\phi=30^\circ}$	Phase vol
$wt\%_\phi$	Weight pe
XRD	X-ray diff
X_i, $X_{i=30^\circ}$	Element c
YS	Yield stre

Q_{app}	Apparent activation energy
R	Universal gas constant
RT	Room temperature
SiC	Silicon carbide
SEM	Scanning electron microscopy
σ	Applied stress
T	Temperature
T_m	Melting temperature
Ti	Titanium
TMF	Thermomechanical fatigue
UTS	Ultimate tensile strength
V, V_f	Fiber volume fraction
V_P	Volume percent
V_α	Phase volume percent of α
V_{O+BCC}	Phase volume percent of O+BCC
wt.%	Weight percent
XRD	X-ray diffraction
X_α, X_{O+BCC}	Element content
YS	Yield strength

The work prese

processing-microstructu

-aluminide/niobium (

ying Mo contents.

24Al-11Nb-2.3Mo (at.

11Nb-9Mo (at.%). T

ficient all alloy an

ecifically stated other

proximately 0.35 vol.

ous SCS-6 SiC fibers,

om-temperature te

mperature fiber matrix

chanical fatigue (TM

om temperature and

ding at the minimum

To the auth

ch procedure and

ensively investig

ve to complete

ural metallurgy

CHAPTER 1

INTRODUCTION

The work presented in this dissertation represents a systematic study of the processing-microstructure–mechanical property relationships of titanium-aluminum-niobium-molybdenum (Ti-Al-Nb-Mo) alloys and metal matrix composites (MMCs) with varying Mo contents. The alloys studied were Ti-24Al-17Nb-0.66Mo (at.%) and Ti-24Al-17Nb-2.3Mo (at.%). The compositions of the composite matrices were Ti-24Al-17Nb-0.66Mo (at.%), Ti-24Al-17Nb-1.1Mo (at.%), and Ti-24Al-17Nb-2.3Mo (at.%). Henceforth, all alloy and matrix compositions are reported in atomic percent unless specifically stated otherwise. Each composite was unidirectionally reinforced with approximately 0.35 volume fraction of silicon carbide-based continuous fibers, termed Ultra SCS-6 SiC fibers. The mechanical properties evaluated were room-temperature and elevated-temperature tensile, elevated-temperature (650° - 710°C) creep, room-temperature fiber/matrix interfacial bond strength, and out-of-phase (OOP) thermo-mechanical fatigue (TMF). In OOP TMF the material was simultaneously exposed to cyclic temperature and load fluctuations in an out-of-phase sequence (i.e. maximum loading at the minimum temperature and vice versa).

To the author's knowledge, the effect of varying Mo content on the microstructure and mechanical properties of Ti-Al-Nb alloys has never been systematically investigated. Therefore, this work presents new information which allows for a more complete understanding of how relatively small Mo additions affect the physical metallurgy of titanium-aluminide alloys and their MMCs. From this, the

stability of the studied

aerospace vehicles can b

The main focus

determine the effect tha

and OOP TMF behavior

model used to predict

fiber/matrix bond strengt

each material (before

electron microscopy (SE

ering and the dominat

strain rate, stress, and

ep deformation evol

ber strength of the SiC

as measured using t

ber structure on the

fibers using an OO

The purpose o

P and OOP TMF

Ti alloys and MM

ehavior and properti

e of Ti matrix c

ortant aims of this d

suitability of the studied materials for use in high-temperature structural applications in aerospace vehicles can be assessed.

The main focus of this work was concentrated on obtaining two objectives: to determine the effect that small Mo additions have on the microstructure, creep, tensile, and OOP TMF behavior of Ti-24Al-17Nb-xMo alloys and MMCs, and to further develop a model used to predict the MMC creep response based on the matrix creep rates and fiber-matrix bond strengths. In order to accomplish these objectives, the microstructures of each material (before and after heat treatment) were carefully analyzed using scanning electron microscopy (SEM). Each microstructure was evaluated in tensile and creep testing, and the dominant creep deformation mechanisms were determined as a function of strain rate, stress, and temperature. Using SEM-based *in-situ* tensile-creep testing, the creep deformation evolution within the alloys' microstructure was characterized. The bond strength of the fiber-matrix interface, used to help model the MMC creep response, was measured using tensile specimens with a cruciform geometry. The effect of microstructure on the TMF behavior of the MMCs was characterized by testing specimens using an OOP cycle.

The purpose of this chapter is to provide the rationale for investigating the tensile, creep, and OOP TMF properties of the alloys and MMCs. Furthermore, an overview of titanium alloys and MMCs is provided. The overview contains a summary of the origin, structure, and properties of Ti and Ti alloys, a section on Mo additions to Ti alloys, and a review of Ti matrix composites. Lastly, an outline of the work performed and the specific aims of this dissertation are provided.

A. Rationale

The research and

sections in gas turbin

improvement in engi

temperatures, which ge

generation. Currently, t

between 850°C to 1500°C,

92). Reed-Hill and A

tensile stresses (250) – 5

about 760°C (Reed-Hi

can be able to not o

service.

Creep is defined

load under constant

deformation and can be

observed in all materials

the deformation and fa

about one-half of the

gas turbine engine

Nickel-based super

These alloys offer

relatively large T/T_m ratio

having limited thermal-

A. Rationale

The research and development of materials capable of withstanding the aggressive conditions in gas turbine engines is of significant interest within the aerospace industry. Improvement in engine efficiency is obtained by achieving higher operating temperatures, which generally result in decreases in fuel consumption and pollution generation. Currently, turbine blades in gas turbine engines see gas temperatures ranging from 650°C to 1500°C, see Figure 1.1, and longitudinal stresses of approximately 140 MPa [Reed-Hill and Abbaschian (1994)]. The root of the blade experiences higher tensile stresses (280 – 560 MPa), but the temperature in this region does not typically exceed 760°C [Reed-Hill and Abbaschian (1994)]. Given these conditions, materials must be able to not only withstand high stresses but also possess sufficient creep resistance.

Creep is defined as a time-dependent, progressive deformation of a material placed under constant load or stress. In many instances creep is an undesirable phenomenon and can be the limiting factor in the lifetime of a part. Creep deformation is observed in all materials and can occur at stresses well below the yield stress. Typically, creep deformation and failure is a concern for metals when temperatures approach and exceed one-half of the absolute melting temperature (T_m) of the material, which is common in turbine engines.

Nickel-based superalloys are regularly used for turbine engine blades, see Figure 1.2, as these alloys offer an attractive balance of high strength and creep resistance at relatively large T/T_m ratios. However, the relatively high density of these materials results in a limited thrust-to-weight ratio. For this reason, alternative materials have been

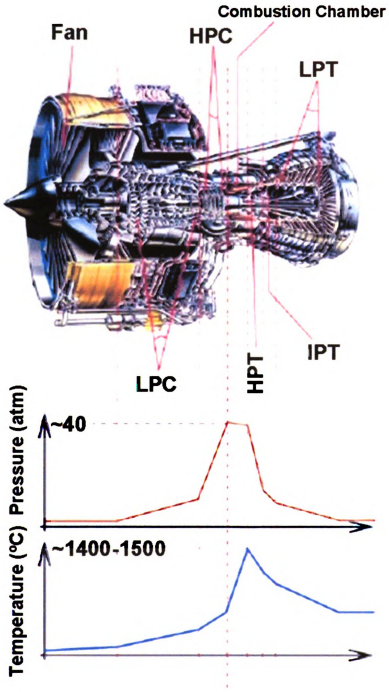

Figure 1.1. A jet engine image displaying the varying pressure and gas temperature profiles along the engine. (LPC – Low Pressure Compressor, HPC – High Pressure Compressor, HPT – High Pressure Turbine, IPT – Intermediate Pressure Turbine, and LPT – Low Pressure Turbine) [Trent 800].

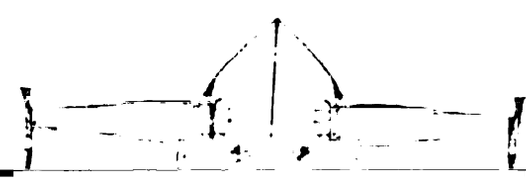

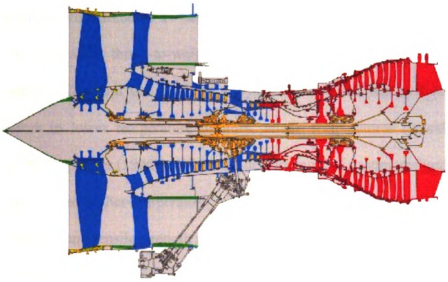

Figure 1.2. A diagram showing the various materials commonly used in a jet turbine engine. The titanium is in blue, nickel-based superalloys in red, and steel in yellow [Trent 800].

sidered. Alloys bas

's have shown pr

ensity reductions offe

ach in increased t

rformance. Comm

mpressors in lower t

°C to 538°C [Miller (

has allowed high

gh-temperature tens

Additional increa

ecently significant im

erheat temperatures a

ajor choice for jet en

been performed on

con carbide fibers, w

ties of the fiber w

Besides operati

mponents are often e

Al alloys have been

ensile loadings [App

ers to study the the

ber composites.

considered. Alloys based on titanium, which have been extensively researched since the 1930's, have shown promise for use in high-temperature environments, see Figure 1.3. Density reductions offered by Ti-based alloys compared with Ni-based superalloys could result in increased thrust-to-weight ratios, leading to enhancements in engine performance. Common use of these alloys is seen in the rear end of high-pressure compressors in lower temperature turbines, where temperatures typically range from 500°C to 800°C [Miller (1996)]. While the development of coating technologies for these alloys has allowed higher-temperature applications to be considered, further improvement in high-temperature tensile strength and creep resistance of the base alloys is desired.

Additional increases in weight savings are offered through use of MMCs. In particular, significant improvements in strength-to-density ratios are achieved both at ambient temperatures and at elevated temperatures. As a result, MMCs have become a popular choice for jet engine components. Over the past fifteen-to-twenty years, research has been performed on continuously-reinforced titanium aluminide alloys reinforced with silicon carbide fibers, which combine the high strength, creep resistance, and Young's modulus of the fiber with a ductile and damage resistant titanium alloy matrix.

Besides operating under sustained stresses at high temperatures, jet engine components are often exposed to varying load conditions and fluctuating temperatures. TiAl alloys have been prone to cleavage fracture, where cracks grow rapidly under repeated loadings [Appel *et al.* (2003), Bowen *et al.* (1995)]. For this reason, it is of interest to study the thermomechanical fatigue properties of titanium alloys and titanium matrix composites.

Temperature (°C)
1300
1200
1100
1000
900
800

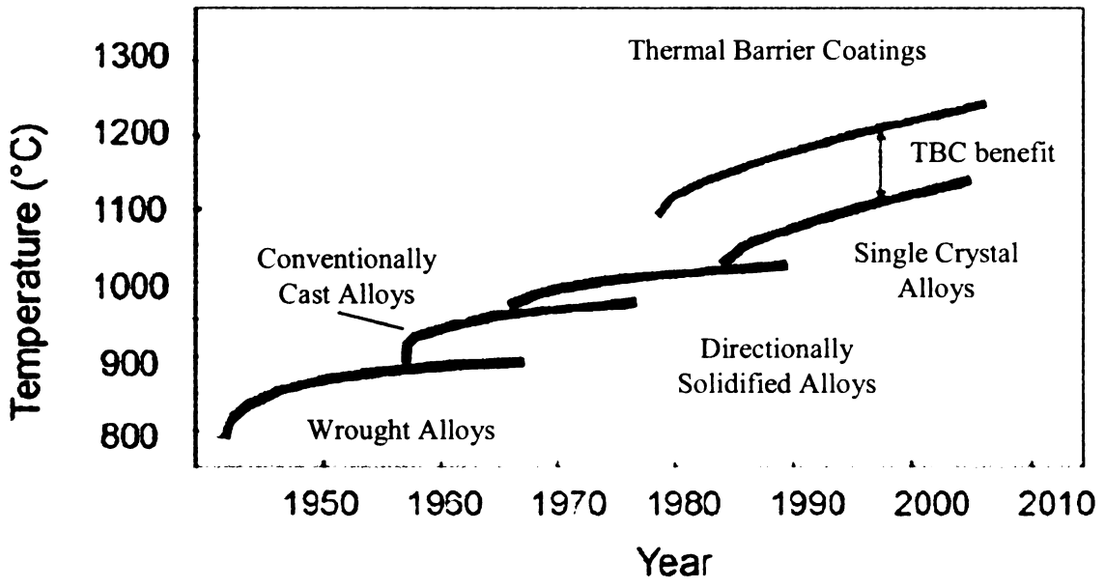

Figure 1.3. Over time, alloy research and development, fabrication technology, and thermal barrier coatings have resulted in higher temperature capabilities for titanium alloys [Shultz *et al.* (2003)].

For materials us

resistance are two of

understanding of the m

required before a mater

B. Origin, Structur

The discovery o

be first to produce an

nium was not name

nium oxide from ru

4 (2001). Over [tw

scovery of the Kr

volutionized the prod

ed shielding with t

ential materials for

ts. In fact, two-th

Bailey (2001). T

structure, chemical

sical, and trans

perties of Ti alloys

).

Pure Ti is a

ties depending o

For materials used in jet engines, creep resistance and thermomechanical fatigue resistance are two of the major mechanical properties needed. Therefore, a thorough understanding of the microstructural features that influence these mechanical properties is required before a material can be considered for use in a gas turbine engine.

B. Origin, Structure, and Properties of Titanium and Titanium Alloys

The discovery of titanium has been credited to William Gregor, who in 1791 was the first to produce an impure oxide of the metal [Peters *et al.* (2003)]. However, titanium was not named until four years later when Martin Heinrich Klaproth isolated titanium oxide from rutile, a mineral composed primarily of titanium dioxide [Peters *et al.* (2003)]. Over 100 years passed before metal Ti was extracted commercially. The discovery of the Kroll process, which creates Ti through the reduction of $TiCl_4$, revolutionized the production of Ti metal [Peters *et al.* (2003)]. Following World War II and coinciding with the boom of aeronautics, titanium-based alloys were considered essential materials for aircraft engines. Today, aerospace applications still utilize Ti alloys. In fact, two-thirds of all Ti metal produced is used in aircraft engines and frames [Emsley (2001)]. Ti has also gained acceptance in other applications involving architecture, chemical processing, power generation, marine, sports and recreation, biomedical, and transportation. The high specific strength and excellent corrosion resistance of Ti alloys are quite attractive compared to many other materials [Peters *et al.* (2003)].

Pure Ti is allotropic, and therefore can crystallize into more than one crystal structure depending on the temperature. At low temperatures it crystallizes into a

hexagonally close pac

temperatures is body-c

ansition temperature

he β-transus temperat

es characterized as n

mperature. The α-

mperature, allowing

abilizing elements (N

The existence

portant importance.

nium alloys. The

acture toughness, and

nsition temperature

ge alloying addition

he practical applicatio

etter workability a

susceptible to a ductile-

fections. A two-ph

enhanced mechan

chanical properties

intermetallic

erature mechanical

ntermetallic alloys have

hexagonally close packed (HCP) structure called α Ti, while the stable phase at higher temperatures is body-centered cubic (BCC), which is referred to as β Ti. For pure Ti, the transition temperature at which this crystallographic phase transformation occurs (termed the β-transus temperature) is 882±2°C [Peters *et al.* (2003)]. Alloying elements, which are characterized as neutral, α-stabilizing, or β-stabilizing, can affect the β-transus temperature. The α-stabilizing elements (Al, O, N, C, etc.) increase the transus temperature, allowing the α-phase field to be stable at higher temperatures, while β-stabilizing elements (Nb, Mo, V, Ta, etc.) shift the β-phase field to lower temperatures.

The existence of the various crystal structures in pure Ti and its alloys is of paramount importance, as they are the basis for the variety of properties exhibited by titanium alloys. The α-phase alloys are generally categorized by their high strength, fracture toughness, and creep resistance. Such alloys do not exhibit a ductile-to-brittle transition temperature and can therefore be used in cryogenic applications. However, for large alloying additions with some elements, low elongation-to-failure (ε_f) values limit the practical application of these alloys. The β-phase alloys are characterized by their greater workability and increased ε_f values compared with α-phase alloys but are susceptible to a ductile-to-brittle transition and are therefore limited in low-temperature applications. A two-phase microstructure consisting of both α and β phases can provide well-balanced mechanical properties. However, insufficient elevated-temperature mechanical properties of these alloys limit their use for some aerospace components.

Intermetallic titanium-aluminum alloys offer an improvement in many high-temperature mechanical properties compared with α, β, and α+β Ti alloys. These intermetallic alloys have the potential to replace nickel-based superalloys commonly used

n gas turbine engines

ne titanium-based in

hexagonal-close packed

ilips. The lack of du

d active slip systems.

iscovered that the add

n increase in ε_f and

[75]. The first gene

al. (Marquardt et al.

ti compositions (rang

mperature and elev

Blackburn and Smith

ti-Al-Nb have sh

sistance (Rowe (1967)

Banerjee and

metallic composit

ys Banerjee et al.

Al-rich compositions

Banerjee (1969), Mozer

ler et al. (1985). The

The O-phase is bet

ses greater elev

Nandy et al. (

in gas turbine engines based on their density-normalized properties. Until recently, the two titanium-based intermetallics receiving the most attention have been the ordered hexagonal-close packed (HCP) Ti_3Al (α_2) alloys and the face-centered tetragonal TiAl (γ) alloys. The lack of ductility of these structural intermetallics, due to the limited number of active slip systems, limits their application. However, investigations of Ti_3Al alloys discovered that the addition of BCC-phase stabilizing elements, specifically Nb, resulted in an increase in ε_f and fracture toughness [Blackburn and Smith (1978), Blackburn *et al.* (1978)]. The first generation of Ti_3Al-Nb alloys evaluated contained Nb contents of 11 at.% [Marquardt *et al.* (1989)]. Research in the 1980's into Ti-Al-Nb alloys with greater Nb compositions (ranging from 13 – 20 at.%) resulted in a good balance of room-temperature and elevated-temperature properties [Blackburn and Smith (1982), Blackburn and Smith (1989)]. Further studies have revealed that alloys containing up to 33 at.% Nb have shown improvements in specific strength, toughness, and creep resistance [Rowe (1991), Rowe *et al.* (1991), Nandy *et al.* (1993), Cowen (2006)].

Banerjee and coworkers found that the orthorhombic (O) phase, based on the intermetallic composition Ti_2AlNb, was a major constituent phase of these Ti-Al-Nb alloys [Banerjee *et al.* (1988)]. In fact, the O phase has been observed in titanium aluminide compositions possessing Nb contents ranging from 12.5 at.% Nb to 33 at.% Nb [Banerjee (1989), Mozer *et al.* (1990), Rowe (1990), Peters and Baasi (1990), Cowen and Boehlert (2008)]. The relation of the O-phase to other Ti phases is depicted in Figure 1.4. The O-phase is beneficial to Ti alloys targeted for high temperature applications in that it offers greater elevated-temperature creep resistance than the α_2-phase and BCC-phases [Nandy *et al.* (1993), Nandy *et al.* (1995)].


40
Nb

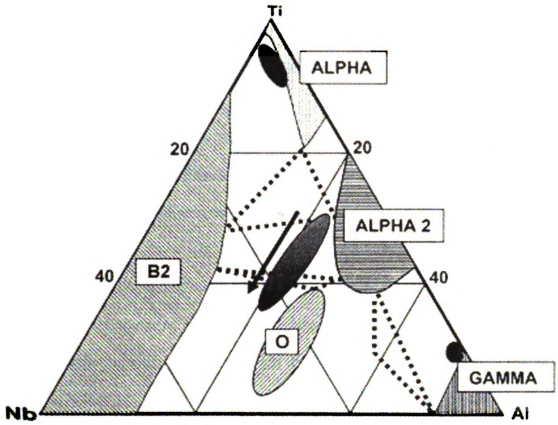

Figure 1.4 The ternary phase diagram of the Ti-Al-Nb system depicting the compositional relationships of the near α-Ti, α_2, B2, γ, and O-phase alloys [Banerjee (2006)].

C. Molybdenum A

It has been sh
minimum creep rate
stabilizers to Ti-Al-V
strengths improved
[90]. Banerjee et al.
Tetsui et al (2002)
such as Mo, have not
shown to be effective
focused on develop
creep relationships
future development
properties through
developments of such
conventional near-α T
effects on the microstru
creep behavior of Ti
direction.

D. Titanium Matri

The current use
of 550°C [Leyens et
to the higher, higher

C. Molybdenum Additions to Titanium Alloys

It has been shown that quaternary additions can have a strong effect on the minimum creep rate of Ti-Al-Nb alloys [Tang *et al.* (2002)]. The addition of β-phase stabilizers to Ti-Al-Nb alloys has resulted in an increase in ε_f values, higher yield strengths, improved creep resistances, and higher fracture toughness values [Rowe (1992), Banerjee *et al.* (1993), Banerjee (1994), Zhang *et al.* (1998), Tang *et al.* (2000), Tang *et al.* (2002)]. These quaternary alloying elements which may substitute for Nb, such as Mo, have not shown significant changes in deformation mechanisms but have shown to be effective strengtheners [Nandy and Banerjee (2000)]. However, research focused on developing a fundamental understanding of processing-microstructure-property relationships of quaternary Ti-Al-Nb alloys is still in its infancy. Therefore, further development to optimize the mechanical properties of O-phase titanium aluminides through quaternary additions of β phase stabilizers is warranted. Developments of such alloys may bridge the gap in temperature capability between conventional near-α Ti alloys and nickel-based superalloys. Understanding the Mo affects on the microstructure, tensile behavior, creep behavior, and thermomechanical fatigue behavior of Ti alloys and MMCs constituted one the main focuses of this dissertation.

D. Titanium Matrix Composites

The current useful service temperature of Ti alloys and Ti aluminides is limited to about 550°C [Leyens *et al.* (2003)]. However, within the aerospace industry there is a desire for lighter, higher-temperature materials that will enable larger mechanical and

thermal loads.

composites could

superform Ti alloy

carbide (SiC) fi

resistance of the

using SiC fiber

The impl

has hindered h

the MMC ma

coefficients betw

matrix interface

composite from

strength decrea

for the specif

Pieces of the

matrix comp

become parallel

[65] Ross et al.

the direction pe

Debbie is ex

between matri

[66] Carnes et

[67] applicat

thermal loads. While Ti alloys may be able to replace some denser alloys, Ti-based composites could potentially provide more significant improvements and would far outperform Ti alloys if successfully implemented. Ti alloys have been joined with silicon carbide (SiC) fibers in an effort to combine the high strength, stiffness, and creep resistance of the fiber with the damage tolerance of the Ti-based matrix. In addition, uniting SiC fibers in a Ti matrix reduces the density compared with the Ti matrix.

The implementation of Ti-matrix composites within the aerospace industry has been hindered by several materials issues. One, the fabrication techniques associated with MMC manufacturing are not conventional. Variations in thermal expansion coefficients between the matrix and the fibers along with reactivity issues at the fiber-matrix interface pose fabrication problems. Moreover, these problems hamper the composite from reaching its optimal mechanical property performance (i.e. lowers strength, decreases creep resistance, and limits fatigue resistance). Anisotropy arising from the specific morphology of the continuous fiber also significantly affects the properties of the MMC. Previous studies have shown that the addition of SiC fibers to a Ti matrix composite increases the strength and creep resistance when loaded in the direction parallel to the fibers' longitudinal axis [Jannson *et al.* (1991), Larsen *et al.* (1995), Russ *et al.* (1995), Rosenberger *et al.* (1997)]. However, when evaluating MMCs in the direction perpendicular to the fibers' longitudinal axis, the creep resistance of the composite is controlled by the creep resistance of the matrix alloy and the strength of the fiber-matrix interface [Smith *et al.* (1994), Majumdar (1997), Krishnamurthy *et al.* (1998), Carrère *et al.* (2002)]. The implementation of MMCs in high-temperature structural applications has been hindered by interfacial failure observed in transverse

eep at low s

Mpamban (199

esistance of M

he matrix all

mproving the M

olume fractio

matrix and inc

Mpamban (199

f the matrix a

ding agents

The hi

akes it des

echanical res

ecreasing ma

he model de

decline in pre

Shermergor h

Mpamban (1

bed matrix c

he theoretica

creep at low stresses [Feillard (1996), Krishnamurthy *et al.* (1998), Miracle and Majumdar (1999), Ghosh *et al.* (2000), Carrère *et al.* (2002)]. In some cases, the creep resistance of MMCs with fibers perpendicular to the loading direction can be worse than the matrix alloy itself [Chatterjee *et al.* (1997), Miracle and Majumdar (1999)]. Improving the MMC creep resistance for this orientation can be achieved by lowering the volume fraction of the fibers, increasing the bond strength between the fiber and the matrix, and increasing the creep resistance of the matrix [Krishnamurthy *et al.* (1998), Majumdar (1999)]. It is therefore important to characterize and understand the behavior of the matrix and the interaction between the fiber and matrix when designing MMC components.

The high fabrication costs and time-consuming nature of mechanical testing makes it desirable to successfully model the properties of composites using the mechanical response of the matrix alloy and the fiber-matrix interface strength rather than performing numerous mechanical-property experiments on several MMC compositions. One model developed by Crossman and further modified by Majumdar has shown promise in predicting the MMC creep response based upon the matrix creep rates and fiber-matrix bond strength [Crossman *et al.* (1974), Majumdar (1997), Miracle and Majumdar (1999)]. This model has yet to be verified for Ti-Al-Nb- or Ti-Al-Nb-Mo-based matrix composites. Evaluation of this model constituted one of the main focuses of this dissertation.

E. Work

E. Work Performed

This study began in September 2005 when the fabricated Ti-24Al-17Nb-xMo alloys and composites were received from the researchers of the Wright-Patterson Air Force Base - Air Force Research Laboratory (Dayton, OH). A thorough investigation of these materials, though intended, had never been conducted by Air Force Research Laboratory researchers to determine the affect that varying Mo additions have on the microstructure–mechanical property relationships.

The first step involved the characterization of the microstructure of these alloys and composites. Some of the materials were subjected to a heat treatment to favorably tailor and stabilize the microstructure at creep temperatures. All the materials' microstructures were characterized using scanning electron microscopy (SEM). Mechanical testing was then performed on the machined specimens. Tensile tests were conducted at room temperature (RT) and elevated temperature on the alloys and MMCs with the SiC fibers parallel to the loading direction. The tensile data was used to evaluate the effect that microstructure had on the yield strength, ultimate tensile strength, and elongation-to-failure (ε_f). The elevated-temperature tensile data was useful in designing creep and OOP TMF experiments at appropriate stress levels.

Creep experiments were conducted starting from the fall of 2005 and continuing through the winter of 2007. From these experiments, the minimum creep rates were measured and the associated creep exponents and activation energies were calculated over the stress range of 30 – 275 MPa for the alloys and 10 – 75 MPa for the MMCs. The MMCs were tested with the fibers perpendicular to the loading direction (For the mechanical testing, the fiber orientation with respect to loading direction was always

chosen in a direction where failure was considered to be matrix dominated rather than fiber dominated). The creep test temperature ranged from 650 – 710°C. *In-situ* SEM tensile-creep experiments were performed on the alloys from winter of 2005 through the spring of 2006. Using this technique, the damage evolution of the sample surface during 650°C creep testing was tracked. This allowed direct microstructural evidence of the creep deformation evolution.

Bond strength experiments were performed in the summer of 2007. These tests used a cruciform specimen geometry, which will be explained in more detail in Chapter 3, to obtain transverse interface property data of the MMCs. Determination of the interface strength was a critical measurement used to model the creep behavior of the MMCs (with fibers oriented 90° with respect to the tensile-creep axis).

Out-of-phase thermomechanical fatigue testing on the alloys and MMCs with fibers parallel to the loading direction was conducted starting in the fall of 2007 and ending in the summer of 2008. Such tests allowed for life predictions and performance predictions of the MMCs in a controlled environment similar to actual component spectrums. OOP TMF is considered to be a matrix dominated property when the loading direction is parallel to the longitudinal fiber axis.

F. Specific A

Microstructure

(1) To unde

evolutio

(2) To quan

chemistr

and to g

microstr

(3) To obtain

Creep Behavior

(1) To evalua

dependen

temperatur

(2) To evalua

dependenc

temperature

were perfo

effects on

(3) To determ

along with

literature fo

F. Specific Aims

Microstructure

(1) To understand the effect of heat treatment and Mo content on the microstructural evolution.

(2) To quantify the microstructural aspects of the alloys and MMCs, such as phase chemistry, grain size, phase transition temperatures, and phase volume fraction, and to gain an understanding of the microstructural features potentially affecting microstructure – property relationships.

(3) To obtain a qualitative assessment of fiber/matrix interface integrity.

Creep Behavior

(1) To evaluate the alloys' creep strain versus time behavior and creep strain rate dependency on temperature and stress over the stress range of 30 – 275 MPa and temperature range of 650 – 710°C.

(2) To evaluate the MMCs' creep strain versus time behavior and creep strain dependency on temperature and stress over the stress range of 10 – 75 MPa and temperature range of 650 – 710°C. Specimens were oriented so that the fibers were perpendicular to the loading direction, so that the matrix and interface effects could be determined.

(3) To determine the creep stress exponents and activation energies. These values along with the minimum creep rates were compared to those found in the literature for similar alloy compositions.

(4) To verify

experime

boundary

(5) To under

the differ

(6) To mode

respect to

this mode

Tensile Behavior

(1) To deter

MMC w

tensile pr

2) To verify

MMC a

3) To evalu

method

(above)

4) To identi

Shear Behavior

1) To evalu

shear ra

(4) To verify the alloys' creep deformation mechanisms using *in-situ* tensile-creep experiments in a SEM. Particular focus was on grain boundary sliding and grain boundary cracking as potential deformation mechanisms.

(5) To understand the effect that varying microstructures (due to heat treatment and the different Mo contents) have on the creep behavior of the alloys and MMCs.

(6) To model and predict the creep performance of the MMCs (loaded 90° with respect to fiber orientation) from the constitutive behavior of the alloys and verify this model with selected 90°-oriented MMC creep experiments.

Tensile Behavior

(1) To determine the RT and 650°C tensile properties of the monolithic alloy and MMC with the fibers parallel to the loading direction, so that microstructure – tensile property relationships could be developed.

(2) To verify whether or not the rule-of-mixtures strength was achieved for the MMC alloys.

(3) To evaluate the interfacial strength of the MMCs using a cruciform-based testing methodology. This was important for the modeling mentioned in creep item #6 (above).

(4) To identify the interface location where deboning occurred.

Out-of-Phase Thermomechanical Fatigue

(1) To evaluate the OOP thermomechanical fatigue behavior of the MMCs over the stress range of 200 – 600 MPa and temperature range of 150°C – 450°C.

(2) To generate applied stress versus cycles-to-failure plots for each MMC tested.

(3) To determine and understand the microstructure – thermomechanical fatigue behavior relationships. Specimens were oriented so that the fibers were parallel to the loading direction, so that the matrix effects could be determined.

B

This chap

he work perform

ed to produce

microstructures a

ssessment of th

esigned Ti-A

Ti-Al-Nb alloys a

roperties of vari

hapter deals with

A. Processing R

1. Conventional

Titanium m

rocess. Typica

ing, pulling, and

Casting is a

ch is then

ediate sp

ent weakn

CHAPTER 2

BACKGROUND AND LITERATURE REVIEW

This chapter presents background information and published literature pertinent to the work performed in this dissertation. Described first are the various processing routes used to produce advanced titanium alloys and metal matrix composites. Next, the microstructures and the phases present in Ti-Al-Nb alloys are reviewed along with an assessment of the effect Mo additions have on the microstructure of previously investigated Ti-Al-Nb alloys. Detailed descriptions of creep and the creep behavior of Ti-Al-Nb alloys and MMCs are provided. The tensile deformation behavior and tensile properties of various titanium alloys and MMCs are presented. The last section of this chapter deals with out-of-phase thermomechanical behavior of MMCs.

A. Processing Routes

1. Conventional Methods for Titanium Alloys

Titanium metal can be formed into slabs, bars, sheets, etc. using various processes. Typical forming processes for titanium alloys include forging, extrusion, rolling, pulling, and casting.

Casting is a relatively simple process that involves pouring molten metal into a mold, which is then allowed to solidify. This processing route is advantageous in that large and intricate shapes can be formed in an economically viable way. However, there are inherent weaknesses in castings which are associated with shrinkage, elemental

segregation resu

Varney (1962),

One alter

shape an alloy.

in part, resultin

castings. Forgi

microstructures a

(1962). Forged

tensile strengt

forging and the

rolling rates with

Titanium a

sheet rolling.

as to produce

rolling appro

Produce significan

Ti-6Al-4V fabricated

Seah et al. (20

It was comp

properties of the

EBC testing.

segregation resulting in a non-homogenous microstructure, and gas porosity [Clark and Varney (1962)].

One alternative to casting is forging, which uses heavy loads and large forces to shape an alloy. As the material is forged, the grains are deformed to follow the shape of the part, resulting in a microstructure that is more continuous than that observed in castings. Forging is advantageous in that it offers the ability to precisely tailor microstructures and properties through deformation and heat treatments [Terlinde *et al.* (2003)]. Forged materials typically contain fewer defects than cast materials and are therefore stronger [Altan (1983)]. However, extensive machining is necessary for forging, and the ability for form complex shapes is sometimes hindered by varying cooling rates within the material, which can lead to warping.

Titanium alloys produced using either of these methods can require hot rolling and cold rolling. Each rolling step may consist of multiple passes, such that the time and cost to produce these alloys can be significant. In this work, an alternative powder metallurgy approach was used, namely tape casting. This method has the potential to produce significant cost and time reductions for the alloy and matrix materials. However, alloys fabricated using the tape cast method has resulted in incomplete consolidation [Smith *et al.* (2000)]. In this work it was also important to use a fabrication technique that was compatible with both alloy and MMC production. By doing this, direct assessments of the results obtained from alloy testing were compared to those found for MMC testing.

2. Metal Matrix Composite Fabrication

There are many processes available to fabricate MMCs. These processes can be separated into two main groups: liquid-state processing and solid-state processing. One major liquid-state process is casting. In this technique, a fiber bundle is infiltrated by liquid metal [Divecha *et al.* (1981), Rohatgi *et al.* (1986)]. However, there has been little success in producing titanium matrix composite via casting [Leyens *et al.* (2003)]. Difficulties arise due to wetting issues of ceramic reinforcements by the molten metal and also due to degraded fiber properties stemming from the reaction between the fiber and the molten metal [Chawla (1998)]. Therefore, solid-state processes are preferred to liquid-state process.

Typical solid-state processing routes include the foil-fiber-foil technique, the monotape technique, and the matrix-coated technique. In the foil-fiber-foil technique, alternating layers of foil and fiber mats are stacked and hot isostatically pressed (HIPed) to form multilayer MMCs. The monotape technique is similar to the foil-fiber-foil technique, but uses a fiber reinforced tape as a starting material. The monotapes are stacked and HIPed to form a MMC. For each of these techniques, homogeneous fiber distribution is difficult to obtain [Leyens *et al.* (2003)]. Optimum fiber distribution can be obtained using the matrix-coated technique, however this method is much more costly than the foil-fiber-foil and monotape technique [Leyens *et al.* (2003)]. The starting material for the matrix-coated technique is a fiber coated with a homogeneous layer of the matrix material. These coated fibers are then bundled and HIPed to produce a MMC.

The alloys and MMCs produced in this work were tape cast. This process was first developed by Glenn Howatt in the late 1940's to produce thin ceramic sheets to be

used in capacitors [Howatt *et al.* (1947)]. Today, this processing technique is still commonly used to create complex circuits and multilayered structures. In fact, tape casting is considered to be a promising alternative to conventional fabrication techniques for Ti-Al-Nb orthorhombic alloys, offering significant cost savings in the processing and production of such materials [Smith *et al.* (1999)]. In some ways, tape casting of MMCs is very similar to the foil-fiber-foil technique commonly used. The major difference is seen in the fabrication of the matrix sheet. Rather than casting and hot working, tape casting is a powder metallurgical approach which involves the hot pressing of an organically-binded metal powder slurry. Further explanation of the processing used for the alloys and MMCs is provided in Chapter 3.

The hot isostatic pressing step is an important stage in the fabrication of the MMCs. During this step relatively high temperatures are used to fully compact the composite. However, during the cool down residual stresses at the fiber/matrix interface are generated due to the differences in thermal expansion coefficients between the fiber and the matrix. Furthermore, high-temperature exposures lead to undesired reactions between the fiber and the matrix, which can embrittle the matrix. Therefore, this consolidation step must be carefully performed so that residual stresses and fiber/matrix reactions are minimized.

B. Microstru

1. Titanium-

Depend

possess consta

nonmetallic e

While it is not

exists as either

remainder of th

ed is discusse

composition and

[Ref. Rhodes

crystal structure

ides with Al, N

Banerjee et al.

based on the o

formed to exis

specific atomic p

hcp structure,

ed is based on

Lattice of the q

Crystal structure

[Ref. the Olympic

[Ref. Moore et al.

B. Microstructure Background

1. Titanium-Aluminum-Niobium Alloys

Dependent upon composition, orthorhombic titanium-aluminum-niobium alloys possess constituent phases including the ordered intermetallic O phase, the ordered HCP intermetallic α_2 phase, the ordered BCC-phase (B2), and the disordered BCC-phase (β). While it is noted that the BCC phase in the alloys and matrices examined in this work exists as either B2 or β it will simply be referred to as the BCC phase throughout the remainder of this dissertation. However, the ordering of the BCC phase was determined and is discussed in Chapter 5. The BCC phase ordering is dependent on alloy composition and heat treatment [Kestner-Weykamp *et al.* (1989), Bendersky *et al.* (1991), Rhodes (1997)]. The B2 crystal structure is ordered and is based on the CsCl crystal structure and the chemical composition Ti_2AlNb. It is composed of Ti atoms at A sites with Al, Nb, and the remaining Ti atoms at the B sites, as shown in Figure 2.1 [Banerjee *et al.* (1987)]. The O phase has cmcm orthorhombic symmetry and is also based on the composition Ti_2AlNb [Banerjee *et al.* (1988)]. The O phase has been observed to exist in two forms, O1 and O2, where Nb atoms were found to occupy specific atom positions in the O2 structure, as opposed to randomly occupying Ti sites in the O1 structure, see Figure 2.2 (a) [Banerjee (1997)]. The α_2 phase has DO_{19} symmetry and is based on the composition Ti_3Al [Krishnamurthy *et al.* (1993)]. The crystal structure of the α_2 phase is similar to that of the O phase, as shown in Figure 2.2 (b). The foremost difference is that one of the Ti sites in the α_2 structure is preferentially occupied by Nb in the O phase, while it is randomly occupied in the α_2 phase, as shown in Figure 2.3 [Mozer *et al.* (1990), Rowe *et al.* (1992), Huang and Siemers (1989)].

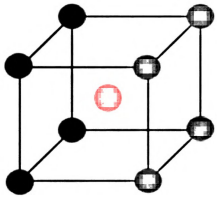

Al, Nb

Ti

Figure 2.1 The crystal structure of the B2 phase observed in Ti-Al-Nb alloys.

b =

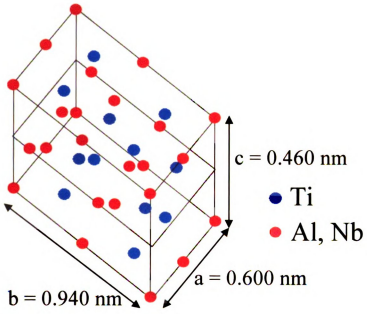

(a)

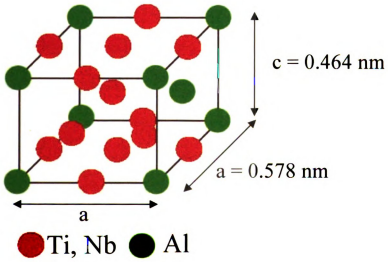

(b)

Figure 2.2 Crystal structures of the constituent phases: (a) the O1 unit cell and (b) one **third** of the α_2 unit cell [Mozer *et al.* (1990), Muraleedharan *et al.* (1995)].

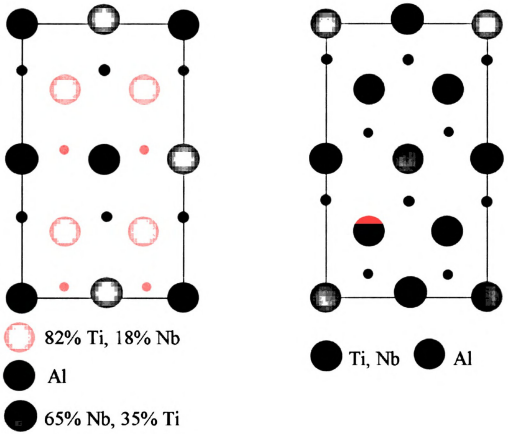

Figure 2.3 Basal plane schematics of the (a) O phase and (b) α_2 phase for Ti-Al-Nb **alloys**. The large circles represent atoms in the plane of the paper, while the smaller **circles** represent atoms in planes above and below the plane of the paper. Taken from [**Mozer** *et al.* (1990)].

The

24A1 Ne

workers

developed

temperatu

the number

this two P

Ab

adding fo

the struct

ATe2SAL-

Affinities

figures re

Bacigee

tied to low

The

Reformer

Pt-Co) m

Berdensky

[24] Ba

A Berdy

A Berdensk

Pt-Co) C

The alloys in this work were all based on the ternary Ti-Al-Nb composition of Ti-24Al-17Nb. A phase map based on Ti-25Al-xNb has been developed by Sagar and coworkers [Sagar *et al.* (1996)] and is presented in Figure 2.4. While this map was developed through evaluations of specific alloy compositions heat treated at different temperatures, it is noted that it is in violation of the Gibbs Phase Rule, which states that the number of phases plus the degrees of freedom is equal to the number of components plus two [Porter and Easterling (1992)]. This will be discussed further in Chapter 5.

Above the transus temperature single-phase BCC microstructures exist. Rapid cooling from above the transus temperature can suppress the α_2 formation and result in a microstructure consisting of only the O+BCC phases [Muraleedharan *et al.* (1992a)]. For a Ti-25Al-17Nb alloy, slow cooling or solutionizing in the α_2+B2 or α_2+B2+O regimes promotes the formation of the α_2 phase. Aging within the α_2+B2+O, O+B2, O+β, or O regimes results in the formation of a rim-O phase along the outer edges of the α_2 phase [Banerjee *et al.* (1988)]. This rim-O phase prevents the α_2 phase from transforming when aged in lower temperature phase fields, acting as a diffusion barrier.

The α_2 and O phase formation from the BCC phase occurs through three different transformation modes: Widmanstatten precipitation of the α_2 or O phase, composition invariant mechanism, and discontinuous precipitation of BCC to α_2+BCC or O+BCC [Bendersky *et al.* (1991), Rowe and Hall (1991), Rowe (1991a) Muraleedharan *et al.* (1992), Banerjee (1994), Majumdar *et al.* (1994), Rowe and Larsen (1996), Boehlert *et al.* (1999)]. A previous study of a Ti-25Al-24Nb and Ti-23Al-27Nb alloy revealed that Widmanstatten precipitation of the O-phase from the parent B2 phase only occurred below 875°C in the O+B2 phase field [Boehlert *et al.* (1999)]. It was determined that as

the temperature decreased, grain boundary diffusion and grain growth kinetics became sluggish. At heat-treatment temperatures lower than 875°C, Widmanstatten precipitation of the O-phase became the dominant phase transformation mechanism [Boehlert *et al.* (1999)]. For the alloys in this work, Widmanstatten precipitation was suggested to be the dominant transformation mechanism, as each alloy was heat treated at 850°C, whereas the compositional invariant mechanism was only observed in supertransus heat-treated microstructures [Bendersky *et al.* (1991), Muraleedharan *et al.* (1992)] and the discontinuous precipitation mechanism was observed when alloys were solutionized at high temperatures, quenched, and aged at lower temperatures (750°C) [Boehlert *et al.* (1999)].

Specific orientation relationships have been identified for the α_2 and O phases with respect to the B2 phase. The orientation relationship for the α_2 and B2 phase is given by: [11-20]α_2//[1-11]B2 and (0001)α_2//(011)B2 [Burgers (1934)]. The orientation relationship formed between the B2 and O phases is: [1-11]B2//[110]O and (110)B2//(001)O [Muraleedharan *et al.* (1992)]. The rim-O phase has an orientation relationship with respect to α_2 of: [0001]α_2//[001]O and (10-10)α_2//(110)O [Banerjee *et al.* (1988)].

14
12
10
8
6
Temperature (C)

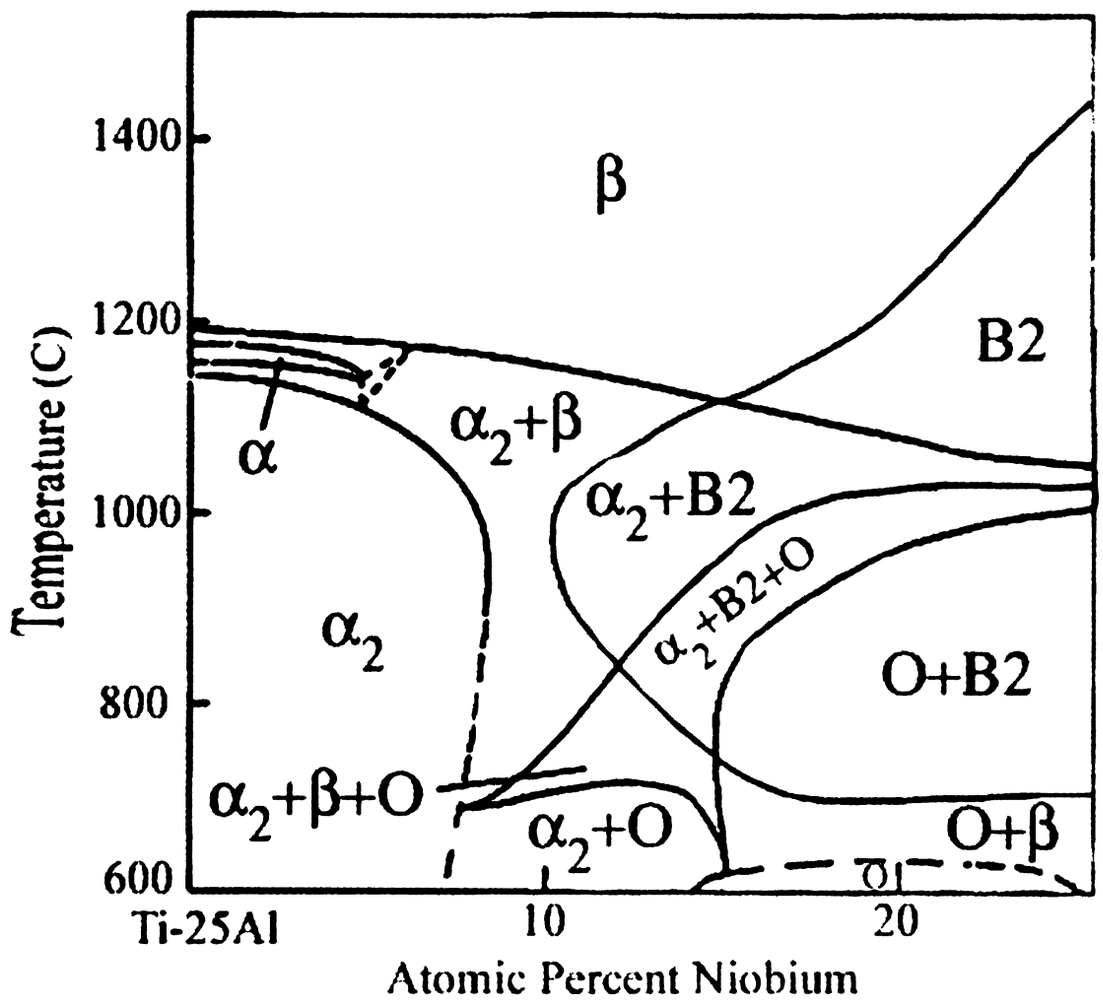

Figure 2.4 A depiction of a phase map based on Ti-25Al-xNb [Sagar *et al.*(1996)].

2. Quater

The

shown to

the BCC p

(Ca4). T

of Nb, wh

atoms pe

equivalen

24Ca1-Nb

19Nb. Th

Th

Ca4 is c

Ca4an. S

24Nb-1

24Ca1-Nb

Isolated

Isolated

Ca-centr

Ca, where

Ca4-Ca4

Ca4-Ca4

Nb1-Ca4

Ca4-Ca4

2. Quaternary Additions to Titanium-Aluminum-Niobium Alloys

The addition of BCC phase stabilizers to Ti_3Al based intermetallics has been shown to increase the RT elongation-to-failure and toughness due to the stabilization of the BCC phase and the formation of the O phase [Banerjee *et al.* (1993), Banerjee (1994)]. The BCC-phase stabilizing ability of Mo has been shown to be greater than that of Nb, where one atomic percent addition of Mo corresponds to the substitution of 4.25 atomic percent of Nb [Ankem and Seagle (1983), Tang *et al.* (2002)]. Therefore, the equivalent ternary Ti-Al-Nb compositions of the alloys investigated in this work, Ti-24Al-17Nb-0.66Mo, Ti-24Al-17Nb-1.1Mo, and Ti-24Al-17Nb-2.3Mo, are Ti-24Al-19.8Nb, Ti-24Al-21.7Nb, and Ti-24Al-26.8Nb, respectively.

The α_2, O, and BCC phase has been observed in a multitude of Ti-Al-Nb-Mo alloys including: Ti-24.5-17Nb-1Mo [Krishnamurthy *et al.* (1995), Krishnamurthy *et al.* (1995a), Smith and Graves (1995)], Ti-24Al-17Nb-1Mo [Zhang *et al.* (1998)], Ti-22Al-24.5Nb-1.5Mo [Smith *et al.* (1999)], Ti-22Al-19Nb-2Mo [Tang *et al.* (2002)], and Ti-22Al-11Nb-4Mo [Tang *et al.* (2002)]. The α_2 and BCC phases were shown to have an equiaxed morphology for a Ti-24Al-17Nb-1Mo alloy, whereas the O phase had either an equiaxed or lath morphology depending on heat treatment [Zhang *et al.* (1998)]. Furthermore, the lath size and spacing was found to be strongly dependent on the cooling rate, where a faster cooling rate (0.5°C/s) was shown to form O phase laths with widths ranging from 0.3 μm – 1.0 μm, while a slower cooling rate (0.2°C/s) resulted in widths ranging from 1 μm – 2 μm [Zhang *et al.* (1998)]. In comparison of a Ti-22Al-24.5Nb-1.5Mo alloy to a Ti-22Al-26Nb alloy, the Mo-containing alloy was shown to exhibit a finer O+BCC structure, which was attributed to the sluggish diffusion kinetics of Mo

[Smith *et al.* (1999)]. While studies have investigated Mo additions to Ti-Al-Nb alloys, to the author's knowledge, no studies have examined varying Mo additions to determine the effects of Mo content on the microstructure. Thus, this is one of the unique aspects examined in this dissertation.

3. Metal Matrix Composite Microstructures

One concern for MMCs is the microstructure at the fiber/matrix interface. An ideal interface is well consolidated and possesses a high bond strength. Previous work on SiC fiber composites revealed the formation of reaction products at the interface [Yang and Jeng (1989), Arsenault (1994), Smith *et al.* (1994), Larsen *et al.* (1995), Pickard and Miracle (1995), Boehlert (1997b)]. Analysis of this reaction zone has found it to be comprised of complex carbides and silicides [Rhodes (1992)]. In the development of SCS-6 and Ultra SCS-6 fibers, an amorphous carbon layer surrounding the SiC fibers was used to reduce the reaction between the fiber and the matrix [Smith *et al.* (1997)]. However, during processing of the MMCs, the carbon diffuses into the matrix of titanium alloys and stabilizes the α_2 phase. This results in the formation of an O+BCC depleted zone around the reaction zone, which can lead to reduced interfacial bond strengths.

C. Mechanical Properties

The varying combination of phases in the microstructure has a direct affect on the mechanical behavior of the alloy. O-phase alloys are advantageous for use in structural applications, when compared to $\alpha+\beta$ Ti-alloys, because they have exhibited greater elevated-temperature strength and creep resistance while also offering significant weight

savings over

Cowen and

(1991), Mis

and Miracle

I. Creep B

The

but the all

Creep testin

Tantamount

ties and pl

Specimen is

Then at a c

Finally (Tan

will be ve

Press here

at the begin

Creep where

Creep behav

Creeper with

Past

Test machine

Test Temp

savings over Ni-based super alloys [Nandy *et al.* (1993), Nandy and Banerjee (2000), Cowen and Boehlert (2006), Mendiratta and Lipsitt (1980), Malakondaiah and Rao (1981), Mishra and Banerjee (1990), Conrad *et al.* (1973), Nandy *et al.* (1995), Boehlert and Miracle (1999), Smith and Graves (1995)].

1. Creep Behavior Background

The main focus of the work performed was the creep deformation behavior of both the alloys and MMCs with fibers oriented perpendicular to the loading direction. Creep testing is performed when a specimen is placed under constant load while maintaining a constant temperature. Using extensometry, strain is measured during these tests and plotted versus time. The resulting curve consists of three regions. When the specimen is initially loaded, it undergoes instantaneous deformation then continues to strain at a continuously decreasing creep rate. This region on the curve is considered primary (transient) creep. The region on the curve in which the creep rate is constant is said to be secondary (steady-state) creep. The constant creep rate is due to a competing process between strain hardening and recovery [Garofalo (1965)]. Creep mechanisms can be suggested based upon the secondary creep rate. Tertiary creep follows secondary creep, where the creep rate deviates from linearity and increases, leading to creep rupture. Creep behavior is affected by stress and temperature, where the steady-state creep rate increases with increasing stress and/or increasing temperature.

Past research on creep deformation has led to the understanding of various microstructure-creep mechanisms. In these studies the steady-state creep rate was used to suggest dominant deformation mechanisms. Major deformation mechanisms include

Nabarro-Herring creep, Coble creep, Harper-Dorn creep, grain boundary sliding, and dislocation climb. The principles of these theories have been based on pure metals or single phase materials. There exists a lack of understanding of the creep deformation behavior for multiphase alloys in which all phases deform during creep testing. At similar testing conditions, the varying crystal structures and lattice arrangements of the phases results in different creep rates for each of the constituent phases, which makes creep difficult to study.

The steady state creep rate of a material is often modeled using a power law given by:

$$\dot{\varepsilon}_s = A\sigma^n \exp\left(\frac{-Q}{RT}\right) \tag{1.1}$$

where A is a constant, σ is the applied stress, n is the creep exponent, Q is the activation energy, R is the universal gas constant, and T is the absolute tempertature. Creep deformation behavior can be grouped as either diffusional or dislocation based. Nabarro-Herring and Coble creep are both considered to be diffusional creep processes. Dislocation glide and dislocation climb result in dislocation creep where a material is deformed due to the movement of dislocations.

1.1 Nabarro-Herring Creep

Diffusion often occurs due to the presence of vacancies in a material. One creep deformation mechanism proposed by Naborro and Herring involves the transport of vacancies through the crystal lattice due to applied stress [Nabarro (1948), Herring (1950)]. On an individual grain, an applied stress generates a tensile stress in the loading

direction and a compressional stress in the direction perpendicular to loading. Vacancies generate along the boundaries experiencing a tensile stress and deplete along the boundaries in compression [Evans and Wilshire (1993)]. There is a constant flow of vacancies from regions above equilibrium concentration to regions below equilibrium concentration. This vacancy flow results in grain elongation in the tensile direction, which is considered Nabarro-Herring creep. The steady state creep rate for Nabarro-Herring creep is given by:

$$\dot{\varepsilon}_s = K_1 \frac{D_{SD}}{d^2} \frac{\Omega \sigma}{kT} \tag{1.2}$$

where K_1 is a constant, D_{SD} is the coefficient of lattice self diffusion, d is the average grain diameter, Ω is the volume of a vacancy, and k is Boltzmann's constant [Evans and Wilshire (1993)]. Nabarro-Herring creep is commonly observed at low stress and high temperature creep conditions [Evans and Wilshire (1993)].

1.2 Coble Creep

Nabarro-Herring creep diffusion is considered to only occur through the crystal lattice. However, Coble proposed that diffusion of vacancies can occur along the grain boundaries as well [Coble (1963)]. This theory still predicted that vacancies were transferred due to an applied stress, where vacancies flowed from grain boundaries under tension to those under compression in an effort to restore an equilibrium concentration. The associated steady-state creep rate derived by Coble to describe the flow of vacancies through the grain boundaries is given by:

where K_2 is a co

suggested to be do

creep, but in lower t

1.3 Harper-Dorn

Harper-Dorn

ested at low stresse

rain rate, but it w

redicted by the N

It was therefore co

nd creep rate was

where A_{HD} is a

agnitude of the B

is the absolute te

It has been

e major deform

Furthe

ect on the strain

Harper-Dorn creep

ster than those

$$\dot{\varepsilon}_S = K_2 \frac{D_{GB}}{d^3} \frac{\delta \Omega \sigma}{kT} \qquad (1.3)$$

where K_2 is a constant and δ is the grain boundary spacing. This mechanism is suggested to be dominant at low stress levels of the same magnitude of Nabarro-Herring creep, but in lower temperature regimes.

1.3 Harper-Dorn Creep

Harper-Dorn creep was first proposed when coarse-grained aluminum creep tested at low stresses and high temperatures gave a linear relationship between stress and strain rate, but it was found that the strain rates were significantly higher than that predicted by the Nabarro-Herring and Coble creep equations [Harper and Dorn (1957)]. It was therefore concluded that a different mechanism controlled the creep deformation, and creep rate was determined to be given by:

$$\dot{\varepsilon}_S = \frac{A_{HD} D_L b \sigma}{kT} \qquad (1.4)$$

where A_{HD} is a material constant, D_L is the lattice diffusion coefficient, b is the magnitude of the Burger's vector, σ is the applied stress, k is Boltzmann's constant, and T is the absolute temperature [Harper and Dorn (1957)].

It has been proposed that intragranular diffusion-controlled dislocation motion is the major deformation mechanism occurring during Harper-Dorn creep [Ruano *et al.* (1988)]. Furthermore, previous work has indicated that variation in grain size had no effect on the strain rate [Owen and Langdon (1996)]. Therefore, it was suggested that Harper-Dorn creep is dominant when the creep exponent equals unity, the creep rates are higher than those predicted by the Nabarro-Herring and Coble creep equations, and

identical creep rate

(1966)].

1.4 Grain Bound

During creep

move relative to ea

process is called gr

and diffusional flow

Mayers and Chaw

grains.

Grain boun

ripped surface s

ligged at the ap

ggested to occur

s in a vacuum) [

e measured to sug

rface sliding, tha

terial as obser

Grain size

ch increases

all grain sizes r

terial, therefore

ticular, grains ty

identical creep rates are found over a wide range of grain sizes [Owen and Langdon (1996)].

1.4 Grain Boundary Sliding

During creep testing, a shear process occurs in which grains in a polycrystalline move relative to each other in the direction of the grain boundary [Dieter (1986)]. This process is called grain boundary sliding. Grain boundaries are translated by both sliding and diffusional flow of atoms from grain boundaries in compression to those in tension [Meyers and Chawla (1999)]. Commonly, there is very little strain exhibited within the grains.

Grain boundary sliding is most easily observed using a metallographically-prepared surface scribed with fiducial marks. The specimen is then creep tested and imaged at the appropriate stress and temperature where grain boundary sliding is suggested to occur and where there are no environmental effects to damage the surface (i.e. in a vacuum) [Dieter (1986)]. The amount of offset in the fiducial markings can then be measured to suggest the amount of sliding occurring. While this method does show surface sliding, there is doubt as to whether this represents the bulk behavior of the material as observations of internal deformations cannot be made.

Grain size has an important effect on the amount of sliding. Smaller grain sizes result in increases in the amount of grain boundary sliding. This is due to the fact that small grain sizes result in an increase in the total number of grain boundaries in the material, therefore presenting more chances for slip to favorably occur along a boundary. In tension, grains typically slide in the direction of the tensile axis.

1.5 Dislocation

Creep defo

by vacancy diffus

when there is a

rearrangement and

during creep testin

controlled by the

governed by atom

deformation mecha

dominant at interm

1.6 Creep Expo

The values

dominant deform

parameters are fou

reep exponent is

ntact log σ. Whi

Slope of the ln

steady-creep r

Creep exp

Bates and W

activities is the

While creep is m

1.5 Dislocation Climb

Creep deformation due to dislocation climb occurs when dislocation glide is aided by vacancy diffusion [Dieter (1986)]. Under this regime, steady state creep is obtained when there is a balance of strain hardening and thermal recovery due to the rearrangement and annihilation of dislocations [Dieter (1986)]. The strain produced during creep testing is a result of dislocation glide, and the velocity this occurs at is controlled by the time it takes for a dislocation to climb to surmount an obstacle, which is governed by atomic diffusion [Dieter (1986)]. The steady state creep rate for this deformation mechanism is given by Equation (1.1). This model is suggested to be dominant at intermediate to high stress levels and at temperatures above $0.5T_m$.

1.6 Creep Exponents and Activation Energies

The values of the creep exponents and activation energies provide insight as to the dominant deformation mechanisms occurring during steady-state creep. These parameters are found using the minimum creep rate determined during creep testing. The creep exponent is found when a power law curve fit is applied to a plot of the log $\dot{\varepsilon}_{min}$ versus log σ, while the activation energy is found when a linear curve fit is applied to a plot of the ln $\dot{\varepsilon}_{min}$ versus 1/T. Using these values, deformation mechanisms active in the secondary-creep regime are suggested.

Creep exponent values tend to range from one to five for pure metals and alloys [Evans and Wilshire (1993)]. Values close to unity suggest that atomic diffusion of vacancies is the dominant deformation mechanism, implying that Nabarro-Herring or Coble creep is most active. In the case of Nabarro-Herring creep, activation energies are

found to be clos

energies are typ

vacancies throug

found to be appr

self diffusion [G

to eight dislocat

activation energi

ring creep expe

ggested at part

While cr

dynamic defor

deep deformatio

help verify the

a microscope

deformation as

grain boundary

electron microsc

dislocation activ

techniques with

to be suggest

found to be close to those for lattice self diffusion, while for Coble creep activation energies are typically 0.5 – 0.6 of those for lattice self diffusion due to diffusion of vacancies through the grain boundaries. For grain boundary sliding, creep exponents are found to be approximately two, and typical activation energies are close to those of lattice self diffusion [Garafalo (1965)]. When the creep exponent falls within the range of three to eight, dislocation climb is said to be dominant [Weertman (1957)]. In this regime, activation energies correspond closely with those of lattice self diffusion. Therefore, by using creep exponent and activation energy values, creep deformation mechanisms can be suggested at particular stress ranges and temperatures.

While creep exponents and activation energies are helpful in suggesting the dominant deformation mechanism, they are not definite. Therefore, techniques in which creep deformation is observed as it occurs have been developed. One such method used to help verify the dominant creep mechanisms is *in-situ* testing, where a sample is imaged in a microscope throughout the creep experiment. In doing this, the evolution of creep deformation as it occurs is documented. This technique is especially useful for observing grain boundary sliding when fiducial markings are on the specimen. Transmission electron microscopy of post-creep deformed microstructures is also used to observe the dislocation activity present within each of the phases. When combining these visual techniques with the creep exponent values and apparent activation energies a more resolute suggestion of the dominant deformation mechanism is obtained.

1.7 Creep of T

The creep

developed. Creep

and BCC. The

increasing volum

Majumdar *et al.*

by the superior c

of available slip

microstructures

warranted.

The creep

ealized in a st

Fig. 1. The all

ariations of gr

experiments were

ree microstructu

= 5 at high stre

= 3 in the low-

as found to be

gh-stress regime

35 kJ/mol. In t

ems to be the d

ments were cl

1.7 Creep of Titanium-Aluminum-Niobium Alloys

The creep behavior of Ti-Al-Nb alloys with various microstructures has been well developed. Creep of these alloys can be correlated to the phase volume percents of α_2, O, and BCC. The creep resistance of Ti-Al-Nb alloys has been shown to increase with increasing volume percent of O phase and with decrease volume percent of α_2 phase [Majumdar *et al.* (1995), Smith *et al.* (1995)]. While this observation can be explained by the superior creep resistance of fully O-phase microstructures due to a small number of available slip systems [Nandy *et al.* (1993)] compared to that of fully α_2-phase microstructures [Mendiratta and Lipsitt (1980)], further understanding of Ti-Al-Nb alloys is warranted.

The creep behavior of α_2, α_2 + BCC, and BCC based Ti-Al-Nb alloys has been evaluated in a study of Ti-24Al-11Nb by Mishra and Banerjee [Mishra and Banerjee (1990)]. The alloys underwent three different heat treatments to produce microstructural variations of: 90% α_2 – 10% BCC, 40% α_2 – 60% BCC, and 100% BCC. Creep experiments were conducted in the stress range of 30 – 400 MPa at 650° C. Tests of all three microstructures revealed a change in creep exponent from n = 1 at low stresses to n = 5 at high stresses. The apparent creep activation energy of the 40% α_2 – 60% BCC alloy in the low-stress regime was 107 kJ/mol, while the 100% BCC in the same regime was found to be 120 kJ/mol, each over the temperature range of 525°C – 725°C. In the high-stress regime the apparent activation energy for the 40% α_2 – 60% BCC alloy was 260 kJ/mol. In the low-stress regime the n values and Qapp values suggested Coble creep to be the dominant creep deformation mechanism, where the apparent activation energies were close to those obtained for grain boundary diffusional creep in pure Ti (104

- 121 kJ mol) [M.

climb was suggest

Qapp values of t

dislocation climb

(900), and pure

Table 2.1.

Table 2.1 Dislocat

Creep Parameter	Ti-24
Qapp (kJ mol)	
n	

The creep be

Q-phase Ti-

Compression creep

55°C – 750°C

activation energy of

creep was suggested

knowledge, no diff

activation energy to

Q-phase are com

– 121 kJ/mol) [Malakondaiah and Rao (1981)]. In the high-stress regime, dislocation climb was suggested to be the dominant creep deformation mechanism. The n and Qapp values of the Ti-24Al-11Nb alloy were found to compare favorably to the dislocation climb controlled creep parameters of α_2 alloys [Mendiratta and H.A. Lipsitt (1980)], and pure Ti [Malakondaiah and Rao (1981), Conrad *et al.* (1973)], as shown in Table 2.I.

Table 2.I Dislocation Climb Controlled Creep Parameters

Creep Parameter	**Ti-24Al-11Nb**	**α_2**	**α-Ti**
Qapp (kJ/mol)	260	285 (Ti_3Al+5Nb) 206 (Ti_3Al)	242 [Conrad *et al.* (1973)] 241 [Malakondaiah and Rao (1981)]
n	5	6 (Ti_3Al+5Nb) 4.3 (Ti_3Al)	4.5 [Conrad *et al.* (1973)] 4.3 [Malakondaiah and Rao (1981)]

The creep behavior of the O-phase was characterized through experimentation of a fully O-phase Ti-27Al-21Nb alloy by Nandy and coworkers [Nandy *et al.* (1993)]. Compression creep tests in the stress range of 240 MPa – 500 MPa and temperature range of 650°C – 750°C revealed creep exponent values ranging from 5.7 to 7.5 and an activation energy of 340 kJ/mol. Based on these values, dislocation climb controlled creep was suggested to be the dominant deformation mechanism. While, to the author's knowledge, no diffusion data is available for the O-phase, comparison of the apparent activation energy to diffusion data of Ti_3Al suggests that the Qapp values determined for the O-phase are consistent with lattice self-diffusion, see Table 2.II.

Table 2.II Se

The Bu

Cowen (Cow

5 MPa and

observed, wh

The apparent

stress regime

grain bounda

[Mor].

A list

Table 2.III

microstructur

ange from a

the apparent

Activation

respectively

the linearity

number of a

Table 2.II Self-Diffusion and Inter-Diffusion Data for Ti_3Al [Rusing and Herzig (1996)]

Element	D_o (m^2s^{-1})	Q (kJ/mol)
Ti in Ti_3Al	$2.44x10^{-5}$	288
Al in Ti_3Al	$2.32x10^{-1}$	374
Ti_3Al	$1x10^{-5}$	312

The BCC phase creep behavior has been characterized for a Ti-5Al-45Nb alloy by Cowen [Cowen (2006)]. Tensile creep tests carried out over a stress range of 10 MPa – 75 MPa and a temperature range of 650°C – 710°C. A change in creep exponent was observed, where in the lower stress regime n = 0.7 and in the higher stress regime n = 2.6. The apparent activation energy in the low-stress regime was 184 kJ/mol and in the high-stress regime was 217 kJ/mol. Indications of Coble creep in the low-stress regime and grain boundary sliding in the high-stress regime were observed for this alloy [Cowen (2006)].

A list of the creep parameters for other Ti-Al-Nb O phase alloys is provided in Table 2.III. A comparison of fully O phase, O+BCC, and fully BCC phase microstructures is shown in Figure 2.5. As shown, the creep exponent in these alloys can range from approximately unity to values greater than five. These values, coupled with the apparent activation energies, suggest Coble creep, grain boundary sliding, and dislocation climb to be active in these alloys at low, intermediate, and high stresses, respectively. As observed in Figure 2.5, the creep resistance of fully O-phase alloys is significantly higher than that of fully BCC and O+BCC phase alloys due to the smaller number of available slip systems in the O-phase.

Table 2.III V

Alloy Com
Ti-22A
Woodard a
(Woo
Ti-21A
Smith et a
Ti-21A
Woodard et
Ti-22A
Hayes
Ti-25A
Bowe and L
Ti-25A
Bowe and L
Ti-24A
Nandy et
Ti-27A
Nandy et
Ti-22A
Bowe and L
Ti-22A
Bowe and L
Ti-27A
Nandy et
Ti-21A
Smith et
40° arc quen
Mill heat as

Table 2.III Various Orthorhombic Alloy Creep Parameters

Alloy Composition	Heat Treatment	Testing Conditions σ/T, (MPa,°C)	n	Qapp, (kJ/mol)
Ti-22Al-23Nb [Woodard and Pollock (1997)]	NA	69-110/650 air + vacuum	1.3	187
Ti-21Al-22Nb [Smith *et al.* (1993)]	NA	30-90/650-760 air	1.4	NA
Ti-21Al-21Nb [Woodard *et al.* (1996)]	NA	69-172/650 vacuum	2.4	NA
Ti-22Al-23Nb [Hayes (1996)]	996°C/1h/AQ	69-172/650-760 air + argon	2.8	327
Ti-25Al-23Nb [Rowe and Larsen (1996)]	815°C/1h	175-310/650 argon	2.8	NA
Ti-25Al-23Nb [Rowe and Larsen (1996)]	1065°C/1h/Ar + 815°C/1h	310-380/650 argon	2.8	NA
Ti-24Al-16Nb [Nandy *et al.* (1995)]	1150°C/1h/CC + 750°C/24h/AQ	150-540/700-750 air	4.2-4.3	371
Ti-27Al-16Nb [Nandy *et al.* (1995)]	1170°C/1h/CC + 750°C/24h/AQ	240-660/700-750 air	4.2-4.3	376
Ti-22Al-27Nb [Rowe and Larsen (1996)]	1090°C/1h/Ar + 815°C/1h	175-310/650 argon	5.3	NA
Ti-22Al-27Nb [Rowe and Larsen (1996)]	815°C/1h	310-380/650 argon	5.3	NA
Ti-27Al-21Nb [Nandy *et al.* (1993)]	1170°C/OQ + 900°C/AQ	240-500/650-750 air	5-6	340
Ti-21Al-22Nb [Smith et al. (1993)]	NA	90-172/650-760 air	8.2	197

AQ: air quench, OQ: oil quench, Ar: cooled in static Ar gas, CC: control cool at 2.5°C/s, NA: not available

- Ti-5Al-45N
- Ti-12Al-38N
- Ti-15Al-33N
- [illegible]
- Ti-26Al-27N
- [illegible]

Minimum Creep Rate (s^{-1})

10^{-7}

10^{-8}

10^{-9}

10^{-10}

[illegible]

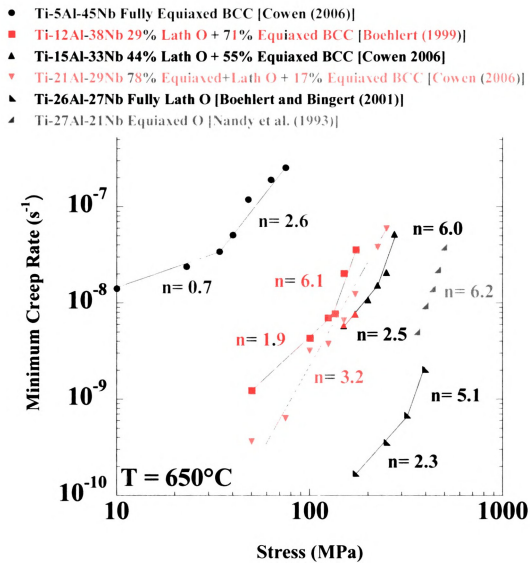

Figure 2.5 A comparison of fully O-phase, O+BCC, and fully BCC phase alloys creep tested at 650ºC [Cowen (2006)].

1.8 Creep of Ti

Only a har

alloys (Rowe (19

Graves (1995). Zr

Mo alloys were s

studies revealed th

Krishnamurthy (19

(1966)]. In fact, a

did not rupture eve

ternary alloy (Ti-22

greater than 20%

comprising Ti-25Al-

et al (1995)]. Such

solid solution stren

active creep mecha

discussed previous

shown to exhibit th

al (1995)]. There

W. Ankem and Se

exhibit equivalent

creep resistance ca

properties than that

1.8 Creep of Titanium-Aluminum-Niobium-Molybdenum Alloys

Only a handful of studies have evaluated the creep behavior of the Ti-Al-Nb-Mo alloys [Rowe (1992), Kerry and Winstone (1995), Kristnamurthy (1995), Smith and Graves (1995), Zhang *et al.* (1998), Smith *et al.* (1999), Tang *et al.* (2002)]. Ti-Al-Nb-Mo alloys were sometimes tested in comparison to ternary Ti-Al-Nb alloys, and all studies revealed that creep resistance is significantly increased for alloys containing Mo [Kristnamurthy (1995), Majumdar *et al.* (1995), Smith and Graves (1995), Smith *et al.* (1999)]. In fact, a Ti-24.5Al-17Nb-1Mo alloy exhibited creep strains less than 2% and did not rupture even after 700 h of testing at 650°C and 172 MPa, whereas the baseline ternary alloy (Ti-24.5Al-17Nb) failed in less than 50 hours and exhibited creep strains greater than 20% [Smith and Graves (1995)]. This trend was also shown for a study comparing Ti-25Al-17Nb-1Mo to Ti-25Al-17Nb, as also shown in Figure 2.6 [Majumdar *et al.* (1995)]. Such improvements in alloys with Mo additions have been attributed to solid solution strengthening of the BCC phase and to a decrease in creep rate for the active creep mechanisms which were diffusion dependent [Smith *et al.* (1999)]. As discussed previously, the O phase, which precipitates out of the BCC phase, has been shown to exhibit the best creep resistance of any of the ordered phases present [Nandy *et al.*(1993)]. Therefore, since Mo is a more effective BCC-phase stabilizing element than Nb [Ankem and Seagle (1983)], smaller additions of Mo than that of Nb are needed to stabilize equivalent amounts of BCC phase. It follows then that an improvement in creep resistance can be obtained in alloys with small additions of Mo and with lower densities than that of Ti-Al-Nb alloys.

ure 26 A plot
Nb-1Mo, a
heat treat
displayed gre

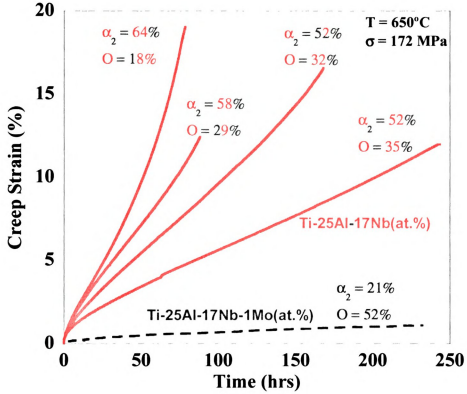

Figure 2.6 A plot of creep strain versus time for a Ti-25Al-17Nb alloy (red) and a Ti-25Al-17Nb-1Mo alloy (blue). Each curve for the Ti-25Al-17Nb alloy represents a different heat treatment used to vary the phase volume percents. The Ti-25Al-17Nb-1Mo alloy displayed greater creep resistance than any of the Ti-25Al-17Nb alloys tested.

In a study

temperature range

(2002)]. This v

mechanism (i.e. d

have a stronger a

Jiang *et al.* (2002

in BCC phase vol

that of the BCC p

the O phase within

Mo alloy, a

than that of coarse-

activation energy f

range of 650°C –

properties of the Ti-

temperatures. For

suggested to be the

Table 2.IV The exce

Microstructur
Fine-lath
Coarse-lath
Equiaxed

In a study of a Ti-22Al-19Nb-2Mo alloy, the apparent activation energy over the temperature range of 650°C – 750°C at 310 MPa was found to be 354 kJ/mol [Tang *et al.* (2002)]. This value was suggested to correspond to a dislocation-controlled creep mechanism (i.e. dislocation climb). This study also found that quaternary additions can have a stronger affect on the minimum creep rate than the BCC phase volume fraction [Tang *et al.* (2002)]. Typically creep strain rates were found to decrease with a decrease in BCC phase volume fraction, as the O and α_2 phases exhibit better creep resistance than that of the BCC phase [Cho *et al.* (1990), Rowe and Larsen (1996)]. The orientation of the O phase within Ti-Al-Nb-Mo alloys affects the creep resistance. For a Ti-25Al-17Nb-1Mo alloy, a fine-lath microstructure was shown to have a higher creep resistance than that of coarse-lath and equixed microstructure [Zhang *et al.* (1998)]. The apparent activation energy for that fine-lath microstructure was found to be 247 kJ/mol in the range of 650°C – 750°C at 300 MPa [Zhang *et al.* (1998)]. Table 2.IV shows the creep properties of the Ti-25Al-17Nb-1Mo alloy with various microstructures tested at different temperatures. For the fine-lath and coarse-lath microstructures dislocation climb was suggested to be the dominant deformation mechanism [Zhang *et al.* (1998)].

Table 2.IV The creep properties of a Ti-24Al-17Nb-1Mo alloy [Zhang *et al.* (1998)]

Microstructure	Phases	Temperature (°C)	n value
Fine-lath	O+BCC	650	4.4
		700	3.4
		750	3.6
Coarse-lath	O+BCC	650	4.3
		750	4.3
Equiaxed	α_2+O+BCC	600	1.3
		650	1.9

1.9 Metal

1.9 Metal Matrix Composite Creep

The addition of SiC fibers to a titanium alloy has the ability to increase the strength and creep resistance when the material is loaded with the fibers parallel to the loading direction. However, the transverse strength and creep resistance can be worse than the matrix itself [Majumdar and Newaz (1992)]. Improvements in transverse creep behavior can be obtained through increases in matrix creep resistance and fiber/matrix interfacial bond strength [Majumdar and Newaz (1992)]. The former method often results in a decrease in elongation to failure, which is undesirable. The latter method is more promising, as damage evolution often begins with fiber debonding, resulting in the material behaving similar to a matrix material with holes [Majumdar and Newaz (1992)].

Previous work has shown the creep response of a MMC tested with fibers perpendicular to the loading direction is similar to that of an alloy in that it exhibits primary, secondary, and tertiary creep regimes [Majumdar and Newaz (1992)]. However, when tested in this orientation, minimum creep rates of MMCs were typically higher than that of the unreinforced matrix [Gambone (1989), Jansson *et al.* (1991), Eggleston and Ritter (1995), John *et al.* (1996)]. In these studies it is generally assumed that the interface has no strength and that separation of the matrix from the fibers occurs as soon as the local stress is sufficient enough to overcome the residual thermal stresses. It has been established that a tensile residual stress singularity exists at the fiber/matrix interface from residual stresses where fibers intersect a free surface [Warrier *et al.* (1996)]. This stress is sufficient enough to result in premature fiber/matrix separation, which limits the creep resistance of the composite [Miracle and Majumdar (1999)]. It was therefore suggested that this stress singularity must be avoided by embedding the

fiber in orde

Miracle an

2. Tensile

The

The von M

grains in a

Due to its

limited nu

HCP struc

{1 1 1} plane

yields thre

shape cha

not allow

and there

this lack

At ambi

shear bu

Schmid's

Fig. 1. (a

Fig. 1. (a

fiber in order to obtain minimum creep rates lower than that of the unreinforced matrix [Miracle and Majumdar (1999)].

2. Tensile Behavior Background

The elongation-to-failure (ε_f) of a material is dependent on dislocation motion. The von Mises Criterion states that five independent slip systems must be operable for grains in a polycrystalline metal to undergo a plastic shape change [von Mises (1913)]. Due to its hexagonal structure, the α_2 phase commonly found in Ti-Al-Nb alloys has a limited number of active slip systems at ambient and elevated temperatures. Slip in the HCP structure has been shown to occur most readily on the (0001), {10-10}, and {10-11} planes in the 1/3<11-20> directions [Reed-Hill and Abbaschian (1994)]. This only yields three slip systems per unit cell, which is less than that necessary to exhibit plastic shape change according to the von Mises Criterion. Furthermore, these slip systems do not allow shape change in the <c> direction. Such slip possesses a larger Burger's vector and therefore a larger critical resolved shear stress than slip in the <a> direction. Due to this lack of slip systems, cracking at α_2/α_2 grain boundaries is often observed for Ti-Al-Nb alloys in order to accommodate the stress concentration due to dislocation pileup at α_2 phase boundaries [Gogia *et al.* (1992), Majumdar *et al.* (1995)].

Although the O phase is similar in structure to the α_2 phase, the deformation mechanisms of each phase differ. A previous study of Ti-26Al-21Nb O-based and Ti-27Al-10Nb α_2-based alloys revealed that <a> and <c+a> slip systems were active in the O phase, while only <a> slip was apparent in the α_2 phase [Banerjee (1995)]. Based on this, it was concluded that the relative critical resolved shear stress for the <c+a> slip

system in the O p

in the [100] direc

the (110) and (0

observed in the (2

The close-

structure lacks a

This phase has bee

and {123} family

slip systems (com

alloys with increa

2.1 Tensile Be

The ten

composition, ph

compositional ch

has a significant

2Nb alloy was

% while a fu

The Boehlert

2Nb alloy had

alloys containi

7.25Al-21Nb

Rae et al

system in the O phase was less than that in the α_2 phase. For O phase alloys, slip occurs in the [100] direction, on the (001) plane. For prismatic slip, [110] dislocations occur in the (110) and (001) planes, and for pyramidal slip [114] and [102] dislocations were observed in the (2-21) plane [Banerjee (1995)].

The close-packed direction in the BCC phase is <111>. However, the BCC structure lacks a true close packed plane in which dislocation motion can easily occur. This phase has been shown to have 48 slip systems, which incorporate the {110}, {112}, and {123} family of planes [Reed-Hill and Abbaschian (1994)]. This large number of slip systems (compared to that of the O phase and α_2 phase) tends to provide Ti-Al-Nb alloys with increases in ε_f and increased fracture toughness.

2.1 Tensile Behavior of Titanium-Aluminum-Niobium Alloys

The tensile properties of Ti-Al-Nb alloys are dependent upon the phase composition, phase volume fraction, and grain size, where all can be adjusted through compositional changes and heat-treatments. In particular, the ordering of the BCC phase has a significant effect on the strength and ε_f of titanium aluminides. A fully B2 Ti-25Al-24Nb alloy was shown to have an ultimate tensile strength (UTS) of 672 MPa and an ε_f of 0.6% while a fully β Ti-12Al-28Nb alloy had an UTS of 566 MPa and an ε_f greater than 27% [Boehlert (2001)]. In the same study, a fully-O phase microstructure of a Ti-25Al-24Nb alloy had an UTS of 704 MPa and an ε_f of 1% [Boehlert (2001)]. Other studies of alloys containing the α_2, BCC, and O phases have shown ε_f values as low as 0.4% for a Ti-25Al-21Nb heat-treated at 1050°C for 1h in argon then aged at 815°C for 2h in argon [Rowe *et al.* (1991)] and as high as 15.1% for a Ti-15Al-45Nb alloy heat-treated at

1650°C for 4

strengths as h

at 1000°C fo

2Nb alloy h

The F

also shown i

on heat trea

temperature

BCC region

simple frac

Boehlert et

Slip

were planar

This obser

<111>{1

Chan et

boundaries

dependen

therefore s

boundaries

Hall-Petch

Hall-Petch a

have and

1050°C for 4h then aged at 800°C for 24h [Austin *et al.* (1993)]. Ultimate tensile strengths as high as 1415 MPa have been observed for a Ti-22Al-25Nb alloy heat-treated at 1000°C for 1h in argon then aged at 815°C for 2 h in argon and also for a Ti-22Al-27Nb alloy heat-treated at 815°C for 1h in argon [Rowe *et al.* (1991)].

The RT tensile properties of Ti-25Al-17Nb alloys are presented in Table 2.V and also shown in Figure 2.7. As shown, ε_f values can range from 1.1% to 10.7% depending on heat treatment. These studies indicate that solutionizing above the BCC transus temperature was detrimental to the ε_f values compared to solutionizing within the α_2 + BCC region. Fracture surfaces revealed a mixture of cleavage, faceted, and ductile dimple fractures in the α_2, O, and BCC phases, respectively [Boehlert *et al.* (1997), Boehlert *et al.* (1997b)].

Slip has been observed to occur within each phase. In the α_2 phase slip bands were planar [Majumdar *et al.* (1995), Boehlert *et al.* (1997), Boehlert *et al.* (1997b)]. This observation was due to the predominant slip system in the α_2 phase being a-type <1120> dislocations on prismatic {01-10} planes and to the lack of <c+a> slip bands [Court *et al.* (1990), Shastry and Lipsitt (1977)]. Cracking between the α_2/α_2 grain boundaries was predominant, which likely resulted from unavailability of five independent slip systems, as previously discussed [Majumdar *et al.* (1995)]. This therefore suggested that it would be beneficial to limit the number of α_2/α_2 grain boundaries in Ti-Al-Nb alloys. Slip in the O phase was also observed to be predominantly planar [Majumdar *et al.* (1995), Boehlert *et al.* (1997)]. However, cracking at grain boundaries was less apparent due to the existence of <c+a> slip in the O phase and the existence of ductile BCC phase adjacent to the O phase, which both

prevent the

Muraleedh

0 and BCC

to one of t

shown to m

been show

around the

Boehlert a

suggestive

plays an im

prevent the development of large stress concentrations due to dislocation pileup [Muraleedharan *et al.* (1992)]. Furthermore, there exists a slip compatibility between the O and BCC phases, where the dominant slip vector in the BCC phase (<111>) is parallel to one of the dominant slip vectors in the O phase (<110>). Dislocations have been shown to transmit from the O phase into the BCC phase without deflection and have also been shown to be jogged at BCC laths [Majumdar *et al.* (1995)]. When cracks form around the O phase, the BCC phase has been shown to be an effective crack blunter [Boehlert *et al.* (1997)]. Slip in the BCC phase has been shown to be wavy, which is suggestive of cross-slip [Majumdar *et al.* (1995)]. Based on these observations, the BCC plays an important role in imparting ductility to O-phase alloys.

Table 2.V RT Te

Alloy
Ti-25Al-17Nb [Majumdar *et al.* (1995)] Forged – Hot Rolled
Ti-25Al-17Nb [Boehlert *et al.* (2007)] Forged – Hot Rolled
Ti-25Al-17Nb [Boehlert *et al.* (2007b)] Forged – Hot Rolled
Ti-24.5Al-17Nb [Krishnamurthy *et al.* (1995b)]* Foil Stack – HIP
Ti-24.5Al-17Nb [Krishnamurthy *et al.* (1995b)] Foil Stack – HIP

* Quenched; TC
Represents av

Table 2.V RT Tensile properties of Ti-25Al-17Nb alloys.

Alloy	Heat Treatment	Phase Volume Percent			YS (MPa)	UTS (MPa)	ε_f (%)
		α_2	BCC	O			
Ti-25Al-17Nb [Majumdar *et al.* (1995)] Forged + Hot Rolled	As-Rolled	64.1	35.9	0	681	775	10.7
	1050°C/1h/q/850°C/ 2h/fc	57.5	23.9	18.6	691	906	14.0
	1050°C/1h/cc/850°C/ 2h/fc	53.4	25.8	20.8	564	805	10.7
	1050°C/1h/q/850°C/ 24h/q	41.3	17.6	41.1	745	912	5.5
	1075°C/1h/cc/850°C/ 24h/fc	43.3	13.0	43.7	587	780	9.5
	1125°C/1h/cc/850°C/ 2h/fc	17.1	18.9	64.0	547	785	10.2
	1190°C/0.25h/a	NA	NA	NA	NA	1154	1.2
	1190°C/0.25h/a/850° C/ 24h/a	NA	5	NA	783	810	1.1
Ti-25Al-17Nb [Boehlert *et al.* (1997)] Forged + Hot Rolled	1125°C/1h/cc/850°C/ 2h/fc	NA	NA	NA	547	785	10.2
Ti-25Al-17Nb [Boehlert *et al.* (1997b)] Forged + Hot Rolled	As-Processed	74.8	16.3	8.9	781	801	1.1
	1050°C/1h/cc/850°C/ 2h/FC	64.1	19.2	16.7	670	759	4.0
Ti-24.5Al-17Nb [Krishnamurthy *et al.* (1995b)]* Foil Stack + HIP	As-Processed	NA	NA	NA	NA	780	1.1
Ti-24.5Al-17Nb [Krishnamurthy *et al.* (1995)] Foil Stack + HIP	As-Processed	75	10	15	750	760	1.3
	1050°C/1h/cc/850°C/ 2h/fc	NA	NA	NA	760	825	4.1

q: quenched; fc: furnace cooled; cc: control cooled 28°C/min; NA: Not available
*Represents averaged results

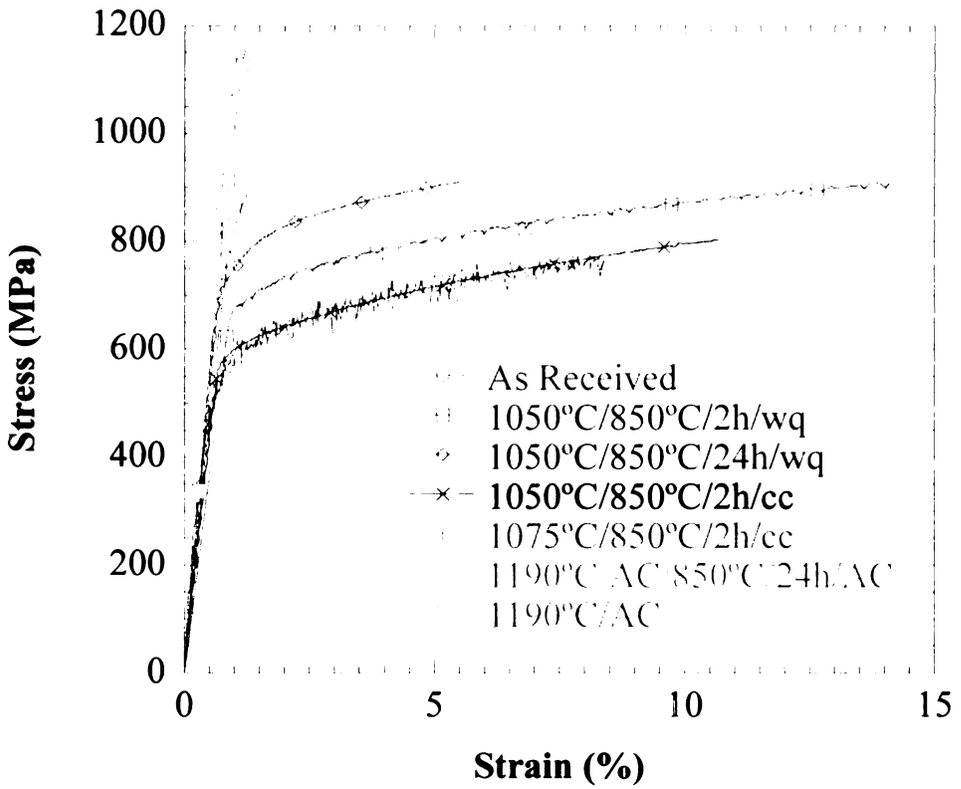

Figure 2.7 Heat treating Ti-25Al-17Nb at 1050°C followed by aging at 850°C for two hours resulted in increases in ε_f values, whereas higher-temperature, supertransus heat treatments embrittled the alloy (unpublished data).

2.2 T
Alloys

Increase

fracture

Targ e

addition

so that

tendency

as Mo, h

shown to

Table 2.

Alloy	
Ti-24.5Al [Krishnam (1995)]	
Ti-22Al-2 [Smith et a	
Ti-22Al-1 [ ] [ ] et a	

Tested in

Tested p

2.2 Tensile Behavior of Titanium-Aluminum-Niobium-Molybdenum Alloys

The addition of BCC phase stabilizers to titanium aluminides has resulted in an increase in ε_f values, higher yield strengths, improved creep resistances, and higher fracture toughness values over ternary Ti_2AlNb-based titanium aluminides [Rowe (1992), Tang *et al.* (2000)]. A compilation of tensile properties of Ti-Al-Nb alloys with Mo additions is presented in Table 2.VI. While the amounts of Al and Nb vary in the alloys so that the sole effect of Mo cannot be deduced, increasing amounts of Mo have the tendency to increase the UTS, but decrease the ε_f. Substitutional additions for Nb, such as Mo, have not resulted in changes to the deformation mechanisms, but Mo has been shown to be an effective strengthening enhancer [Nandy and Banerjee (2000)].

Table 2.VI The RT tensile properties of Ti-Al-Nb-Mo alloys.

Alloy	Processing Route	Heat Treatment	YS (MPa)	UTS (MPa)	ε_f (%)
Ti-24.5Al-17Nb-1Mo [Krishnamurthy *et al.* (1995)]	Foil Stack + HIP + Hot Rolled*	As-Processed	688	845	8.4
	Foil Stack + HIP + Hot Rolled**	As-Processed	-	806	0.54
Ti-22Al-24.5Nb-1.5Mo [Smith *et al.* (1995)]	Tape Cast	As-Processed	NA	1070	0.9
	Tape Cast	1150°C/10min/cc +815°C/8h/fc	NA	985	2.0
Ti-22Al-11Nb-4Mo [Tang *et al.* (2002)]	Forged	1050°C/1h/wq +850°C/33h/wq	950	1000	0.3

*Tested in rolling direction

**Tested perpendicular to rolling direction

2.3 Tensile Be

Titanium

strength and stiff

the matrix has be

during longitudi

parallel to the loa

of the matrix to d

the tensile proper

the room-temper

2.VII. As shown

fracture was loca

indicated the lac

would be expecte

Table 2.VII RT t

MMC

SCS-6 Ti-25Al-

B. Gilbert et al. (

SCS-6 Ti-24.5A

Konstantinsky e

SCS-6 Ti-24.5A

Konstantinsky e

2.3 Tensile Behavior of Metal Matrix Composites

Titanium alloys are joined with SiC fibers in an attempt to combine the high strength and stiffness of the fiber with the damage tolerance of the alloy. The ductility of the matrix has been shown to significantly influence efficient utilization of fiber strength during longitudinal loading [Boehlert (1997b)]. When tensile tested with the fibers parallel to the loading direction, the properties of the MMC are dependent on the ability of the matrix to distribute the applied load to the fibers. Recent studies have investigated the tensile properties of various titanium alloys with SCS-6 fiber additions. Several of the room-temperature (RT) tensile properties of these MMCs are presented in Table 2.VII. As shown, ε_f values are typically less than 1.5%. Fractography revealed that fiber fracture was localized around the fracture plane [Boehlert *et al.* (1997b)]. This behavior indicated the lack of global load sharing among the fibers, where if present fiber pull-out would be expected.

Table 2.VII RT tensile data of MMCs tested with fibers parallel to the loading direction.

MMC	Heat Treatment	UTS (MPa)	ε_f (%)	E (GPa)
SCS-6/Ti-25Al-17Nb [Boehlert *et al.* (1997b)]	As-Processed	1367	0.86	192.6
	1050°C/1h/cc/850°C/2h/fc	1579	1.15	170.3
SCS-6/Ti-24.5Al-17Nb [Kristnamurthy *et al.* (1994)]	As-Processed	1490	0.85	NA
SCS-6/Ti-24.5Al-17Nb-1Mo [Kristnamurthy *et al.* (1995)]	As-Processed	1585	1.0	184.6

3. Out-of-Pha

Materials

temperatures th

thermomechanic

there exists a lar

leads to high inte

al. [1992]]. Simp

situations. Simp

loads and tempera

maximum load o

condition are show

Under sim

fatigue lifetimes

shown to overes

real life-limiting

Previous testing

phase TMF is do

(1991). Russ et a

the fiber and m

the fiber and the

for the fiber d

experience a tem

the tensile stres

3. Out-of-Phase Thermomechanical Fatigue Background

Materials used in aerospace applications are subjected to stresses and temperatures that can vary simultaneously. These conditions are recognized as thermomechanical fatigue (TMF). TMF tests are important to MMCs in particular since there exists a large thermal expansion mismatch between the matrix and the fiber, which leads to high interfacial stresses when subjected to thermomechanical loadings [Mall *et al.* (1992)]. Simple TMF conditions are typically used as the basis for more complex situations. Simple conditions include in-phase TMF, where the maximum/minimum loads and temperatures occur simultaneously, and out-of-phase (OOP) TMF, where the maximum load occurs at the minimum temperature and vice versa. Schematics of each condition are shown in Figure 2.8 and Figure 2.9, respectively.

Under similar stress and temperature levels, TMF testing tends to result in lower fatigue lifetimes in comparison to isothermal fatigue. Isothermal fatigue tests have been shown to overestimate lives compared to TMF testing. Therefore TMF better predicts real life-limiting component behavior [Neu and Sehitoglu (1989), Mall *et al.* (1992)]. Previous testing indicates that OOP TMF is dominated by matrix stresses, whereas in-phase TMF is dominated by the fiber maximum stress [Nicholas *et al.* (1996), Russ *et al.* (1991), Russ *et al.* (1995)]. During OOP TMF testing, varying stress states arise within the fiber and matrix due to the coefficient of thermal expansion (CTE) mismatch between the fiber and the matrix. At higher temperatures the matrix will attempt to expand more than the fiber due to the higher CTE of the matrix. In this condition the fiber will experience a tensile stress while the matrix experiences a compressive stress. Since only low tensile stresses are placed on samples at high temperatures during OOP TMF, only

slight increases
the CTE mismat
in a tensile stres
low temperature
is summed with
also negating the
the matrix of the
of the fiber, whi
remains sufficient
(1963).

slight increases in stress in the fiber and matrix will occur. At lower temperatures, due to the CTE mismatch, the matrix will attempt to contract more than the fiber, which results in a tensile stress state in the matrix and a compressive stress state in the fiber. At the low temperatures the tensile load on the sample is the greatest. This mechanical loading is summed with the thermal loading causing an increase in the stress in the matrix and also negating the thermal compressive stress on the fiber. Therefore, OOP TMF causes the matrix of the composite to experience a wide range of stress states compared to that of the fiber, which results in a matrix dominated failure. The maximum fiber stress remains sufficiently low enough that the fibers do not readily fracture [Neu and Roman (1993)].

Stress

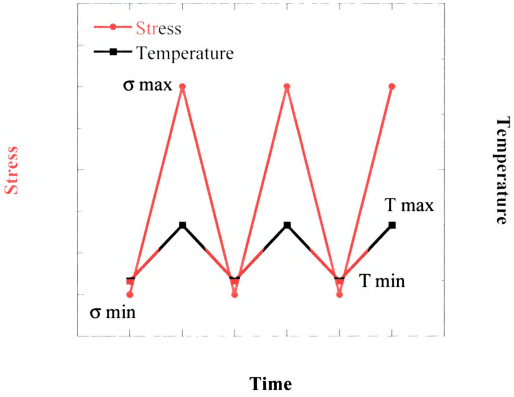

Figure 2.8 A schematic of in-phase thermomechanical fatigue cycling.

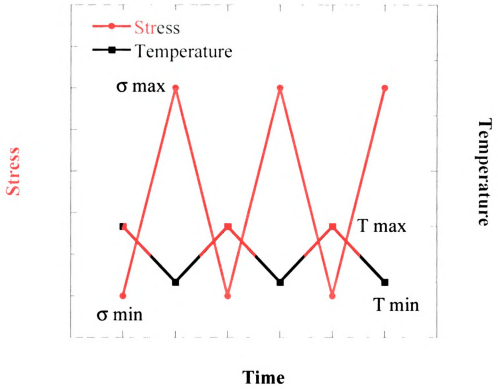

Figure 2.9 A schematic of out-of-phase thermomechanical fatigue cycling.

3.1 Out-of-Ph
Niobium Met

While the

primarily involv

[Russ *et al.* (1

and granular, lack

results suggested

exhibits less ductil

Nb-based MMCs

the crack plane a

3.1 Out-of-Phase Thermomechanical Fatigue of Titanium-Aluminum-Niobium Metal Matrix Composites

While the literature is limited, OOP TMF failures of Ti-Al-Nb-based MMCs have primarily involved extensive cracking initiating at the surface and edges of specimens [Russ *et al.* (1991)]. Fracture surfaces of the matrix overload region tended to be smooth and granular, lacking ductile dimpling [Russ *et al.* (1991), Russ *et al.* (1995)]. These results suggested that failure occurred at low temperatures (150°C), where the matrix exhibits less ductility. The lack of fiber pull-out observed in OOP TMF failures of Ti-Al-Nb-based MMCs indicate that fiber bridging does not occur and that the fibers broke in the crack plane as the crack tip progressed through the composite [Russ *et al.* (1991)].

This cha

the specific aim

the microstructu

pparati and me

phase (OOP) the

A. Material Pr

1. Alloy Fabric

Two nom

2.3 at.% Mo q

gas (argon) atomi

powders were siz

46 μm so that

was done by pass

of a plastic film

ed to limit th

ness composite

easured roughly

m the plastic b

ation in an en

CHAPTER 3

EXPERIMENTAL PROCEDURES

This chapter describes the general experimental methodology used to complete the specific aims of this study. Included in this chapter are material processing details, the microstructural characterization equipment and techniques utilized, and the testing apparati and methods used for the tensile, creep, *in-situ* creep, bond strength, and out-of-phase (OOP) thermomechanical fatigue (TMF) testing.

A. Material Processing

1. Alloy Fabrication

Two nominally Ti-24Al-17Nb (at.%) alloys containing approximately 0.66 at.% or 2.3 at.% Mo quaternary additions were produced in spherical powder form using inert gas (argon) atomization. All compositions are given in at.% unless otherwise noted. The powders were size fractioned through mesh size -140/+270 (particle size variation of 53 – 106 μm) so that they were compatible with the tape casting process. Alloy tape casting was done by passing a blade over a powder/binder slurry, which formed a flat, thin sheet on a plastic film upon drying. Poly(isobutylene) was used as the binder, as it has been shown to limit the interstitial content of oxygen and carbon in titanium-aluminide metal matrix composites [Niemann and Edd (1991)]. The rectangular panel dimensions measured roughly 150 mm x 150 mm x 1 mm. After drying, the cast tape was removed from the plastic backing before further processing. Binder burn off was performed under vacuum in an enclosed stainless-steel envelope and was followed by a hot isostatic

pressing (HIP)

from the sheets

o Ti-24Al-17Nb

evaluated due pr

2. Metal Matr

The four-

manner as the al

17Nb-1.1Mo, and

fibers, termed U

Smith *et al.* (19

ver a fiber mat

around a drum c

the sheet before

removed and trim

outer ply. The V

binder burn off.

for the Ultra S

WCs is given i

HIPed at a temper

for this pressure

6Mo and Ultra

for the consolid

pressing (HIP) consolidation step, which is shown in Figure 3.1. Specimens were cut from the sheets using electron discharge machining (EDM). Although an Ultra SCS-6/Ti-24Al-17Nb-1.1Mo MMC was evaluated, the Ti-24Al-17Nb-1.1Mo alloy was not evaluated due primarily to monetary funding limitations.

2. Metal Matrix Composite Fabrication

The four-ply metal matrix composites (MMCs), which were tape cast in a similar manner as the alloys, contained matrix compositions of Ti-24Al-17Nb-0.66Mo, Ti-24Al-17Nb-1.1Mo, and Ti-24Al-17Nb-2.3Mo. The MMCs contained continuous SiC-based fibers, termed Ultra SCS-6 due to their increased strength compared with SCS-6 fibers [Smith *et al.* (1997), Rosenberger *et al.* (1997)]. For the MMCs, the blade was passed over a fiber mat. The fiber mat was prepared by winding fibers at a desired spacing around a drum covered with a silicon-coated plastic sheet. The binder was coated onto the sheet before and after the fibers were wrapped, and upon drying the mats were removed and trimmed. One fiber ply sheet was tape cast on both sides and used as the outer ply. The MMC was formed when four mats were stacked, encapsulated to enable binder burn off, and HIPed for consolidation. A schematic of the MMC HIP conditions for the Ultra SCS-6/Ti-24Al-17Nb-0.66Mo and Ultra SCS-6/Ti-24Al-17Nb-2.3Mo MMCs is given in Figure 3.2. The Ultra SCS-6/Ti-24Al-17Nb-1.1Mo MMC panel was HIPed at a temperature of 1093 °C and pressure of 103.4 MPa for three hours. It is noted that this pressure is slightly higher than that used on the Ultra SCS-6/Ti-24Al-17Nb-0.66Mo and Ultra SCS-6/Ti-24Al-17Nb-2.3Mo MMCs. EDM was used to cut samples from the consolidated sheets.

Temperature (°C)
1200
1000
800
600
400
20
2

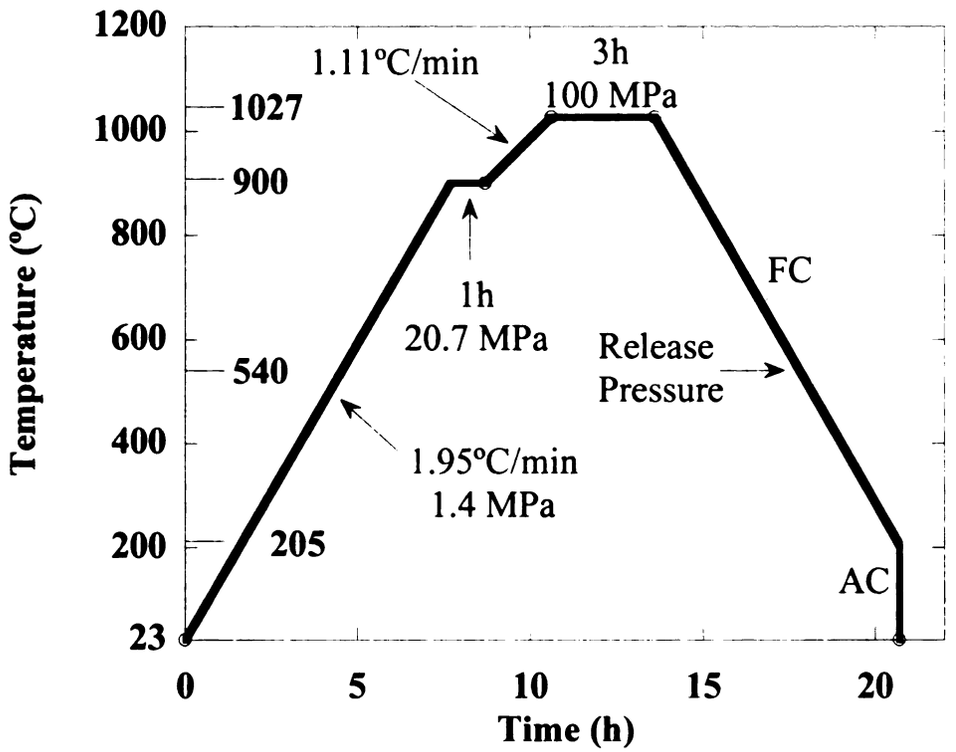

Figure 3.1 A schematic depicting the time-temperature-pressure relationship for processing the alloys. FC = controlled furnace cool at -1.94°C/min. AC = air cooled.

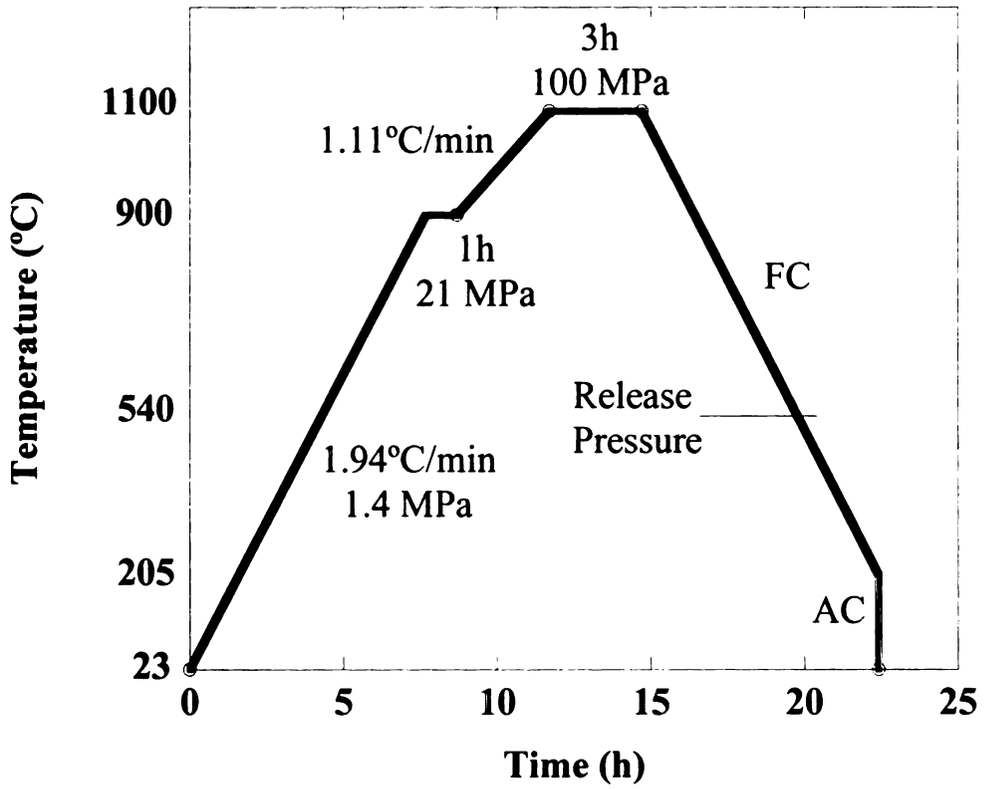

Figure 3.2 A schematic of the time-temperature-pressure relationship for processing the Ultra SCS-6/Ti-24Al-17Nb-0.66Mo and Ultra SCS-6/Ti-24Al-17Nb-2.3Mo MMCs. FC = controlled furnace cool at -1.94°C/min. AC = air cooled.

3. Post-Consolidation Heat Treatment

The as-processed (AP) materials were evaluated in room-temperature (RT) tensile experiments. Previous investigations on Ti-22Al-23Nb and Ti-25Al-17Nb alloys had indicated improvements in tensile properties (particularly RT ε_f) could be achieved by heat treating near the BCC transus to reduce the volume fraction of primary α_2 phase [Boehlert *et al.* (1997b), Smith and Porter (1997), Krishnamurthy *et al.* (1998)]. Thus, a heat-treatment schedule was developed to dissolve some of the primary α_2 phase and stabilize the orthorhombic phase (O-phase), without significantly increasing the prior-BCC grain size. This heat-treatment schedule, depicted in Figure 3.3, was performed on alloy and MMC coupons used for the RT and 650°C tensile experiments, bond strength tests, and all the creep and OOP TMF experiments.

Temperature (°C)

1500

1000

500

0

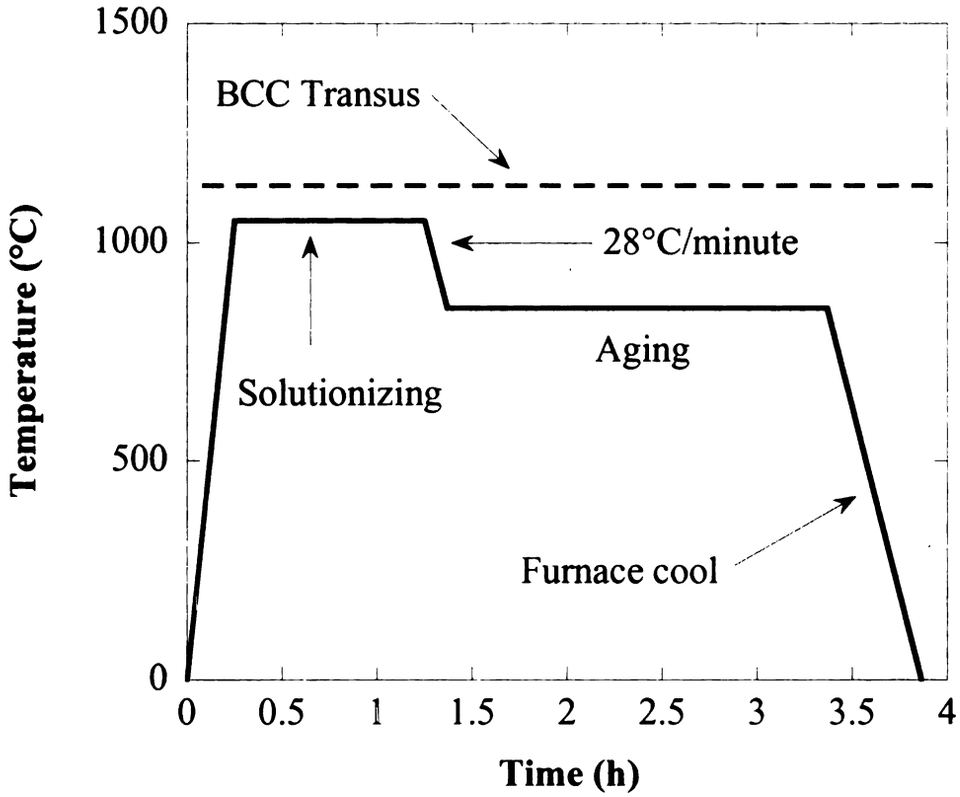

Figure 3.3 A sketch of the subtransus heat treatment used for each alloy and MMC.

B. Material Characterization

1. Chemical Composition Analysis

Samples of the Ti-24Al-17Nb-xMo alloys and MMCs were submitted to the Leco Corporation (St. Joseph, MI) for bulk chemical analysis. Weight percentages of Ti, Al, Nb, Mo, and Fe were determined using inductively coupled plasma optical emission spectroscopy (ICP-OES) and inert gas fluorescence (IGF). Oxygen and nitrogen weight percentages were found using a Leco Corporation TC600 oxygen/nitrogen analyzer. Each test was performed in triplicate and the average numbers were reported. Microprobe analysis was conducted on a JEOL 8200 electron probe microanalyzer using a filament voltage of 15 kV and an emission current of 20 mA to determine the atomic percentages of Ti, Al, Nb, and Mo in each phase. Multiple points in each phase were analyzed, and the results were averaged. Energy dispersive spectroscopy (EDS) was also performed to qualitatively analyze the distribution of the elements in each phase.

2. Metallography Preparation

Samples were prepared for backscattered electron (BSE) scanning electron microscopy (SEM) by sectioning the material into three different orientations (labeled face (F), transverse (T), and longitudinal (L)), as shown in Figure 3.4. The sections were made using a Struers Labotom-3 abrasive saw with a silicon carbide (SiC) blade or a Buehler Isomet™ low speed saw with a diamond blade. Sectioned samples were cleaned in acetone and ethanol and then mounted in Konductomet™ using a Buehler Pneumet®-I mounting press forming 2.54 cm diameter mounts. The mounts were collectively ground using SiC paper of successively finer grit size. A typical schedule consisted of 60 grit,

240 grit, 400 grit, and then 600 grit. Following grinding, 9 μm and 1μm diamond paste suspensions were used to polish the mounted samples. Colloidal silica containing an average particle size of 0.05 μm was the final polish used to produce a mirror finish. After polishing, the mounted samples were rinsed again in acetone and ethanol to remove any residual colloidal silica solution. Total polishing times ranged from 30 minutes to greater than 2 hours.

3. Microscopy

Scanning electron microscopy was performed to characterize the as-processed (AP) and heat-treated (HT) microstructures of both the alloys and MMCs. The microstructures were imaged using backscattered electron (BSE) mode on a CamScan 44FE field emission scanning electron microscope (SEM) and a Quanta FEG 600 Environmental SEM. The magnifications ranged from 100X to 30,000X. The micrographs were used to determine the grain size, phase volume percentage, and phase morphology.

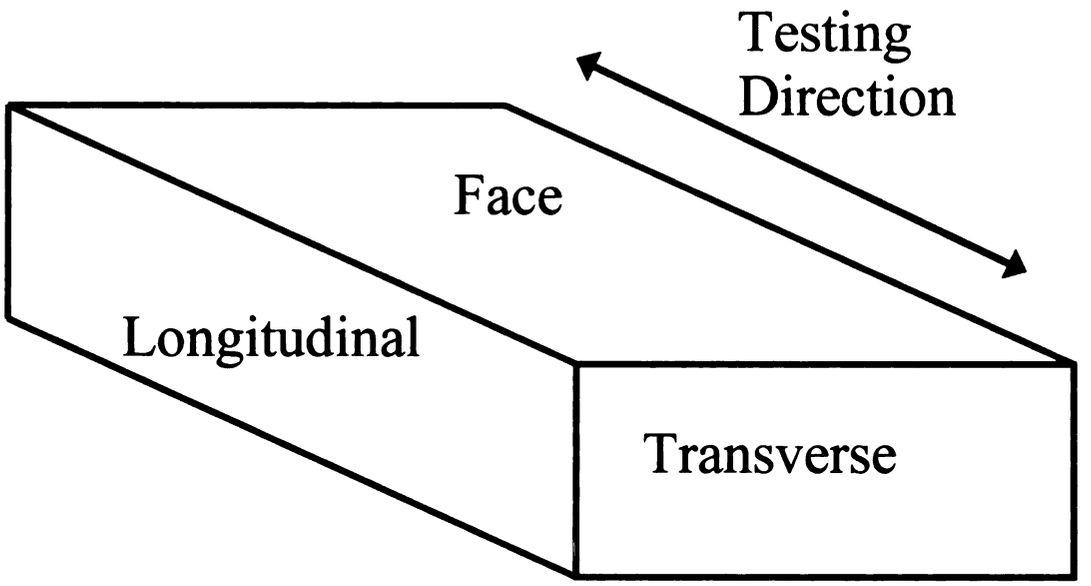

Figure 3.4 A schematic of the three different sheet orientations which were evaluated for the materials in the microstructural characterization.

4. Phase Volume Percentages

When imaging in BSE mode, the contrast in the micrographs is dependent on the density of the material being bombarded with electrons within the SEM. The number of backscattered electrons escaping from the sample is proportional to the atomic number of the material being imaged. Therefore, phases containing lighter elements appear darker in contrast compared to phases containing heavier elements. The α_2 phase exhibited the darkest contrast, the BCC phase exhibitied the lightest contrast, and the O-phase exhibited intermediate contrast between that of the α_2 and BCC phases. The SiC fibers yielded smaller amounts of backscattered electrons compared with the phases present within the alloys. Therefore, the fibers exhibited darker contrast than the alloy phases. To determine the phase volume percentages of the alloys and matrices a minimum of five low magnification (500X – 2000X) images, taken from each of the three sheet orientations, were analyzed using ImageJ software. Using this software the pixels within the phases were shaded to different contrasts and evaluated with an area-fraction analysis macro. The macro counts the pixels shaded and divides that value by the total number of pixels in the image. This analysis was conducted on each alloy and MMC matrix and the average phase volume percentages were determined. Fiber volume fractions were also determined for each MMC in the same manner. In some cases the contrast between the fine BCC and O-phases within the alloys and matrices was indiscernible to the ImageJ software. Therefore, the phase volume percentages were determined as α_2 and O + BCC phase volume percentages.

5. Grain Size Determination

The average equiaxed grain size of the alloys and MMCs was determined using the Mean Line Intercept Method [Hilliard (1964)]. A minimum of seven photomicrographs of different magnification, taken from various locations of the alloy and matrix, were analyzed, and the results were averaged. The grains containing a lath morphology were excluded from the analysis. Therefore, the grain sizes represent the average size of the equiaxed phases present in the microstructures (i.e. the α_2 phase grains and the O+BCC colonies).

Grain sizes were also determined individually for the α_2 phase grains and the O+BCC colonies using micrographs taken at 2000x and representative of the bulk of the microstructure (i.e. each micrograph contained a minimum of roughly 100 total grains and colonies). Each grain or colony size was determined by finding the approximate center then drawing a minimum of four diagonals through this point to the edge of the grain or colony. A minimum of ten grains and colonies were analyzed for each composition, and the results were averaged. The average diameters were multiplied by 1.74 (similar to the Mean Line Intercept Method) to obtain the average grain size of each α_2 grain and O+BCC colony. It is noted that the O-phase transformed from the BCC-phase and thus the O+BCC colony size represented the prior BCC grain size.

6. Differential Thermal Analysis and Disappearing-Phase Technique

An estimation of the BCC transus temperature for each alloy composition was obtained using differential thermal analysis (DTA). Tests were conducted on a TA Instruments Thermal Analysis Differential Scanning Calorimeter. The Ti-24Al-17Nb-

0.66Mo and Ti-24Al-17Nb-2.3Mo alloys were sectioned into small samples weighing 34.7 mg and 37.5 mg, respectively. Each sample was individually placed into an alumina pan. The samples were heated separately in an argon atmosphere using a blank alumina pan as a reference standard. The heating schedule consisted of an equilibration at 600°C followed by a heating to 1200°C at a rate of 5°C/minute. The temperature difference between the reference pan and the sample pan were recorded throughout the test, and the phase transformations were determined where endothermic and exothermic fluctuations occurred, as noted by peaks and valleys in the temperature difference versus temperature plots.

The disappearing phase technique was used to verify the BCC transus temperatures. Using this method samples were heat treated at a given temperature for a minimum of 8 h then quenched. The alloys in this study were heated at temperatures of 1100°C, 1115°C, 1130°C, 1145°C, 1160°C, and 1200°C. The samples were wrapped in tantalum foil then encapsulated in quartz tubing backfilled with argon. After the heat treatments were complete the quartz tubes were quenched in water and the tubes were broken to remove the samples. Once cooled the alloys were mounted in a conductive resin, ground using SiC paper, and metallographically polished through 0.05 μm colloidal silica. The polished samples were viewed in an SEM in backscattered electron mode to observe the phases within the microstructure. The BCC-transus temperature was suggested to occur at a temperature between that temperature where the α_2 and BCC phases were observed and the lowest temperature where no α_2 phase was observed.

7. BCC Pha

Depen

alloys can be

et al. (1991).

accomplished

TNb-2.3Mo

superlattice re

ordered. With

a 2θ angle of

XDS 2000™

7. BCC Phase Ordering Analysis

Depending on the composition and heat treatment, the BCC phase in Ti-Al-Nb alloys can be ordered (B2) or disordered (β) [Kestner-Weykamp *et al.* (1989), Bendersky *et al.* (1991), Rhodes *et al.* (1993)]. Determination of BCC phase ordering was accomplished using x-ray diffraction (XRD), where Ti-24Al-17Nb-0.66Mo and Ti-24Al-17Nb-2.3Mo alloy samples were scanned to examine the existence of the (210) superlattice reflection. This superlattice reflection only occurs when the BCC phase is ordered. With a lattice parameter of 0.323 nm, the (210) superlattice reflection occurs at a 2θ angle of approximately 64°. XRD scans were performed at 35kv and 25mA on an XDS 2000^{TM} (Scintag Inc. USA) using a count time of 30s with a 0.01° 2θ step size.

C. Mechani

1. Sample P

1.1 Tensile

The te

measured 101

sample (to scal

1.2 Creep E

For the

samples were

the sample w

have formed

sample with

1.3 *In-situ*

For th

gage sectio

the sample

maximum str

creep specim

area finish.

using BSE SE

C. Mechanical Testing

1. Sample Preparation

1.1 Tensile Experiments

The tape cast sheets were cut into dog bone specimens whose dimensions measured 101 mm in length with a 7.5 mm wide reduced gage section. An image of the sample (to scale) is provided in Figure 3.5.

1.2 Creep Experiments

For the creep experiments, typical coupon dimensions of the alloy and MMC samples were 125 mm in length with a 12 mm wide reduced gage section. The edges of the sample were ground with 240 grit SiC paper to remove any recast layers that may have formed during the EDM cutting process. Figure 3.6 depicts a sketch of the MMC sample with fibers perpendicular (90°) to the loading direction used for creep testing.

1.3 *In-situ* Creep Experiments

For the *in-situ* tensile-creep experiments, specially-designed specimens containing a gage section of 10 mm in length were used. A slight (0.6 mm) reduction in the width of the sample near the middle of the gage section was introduced to ensure that the maximum stresses and failure occurred at this location. Prior to testing, *in-situ* tensile-creep specimens were glued to a metallic platen and polished through a 0.06 μm colloidal silica finish using an automatic polishing machine, which allowed for optimal analysis using BSE SEM. An image of the specimen geometry used is provided in Figure 3.7.

Figure 3.5 A d
tensile tests.

Figure 3.6 A s
ontains fibers

Figure 3.5 A digital scan of the samples used for room temperature and high temperature tensile tests.

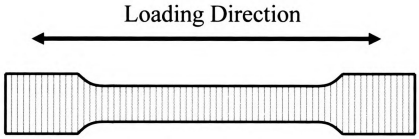

Figure 3.6 A schematic of the MMC samples used for creep testing. The dog bone contains fibers that are perpendicular (90°) to the loading direction.

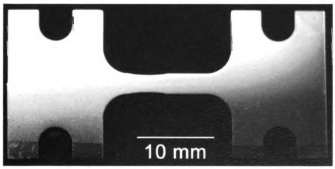

Figure 3.7 A photograph of the alloy tensile-creep dog bones used for *in-situ* creep testing.

1.4 Bond St

For e

specimens w

perpendicular

singularity at

matrix interfa

explanation o

Micromeasure

the center of

low-temperatu

1.5 Out-of-

The M

(TMF) testing

the dimension

MMCs were

with 240 grit

sample cutting

1.4 Bond Strength Experiments

For evaluating the interfacial bond strength, specially-designed cruciform specimens were used, Figure 3.8 and Figure 3.9, which contained fibers oriented perpendicular to the loading direction. This geometry was used to avoid the stress singularity at the edges of the sample, forcing the maximum tensile stress at the fiber-matrix interface to occur at the center of the cross [Boehlert *et al.* (2001)]. Further explanation of the stress state in cruciform samples is provided in Chapter 5. Micromeasures, Inc. strain gages were used for these experiments and were adhered to the center of the cruciform section using standard procedures involving high strength, low-temperature resin-based glue.

1.5 Out-of-Phase Thermomechanical Fatigue Experiments

The MMC test coupons used for out-of-phase (OOP) thermomechanical fatigue (TMF) testing measured 125 mm in length with a 12 mm reduced gage section, similar to the dimension of the samples used for creep testing. For these tests, the fibers in the MMCs were aligned parallel (0°) to the loading direction. Sample edges were ground with 240 grit paper to remove any recast layers that may have formed during EDM sample cutting. A sketch of the coupons is shown in Figure 3.10.

Figure 3.8 A
evaluation. The

33 mm

Figure 3.9 A
perpendicular to
the center of th

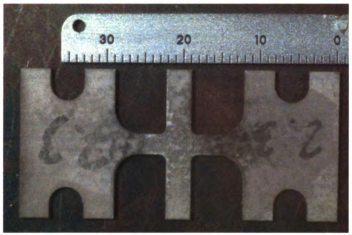

Figure 3.8 A photograph of a cruciform MMC specimen used for bond strength evaluation. The scale is in mm and the fibers were oriented vertically in the MMC.

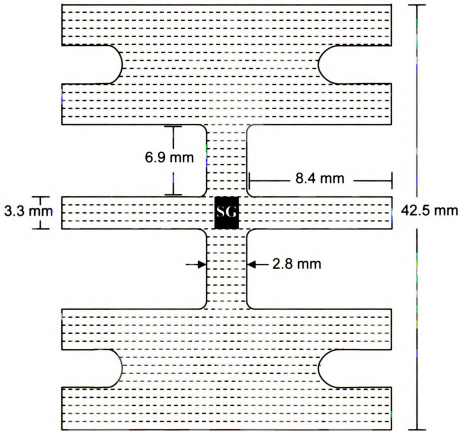

Figure 3.9 A schematic of the cruciform specimen geometry with fibers oriented perpendicular to the loading direction (vertical) showing the strain gage (SG) placement in the center of the cruciform.

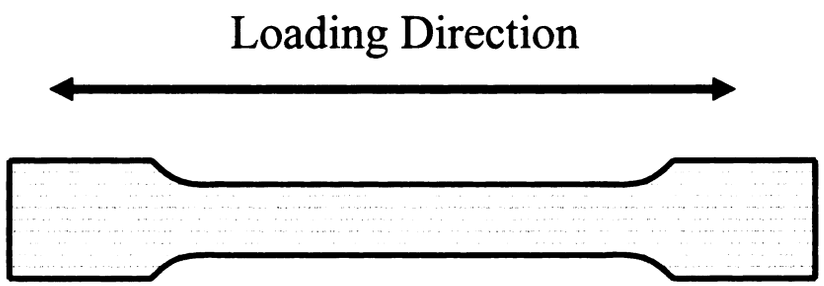

Figure 3.10 A schematic of the samples used for OOP TMF testing. The dog bones contains fibers that run parallel (0°) to the loading direction.

2. T

2.1 F

using

cell.

length

cond

streng

record

the e

compo

2. Tensile Testing

2.1 Room Temperature Tensile Tests

The RT tensile tests were performed on AP and HT alloy and MMC coupons using an Instron 4206 tensile testing machine (Figure 3.11) equipped with a 100 kN load cell. Strain was measured during the tests with an MTS model 632.31F-24 12 mm gage-length extensometer attached directly to the gage section of the sample. All tests were conducted in displacement control at an equivalent strain rate of 10^{-3} s^{-1}. The 0.2% yield strength (YS), ultimate tensile strength (UTS), and elongation-to-failure (ε_f) values were recorded for each test. Young's modulus (E) values were determined from the slope of the elastic portion of the stress-strain curve. At least one test was conducted for each composition and heat treatment.

Figure 3.11 A photograph of the Instron 4206 tensile testing machine used for room-temperature tensile testing.

2.2 Elevated T

Elevated

MMC specimen

direction. These

hydraulic test m

software (Hartm

truly uniaxial lo

using a high-tem

15 mm. The ho

oriented perpen

Temperature con

spot-welded to e

A 25 mm section

temperature), wh

use of the water-

ramp to temperat

loading. Such te

YS, UTS, ε_f, and

determined by

Two Ti-24Al-

were tensile te

properties wer

2.2 Elevated Temperature Tensile Tests

Elevated temperature tensile experiments were conducted on only HT alloy and MMC specimens. The MMCs were tested with the fibers parallel to the loading direction. These experiments were performed in laboratory air, using a horizontal servo-hydraulic test machine (Figure 3.12 and Figure 3.13) controlled by automated test software [Hartman and Russ (1989)]. The specimens were precisely aligned, ensuring truly uniaxial loading, using uniquely-designed friction grips. Strain was monitored using a high-temperature extensometer containing alumina rod arms with a gage length of 13 mm. The heating unit contained six quartz lamps, two banks of three lamps each, oriented perpendicular to the loading axis, one above and one below the specimen. Temperature control and measurement were accomplished using three thermocouples spot-welded to each specimen providing three zones of control with two lamps per zone. A 25 mm section in the center of the specimen was uniformly heated (±3°C of the target temperature), while the specimen ends were kept near ambient temperature through the use of the water-cooled friction grips. The 650°C tensile tests incorporated a 600 second ramp to temperature with a minimum of 20 minutes hold at the target temperature before loading. Such tests were conducted using a stress rate of approximately 2 MPa/s. The YS, UTS, ε_f, and temperature were recorded for each test. The Young's modulus was determined by fitting a linear trend line to the elastic portion of the stress-strain curve. Two Ti-24Al-17Nb-0.66Mo alloy samples and one Ti-24Al-17Nb-2.3Mo alloy sample were tensile tested at 650°C. For the Ti-24Al-17Nb-0.66Mo alloy, the average tensile properties were reported. Only one test for each MMC composition was performed.

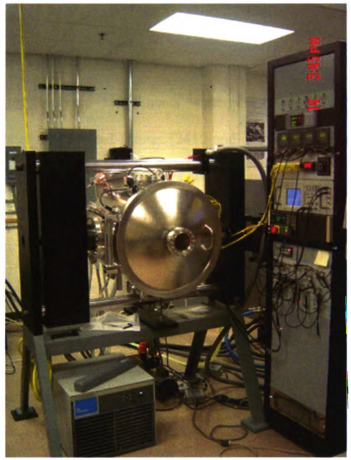

Figure 3.12 A photograph of the servo-hydraulic testing frame used for high-temperature tensile, MMC creep, and OOP TMF MMC testing.

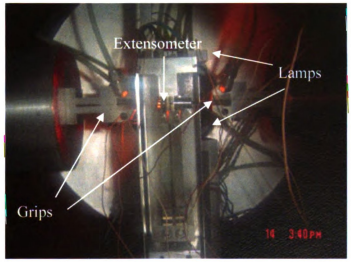

Figure 3.13 A photograph of the horizontal servo-hydraulic testing chamber showing a gripped sample with an attached extensometer and two banks of quartz lamps.

3. Creep Testing

3.1 Alloy Creep Testing

Open-air tensile creep experiments were performed on vertical Applied Test System, Incorporated (ATS) load frames (2410 and 2710 series) with a 20:1 lever-arm ratio, see Figure 3.14. The test temperatures and applied stresses ranged between 650°C-710°C and 29-275 MPa, respectfully. The load cells used for the 2410 and 2710 series frames were a WSM 500 lb (Model AB) and a WSM 100 lb (Model AB100-T), respectively. The load cells were located above the weights (see Figure 3.14), thus the specimens could be examined at loads up to 20 times the maximum capacity of the load cell. Although the experiments were constant load, in most cases the reduction in cross-sectional area was not sufficient to significantly alter the stress. Therefore, the stresses were assumed to be constant. Strain was measured using a 25.4 mm gage length ATS high-temperature extensometer attached directly the specimen's gage length. Linear variable differential transformers (LVDTs), with a strain resolution of 0.0001, were used to track the displacement of the extensometers and output the data to the computerized data acquisition system. The data acquisition system software utilized was Labview Version 7.1. This system did not control the experiment, but it collected strain, LVDT displacement, load, and time data at desired time intervals.

Specimen temperatures were monitored by three chromel-alumel type K thermocouples located within the reduced section of the specimen. One thermocouple was spot-welded directly to the gage section of the sample and two thermocouples were placed near the gage of the sample. Targeted temperatures were maintained within ± 3°C. ATS single-zone (3320 series) furnaces with $MoSi_2$ heating elements were used for

Figure 3.14 A picture of an ATS creep frame used to test the alloys in this work.

the creep testing. The experiments were conducted such that the specimens were soaked at the creep temperature for at least 60 minutes prior to applying load in order to minimize the thermal stresses. After the creep strain had proceeded well into the secondary regime and a steady-state creep rate was achieved, either the load or temperature was changed or the creep test was discontinued. The tested specimens were cooled under load to minimize recovery of the deformed structures. Selected specimens were taken to failure. Calculated steady-state creep rates were determined for each stress/temperature combination. These values were then used to determine creep stress exponents and apparent activation energies.

3.2 Metal Matrix Composite Creep Testing

Open-air experiments were performed using the horizontal servohydraulic test machine described previously for the high temperature tensile tests. The test temperatures and applied stresses ranged between 650°C – 710°C and 10 – 75 MPa, respectfully. The experiments were constant load, and in most cases the reduction in cross-sectional area was not sufficient to significantly alter the stress. Therefore, the stresses were assumed to be constant. Specimen temperatures were monitored by three or four chromel-alumel type K thermocouples located within the reduced section of the specimen. Targeted temperatures were maintained within ± 3°C. The experiments were conducted such that the specimens were soaked at the creep temperature for at least 60 minutes prior to applying load in order to minimize the thermal stresses. The time to reach the maximum creep load was five seconds or less, and the time, load, temperature, and strain were recorded periodically throughout the experiments. After the creep strain

had

eith

spec

Sele

3.3

expe

mark

resea

allow

how

phen

given

tempe

mag

the

[illegible]

[illegible]

[illegible]

[illegible]

[illegible]

had proceeded well into the secondary regime and a steady-state creep rate was achieved, either the load or temperature was changed or the creep test was discontinued. The tested specimens were cooled under load to minimize recovery of the deformed structures. Selected specimens were taken to failure.

3.3 *In-Situ* Creep Testing

One method previously used to evaluate grain-boundary sliding during creep experimentation involved fiducially marking a metallographically polished sample. Once marked, the sample was imaged prior to testing in a vacuum environment then creep tested and imaged after different strain intervals were imposed. While this methodology allows for localized strains to be calculated using the offset in the fiducial marking between grains, it is not optimal for characterizing the grain-boundary sliding phenomenon because such tests need to be discontinued to image the deformation at a given strain level. Therefore, the test must be restarted from zero load and room temperature causing a new transient creep stage each time the sample is discontinued and imaged. Such unloading and reloading can affect the creep deformation behavior. Using the *in-situ* testing methodology performed in this work the creep test is conducted continuously, and therefore undergoes similar deformation mechanisms experienced in conventional creep experiments without interruption.

The *in-situ* tensile-creep tests were performed at temperatures between 650-710°C using a screw-driven tensile stage (built by Ernest F. Fullam, Incorporated, Clifton Park, NY) placed inside a CamScan 44FE SEM chamber. A depiction of the setup is given in Figure 3.15. Temperature was controlled using a constant-voltage power supply which

provided output to a 1 cm diameter tungsten-based heater located just below the gage section of the sample. An open-bath, closed-loop chiller was used to circulate distilled water at RT through copper tubes to prevent the tensile stage from overheating. A fine-gage type K thermocouple was spot-welded to the gage section of each sample. After the sample's gage-section temperature reached the desired creep temperature, a 30 minute period was given to stabilize the thermal stress prior to applying load. The load, which was measured using a 4,448 N load cell, was applied at 3.7 N/s until reaching the desired creep stress. The tests were considered constant load, where the stress fluctuation varied ±3 MPa. The load-displacement relationship was recorded and depicted live during the experiments using MTESTW version F 8.8e data acquisition and control software (Admet, Inc., Norwood, MA). It is noted that the displacement data acquired during the experiments comprised that of the sample as well as the gripping fixtures. Backscattered electron SEM images were taken before loading and at periodic displacements throughout the creep experiments without interrupting the experiment. Such experiments lasted up to six days while the SEM chamber vacuum pressure never fell below 10^{-6} torr. Therefore, oxidation did not significantly affect the imaging characterization. A detailed procedure involving the steps used to conduct such experiments can be found in reference Cowen (2006).

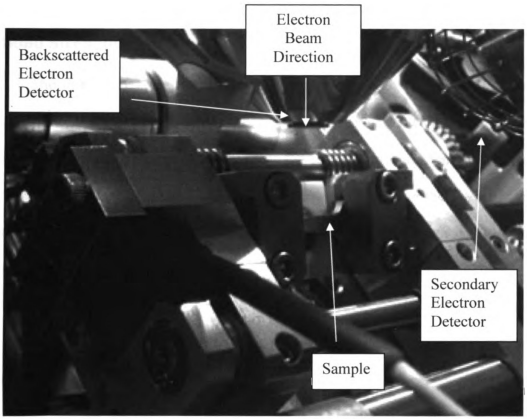

Figure 3.15 A photograph of the *in-situ* tensile-creep stage inside a Quanta 200 Environmental SEM chamber.

4. Bond Strength Testing

The interfacial bond strength was determined through RT tensile experiments using cruciform-geometry specimens, where the fibers were oriented perpendicular to the loading direction. The cruciform geometry forces the maximum tensile stress at the fiber-matrix interface to occur at the center of the cross removing the stress singularity that exists where the fiber-matrix interface intersects the free surface. Rectangular specimen geometries have been shown to result in premature debonding and invalid bond strength measurements [Majumdar *et al.* (1998), Boehlert *et al.* (2001), Gundel *et al.* (1995), Gundel *et al.* (1995a), Warrier *et al.* (1996), Gundel and Miracle (1998), Gundel *et al.* (1997)]. A uniaxial strain gage was attached directly to the center of the cruciform to locally monitor the strain. These experiments were performed at room temperature under a constant loading of 25 lbs/min (0.74 MPa/s) using the Ernest Fullam, Inc. tensile stage described in Section 3.3 of this chapter. At least three tests were conducted for each MMC composition and the interfacial bond strength was determined from the onset of nonlinearity of the engineering stress/strain curve using the Pearson correlation. The fracture surfaces and longitudinal surfaces of deformed samples were imaged using SEM to determine the debonding location.

5. Out-of-Phase Thermomechanical Fatigue Testing

OOP TMF tests were conducted on the same test frame as that described in Section 2.2 of this chapter, and the setup is shown in Figure 3.16. All tests were conducted in load control with a stress ratio (R) of 0.1. The maximum applied stress ranged from 200 – 600 MPa, and the temperature ranged from 150°C – 450°C. The temperature and load frequency was 0.00556 Hz (3 minute cycles), where the maximum loading occurred at the minimum temperature. Both the load and temperature were driven by an MTS Flex Test SE Controller using Multipurpose Testware software. The specimens were precisely aligned, ensuring truly uniaxial loading, using uniquely-designed friction grips. Strain was monitored using a high-temperature extensometer containing alumina rod arms with a gage length of 13 mm. The temperature was monitored and controlled using four thermocouples placed directly over the heated zone. Two sets of quartz lamps (four lamps total) were used to heat the sample, allowing for local control of the temperature. Forced air was blown over and under the sample to assist in cooling. The time, temperature, load, displacement, and strain were measured at periodic intervals along with the peak and valley strain data. All samples were run until failure or until deemed 'run-out' (> 8000 cycles, which was achieved in more than 16 days). Microstructure-fatigue relationships were developed using S-N (stress vs. cycle) and strain vs. time plots.

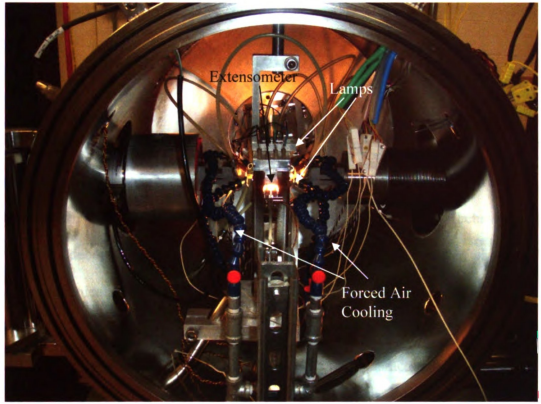

Figure 3.16 A photograph of the servo-hydraulic test frame set up for OOP TMF testing of the MMCs.

CHAPTER 4

RESULTS

This chapter presents the results obtained from the microstructural characterization, mechanical property testing, and deformation characterization. It is broken down into subsections of microstructure analysis, creep behavior, MMC interfacial debond analysis, tensile behavior, and MMC out-of-phase (OOP) thermomechanical fatigue (TMF) behavior. The microstructural analysis of the alloys is described first followed by the microstructural analysis of the MMCs. The creep behavior is described for the alloys and 90° MMCs, and characteristics of the interfacial debonding of the 90° MMCs is also included. The tensile behavior of the alloys and 0° MMCs is described prior to the final section on 0° MMC OOP TMF behavior.

A. Microstructure Analysis

1. Bulk Chemical Compositions

The chemical compositions of each of the alloys and each of the matrices within the MMCs are provided in atomic percent in Table 4.I. It is noted that the targeted compositions were maintained adequately well in each alloy and MMC, and that the oxygen content was typical for powder-processed titanium alloys, but significantly greater than that observed in alloys processed by more conventional methods [Rhodes *et al.* (2000), Smith *et al.* (1999), Smith *et al.* (2000), Zhang *et al.* (1998)]. The oxygen content of the Ti-24Al-17Nb-0.66Mo alloy was approximately 200 ppm larger than that for the Ti-24Al-17Nb-2.3Mo alloy. The oxygen content is important because oxygen

atoms occupy the interstitial sites and serve to stabilize the α_2 phase. This results in an increase in the BCC-transus temperature, and in turn a greater α_2-phase volume percent. Greater α_2-phase volume percents can be detrimental to some mechanical properties. In particular, such increases have been shown to decrease elongation-to-failure (ε_f) values [Akkurt *et al.* (1991), Boehlert *et al.* (1997), Gogia *et al.* (1992), Gogia *et al.* (1998)].

Table 4.I. Chemical compositions of the alloys and matrices in the MMCs.

Nominal Composition	Ti (at%)	Al (at%)	Nb (at%)	Mo (at%)	O (ppm)
Ti-24Al-17Nb-0.66Mo	balance	22.2	16.3	0.66	1830
Ti-24Al-17Nb-2.3Mo	balance	24.4	17.2	2.3	1670
Ti-24Al-17Nb-0.66Mo MMC	balance	24.6	16.1	0.65	na
Ti-24Al-17Nb-1.1Mo MMC	balance	24.9	17.3	1.1	na
Ti-24Al-17Nb-2.3Mo MMC	balance	25.2	17.3	2.3	na

na: not available

2. Differential Thermal Analysis and Disappearing Phase Technique

The differential thermal analysis curves for the Ti-24Al-17Nb-0.66Mo alloy and the Ti-24Al-17Nb-2.3Mo alloy are shown in Figure 4.1. Phase changes are indicated by peaks and valleys, corresponding to endothermic and exothermic reactions associated with a phase change within the material. In particular, the temperature at which the O+BCC phase field and the fully-BCC phase field intersect is important to determine so that heat-treatment schedules can be used to tailor the microstructure and in particular the grain size of the alloys. It is well documented that the BCC grain size increases rapidly for heat treatments performed above the BCC-phase transus temperature. Based on the

reactions indicated in Figure 4.1, the BCC transition temperature for the Ti-24Al-17Nb-0.66Mo alloy occurred between 1111°C – 1151°C. Similarly, the transus temperature for the Ti-24Al-17Nb-2.3Mo alloy occurred between 1124°C – 1164°C.

The Ti-24Al-17Nb-0.66Mo and Ti-24Al-17Nb-2.3Mo alloy microstructures resulting from the 8 h heat treatments ranging from 1100°C – 1200°C are shown in Figure 4.2 and Figure 4.3, respectively. In these backscattered electron (BSE) scanning electron microscope (SEM) photomicrographs the dark, equiaxed grains, which were less than 10 μm in diameter, correspond to the α_2 phase, while the BCC phase is represented by the larger and brighter equiaxed grains. No O phase was present in any of the microstructures. For the Ti-24Al-17Nb-0.66Mo alloy, the α_2 phase was present in the microstructures heat treated at 1100°C and 1115°C, but the α_2 phase was not present in the microstructures of the samples heat treated at higher temperatures. For the Ti-24Al-17Nb-2.3Mo alloy, the α_2 phase was present within the 1100°C, 1115°C, and 1130°C heat-treated microstructures, but was not present in alloys heat treated at 1145°C, 1160°C, and 1200°C. These results indicate that the BCC transus temperature lies between 1115°C – 1130°C for the Ti-24Al-17Nb-0.66Mo alloy and between 1130°C – 1145°C for the Ti-24Al-17Nb-2.3Mo alloy. These values fall within the expected range based on the phase map presented in Chapter 2, and closely match the 1130°C transition temperature of a Ti-22Al-14Nb alloy [Boehlert *et al.* (1997a)].

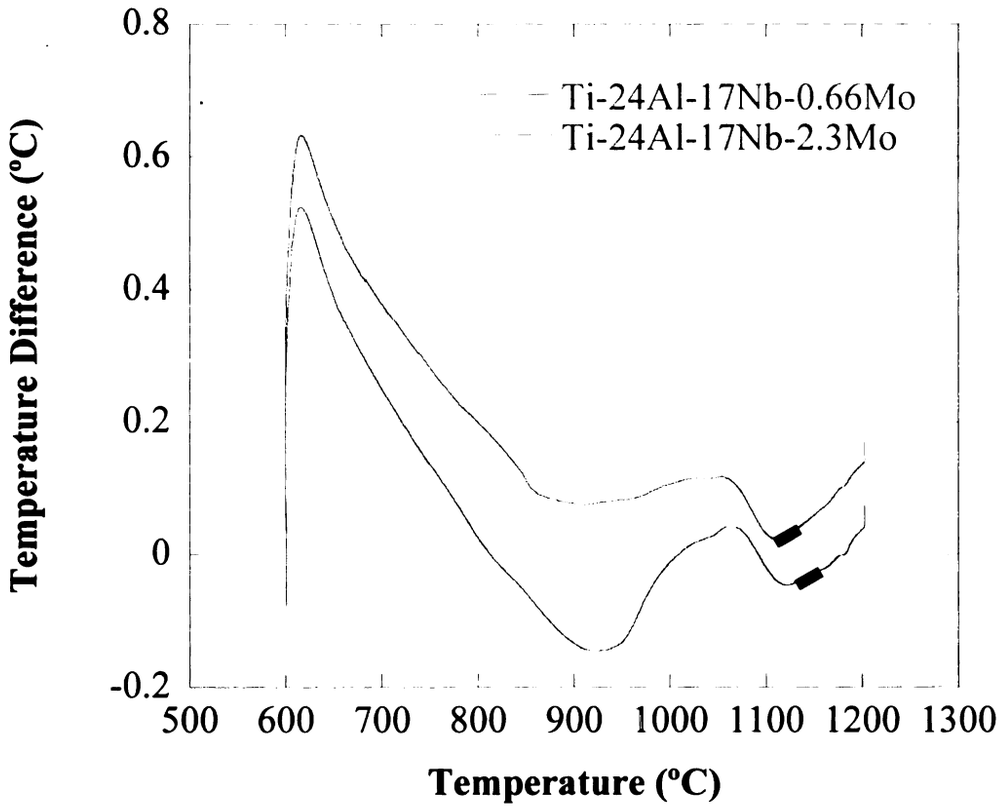

Figure 4.1 Differential thermal analysis scans for the Ti-24Al-17Nb-0.66Mo alloy and the Ti-24Al-17Nb-2.3Mo alloy plotting the temperature difference between the standard and the sample versus temperature of the standard. Based on the reactions indicated, the BCC transition temperature for the Ti-24Al-17Nb-0.66Mo alloy occured between 1111°C and 1151°C. Similarly, the transus temperature for the Ti-24Al-17Nb-2.3Mo alloy occurred between 1124°C and 1164°C. The transition temperature range determined using the disappearing phase technique is indicated on each scan by a thick black line.

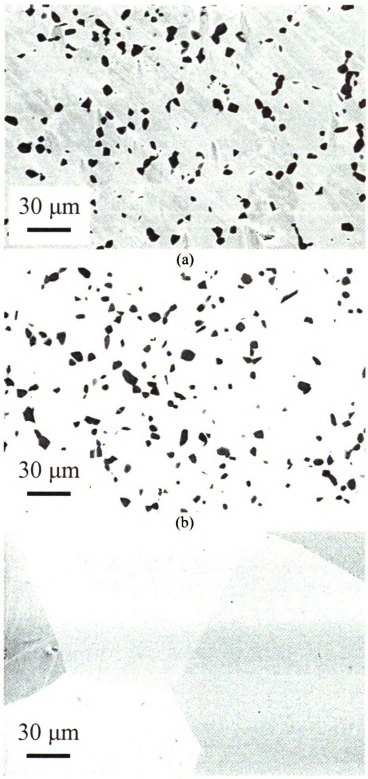

Figure 4.2 BSE SEM images of the Ti-24Al-17Nb-0.65Mo alloy heat treated at (a) 1100°C, (b) 1115°C, (c) 1130°C, (d) 1145°C, (e) 1160°C, and (f) 1200°C.

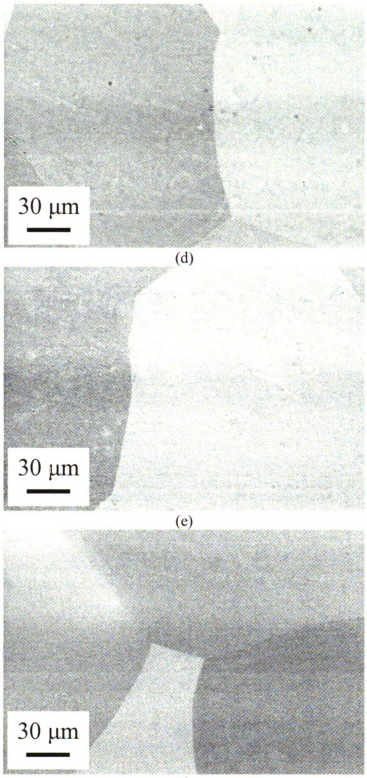

Figure 4.2 BSE SEM images of the Ti-24Al-17Nb-0.65Mo alloy heat treated at (a) 1100°C, (b) 1115°C, (c) 1130°C, (d) 1145°C, (e) 1160°C, and (f) 1200°C.

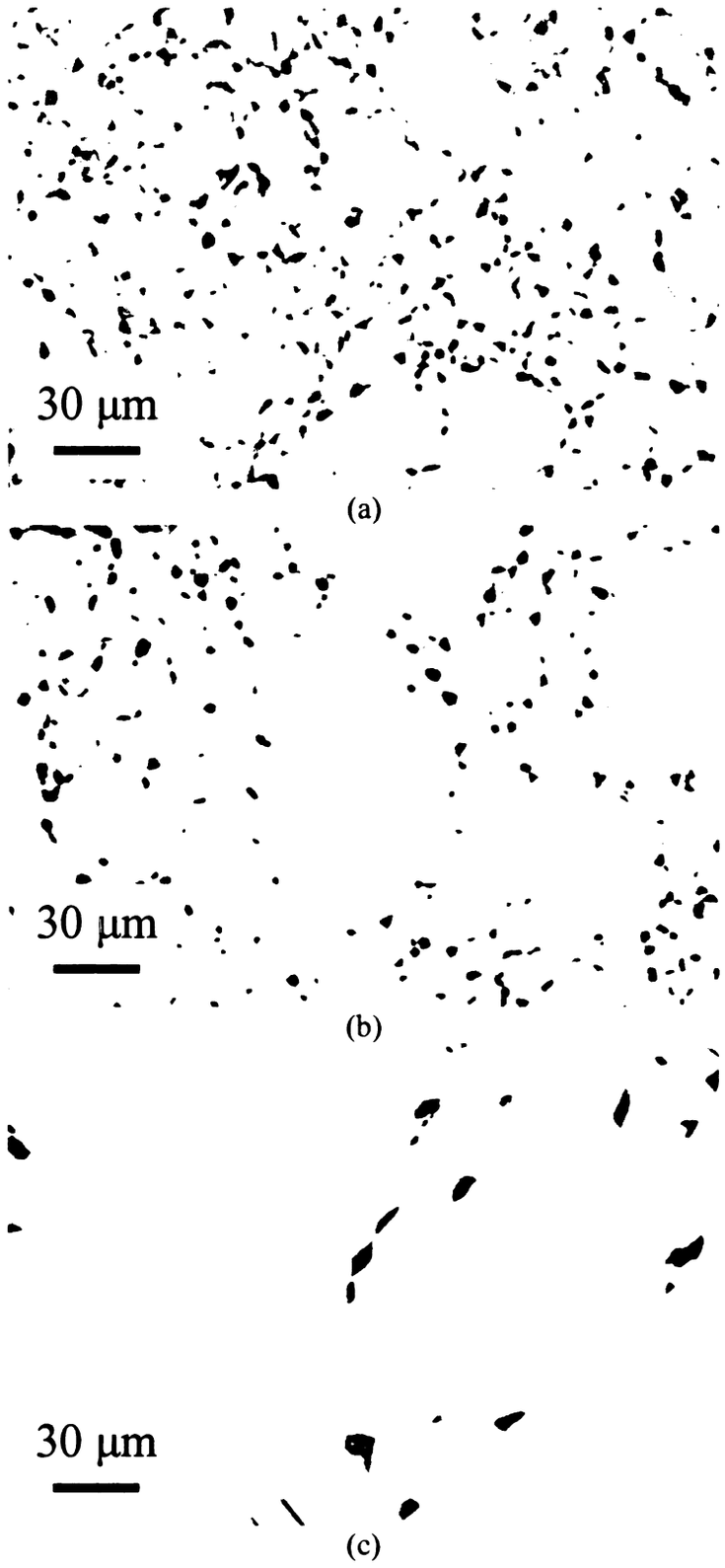

Figure 4.3 BSE SEM images of the Ti-24Al-17Nb-2.3Mo alloy heat treated at (a) 1100°C, (b) 1115°C, (c) 1130°C, (d) 1145°C, (e) 1160°C, and (f) 1200°C.

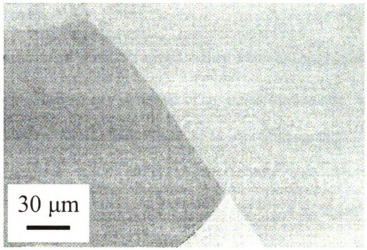

(d)

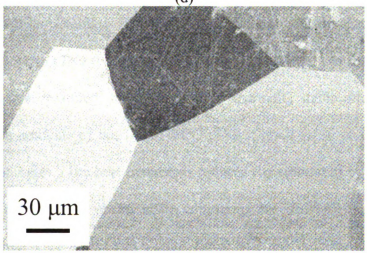

(e)

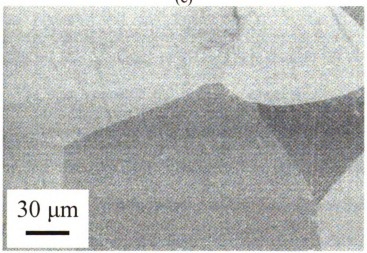

(f)

Figure 4.3 BSE SEM images of the Ti-24Al-17Nb-2.3Mo alloy heat treated at (a) 1100°C, (b) 1115°C, (c) 1130°C, (d) 1145°C, (e) 1160°C, and (f) 1200°C.

3. Microstructures

3.1. As-Processed and Heat-Treated Alloy Microstructures

The alloy microstructures consisted of α_2 grains (dark phase) and O laths (gray phase) in a BCC matrix (white phase). BSE SEM photomicrographs of the as-processed (AP) and heat-treated (HT) Ti-24Al-17Nb-0.66Mo and Ti-24Al-17Nb-2.3Mo microstructures are shown in Figure 4.4 – Figure 4.7. The α_2 phase morphology was equiaxed, while the O phase precipitated out of the equiaxed BCC phase in a Widmanstatten lath morphology. There was a semi-continuous network of α_2 observed throughout the Ti-24Al-17Nb-0.66Mo and Ti-24Al-17Nb-2.3Mo alloys in the AP and HT conditions. The heat treatment served to produce thermally stable microstructures that contained varying amounts of the O and BCC phases, grain sizes, phase compositions, and phase morphologies. The heat treatments reduced the amount of α_2-phase contiguity within the microstructure, as observed by comparing the Ti-24Al-17Nb-0.66Mo alloy microstructures in Figure 4.4(a) and Figure 4.6(a) and the Ti-24Al-17Nb-2.3Mo alloy microstructures in Figure 4.5(a) and Figure 4.7(a). The Ti-24Al-17Nb-2.3Mo microstructure exhibited less contiguity of the α_2 phase than the Ti-24Al-17Nb-0.66Mo microstructures. The heat treatment and higher amounts of Mo resulted in a finer, submicron O+BCC structure, as shown in Figure 4.5(b), Figure 4.6(b) and Figure 4.7(b). A modest amount (less than 1 vol.%) of porosity was observed within the alloys, as shown in Figure 4.4(a). This porosity was most likely due to incomplete consolidation during the HIP cycle and was expected to have had a detrimental effect on all mechanical properties, especially elongation-to-failure (ε_f), due to the associated stress concentration at the pores.

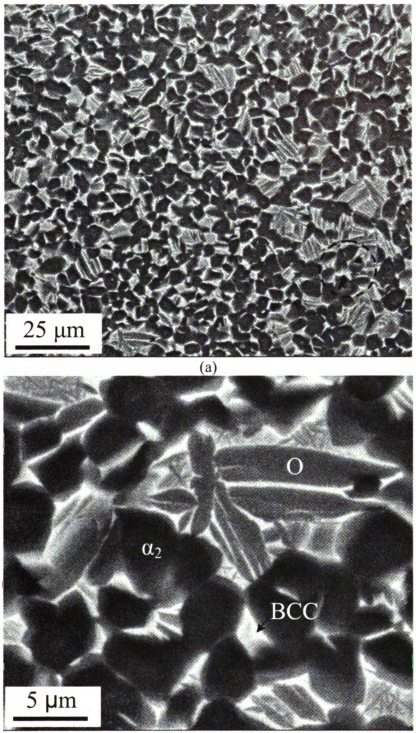

Figure 4.4 (a) Low-magnification and (b) high-magnification BSE SEM micrographs of AP Ti-24Al-17Nb-0.66Mo alloy. Some residual porosity remained (< 1%) and is shown in (a) within the dashed circle. The O-phase (gray) lath thickness was considered to be relatively large compared to that observed in the HT Ti-24Al-17Nb-0.66Mo and the AP and HT Ti-24Al-17Nb-2.3Mo alloys.

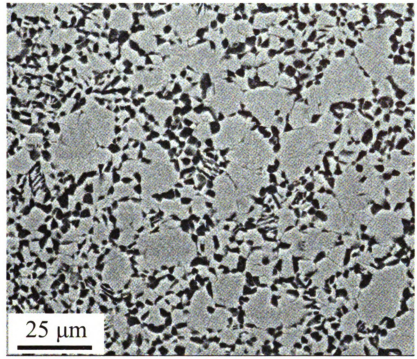

(a)

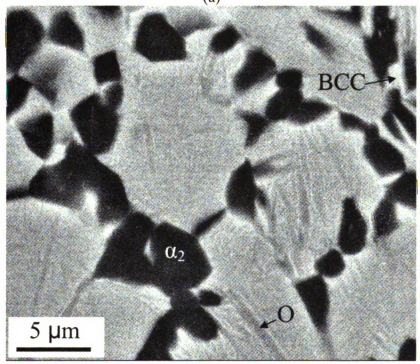

(b)

Figure 4.5 (a) Low-magnification and (b) high-magnification BSE SEM micrographs of AP Ti-24Al-17Nb-2.3Mo alloy. The O-phase lath (gray) size is much finer for the AP Ti-24Al-17Nb-2.3Mo alloy as compared to the AP Ti-24Al-17Nb-0.66Mo alloy (see Figure 4.4 (b)).

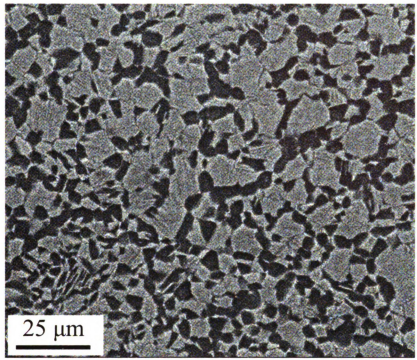

(a)

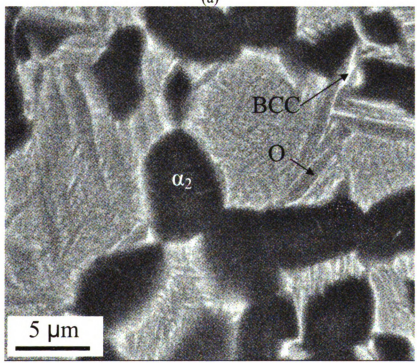

(b)

Figure 4.6 (a) Low-magnification and (b) high-magnification BSE SEM micrographs of HT Ti-24Al-17Nb-0.66Mo alloy. The heat treatment resulted in finer O-phase lath widths (see Figure 4.4 (b) for comparison) and less α_2 phase volume fraction.

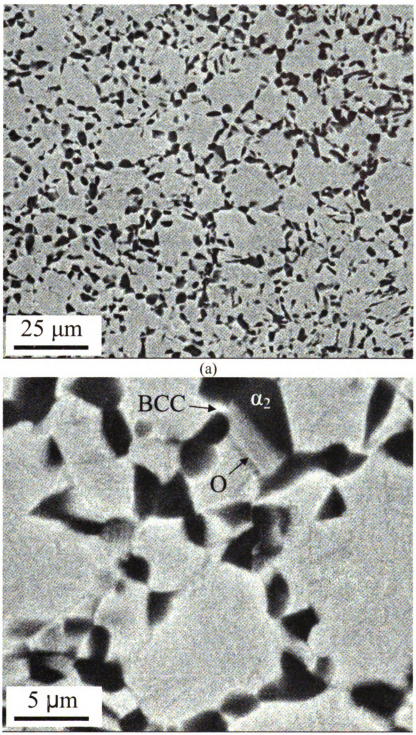

Figure 4.7 (a) Low-magnification and (b) high-magnification BSE SEM micrographs of HT Ti-24Al-17Nb-2.3Mo alloy. The heat treatment resulted in finer O-phase lath widths (see Figure 4.5 (b) for comparison) and less α_2 phase volume fraction.

3.2 Heat-Treated Metal Matrix Composite Microstructures

All of the microstructures of the MMCs were heat-treated prior to imaging. Provided in Figure 4.8 – Figure 4.10 are BSE SEM micrographs of the matrices. In general, the Ultra SCS-6/Ti-24Al-17Nb-0.66Mo and Ultra SCS-6/Ti-24Al-17Nb-2.3Mo matrices were similar in microstructure and make up to their alloy counterparts. The Ultra SCS-6/Ti-24Al-17Nb-1.1Mo matrix revealed differences compared with the other MMC matrix microstructures. The O-phase laths appeared more coarse that those in the Ultra SCS-6/Ti-24Al-17Nb-0.66Mo and Ultra SCS-6/Ti-24Al-17Nb-2.3Mo matrices. Reductions in the size of the equiaxed α_2 grains were evident in the Ultra SCS-6/Ti-24Al-17Nb-2.3Mo matrix compared to that of the Ultra SCS-6/Ti-24Al-17Nb-0.66 and Ultra SCS-6/Ti-24Al-17Nb-1.1Mo matrices. The Ultra SCS-6/Ti-24Al-17Nb-1.1Mo matrix exhibited the largest α_2 grain size. Therefore, the smaller amounts of Mo tended to have a less significant affect on reducing the α_2 grain size.

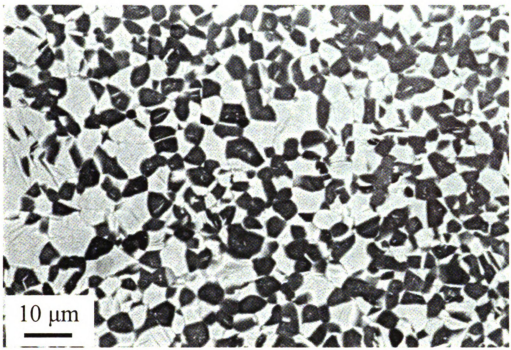

(a)

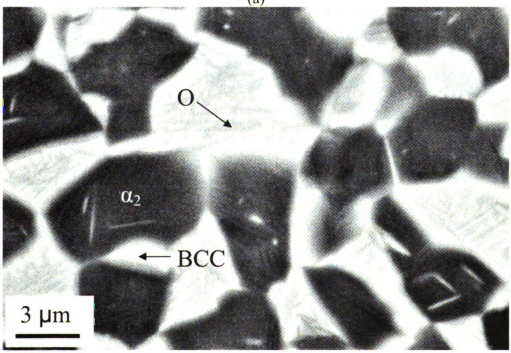

(b)

Figure 4.8. (a) Low-magnification and (b) high-magnification BSE SEM micrographs of matrix microstructure for the HT Ultra SCS-6/Ti-24Al-17Nb-0.66Mo MMC.

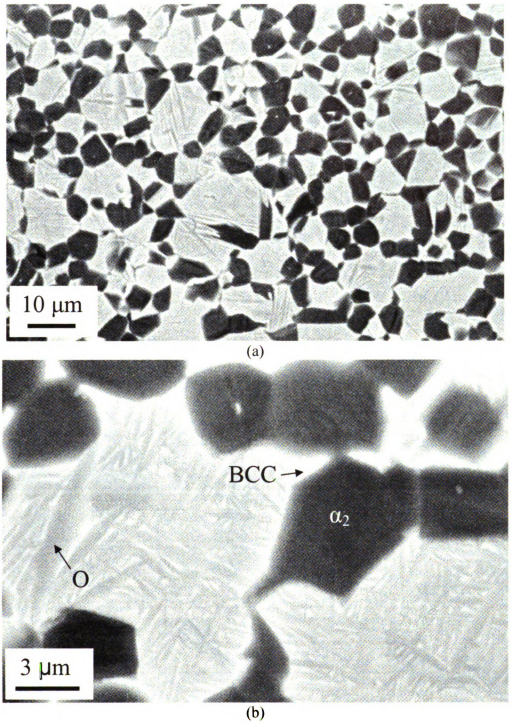

Figure 4.9 (a) Low-magnification and (b) high-magnification BSE SEM micrographs of matrix microstructure for the HT Ultra SCS-6/Ti-24Al-17Nb-1.1Mo MMC.

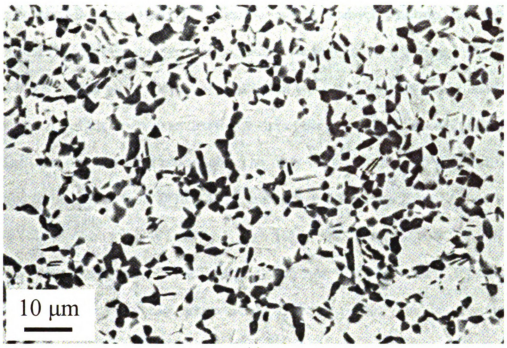

(a)

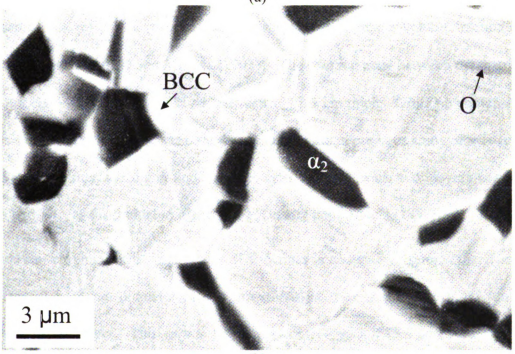

(b)

Figure 4.10 (a) Low-magnification and (b) high-magnification BSE SEM micrographs of matrix microstructure for the HT Ultra SCS-6/Ti-24Al-17Nb-2.3Mo MMC.

For the MMC panels, the fiber distribution was relatively uniform, and in general, the fiber-matrix interface was well consolidated, see Figure 4.11 – Figure 4.13. Each of the MMCs consisted of four layers of continuous Ultra SCS-6 fibers sandwiched within the matrix. All of the fibers extended to the end of the consolidated sheets, and no fully-embeded fiber samples were processed. The fiber volume fraction of the MMCs were measured to be 0.35 ± 0.05, 0.35 ± 0.02, and 0.35 ± 0.1 for the Ultra SCS-6/Ti-24Al-17Nb-0.66Mo, Ultra SCS-6/Ti-24Al-17Nb-1.1Mo, and Ultra SCS-6/Ti-24Al-17Nb-2.3Mo MMCs, respectively. The matrix region near the fiber-matrix interface was depleted of the O+BCC phases and enriched in the α_2 phase. This is a result of the reaction between the fiber and matrix during consolidation and subsequent heat treatment as when carbon diffuses across the interface it stabilizes a greater volume fraction of the α_2 phase [Krishnamurthy and Miracle (1997)]. The reaction zone between the matrix and the outer coating for each MMC was between 1 – 2.5 μm thick. While no compositional analysis of the reaction zone was performed in this work, a previous study of a Ti-6Al-4V (wt.%)/SCS-6 interface determined the reaction zone to consist of layers containing Ti_5Si_3 and TiC, as diagramed in Figure 4.14 [Gundel and Miracle (1997)].

A micrograph of a single Ultra SCS-6 fiber is shown in Figure 4.15. The fiber consisted of a 33 μm diameter carbon monofilament over-coated with a 1.5 μm thick pyrolytic carbon layer. This carbon layer was covered with a 48.7 μm thick very fine-grained β SiC, which comprised the bulk of the fiber. A 3.3 μm multi-layered, carbon-containing coating was applied to protect the fiber during handling and to reduce potential chemical reactions between the SiC and matrix.

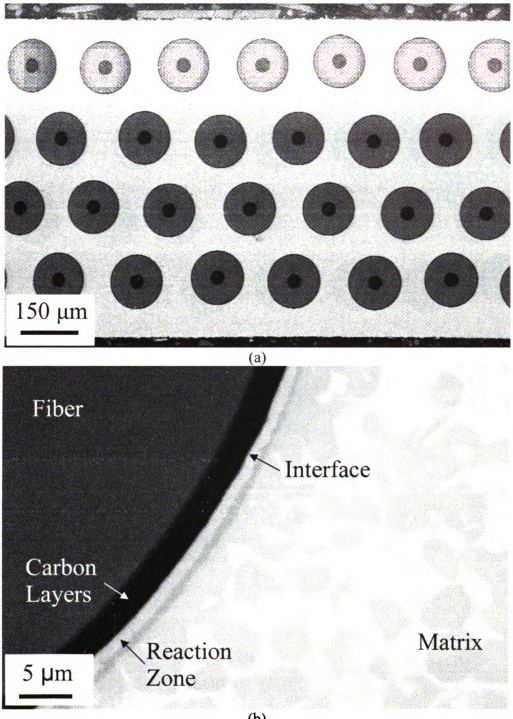

Figure 4.11 (a) Low magnification and (b) high magnification BSE SEM photomicrographs representing a view of the Ultra SCS-6/Ti-24Al-17Nb-0.66Mo MMC fiber-matrix interface.

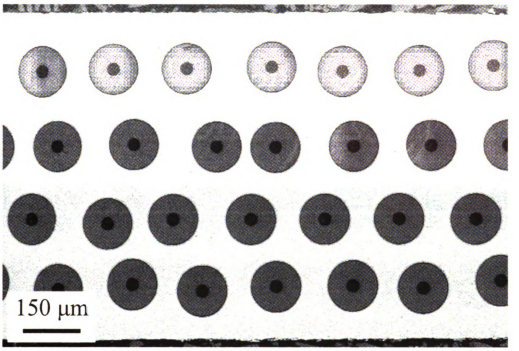

(a)

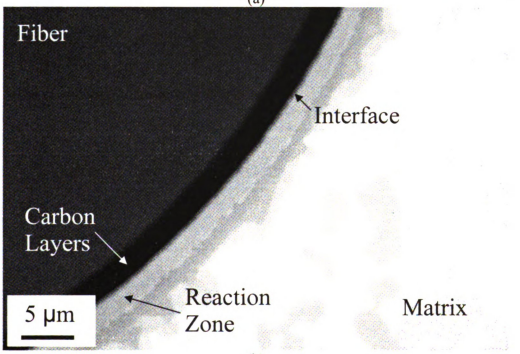

(b)

Figure 4.12 (a) Low magnification and (b) high magnification BSE SEM photomicrographs representing a view of the Ultra SCS-6/Ti-24Al-17Nb-1.1Mo MMC fiber-matrix interface.

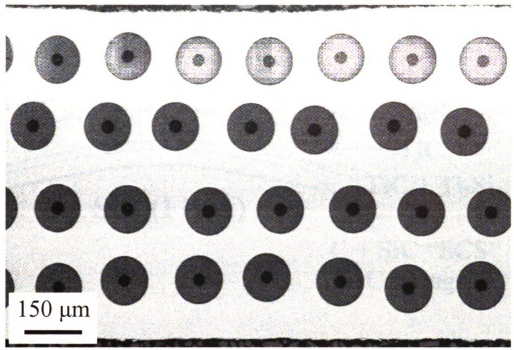

(a)

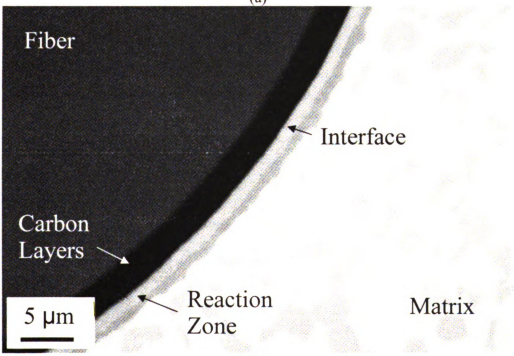

(b)

Figure 4.13 (a) Low magnification and (b) high magnification BSE SEM photomicrographs representing a view of the Ultra SCS-6/Ti-24Al-17Nb-2.3Mo MMC fiber-matrix interface.

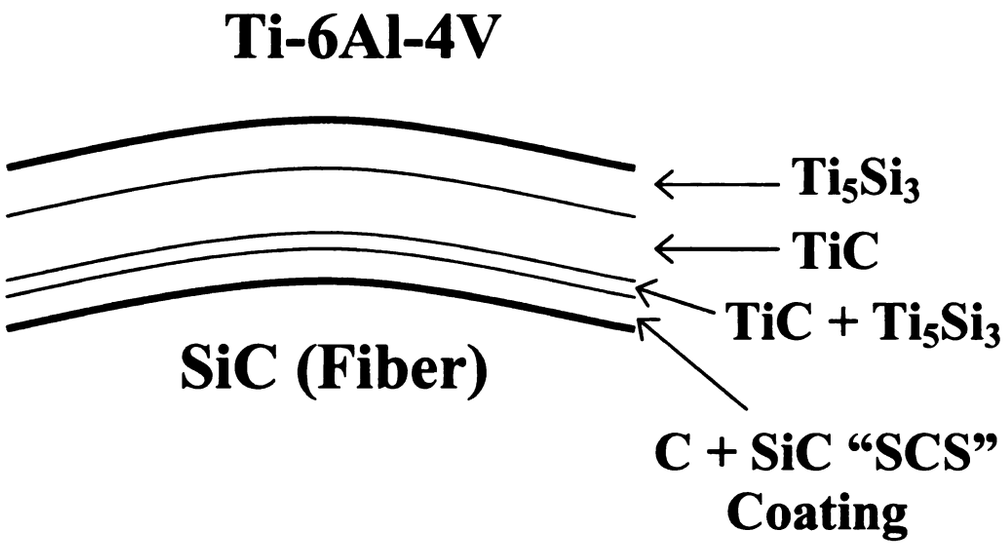

Figure 4.14 A sketch of the fiber-matrix interface reaction zone products in a Ti-6Al-4V (wt.%)/SCS-6 MMC.

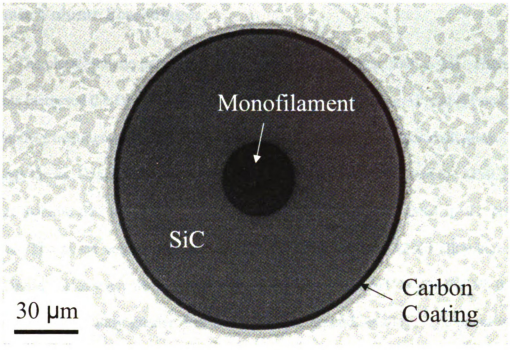

Figure 4.15 The fiber consisted of a carbon monofilament inner core surrounded by fine-grained SiC encased by a protective carbon coating.

4. Phase Volume Percentages

The phase volume percents of the alloys are provided in Tables 4.II. Higher Mo contents increased the O+BCC-phase volume percents for both the AP and HT condition, and the heat treatment resulted in lower α_2 phase volume percents for each alloy. Table 4.III lists the α_2, O, and BCC-phase volume percents for the matrices in the MMCs. The average volume percent of the fibers in each MMC was 35 as stated in the previous section. The phase volume percents of the HT Ti-24Al-17Nb-2.3Mo alloy and MMC were similar. However, the α_2 phase volume percent in the HT Ti-24Al-17Nb-0.66Mo matrix was significantly greater than that in the corresponding alloy. The phase volume percentages of the Ti-24Al-17Nb-1.1Mo matrix fell between the values obtained for the Ti-24Al-17Nb-0.66Mo and Ti-24Al-17Nb-2.3Mo matrices, as expected.

Table 4.II. Phase volume percents (Vp) for the alloys

Composition	Condition	α_2 Vp	O+BCC Vp
Ti-24Al-17Nb-0.66Mo	AP	49.6±2.9	50.4±2.9
Ti-24Al-17Nb-0.66Mo	HT	38.3±2.5	61.7±2.5
Ti-24Al-17Nb-2.3Mo	AP	26.3±3.4	73.7±3.4
Ti-24Al-17Nb-2.3Mo	HT	24.1±1.0	75.9±1.0

AP: As processed, HT: Heat treated

Table 4.III. Phase volume percents (Vp) for the matrix within the composites

Composition	Condition	α_2 Vp	O+BCC Vp
Ultra SCS-6/Ti-24Al-17Nb-0.66Mo	HT	47.0±0.3	53.0±0.3
Ultra SCS-6/Ti-24Al-17Nb-1.1Mo	HT	41.0±0.2	59.0±0.2
Ultra SCS-6/Ti-24Al-17Nb-2.3Mo	HT	24.9±0.4	75.1±0.4

HT: Heat treated

5. Grain Sizes

The average equiaxed α_2 and O+BCC colony grain sizes for the alloys and MMCs is given in Table 4.IV. For all the materials, the O+BCC colony were larger than the average α_2 grains. An increase in O+BCC colony grain size was apparent after heat treating the alloys. The addition of Mo tended to reduce the α_2 grain size, except in the case of the Ultra SCS-6/Ti-24Al-17Nb-1.1Mo MMC, where an increase was observed. The average grain size of alloys and MMCs with similar compositions was well maintained, showing only small variations in size. Overall, the average grain size of the alloys and MMCs did not deviate greatly, with diameters only fluctuating a few microns.

Table 4.IV. Grain sizes for the alloys and matrices within the composites

Composition	Condition	Average α_2 grain size (μm)	Average O+BCC grain size (μm)	Average equiaxed grain size (μm)*
Ti-24Al-17Nb-0.66Mo	AP	6.8±0.8	7.8±1.8	7.1±0.5
Ti-24Al-17Nb-0.66Mo	HT	6.6±1.1	11.5±2.3	7.9±0.8
Ti-24Al-17Nb-2.3Mo	AP	4.7±0.9	11.3±1.9	7.4±0.5
Ti-24Al-17Nb-2.3Mo	HT	4.6±1.2	15.6±3.2	9.2±0.9
Ultra SCS-6/Ti-24Al-17Nb-0.66Mo	HT	6.5±1.3	8.4±2.1	6.3±0.4
Ultra SCS-6/Ti-24Al-17Nb-1.1Mo	HT	8.2±0.9	14.3±2.9	9.0±1.1
Ultra SCS-6/Ti-24Al-17Nb-2.3Mo	HT	4.7±1.3	14.6±2.8	6.8±0.5

*Measured using the line intercept method

6. BCC Phase Ordering

Depending on the composition and heat treatment, the BCC phase in Ti-Al-Nb alloys can be ordered (B2) or disordered (β) [Kestner-Weykamp *et al.* (1989), Bendersky *et al.* (1991), Rhodes *et al.* (1993)]. Determination of β/B2 phase ordering was accomplished using x-ray diffraction (XRD), where Ti-24Al-17Nb-0.66Mo and Ti-24Al-17Nb-2.3Mo alloy samples were scanned to examine the existence of the (210) superlattice reflection. This superlattice reflection only occurs when the β phase is ordered (i.e. B2). With a lattice parameter of 0.323 nm, the (210) superlattice reflection occurs at a 2θ angle of approximately 64°.

XRD scans were performed using copper K alpha radiation and a nickel filter at 35kv and 25mA on an XDS 2000™ (Scintag Inc. USA) with a count time of 30s with a 0.01° 2θ step size. Figure 4.16 depicts the scans that were run for each alloy composition. For each composition a peak corresponding to the (210) superlattice reflection site exists. However, the intensity was not significantly greater than the background, whereas the peak height of a fully ordered alloy would be expected to be greater than twice the background. Therefore, this suggests that while the β phase within these alloys was capable of forming the ordered B2 crystal structure it may not have been favored and the presence of the disordered β crystal structure within the alloys was highly probably.

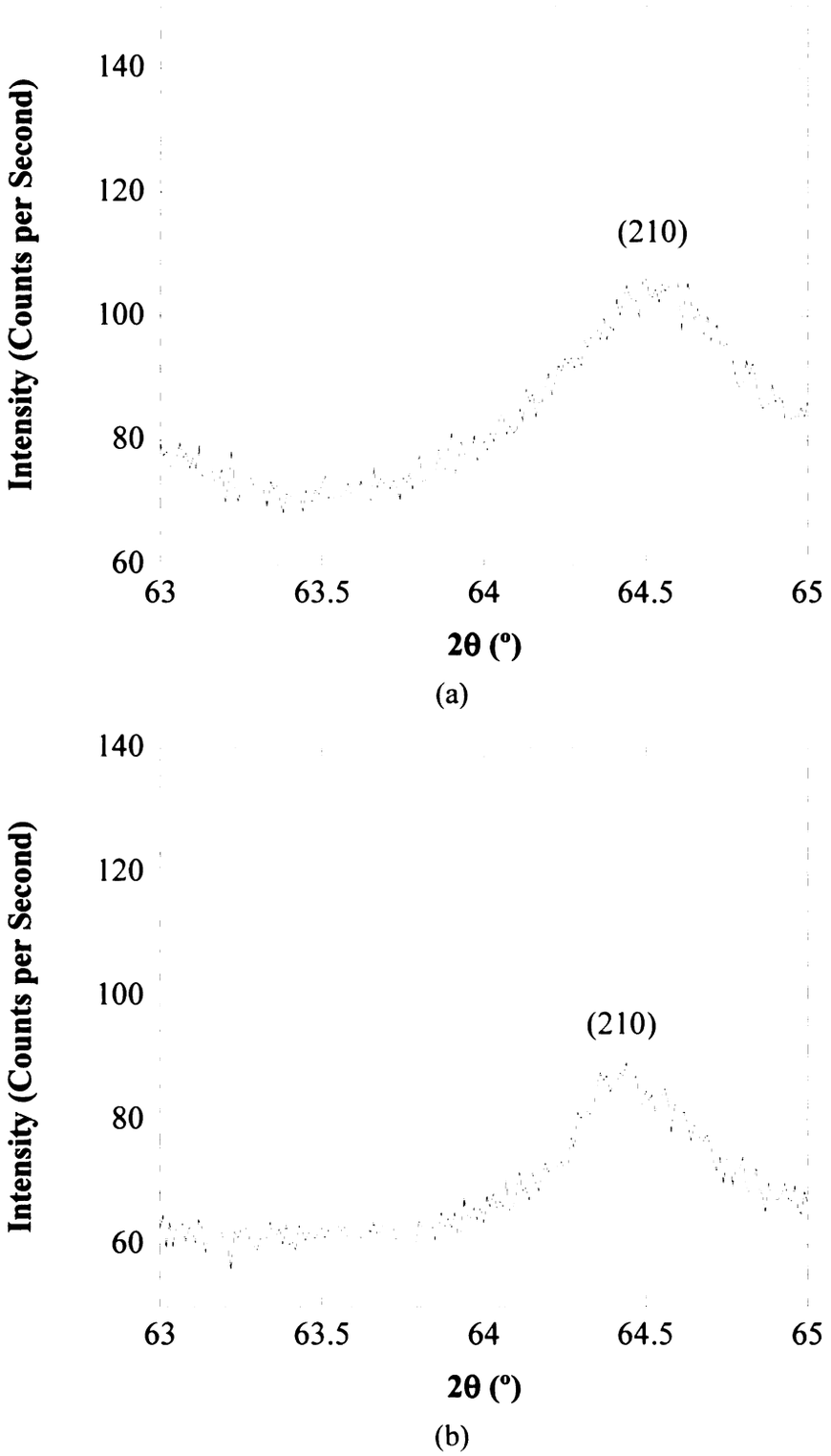

Figure 4.16 Long time count scans of (a) the Ti-24Al-17Nb-0.66Mo alloy and (b) the Ti-24Al-17Nb-2.3Mo alloy showing weak intensities at the (210) superlattice reflection.

7. Microprobe and Energy Dispersive Spectroscopy Analysis

Microprobe analysis was conducted on the HT alloys to determine the chemical composition of each phase and to reveal the preferential distribution of the Mo within the phases. Micrographs showing some of the points where the analysis was conducted are provided in Figure 4.17 and Figure 4.18 for the Ti-24Al-17Nb-0.66Mo and Ti-24Al-17Nb-2.3Mo alloys, respectively. The resulting data is presented in Table 4.V. The greatest atomic percentage of Ti was observed in the α_2 phase, containing more than 60 at.% Ti in each alloy. The average Ti content in the α_2 phase in the Ti-24Al-17Nb-0.66Mo alloy was 61.8%, while the average Ti content in the α_2 phase in the Ti-24Al-17Nb-2.3Mo alloys was 60.9%. The BCC phase, with respect to the Ti content, was the most depleted. The Al content was similar for the α_2 and O phases for each alloy, measuring approximately 25 at.% for each alloy. This was expected based on the stoichiometry of these intermetallic phases (α_2 – Ti_3Al, O – Ti_2AlNb). A significant decrease in Al content was observed for both alloys in the BCC phase. The greatest atomic percent of Nb and Mo was observed in the BCC phase for both alloys. This was expected as these are both BCC-phase stabilizing elements. The α_2 phase was significantly depleted of both Nb and Mo. For the Ti-24Al-17Nb-0.66Mo alloy the Mo content was greater in the BCC phase than the O phase, whereas for the Ti-24Al-17Nb-2.3Mo alloy the Mo content was similar in the O phase and the BCC phase.

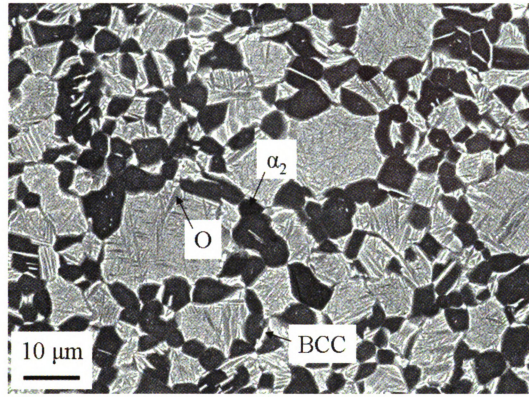

Figure 4.17 A BSE SEM image of a HT Ti-24Al-17Nb-0.66Mo alloy microstructure **where** the arrows indicate where microprobe analysis was conducted.

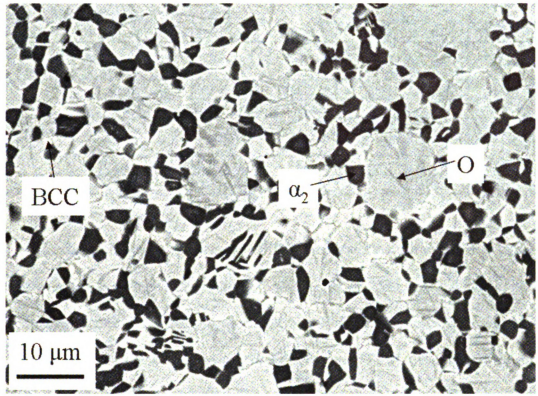

Figure 4.18 A BSE SEM image of the HT Ti-24Al-17Nb-2.3Mo alloy microstructure **where** the arrows indicate where microprobe analysis was conducted.

Table 4.V Microprobe Analysis Results

Material	Phase	Ti (at. %)	Al (at. %)	Nb (at. %)	Mo (at. %)
Ti-24Al-17Nb-0.66Mo	α_2	61.8 ± 0.2	26.5 ± 0.2	11.6 ± 0.2	0.1 ± 0.03
	O	58.7 ± 1.7	24.5 ± 1.8	16.3 ± 3.0	0.6 ± 0.3
	BCC	56.6 ± 0.5	24.2 ± 2.1	17.6 ± 1.9	1.5 ± 0.2
Ti-24Al-17Nb-2.3Mo	α_2	60.9 ± 1.2	26.7 ± 0.4	11.9 ± 1.2	0.5 ± 0.4
	O	54.9 ± 0.8	25.5 ± 0.5	17.3 ± 1.3	2.3 ± 0.1
	BCC	53.8 ± 0.6	25.3 ± 0.4	18.3 ± 0.6	2.6 ± 0.4

An energy dispersive spectroscopy (EDS) map was obtained using the microprobe to qualitatively access the distribution of the Ti, Al, Nb, and Mo elements within patches of the microstructure. Micrographs of the elemental scans are presented in Figure 4.19 and Figure 4.20 for the Ti-24Al-17Nb-0.66Mo and Ti-24Al-17Nb-2.3Mo alloys, respectively. The corresponding BSE SEM images for Figure 4.19 and Figure 4.20 are given in Figure 4.17 and Figure 4.18, respectively. For each micrograph the scanned element is indicated by a variance in contrast, where brighter locations indicated a greater content of the scanned element. Shown in Figure 4.19 (a) and (b) and Figure 4.20 (a) and (b), the presence of Ti and Al more substantial in the α_2 phase than the O and BCC phases. Figure 4.19 (c) and (d) and Figure 4.20 (c) and (d) indicate that Nb and Mo are more prevalent within the O and BCC phases than the α_2 phase. Therefore, the EDS results match well with those found using the microprobe analysis.

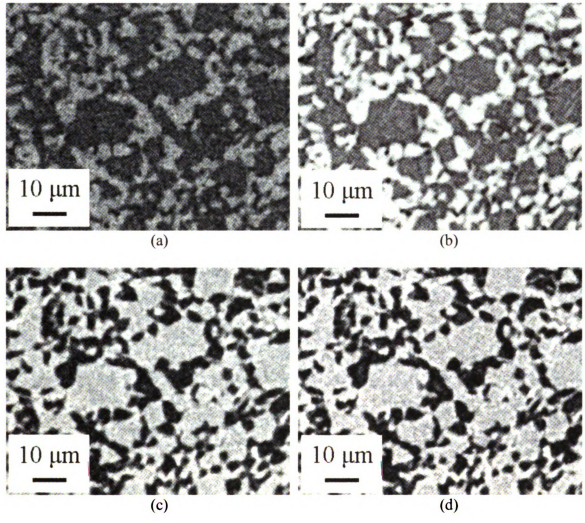

Figure 4.19 Micrographs, formed using EDS data, of the HT Ti-24Al-17Nb-0.66Mo alloy displaying the amount of (a) Ti, (b) Al, (c) Nb, and (d) Mo present within the microstructure. The brighter areas indicate a greater presence of the element. The corresponding micrograph is given in Figure 4.17.

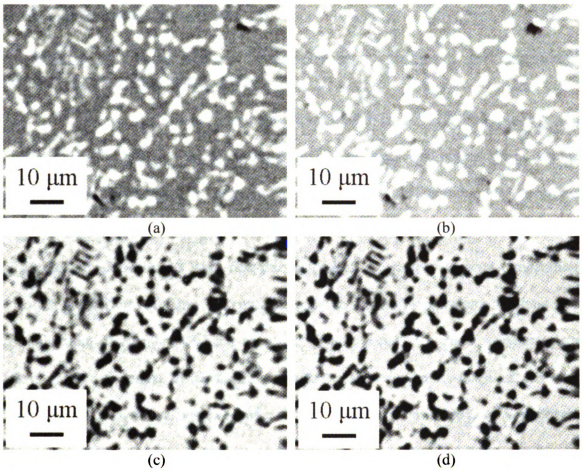

Figure 4.20 Micrographs, formed using EDS data, of the HT Ti-24Al-17Nb-2.3Mo alloy displaying the amount of (a) Ti, (b) Al, (c) Nb, and (d) Mo present within the microstructure. The brighter areas indicate a greater presence of the element. The corresponding micrograph is given in Figure 4.18.

B. Creep Behavior Results

1. Minimum Creep Rates, Creep Stress Exponents, and Apparent Activation Energies of the Alloys

The creep strain versus time relationship of the Ti-24Al-17Nb-xMo alloys was similar to that for pure metals, exhibiting primary, secondary, and tertiary creep regimes [Evans and Wilshire (1985)]. Creep strain rates were regarded as minimum creep rates when the strain rate remained constant over a minimum of 50 hours at each condition. The creep stress exponents were determined through a series of constant temperature, load-jump experiments. These experiments were performed by increasing the load after the minimum creep rate had been achieved. The apparent activation energies of the alloys were determined by performing constant load, temperature-jump experiments, where the temperature was increased after reaching the minimum creep rate. For both the load-jump and temperature-jump experiments, after the load or temperature was increased, the minimum creep rate increased. Experimental data obtained from typical load and temperature jump tests are shown in Figure 4.21 and Figure 4.22, respectively.

Creep strain versus time curves for Ti-24Al-17Nb-0.66Mo and Ti-24Al-17Nb-2.3Mo samples at T = 650°C and σ = 172 MPa are depicted in Figure 4.23, which also depicts curves for the baseline ternary alloy and a Ti-24Al-17Nb-1Mo alloy. The Ti-24Al-17Nb-2.3Mo and Ti-24Al-17Nb-1Mo alloys exhibited the lowest primary creep strains and minimum creep rates, while the baseline ternary alloy exhibited the greatest primary creep strains and minimum creep rates. As also illustrated in Figure 4.24, the creep resistance of the Ti-24Al-17Nb-2.3Mo alloy was superior to that of the Ti-24Al-17Nb-0.66Mo alloy. The measured minimum creep rates for the Ti-24Al-17Nb-0.66Mo and Ti-24Al-17Nb-2.3Mo alloys are given as a function of stress and temperature in

Table 4.VI and Table 4.VII, respectively. The average creep strain at failure for the Ti-24Al-17Nb-0.66Mo and Ti-24Al-17Nb-2.3Mo alloys was 6.9% and 1.7%, respectively.

Minimum creep strain rate versus applied stress and ln minimum creep rate versus 1/T plots were used to calculate the creep exponent (n) and activation energy (Qapp) values, respectively. Shown in Figure 4.25 is the minimum creep rate versus applied stress plot for the Ti-24Al-17Nb-0.66Mo and Ti-24Al-17Nb-2.3Mo alloys. Over all the stresses examined, the Ti-24Al-17Nb-2.3Mo alloy exhibited significantly lower minimum creep rates than the Ti-24Al-17-0.66Mo alloy. In fact, approximately one order of magnitude difference in minimum creep rate was observed at 650°C. Each alloy exhibited a change in creep exponent at an applied stress between 170-225 MPa, suggesting two dominant creep mechanisms may be active. At lower stress values n was approximately two, while at higher stress levels n was between four and five. Apparent activation energies determined from the temperature dependence of the minimum creep rate are given in Figure 4.26 and Figure 4.27. The activation energy of the Ti-24Al-17Nb-0.66Mo alloy was significantly larger at 150 MPa than 29 MPa, suggesting the possibility of two different dominant diffusion mechanisms at different stress regimes. The creep exponent and apparent activation energy values for each alloy is provided in Table 4.VIII.

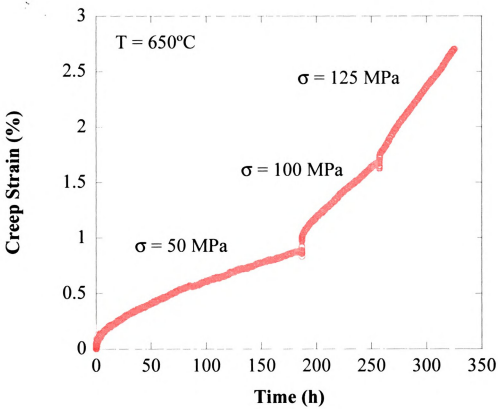

Figure 4.21 Creep strain versus time data obtained for a Ti-24Al-17Nb-0.66Mo alloy sample at 650°C during a load-jump experiment.

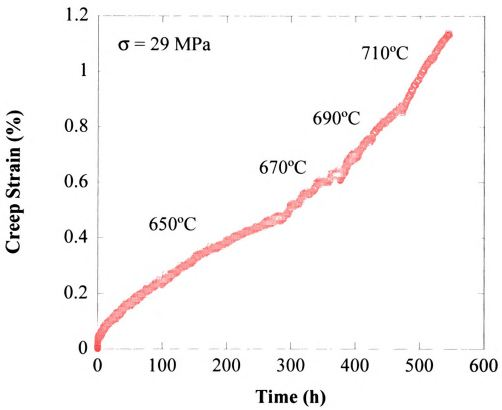

Figure 4.22 Creep strain versus time data obtained for a Ti-24Al-17Nb-0.66Mo alloy sample at 29 MPa during a temperature-jump experiment.

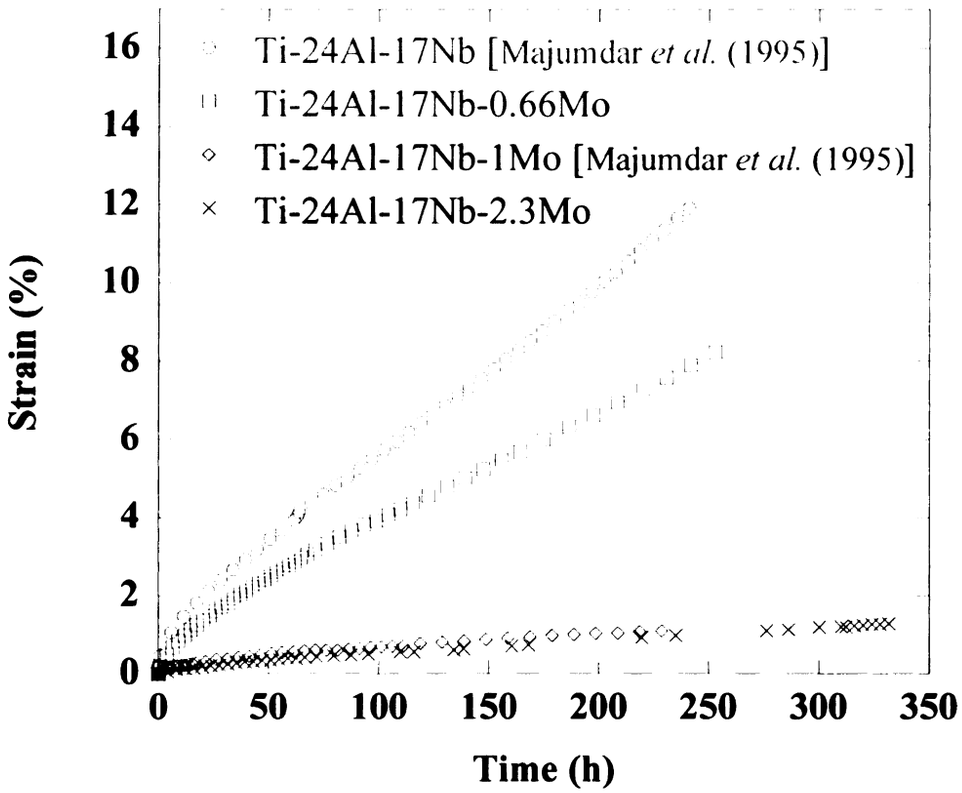

Figure 4.23 Creep strain versus time curves for the studied Ti-24Al-17Nb-xMo samples, a Ti-24Al-17Nb-1Mo, and a ternary Ti-24Al-17Nb alloy at T = 650°C and σ = 172 MPa.

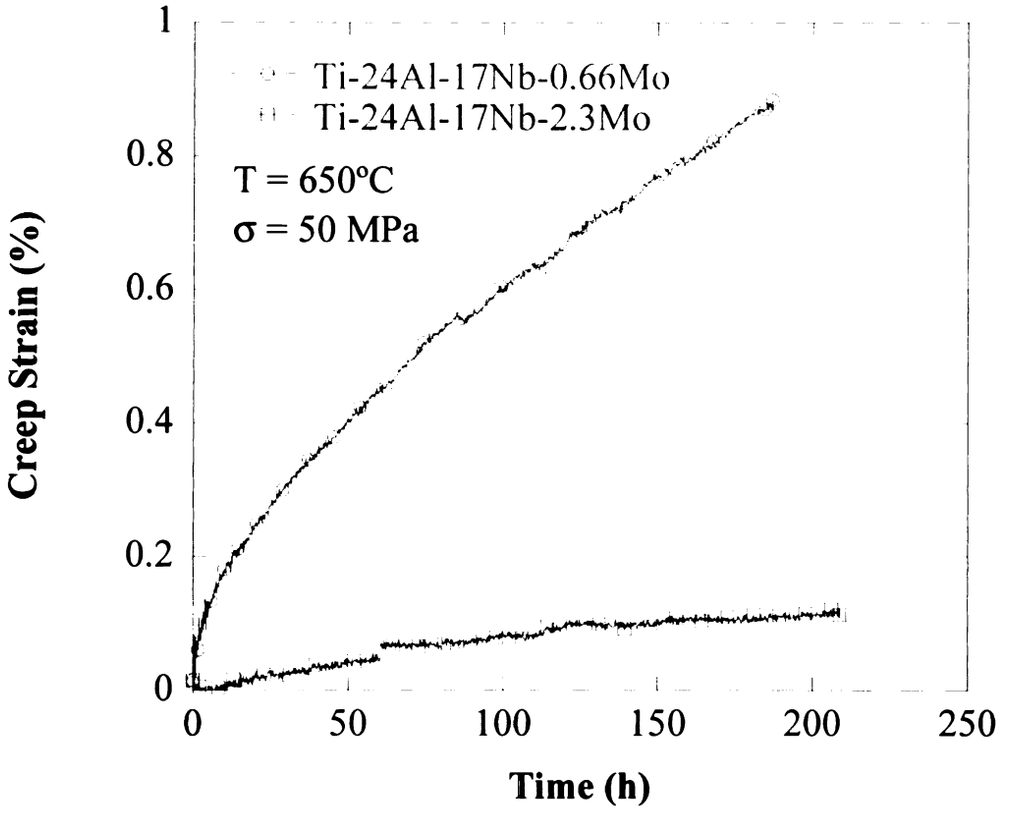

Figure 4.24 Creep strain versus time curves for the Ti-24Al-17Nb-0.66Mo and Ti-24Al-17Nb-2.3Mo alloy samples at a temperature of 650°C and a stress of 50 MPa portraying the greater creep resistance of the Ti-24Al-17Nb-2.3Mo alloy.

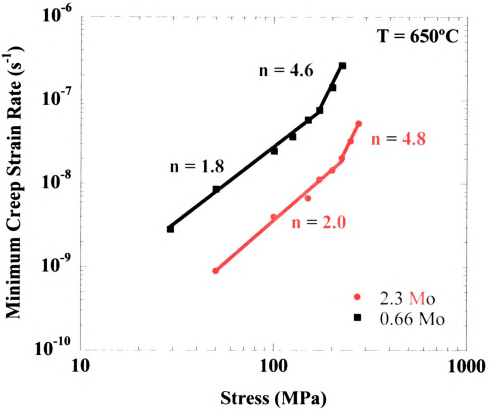

Figure 4.25 A log-log plot of the minimum creep strain rate versus stress for the Ti-24Al-17Nb-0.66Mo and Ti-24Al-17Nb-2.3Mo alloys tested at 650°C. The indicated creep exponent n values were determined from power law curve fits of the data.

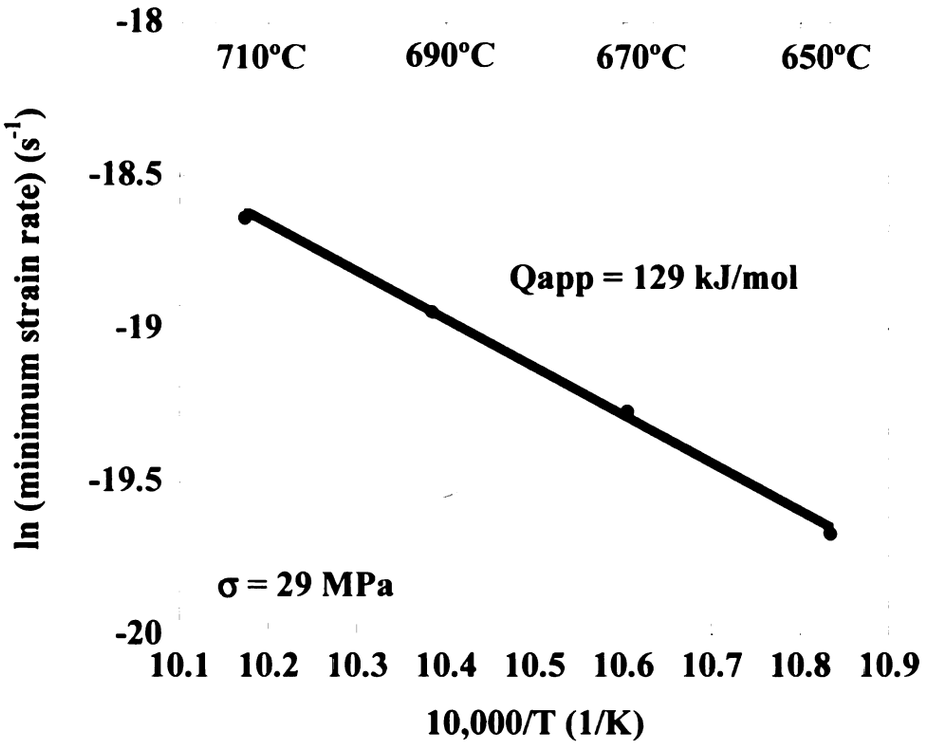

(a)

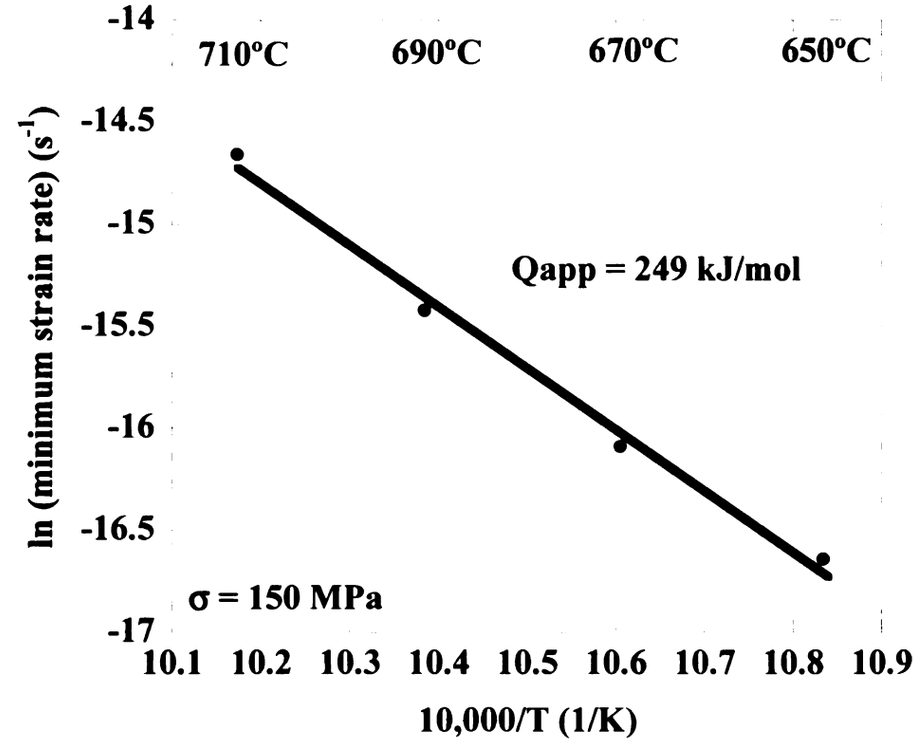

(b)

Figure 4.26 ln of the minimum creep rate versus 10,000/T plot for the Ti-24Al-17Nb-0.66Mo alloy at (a) 30 MPa and (b) 150 MPa. The indicated apparent activation energies were determined from the linear curve fits of the data.

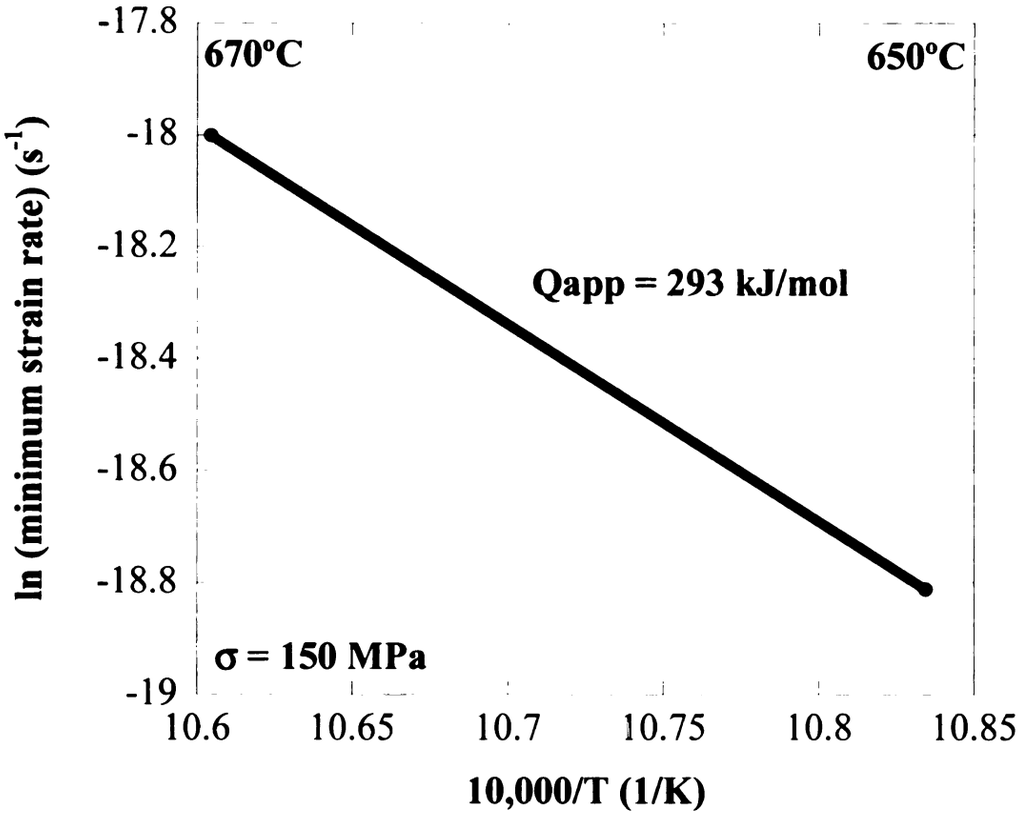

Figure 4.27 ln of the minimum creep rate versus 10,000/T plot for the Ti-24Al-17Nb-2.3Mo alloy at 150 MPa. The indicated apparent activation energies were determined from the linear curve fits of the data.

Table 4.VI The measured minimum creep rates for the Ti-24Al-17Nb-0.66Mo alloy

Stress (MPa)	Temperature (°C)	Minimum Creep Rate (s^{-1})
29	650	$2.85x10^{-9}$
29	670	$4.29x10^{-9}$
29	690	$5.93x10^{-9}$
29	710	$8.07x10^{-9}$
50	650	$8.63x10^{-9}$
100	650	$2.48x10^{-8}$
125	650	$3.69x10^{-8}$
150	650	$5.87x10^{-8}$
150	670	$1.03x10^{-7}$
150	690	$2.01x10^{-7}$
150	710	$4.30x10^{-7}$
172	650	$7.68x10^{-8}$
200	650	$1.44x10^{-7}$
225	650	$2.63x10^{-7}$

Table 4.VII The measured minimum creep rates for the Ti-24Al-17Nb-2.3Mo alloy

Stress (MPa)	Temperature (°C)	Minimum Creep Rate (s^{-1})
50	650	$8.93x10^{-10}$
100	650	$3.97x10^{-9}$
150	650	$6.73x10^{-9}$
150	670	$1.52x10^{-8}$
172	650	$1.12x10^{-8}$
200	650	$1.45x10^{-8}$
225	650	$2.02x10^{-8}$
250	650	$3.26x10^{-8}$
275	650	$5.30x10^{-8}$

Table 4.VIII The measured creep exponents and apparent activation energies for the Ti-24Al-17Nb-0.66Mo and Ti-24Al-17Nb-2.3Mo alloys

Alloy	σ/T (MPa/°C)	n	σ/T (MPa/°C)	Q_{app} (kJ/mol)
Ti-24Al-17Nb-0.66Mo				
	29-172/650	1.8		
	172-225/650	4.6		
			29/650-710	129
			150/650-710	249
Ti-24Al-17Nb-2.3Mo				
	50-225/650	2.0		
	225-275/650	4.8		
			150/650-670	293

2. Creep Deformation Behavior of the Alloys

Using the creep exponent values, deformation mechanisms can be proposed. However, this technique is limited to the interpretation of the empirical data. The effect of microstructure on the creep behavior can be evaluated using *in-situ* tensile-creep experiments conducted within a SEM chamber. This technique, as described in Chapter 3, allows for direct microstructural evidence of the potentially dominant creep deformation mechanisms. In this study, multiple BSE SEM images were taken, allowing for surface deformation to be recorded as a function of displacement and time. These images, when linked together in a series, provide evidence of the microstructural features that control creep deformation behavior.

Performing creep experiments on metalographically polished samples in a SEM chamber provides the further advantage of testing within a vacuum atmosphere. Under such conditions the integrity of the surface is maintained throughout the entire test, and therefore oxidation assisted cracking is prevented. Comparative tests performed at similar stress levels and temperatures can be used to study the effect of oxidation on creep behavior, as shown in Figure 4.28. The Ti-24Al-17Nb-2.3Mo alloy exhibited a similar amount of primary strain in each atmosphere. However, the minimum creep rate for the sample tested in vacuum was considerably smaller, therefore, suggesting the environmental stability of these Ti-Al-Nb-Mo alloys is a concern.

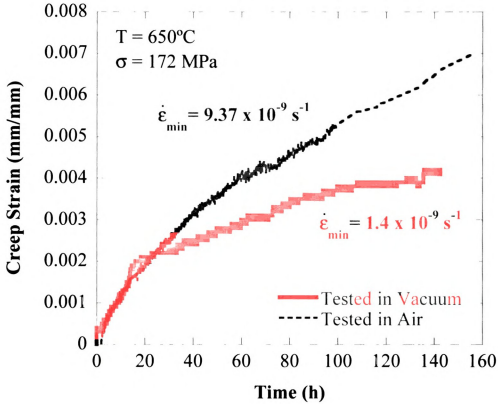

Figure 4.28 A plot of creep strain versus time for Ti-24Al-17Nb-2.3Mo alloy samples tested at 650ºC and 172 MPa in vacuum (10^{-6} torr) and in ambient air.

The Ti-24Al-17Nb-0.66Mo alloy was *in-situ* creep tested at 180 MPa and 650°C. This stress level was chosen because it lies near the top of the regime where grain-boundary sliding was considered to be the dominant deformation mechanism (based on the creep stress exponent value, see Figure 4.25). A plot of the displacement versus time for this test is given in Figure 4.29. The evolution of the grain boundary sliding/cracking as a function of creep displacement is apparent in Figure 4.30 (a) – 4.30 (f), where the loading direction is horizontal. It is noted that all the cracking was limited to grain boundary locations. While the progression of grain-boundary sliding was not captured for the Ti-24Al-17Nb-2.3Mo alloy, a post-test image for the Ti-24Al-17Nb-2.3Mo alloy creep tested at 190 MPa and 670°C in a vacuum displayed similar surface deformation behavior as the Ti-24Al-17Nb-0.66Mo alloy, see Figure 4.31.

The *in-situ* creep experiments indicated that grain boundaries were the locus of deformation and cracking in each of the alloys investigated. No transgranular cracking was apparent, even at high displacement levels. Deformation, in the form of cracks, tended to originate at α_2/α_2 or α_2/O+BCC grain boundaries. As displacements increased these α_2 grain boundary cracks increased in length and width. Therefore, such experiments verify that cracking and crack accommodated sliding is a dominant deformation mechanism for these alloys at stresses between 29 MPa – 172 MPa for the Ti-24Al-17Nb-0.66Mo alloy and at stresses between 50 MPa – 225 MPa for the Ti-24Al-17Nb-2.3Mo alloy.

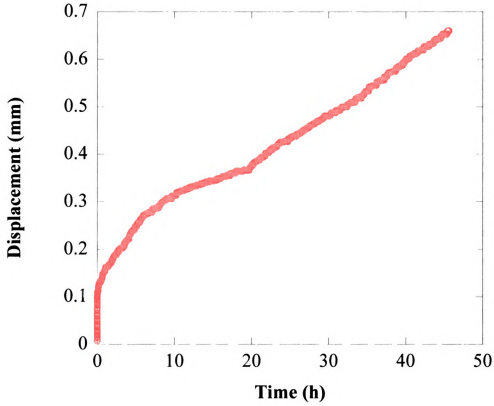

Figure 4.29 Displacement versus time plot for a Ti-24Al-17Nb-0.66Mo alloy sample creep tested at 180 MPa and 650ºC using an *in-situ* tensile creep methodology.

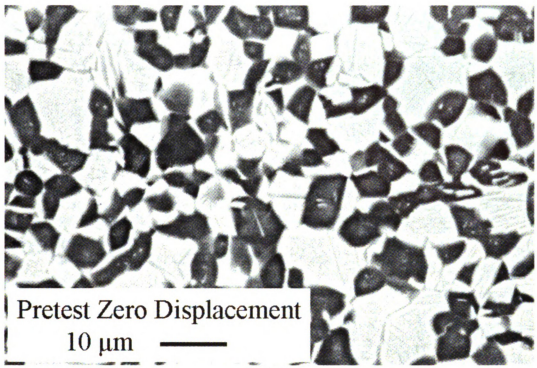

(a)

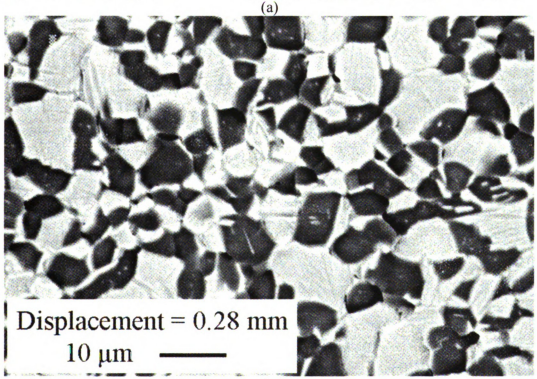

(b)

Figure 4.30 BSE SEM micrographs (a) – (f) of Ti-24Al-17Nb-0.66Mo creep tested at 180 MPa and 650ºC showing the evolution of creep deformation. The loading direction was horizontal in all images and the creep displacement values are indicated.

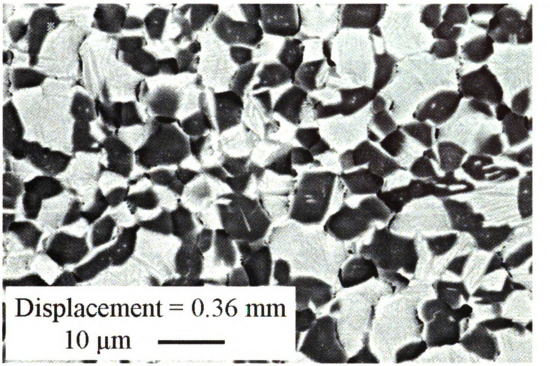

(c)

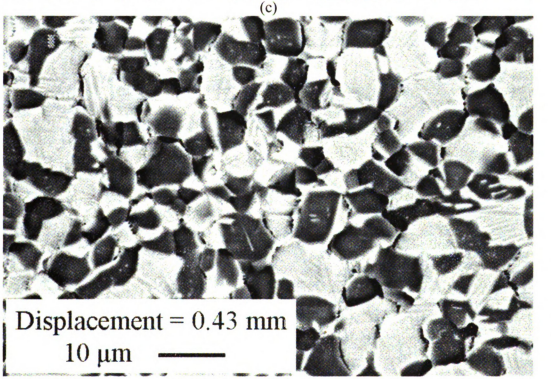

(d)

Figure 4.30 BSE SEM micrographs (a) – (f) of Ti-24Al-17Nb-0.66Mo creep tested at 180 MPa and 650ºC showing the evolution of creep deformation. The loading direction was horizontal in all images and the creep displacement values are indicated.

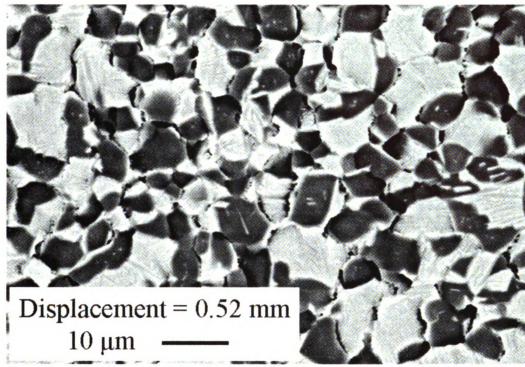

(e)

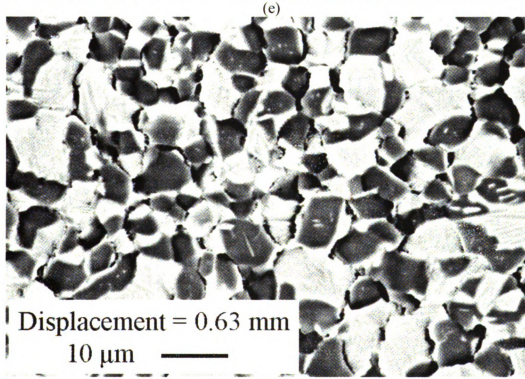

(f)

Figure 4.30 BSE SEM micrographs (a) – (f) of Ti-24Al-17Nb-0.66Mo creep tested at 180 MPa and 650ºC showing the evolution of creep deformation. The loading direction was horizontal in all images and the creep displacement values are indicated.

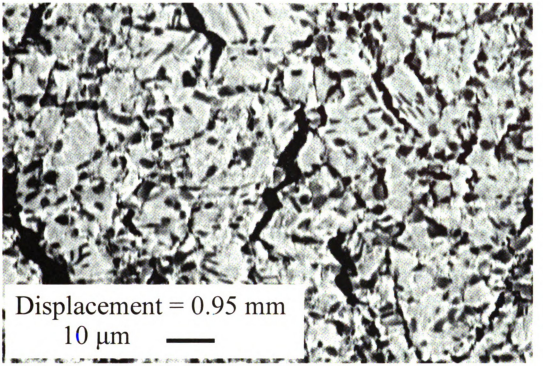

Figure 4.31 BSE SEM micrograph of Ti-24Al-17Nb-2.3Mo tested at 190 MPa and 670ºC showing cracking predominantly at the grain boundaries. The loading direction was horizontal in all images and the creep displacement values are indicated.

While *in-s*

deformation, observ

to bulk material be

alloy creep tested a

tested at 100 MPa

along α_2 grain boun

However, the amou

that in the bulk. A

constraint on the m

energy than cracki

was apparent, see

surface, these cra

α_2 grains, as sh

clusters of α_2 gr

While *in-situ* creep testing is a useful methodology to evaluate surface deformation, observations of the bulk material are necessary to compare surface behavior to bulk material behavior. Bulk microstructural observations of a Ti-24Al-17Nb-0.66Mo alloy creep tested at 150 MPa and 650°C along with a Ti-24Al-17Nb-2.3Mo alloy creep tested at 100 MPa and 650°C (both tested in air) are presented in Figure 4.32. Cracking along α_2 grain boundaries was evident and was in agreement with surface observations. However, the amount of grain boundary cracking on the surface was more extensive than that in the bulk. A greater degree of cracking was expected on the surface as there is less constraint on the material than in the bulk, and therefore surface cracking requires less energy than cracking within the bulk. For the alloys tested in air, severe edge cracking was apparent, see Figure 4.33. Unlike the cracks observed within the bulk and on the surface, these cracks appeared to be transgranular, cutting through O+BCC colonies and α_2 grains, as shown in Figure 4.34. Such cracks predominately propagated through clusters of α_2 grains in a direction perpendicular to the loading axis.

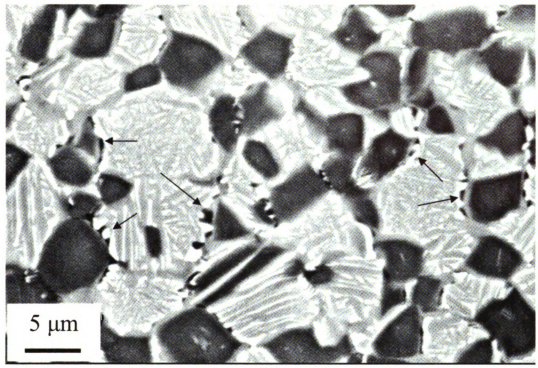

(a)

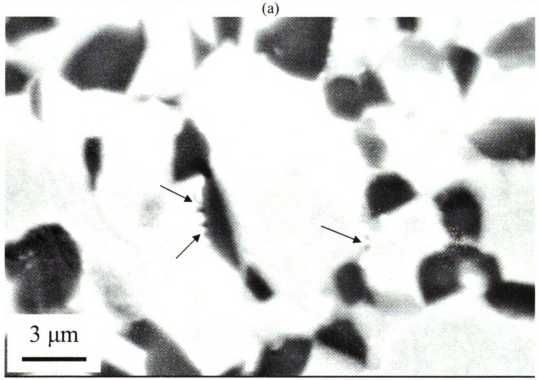

(b)

Figure 4.32 BSE SEM photomicrographs taken from creep tests showing intergranular cracking (indicated by arrows) within the bulk (interior) of the sample for the (a) Ti-24Al-17Nb-0.66Mo alloy and the (b) Ti-24Al-17Nb-2.3Mo alloy. Both alloys were tested within the stress regime that suggests grain boundary sliding to be the dominant deformation mechanism.

Figure
= 1.5
550
active

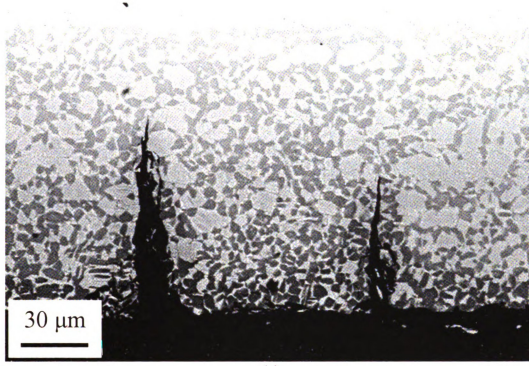

(a)

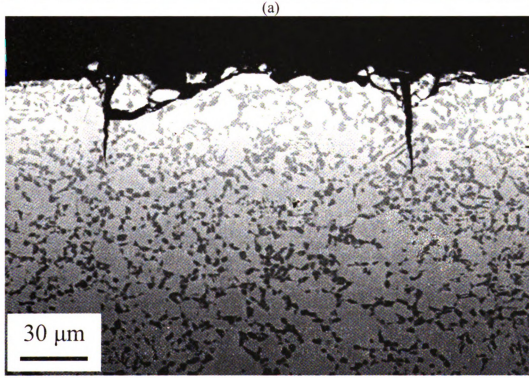

(b)

Figure 4.33 Edge cracking was apparent for both the (a) Ti-24Al-17Nb-0.66Mo alloy (σ = 150 MPa, T = 710ºC, ε = 8.4%) and the (b) Ti-24Al-17Nb-2.3Mo (σ = 275 MPa, T = 650ºC, ε = 3.2%) alloys creep tested in air, suggesting that oxidation assisted cracking is active.

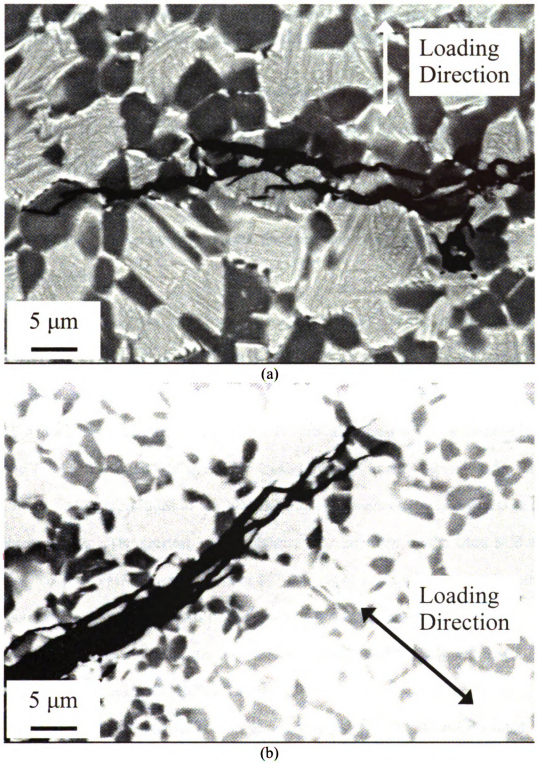

Figure 4.34 The (a) Ti-24Al-17Nb-0.66Mo alloy (σ = 200 MPa, T = 650ºC, ε = 11.4%) and the (b) Ti-24Al-17Nb-2.3Mo alloy (σ = 275 MPa, T = 650ºC, ε = 3.2%) exhibited transgranular cracking.

3. Minimum
Activation En

The MM

perpendicular t

deformation of

experiment was

temperature ju

given test cond

Creep

SCS-6 Ti-24

are depicted

650°C and a

for the Ti-24

conditions.

respective a

24Al-17Nb-

the poorest

average cre

24Al-17Nb

respectivel

function o

3. Minimum Creep Rates, Creep Stress Exponents, and Apparent Activation Energies of the Metal Matrix Composites

The MMC creep testing was conducted on samples oriented with fibers perpendicular to the loading direction. This configuration allows for the creep deformation of the MMC to be dominated by the matrix and interface behavior. Each experiment was carried out in a manner similar to the alloy creep testing, where load and temperature jumps were performed after the minimum creep rate was achieved for a given test condition.

Creep strain versus time curves for Ultra SCS-6/Ti-24Al-17Nb-0.66Mo, Ultra SCS-6 Ti-24Al-17Nb-1.1Mo, and Ultra SCS-6 Ti-24Al-17Nb-2.3Mo MMC specimens are depicted in Figure 4.35, where each experiment was performed at a temperature of 650°C and a stress of 50 MPa. Figure 4.35 also provides creep strain versus time curves for the Ti-24Al-17Nb-0.66Mo and the Ti-24Al-17Nb-2.3Mo alloys tested under similar conditions. All compositions of the MMCs exhibited poorer creep resistance than their respective alloys. The greatest creep resistance was exhibited by the Ultra SCS-6/Ti-24Al-17Nb-2.3Mo MMC, while the Ultra SCS-6/Ti-24Al-17Nb-0.66Mo MMC exhibited the poorest creep resistance. All of the creep experiments were taken to failure. The average creep failure strains for the Ultra SCS-6/Ti-24Al-17Nb-0.66Mo, Ultra SCS-6/Ti-24Al-17Nb-1.1Mo, and Ultra SCS-6/Ti-24Al-17Nb-2.3Mo were 2.6%, 1.5%, and 1.1%, respectively. The measured minimum creep rates for each MMC are provided as a function of stress and temperature in Table 4.IX.

Creep Strain (%)

3
2.5
2
1.5
1
0.5
0

Figure 4.35 Cree
650°C and 50 M

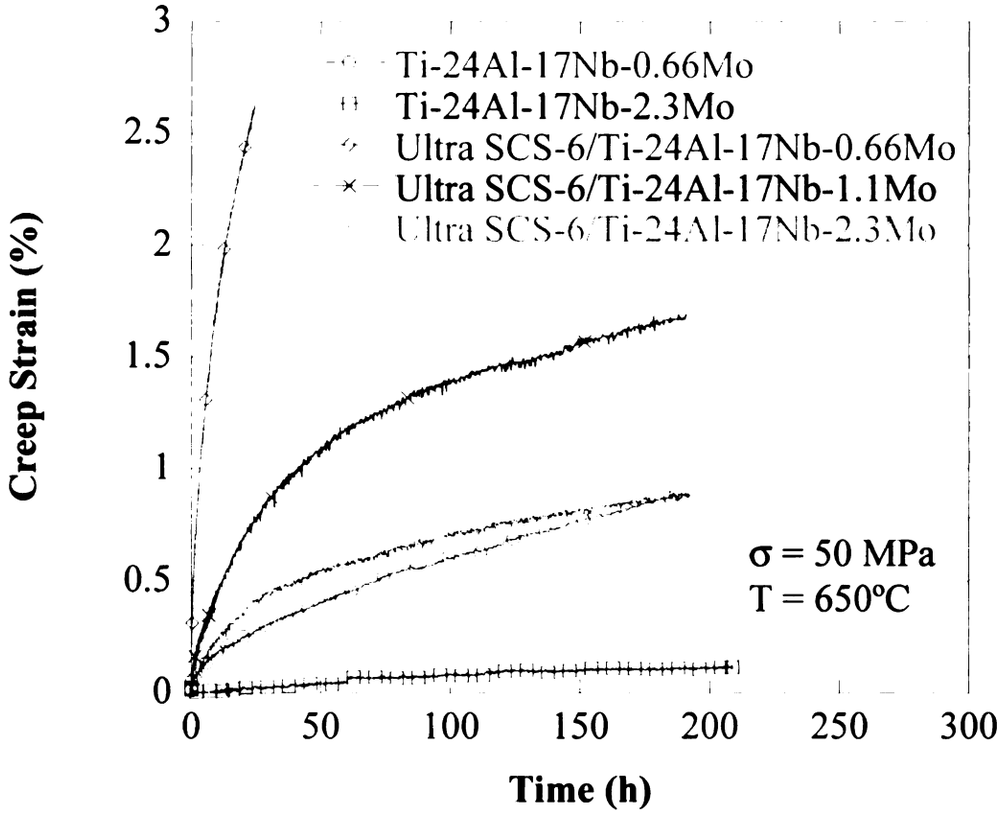

Figure 4.35 Creep strain versus time curves comparing the MMCs and the alloys tested at 650°C and 50 MPa.

Table 4.IX The m
17Nb-1.1Mo, and
MMC Composition

Ultra SCS-6 Ti-24
Ultra SCS-6 Ti-24
Ultra SCS-6 Ti-24

Table 4.IX The measured minimum creep rates for the Ti-24Al-17Nb-0.66, Ti-24Al-17Nb-1.1Mo, and Ti-24Al-17Nb-2.3Mo MMCs at 650°C

MMC Composition	Stress (MPa)	Temperature (°C)	Minimum Creep Rate (s^{-1})
Ultra SCS-6/Ti-24Al-17Nb-0.66Mo			
	10	650	2.05×10^{-9}
	10	670	2.90×10^{-9}
	10	690	3.61×10^{-9}
	10	710	4.38×10^{-9}
	30	650	1.01×10^{-8}
	40	650	1.54×10^{-8}
Ultra SCS-6/Ti-24Al-17Nb-1.1Mo			
	30	650	3.37×10^{-9}
	30	666	5.58×10^{-9}
	30	690	7.71×10^{-9}
	30	710	1.05×10^{-9}
	40	650	4.31×10^{-9}
	50	650	6.97×10^{-9}
Ultra SCS-6/Ti-24Al-17Nb-2.3Mo			
	30	650	2.75×10^{-9}
	50	650	4.63×10^{-9}
	75	650	1.13×10^{-8}

Figure

and MMCs at

the MMCs. Th

range of 10 Mi

17Nb-1.1Mo M

2.3Mo MMC h

values is close

creep rates for

17Nb-2.3Mo M

each of these r

Ti-24Al-17Nb-

similar creep r

similarly obser

4.23).

Plots of

determine the a

MMC, the appa

MPa from 650°

MMC apparent

shown in Figure

24Al-17Nb-0.66

Figure 4.36 compares the minimum creep rate versus stress for all of the alloys and MMCs at a temperature of 650°C. No transition in n value was observed for any of the MMCs. The Ultra SCS-6/Ti-24Al-17Nb-0.66Mo MMC had an n of 1.5 over a stress range of 10 MPa to 40 MPa. An n of 1.4 was determined for the Ultra SCS-6/Ti-24Al-17Nb-1.1Mo MMC from a stress of 30 MPa to 50 MPa. The Ultra SCS-6/Ti-24Al-17Nb-2.3Mo MMC had an n of 1.5 spanning the stress of 30 MPa to 75 MPa. Each of these n values is close to that observed for the lower stress regime of the alloys. The minimum creep rates for the Ultra SCS-6/Ti-24Al-17Nb-1.1Mo MMC and Ultra SCS-6/Ti-24Al-17Nb-2.3Mo MMC were similar to those for the Ti-24Al-17Nb-0.66Mo alloy. However, each of these remained approximately one order of magnitude greater than those for the Ti-24Al-17Nb-2.3Mo alloy. The Ultra SCS-6/Ti-24Al-17Nb-1.1Mo MMC experienced similar creep rates to those for the Ultra SCS-6/Ti-24Al-17Nb-2.3Mo MMC, as was similarly observed for their respective alloys tested at 172 MPa and 650°C (see Figure 4.23).

Plots of the ln minimum creep rate versus inverse temperature were used to determine the apparent activation energy. For the Ultra SCS-6/Ti-24Al-17Nb-0.66Mo MMC, the apparent activation energy was calculated to be 80 kJ/mol at a stress of 10 MPa from 650°C – 710°C, see Figure 4.37, and the Ultra SCS-6/Ti-24Al-17Nb-1.1Mo MMC apparent activation energy at 30 MPa was 126 kJ/mol from 670°C – 710°C, as shown in Figure 4.38. These values were comparable to the apparent activation of the Ti-24Al-17Nb-0.66Mo alloy tested at 29 MPa from 650°C – 710°C, which was 129 kJ/mol.

Minimum Stress Rate (s^{-1})

10^{-5}

10^{-6}

10^{-7}

10^{-8}

10^{-9}

10^{-10}

Figure 4.36 A plot
alloy examined. T
while the Ultra
resistance.

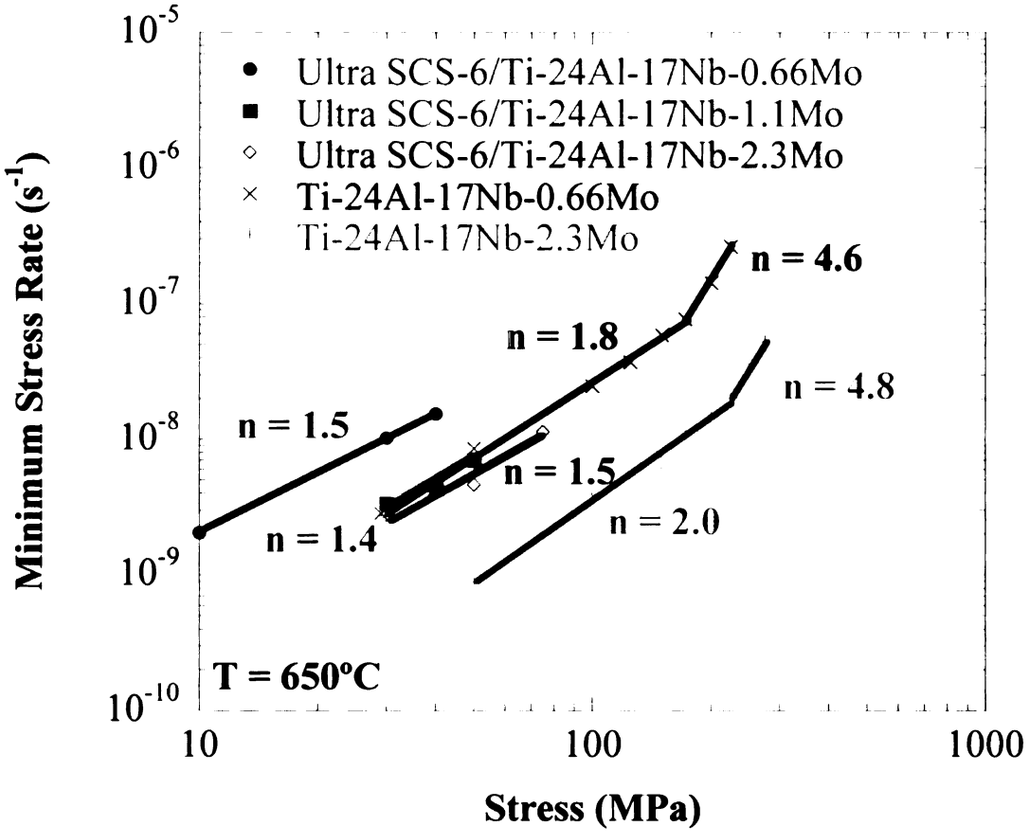

Figure 4.36 A plot of the minimum creep rate versus stress at 650°C for each MMC and alloy examined. The Ti-24Al-17Nb-2.3Mo alloy exhibited the greatest creep resistance, while the Ultra SCS-6/Ti-24Al-17Nb-0.66Mo MMC exhibited the poorest creep resistance.

Figure 4.3
2 Al-17
determin

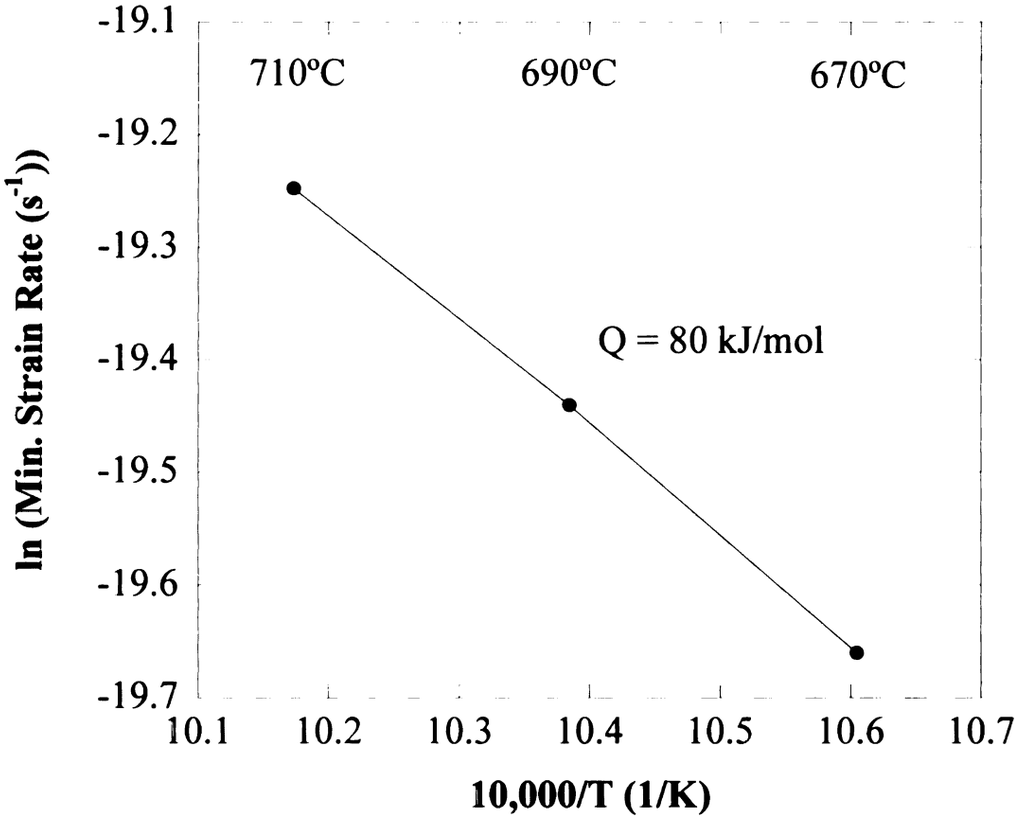

Figure 4.37 ln of the minimum creep rate versus 10,000/T plot for the Ultra SCS-6/Ti-24Al-17Nb-0.66Mo alloy at 10 MPa. The indicated apparent activation energies were determined from the linear curve fits of the data.

Figure 4.38
24Al-17Nb-
determined

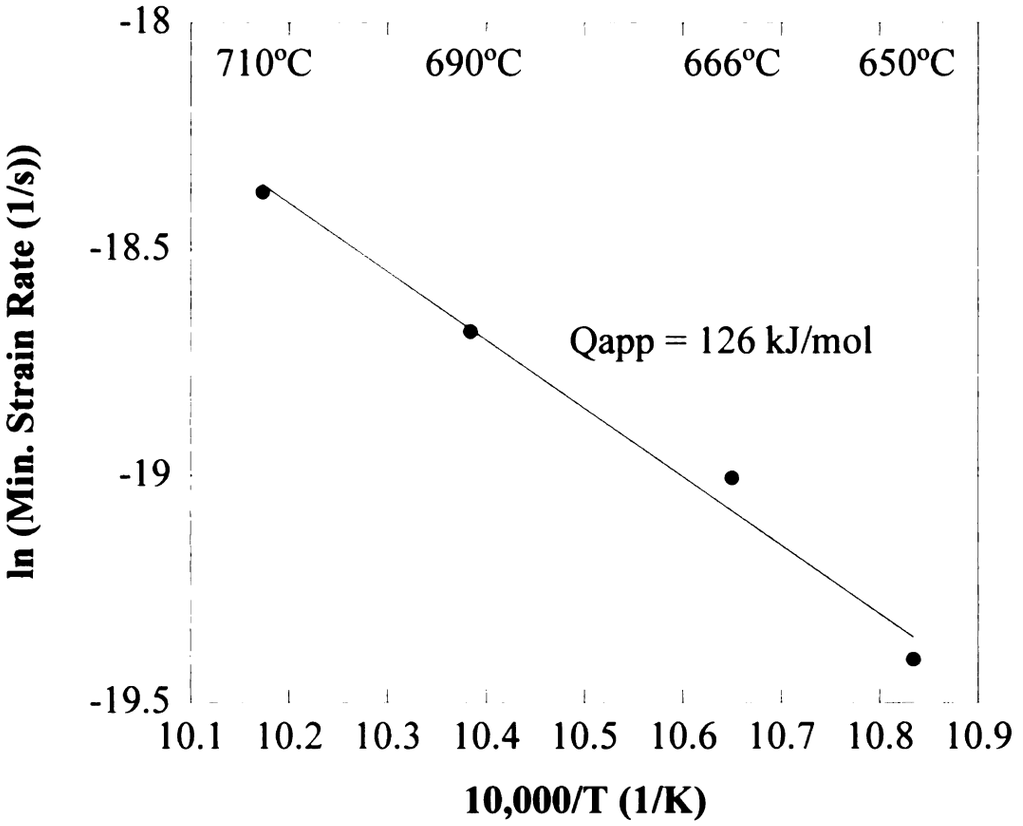

Figure 4.38 ln of the minimum creep rate versus 10,000/T plot for the Ultra SCS-6/Ti-24Al-17Nb-1.1Mo alloy at 30 MPa. The indicated apparent activation energies were determined from the linear curve fits of the data.

4. Creep Def

An inve

creep tested M

and imaged usi

A major deform

the fiber-matri

direction perpe

whereas interg

tested in a vac

traversed throu

cracking, show

4. Creep Deformation Behavior of the Metal Matrix Composites

An investigation of the post-deformation microstructures was conducted on the creep tested MMC samples. Tested specimens were sectioned, mounted and polished, and imaged using BSE mode to reveal creep deformation that occurred within the sample. A major deformation behavior observed for all the MMCs was cracking that originated at the fiber-matrix interface, as observed in Figure 4.39. Nearly all of the cracks grew in a direction perpendicular to the loading direction. They also propagated transgranularly, whereas intergranular cracking was observed within the bulk of the alloys and for alloys tested in a vacuum. The O+BCC colonies did not effectively blunt the cracks, as cracks traversed through both the α_2 phase and the O+BCC colonies, see Figure 4.40. Surface cracking, shown in Figure 4.41, was also evident for each MMC composition.

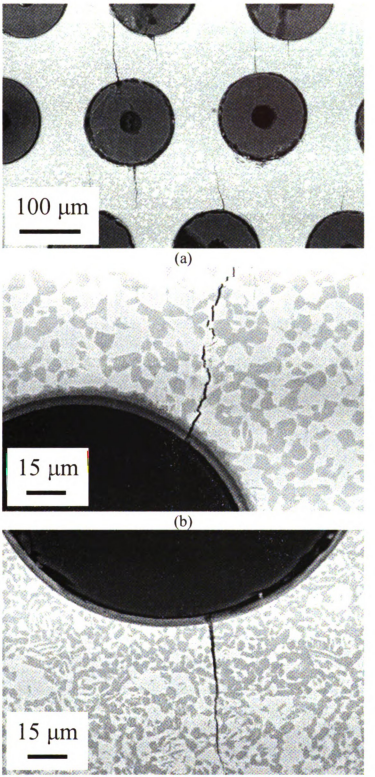

Figure 4.39 BSE SEM images of the (a) Ultra SCS-6/Ti-24Al-17Nb-0.66Mo, (b) Ultra SCS-6/Ti-24Al-17Nb-1.1Mo, and (c) Ultra SCS-6/Ti-24Al-17Nb-2.3Mo MMCs showing radial cracks propagating from fiber-matrix interfaces during creep experimentation. Note the loading direction is horizontal in each image.

Figure 4.40 BSE SE
SCS-6 Ti-24Al-17N
transgranular crackir

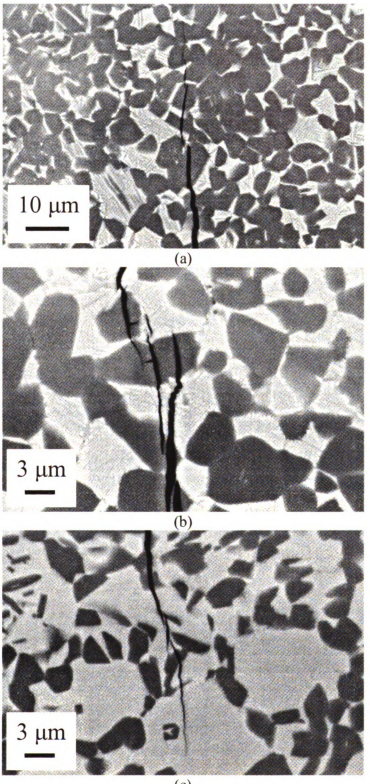

Figure 4.40 BSE SEM images of the (a) Ultra SCS-6/Ti-24Al-17Nb-0.66Mo, (b) Ultra SCS-6/Ti-24Al-17Nb-1.1Mo, and (c) Ultra SCS-6/Ti-24Al-17Nb-2.3Mo MMCs showing transgranular cracking during creep testing. The loading direction is horizontal.

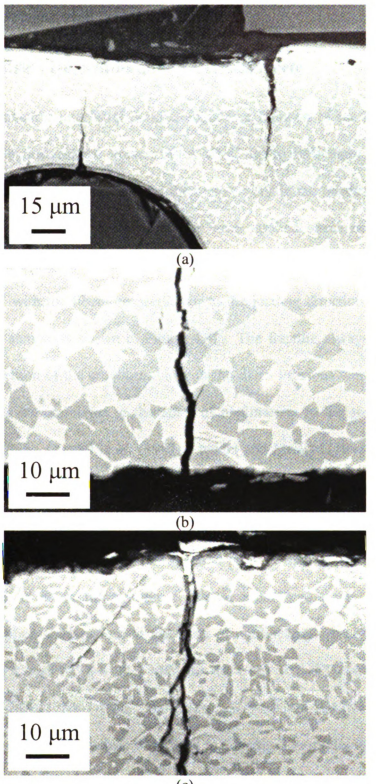

Figure 4.41 BSE SEM images of the (a) Ultra SCS-6/Ti-24Al-17Nb-0.66Mo, (b) Ultra SCS-6/Ti-24Al-17Nb-1.1Mo, and (c) Ultra SCS-6/Ti-24Al-17Nb-2.3Mo MMCs showing surface cracking apparent for each composition experienced during creep testing.

C. Interface Debond Behavior Results

1. Localized Stress Determination at Debond Event

The fiber/matrix interfacial bond strength is a function of the localized applied stress at debonding and residual stresses in the MMC due to differences in coefficients of thermal expansion between the fiber and the matrix. While the residual stresses can be estimated using finite element modeling, the local applied stress needed to achieve interface debonding can be obtained through RT tensile testing of cruciform-geometry samples oriented with the fibers perpendicular to the loading direction. An image of a tested cruciform sample is shown in Figure 4.42. The fracture always occurred in the uniform width section of the cruciform close to the filet. Previous work has shown that debonding events are correlated to the onset of nonlinearity in the stress-strain curves [Gundel *et al.* (1995), Gundel *et al.* (1997), Gundel and Miracle (1998), Boehlert *et al.* (2001)]. This deviation in slope is shown in Figure 4.43, where one experiment for each MMC composition is depicted. Through the use of an incremental slope method [Boehlert *et al.* (2001)], which used the Pearson product moment correlation [Pearson (1896)], the error in determining where a debond event occurs was minimized. The average local applied stress values at the onset of nonlinearity were 98.5 ± 12.0 MPa, 158.3 ± 32.3 MPa, and 105.8 ± 22.2 MPa for the Ultra SCS-6/Ti-24Al-17Nb-0.66Mo, Ultra SCS-6/Ti-24Al-17Nb-1.1Mo, and Ultra SCS-6/Ti-24Al-17Nb-2.3Mo MMCs, respectively. These strength values were used in Chapter 5 to model the creep behavior of the MMCs based on the matrix alloy creep rates and the fiber-matrix interfacial bond strengths.

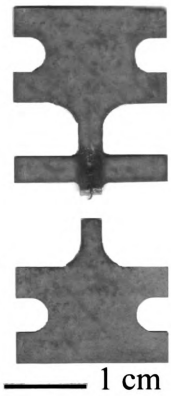

Figure 4.42 A fractured specimen which was tensile tested at room temperature. The strain was monitored only within the cruciform section of the sample. The strain gage (orange) is shown in the middle of the cruciform.

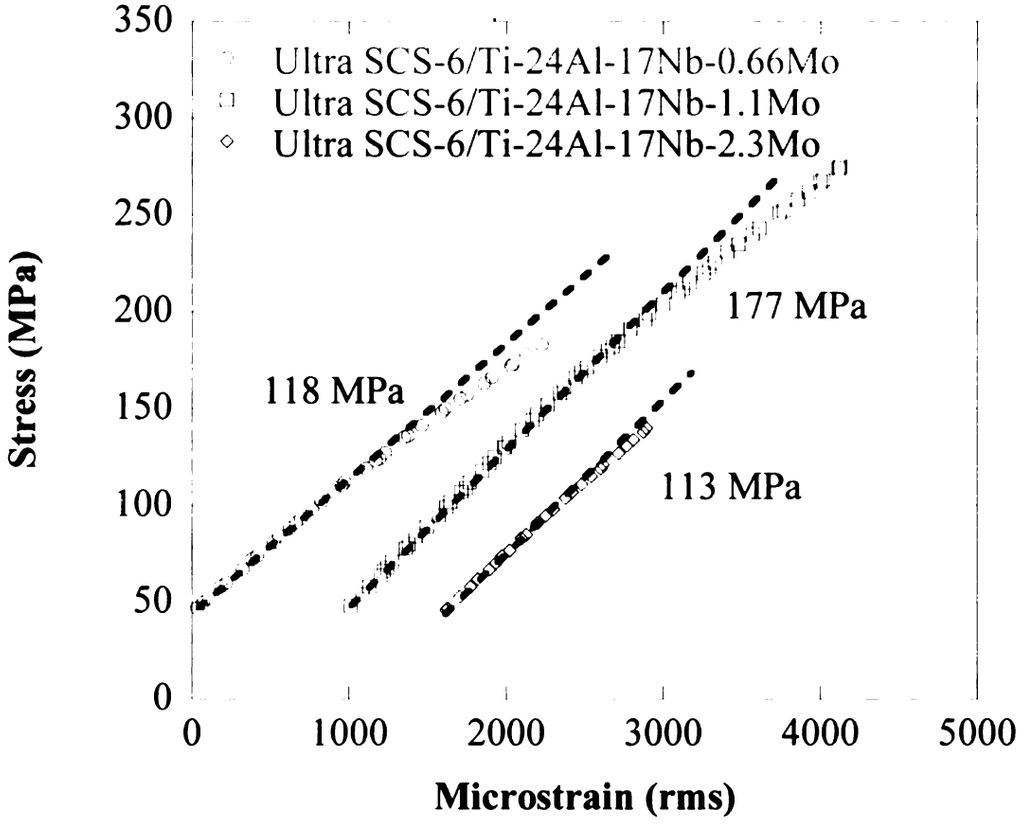

Figure 4.43 RT Stress versus microstrain plots from the tensile experiments performed on the cruciform MMC specimens. The stress value at the first point of nonlinearity is indicated on the plots. This value was used to calculate the interfacial debond strengths of the MMCs.

2. Microstructural Evidence of Debonding

After testing, the center of the cruciform of each sample was sectioned, mounted, polished, and viewed in a SEM. The debonding for each MMC composition was primarily found within the outer carbon layers of the fiber, which is illustrated for the Ultra SCS-6/Ti-24Al-17Nb-0.66Mo, Ultra SCS-6/Ti-24Al-17Nb-1.1Mo, and Ultra SCS-6/Ti-24Al-17Nb2.3Mo MMCs in Figure 4.44 – Figure 4.46, respectively. The carbon layer cracks propagated radially through the reaction layer and O+BCC depleted layer but were typically blunted by the O+BCC regions, as shown in Figure 4.47.

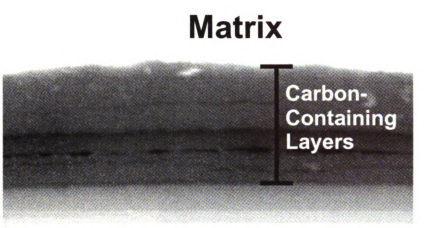

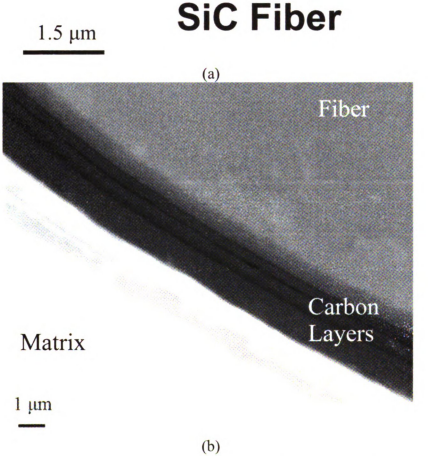

Figure 4.44 Carbon layer cracking was observed for a fiber near the fracture surface for tensile-tested cruciform sample for the Ultra SCS-6/Ti-24Al-17Nb-0.66Mo MMC (a) above the fiber and (b) below the fiber.

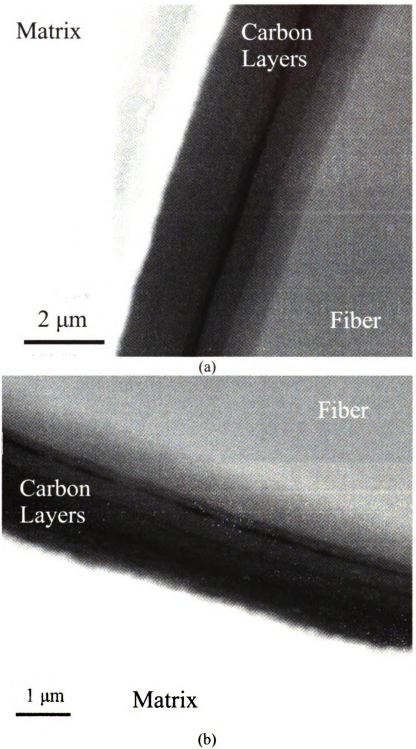

Figure 4.45 Carbon layer cracking was observed for a fiber near the fracture surface for tensile-tested cruciform sample for the Ultra SCS-6/Ti-24Al-17Nb-1.1Mo MMC (a) on the side of the fiber and (b) below the fiber.

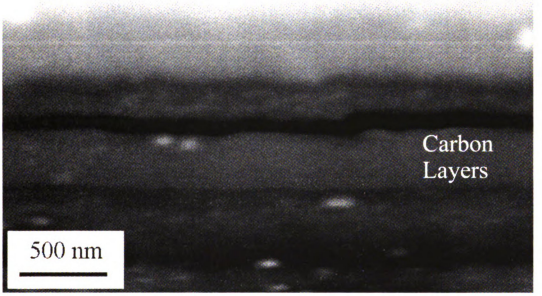

Figure 4.46 Carbon layer cracking was observed for a fiber near the fracture surface for tensile-tested cruciform sample for the Ultra SCS-6/Ti-24Al-17Nb-2.3Mo MMC.

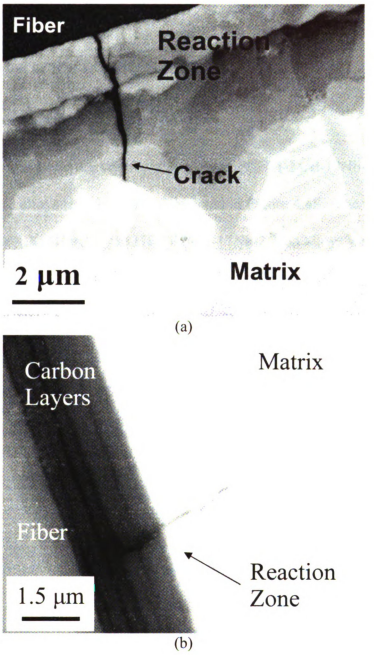

Figure 4.47 BSE SEM micrographs of radial cracks emanating from the debonded carbon layers. The radial cracking was blunted by the matrix.

D. Tensile Behavior Results

1. Room-Temperature Tensile Testing

1.1 Stress-Strain Behavior of the Alloys

Stress versus strain curves for the AP and HT Ti-24Al-17Nb-0.66Mo and Ti-24Al-17Nb-2.3Mo alloys tested at RT are depicted in Figure 4.48. The tensile properties are listed in Table 4.X. The AP and HT Ti-24Al-17Nb-2.3Mo alloys were brittle, having little plastic deformation prior to failure. While plastic deformation was observed for the AP and HT Ti-24Al-17Nb-0.66Mo alloys, ε_f values were less than 2%. The increasing Mo content resulted in higher Young's modulus values. The HT alloys appeared to have a varying effect on the tensile properties of the alloys, where no clear trend was observed.

Table 4.X Room temperature tensile properties of the AP and HT Ti-24Al-17Nb-0.66Mo and Ti-24Al-17Nb-2.3Mo alloys

Alloy	Condition	E (GPa)	0.2% YS (MPa)	UTS (MPa)	ε_f (%)
Ti-24Al-17Nb-0.66Mo	AP	108	746	765	1.19
Ti-24Al-17Nb-0.66Mo	HT	101	736	769	1.93
Ti-24Al-17Nb-2.3Mo	AP	125	n/a	645	0.52
Ti-24Al-17Nb-2.3Mo	HT	128	n/a	498	0.39

n/a indicates 0.2% requirement was not met and the fracture stress was taken as the UTS

1.2 Room-Temperature Tensile Deformation Behavior of the Alloys

Secondary electron SEM images of the fracture surfaces of the AP and HT Ti-24Al-17Nb-0.66Mo and Ti-24Al-17Nb-2.3Mo alloys are shown in Figure 4.49 and Figure 4.50. Brittle failure was evident in the fracture surface morphologies of all the alloys. Each fracture surface exhibited an intergranular failure. No evidence ductile dimpling was found in any of the alloys tested at room temperature.

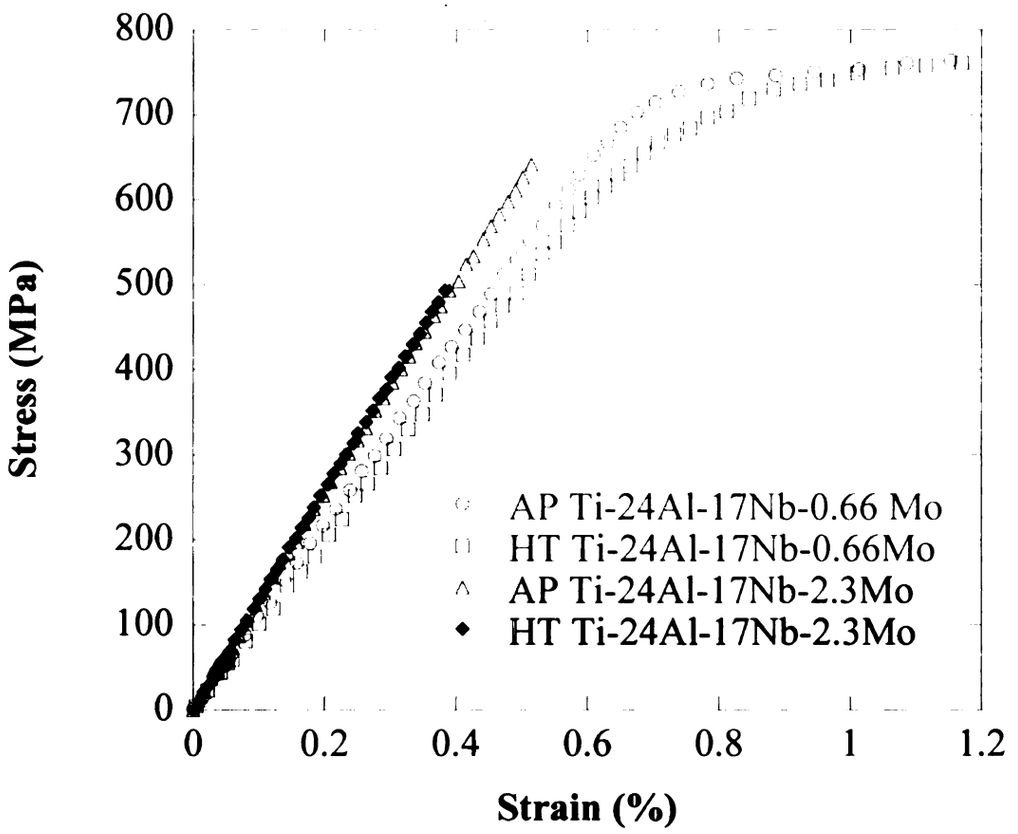

Figure 4.48 Room-temperature tensile curves for the AP and HT alloys.

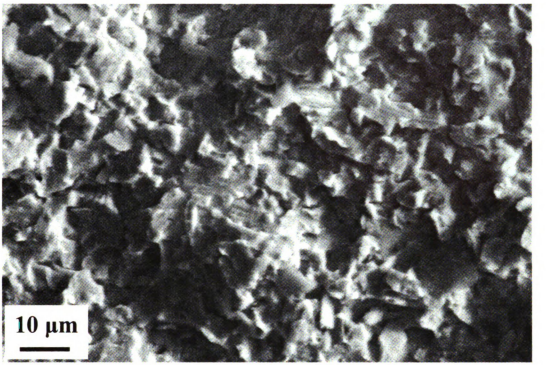

(a)

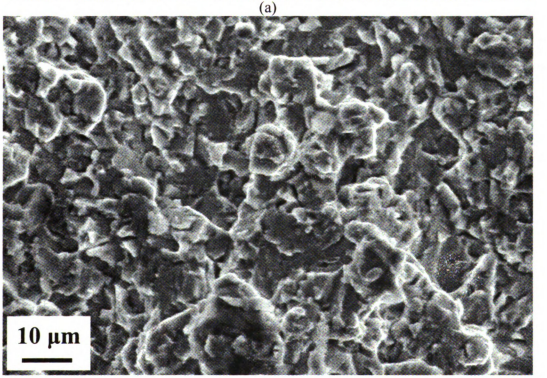

(b)

Figure 4.49 Secondary electron SEM images of RT tensile fracture surfaces for the (a) AP and (b) HT Ti-24Al-17Nb-0.66Mo alloys.

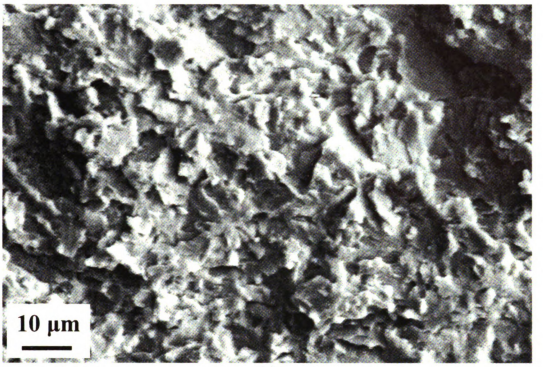

(a)

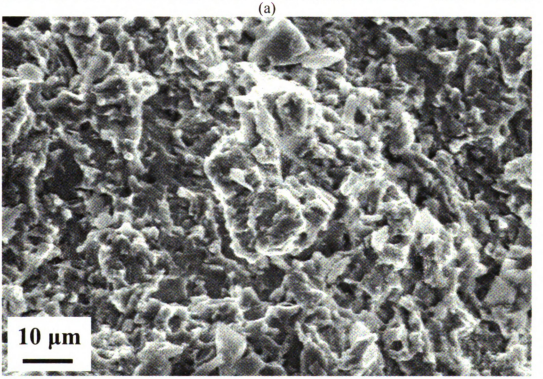

(b)

Figure 4.50 Secondary electron SEM images of RT tensile fracture surfaces for the (a) AP and (b) HT Ti-24Al-17Nb-2.3Mo alloys.

1.3 Stress-Strain Behavior of the Metal Matrix Composites

The stress versus strain curves for the AP and HT Ultra SCS-6/Ti-24Al-17Nb-0.66Mo and Ultra SCS-6/Ti-24Al-17Nb-2.3Mo MMCs are provided in Figure 4.51, and the tensile properties are listed in Table 4.XI. All the MMCs were tensile tested with the fibers parallel to the loading direction. Each tensile curve consisted of two regimes, each represented by a linear region. In the first regime, the fibers bear the bulk of the load and the Young's modulus followed the rule-of-mixtures equation. As the load increases and the fibers begin to break localized load sharing occurs, causing the second regime to initiate. A lower Young's modulus is evident in the second regime compared to the first regime. Failure occurred at the end of the second regime. The ε_f values for all of the MMCs tested were less than 1%. Higher strengths were observed for the AP and HT Ultra SCS-6/Ti-24Al-17Nb-0.66Mo MMC compared to the AP and HT Ultra SCS-6/Ti-24Al-17Nb-2.3Mo MMC, suggesting that greater ε_f values for the matrix enhance the ability of the material to transfer load among fibers through the matrix. In addition, the stress at the transition between the first and second regimes was higher for the Ultra SCS-6/Ti-24Al-17Nb-0.66Mo MMC compared to the Ultra SCS-6/Ti-24Al-17Nb-2.3Mo MMC.

Table 4.XI Room temperature tensile properties of the AP and HT Ultra SCS-6/Ti-24Al-17Nb-0.66Mo and Ultra SCS-6/Ti-24Al-17Nb-2.3Mo MMCs

MMC	Condition	E (GPa)	0.2% YS (MPa)	UTS (MPa)	ε_f (%)
Ultra SCS-6/Ti-24Al-17Nb-0.66Mo	AP	211	n/a	1332	0.78
Ultra SCS-6/Ti-24Al-17Nb-0.66Mo	HT	205	n/a	1483	0.91
Ultra SCS-6/Ti-24Al-17Nb-2.3Mo	AP	205	738	775	0.64
Ultra SCS-6/Ti-24Al-17Nb-2.3Mo	HT	214	844	949	0.76

n/a indicates 0.2% requirement was not met and the fracture stress was taken as the UTS

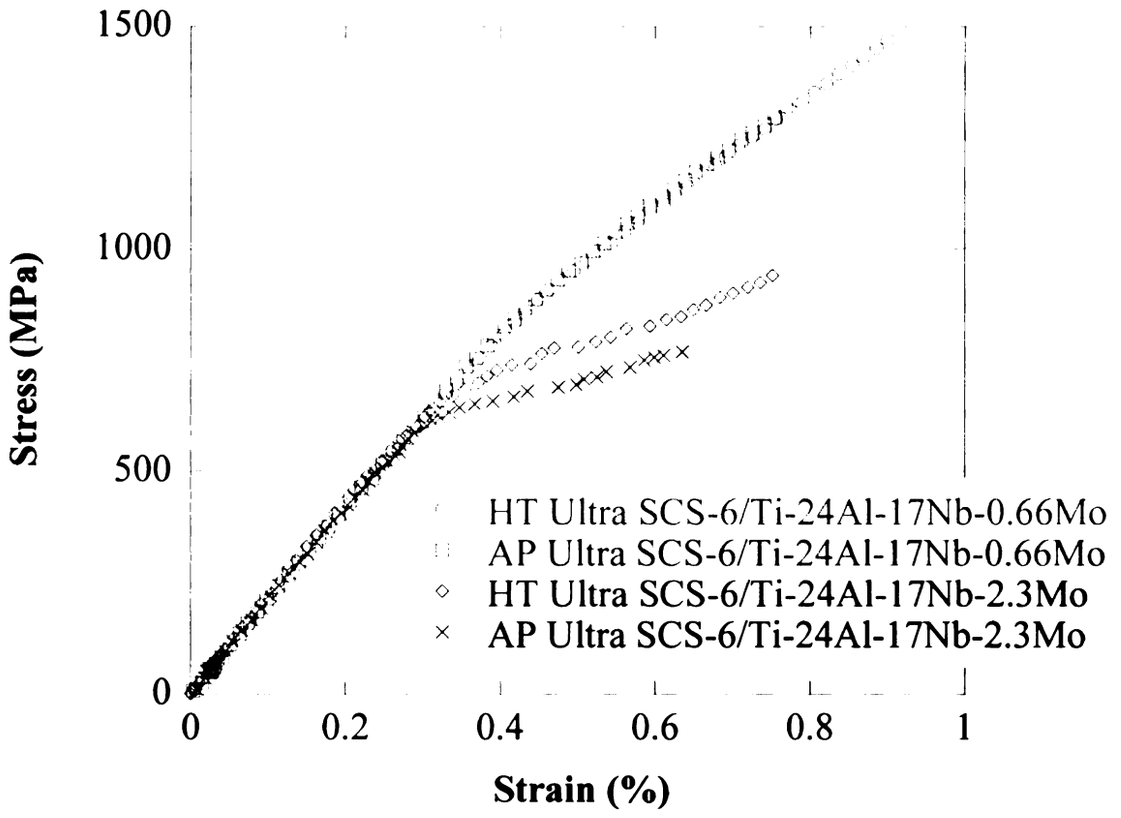

Figure 4.51 Room temperature tensile curves of the AP and HT MMCs.

1.4 Room-Temperature Tensile Deformation Behavior of the Metal Matrix Composites

Secondary electron SEM images of the AP and HT Ultra SCS-6/Ti-24Al-17Nb-0.66Mo and Ultra SCS-6/Ti-24Al-17Nb-2.3Mo MMC fracture surfaces are shown in Figure 4.52 and Figure 4.53. Brittle fracture was observed throughout the fracture surfaces. The matrix exhibited characteristics typical of intergranular fracture similar to that observed for the alloy fracture surfaces for each respective composition and heat treatment. Some fiber pull-out, where a fiber fails in a different plane than that of the matrix fracture surface, was observed. The majority of fiber fracture surfaces were flat, indicating brittle cleavage. The fiber-matrix interface was commonly cracked and damaged and often appeared to have separated from the fiber.

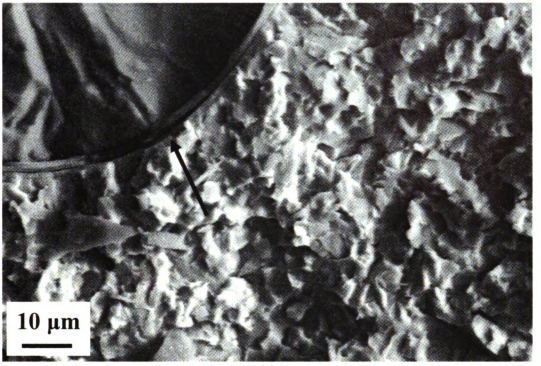

(a)

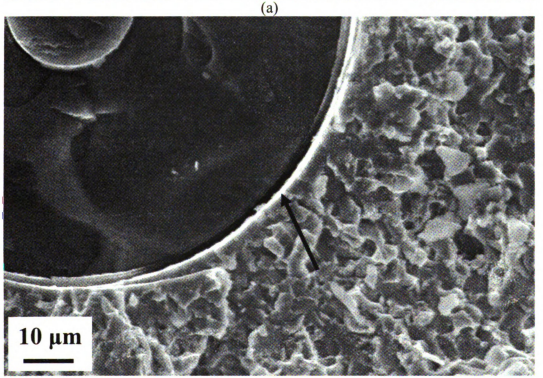

(b)

Figure 4.52 Secondary electron SEM images of RT tensile fracture surfaces for the (a) AP and (b) HT Ultra SCS-6/Ti-24Al-17Nb-0.66Mo MMCs. Note the fiber/matrix interface cracking exhibited by the arrows.

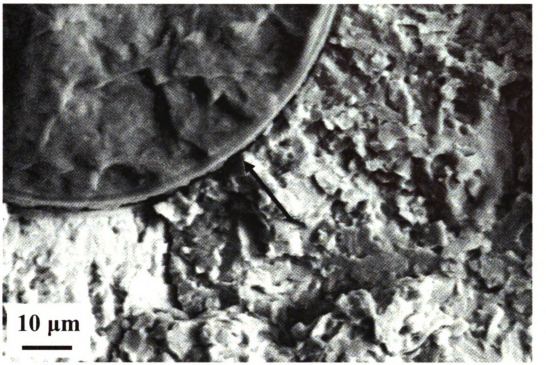

(a)

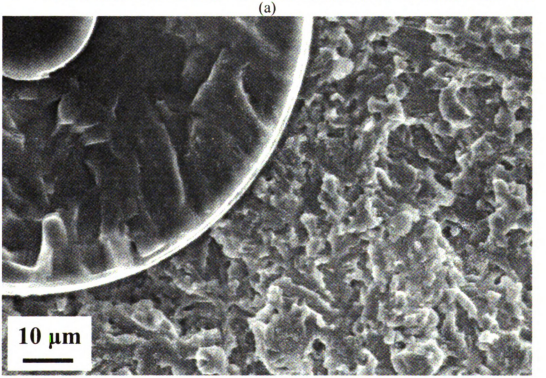

(b)

Figure 4.53 Secondary electron SEM images of RT tensile fracture surfaces for the (a) AP and (b) HT Ultra SCS-6/Ti-24Al-17Nb-2.3Mo MMCs. Note the fiber/matrix interface cracking exhibited by the arrows.

2. Elevated-Temperature Tensile Behavior

2.1 Stress-Strain Behavior of the Alloys at 650°C

The stress versus strain curves for the HT Ti-24Al-17Nb-0.66 and Ti-24Al-17Nb-2.3Mo alloys tested at 650°C are provided in Figure 4.54. The tensile properties of each alloy tested at 650°C are listed in Table 4.XII. Table XIII shows the comparison of the RT results to the 650°C results. The Ti-24Al-17Nb-0.66Mo tested at 650°C exhibited a lower Young's modulus, yield strength, and UTS value and a higher ε_f value than the Ti-24Al-17Nb-0.66Mo alloy tested at RT. While the Ti-24Al-17Nb-2.3Mo alloy tested at 650°C did have a lower Young's modulus and higher ε_f, it did not have a lower UTS than the Ti-24Al-17Nb-2.3Mo alloy tested at RT. Even at high temperature the Ti-24Al-17Nb-2.3Mo alloy did not exhibit much plastic deformation, whereas the Ti-24Al-17Nb-0.66Mo alloy displayed an increase in ε_f compared to that at RT.

Table 4.XII 650°C tensile properties of the HT alloys

Alloy	Condition	E (GPa)	0.2% YS (MPa)	UTS (MPa)	ε_f (%)
Ti-24Al-17Nb-0.66Mo	HT	80	524	608	3.68
Ti-24Al-17Nb-2.3Mo	HT	92	n/a	569	0.64

n/a indicates 0.2% requirement was not met and the fracture stress was taken as the UTS

Table 4.XIII Difference in tensile properties of the alloys at 650°C compared to room temperature

Alloy	Condition	% Decrease in E (GPa)	% Decrease in 0.2% YS (MPa)	% Decrease in UTS (MPa)	% Increase in ε_f (%)
Ti-24Al-17Nb-0.66Mo	HT	21	29	21	91
Ti-24Al-17Nb-2.3Mo	HT	28	n/a	n/a	64

n/a: not applicable

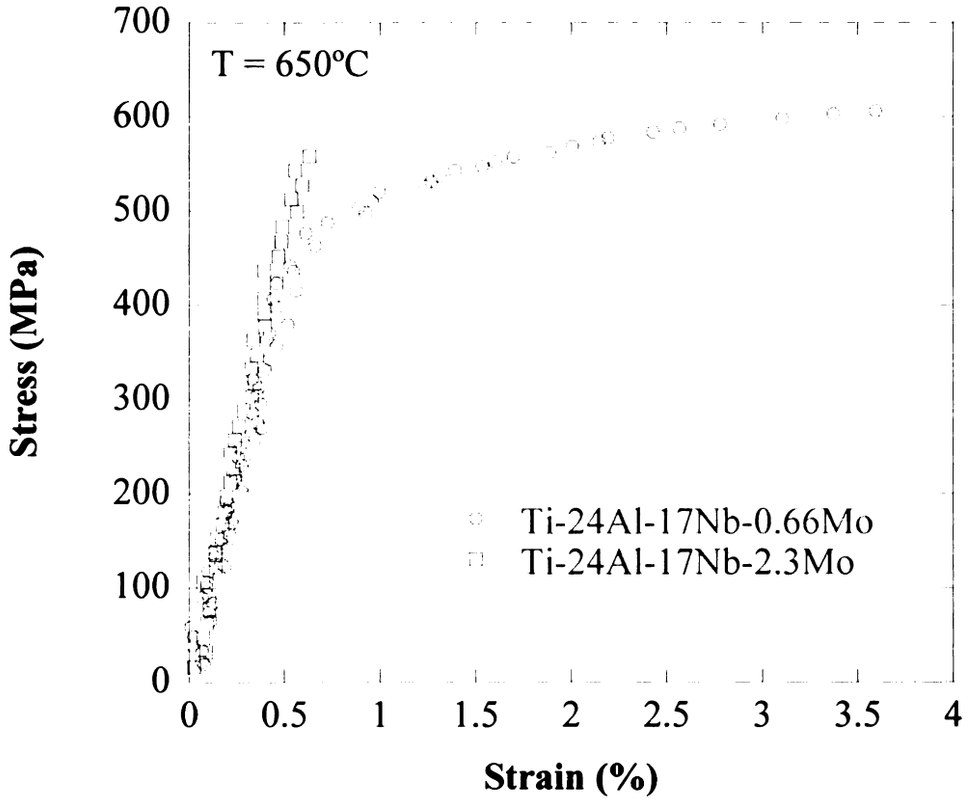

Figure 4.54 650°C tensile stress versus strain curve for Ti-24Al-17Nb-0.66Mo and Ti-24Al-17Nb-2.3Mo alloy samples.

2.2 650°C Tensile Deformation Behavior of the Alloys

Secondary electron SEM images of the HT Ti-24Al-17Nb-0.66Mo and Ti-24Al-17Nb-2.3Mo alloy fracture surfaces are presented in Figure 4.55. The surface morphology of the Ti-24Al-17Nb-0.66Mo alloy displayed a greater fraction of ductile dimpling than that of the Ti-24Al-17Nb-2.3Mo alloy. Furthermore, this fracture surface appeared torn and more fibrous in character. No evidence of slip was observed on the surface other than at the fracture location. The fracture surface of the Ti-24Al-17Nb-2.3Mo alloy tested at 650°C appeared similar to the fracture surfaces of the Ti-24Al-17Nb-2.3Mo alloy tested at RT. Cleavage and intergranular fracture was observed throughout the fracture surface, confirming that little or no plastic deformation occurred.

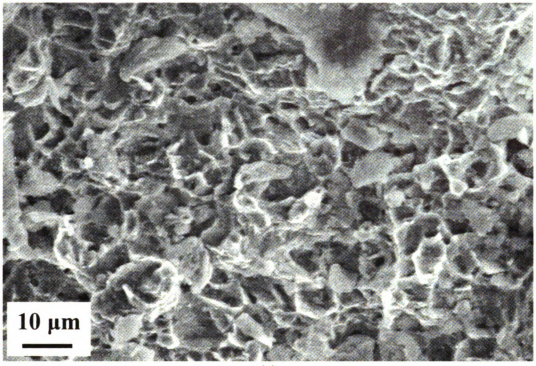

(a)

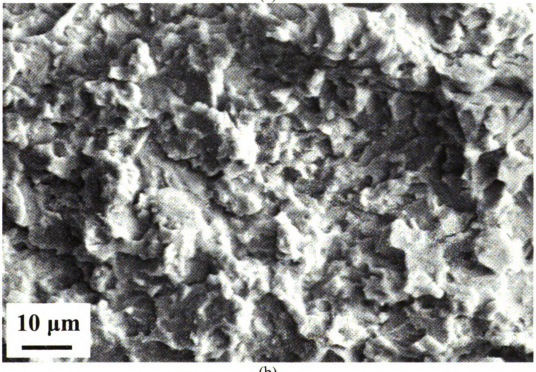

(b)

Figure 4.55 Secondary electron SEM images of 650ºC tensile fracture surfaces for the (a) HT Ti-24Al-17Nb-0.66Mo and the (b) HT Ti-24Al-17Nb-2.3Mo alloys.

2.3 Stress-Strain Behavior of the Metal Matrix Composites at 650°C

The stress versus strain curves for the HT Ultra SCS-6/Ti-24Al-17Nb-0.66Mo and Ultra SCS-6/Ti-24Al-17Nb-2.3Mo MMCs are shown in Figure 4.56. The tensile properties and the comparison of the 650°C properties to the RT properties are given in Table 4.XIV and Table 4.XV, respectively. The Ultra SCS-6/Ti-24Al-17Nb-0.66Mo MMC exhibited higher UTS and ε_f values than the Ultra SCS-6/Ti-24Al-17Nb-2.3Mo MMC. A decrease in Young's modulus and an increase in ε_f for the MMCs tested at 650°C were observed compared to those tested at RT. However, the ε_f values of the MMCs were always less than 1.2% at 650°C.

Table 4.XIV 650°C tensile properties of the HT MMCs

MMC	Condition	E (GPa)	0.2% YS (MPa)	UTS (MPa)	ε_f (%)
Ultra SCS-6/Ti-24Al-17Nb-0.66Mo	HT	157	1375	1403	1.08
Ultra SCS-6/Ti-24Al-17Nb-2.3Mo	HT	147	1013	1214	1.07

Table 4.XV Difference in tensile properties of the MMCs at 650°C compared to room temperature

MMC	Condition	% Decrease in E (GPa)	% Increase in 0.2% YS (MPa)	% Decrease in UTS (MPa)	% Increase in ε_f (%)
Ultra SCS-6/Ti-24Al-17Nb-0.66Mo	HT	23	n/a	5	19
Ultra SCS-6/Ti-24Al-17Nb-2.3Mo	HT	31	20	n/a	32

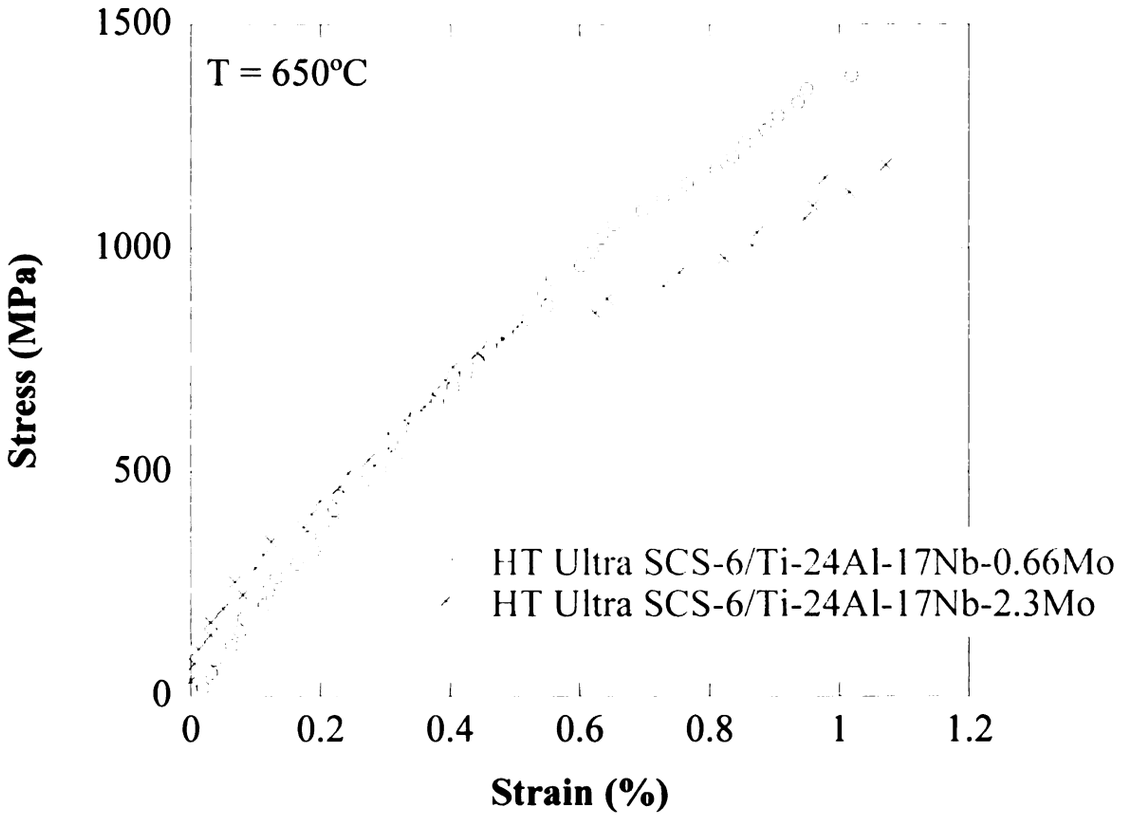

Figure 4.56 650°C tensile stress versus strain curves of the Ultra SCS-6/Ti-24Al-17Nb-0.66Mo and Ultra SCS-6/Ti-24Al-17Nb-2.3Mo MMCs.

2.4 650°C Tensile Deformation Behavior of the Metal Matrix Composites

Secondary electron SEM images of the HT Ultra SCS-6/Ti-24Al-17Nb-0.66Mo and Ultra SCS-6/Ti-24Al-17Nb-2.3Mo MMC fracture surfaces are shown in Figure 4.57. Ductile dimpling was evident within the matrix of the Ultra SCS-6/Ti-24Al-17Nb-0.66Mo MMC suggesting a ductile fracture. The fracture surface of the matrix of the Ultra SCS-6/Ti-24Al-17Nb-2.3Mo MMC exhibited intergranular failure similar to that seen for the Ti-24Al-17Nb-2.3Mo alloy tested at 650°C. The fiber fracture surface morphology was smooth, representative of a cleavage failure. Fiber pull-out was more prevalent in the Ultra SCS-6/Ti-24Al-17Nb-0.66Mo MMC than the Ultra SCS-6/Ti-24Al-17Nb-2.3Mo MMC, and the fiber-matrix interface tended to exhibit more deformation in the form of debonding than the Ultra SCS-6/Ti-24Al-17Nb-2.3Mo MMC.

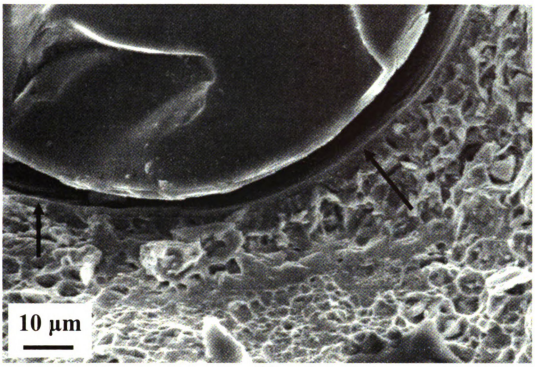

(a)

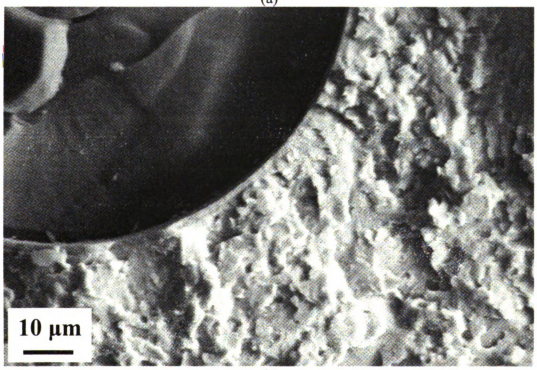

(b)

Figure 4.57 Secondary electron SEM images of 650ºC tensile fracture surfaces for the (a) HT Ultra SCS-6/Ti-24Al-17Nb-0.66Mo and the (b) HT Ultra SCS-6/Ti-24Al-17Nb-2.3Mo MMCs. Note the fiber/matrix debonding indicated by the arrows.

E. Out-of-Phase Thermomechanical Fatigue Behavior Results

1. Out-of-Phase Thermomechanical Fatigue Data

The fatigue life data for the Ti-24Al-17Nb-0.66Mo, Ti-24Al-17Nb-1.1Mo, and Ti-24Al-17Nb-2.3Mo MMCs are shown in Figure 4.58 - Figure 4.60, respectively, and a comparison plot of each set of data is given in Figure 4.61. The fatigue life data is also listed in Table 4.XVI. In each figure the maximum cyclic stress is plotted as a function of cycles-to-failure (N_f). Run-out tests, where the specimen did not fail, were considered to occur at 8000 cycles and are indicated on the plots by an arrow next to the data point. From 300 MPa to 450 MPa, the Ultra SCS-6/Ti-24Al-17Nb-0.66Mo MMC exhibited more cycles-to-failure than that of the Ultra SCS-6/Ti-24Al-17Nb-1.1Mo and Ultra SCS-6/Ti-24Al-17Nb-2.3Mo MMCs. The N_f for the Ultra SCS-6/Ti-24Al-17Nb-2.3Mo MMC was 1017 at 600 MPa. This value is greater than the 736 and 529 N_f observed for the Ultra SCS-6/Ti-24Al-17Nb-0.66Mo and Ultra SCS-6/Ti-24Al-17Nb-1.1Mo MMCs, respectively. Run-out was observed for the Ti-24Al-17Nb-0.66Mo MMC at 200 MPa and also for the Ti-24Al-17Nb-2.3Mo MMC at 200 MPa and 250 MPa. The Ultra SCS-6/Ti-24Al-17Nb-1.1Mo MMC displayed the lowest number of N_f for all the conditions examined.

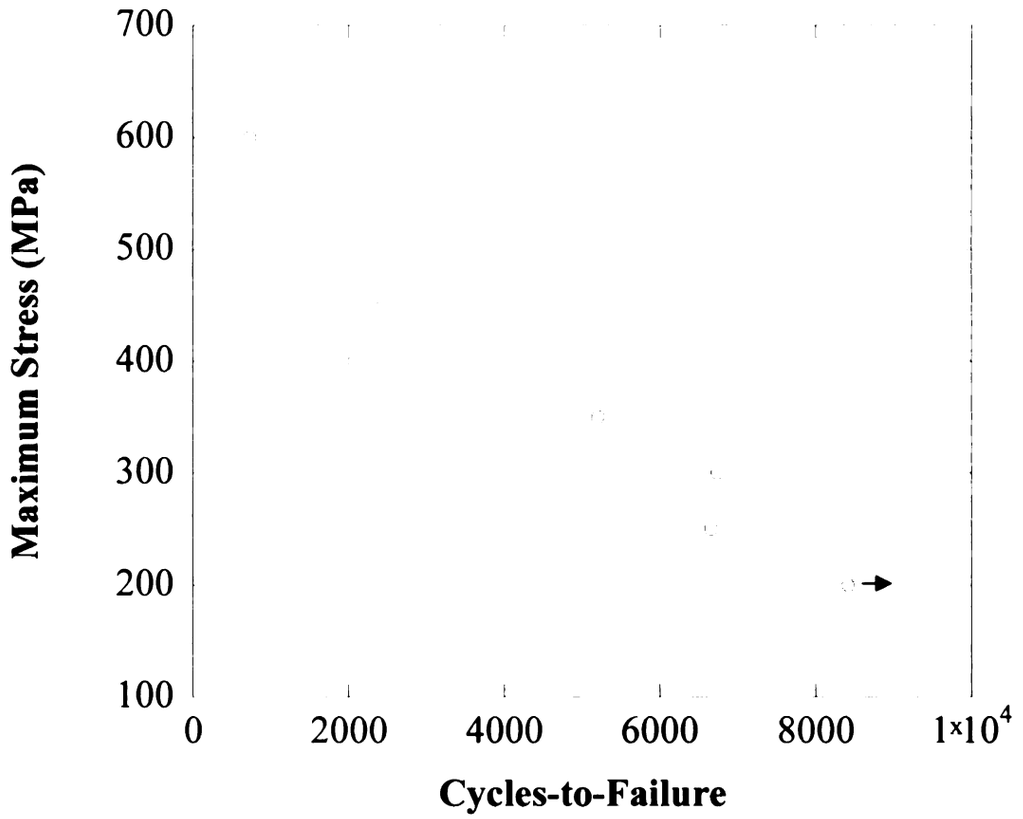

Figure 4.58 OOP TMF data for the Ti-24Al-17Nb-0.66Mo MMC tested with temperature cycling from 150°C to 450°C. Note that the arrow indicates run-out.

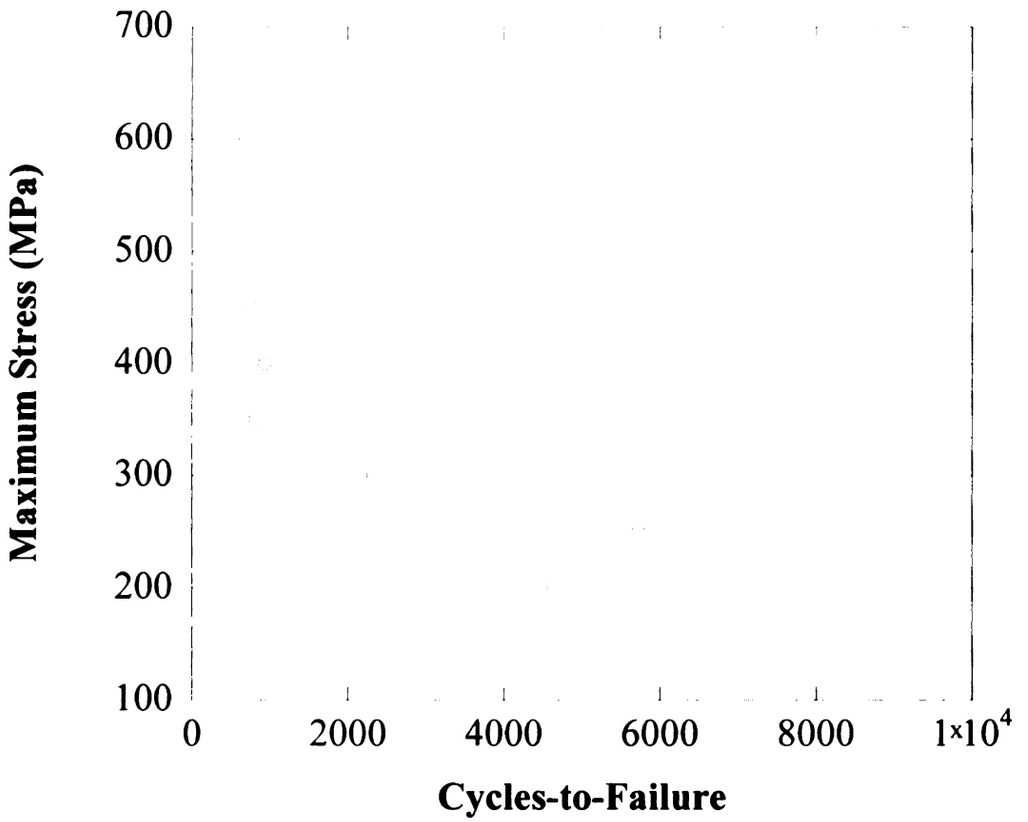

Figure 4.59 OOP TMF data for the Ti-24Al-17Nb-1.1Mo MMC tested with temperature cycling from 150°C to 450°C.

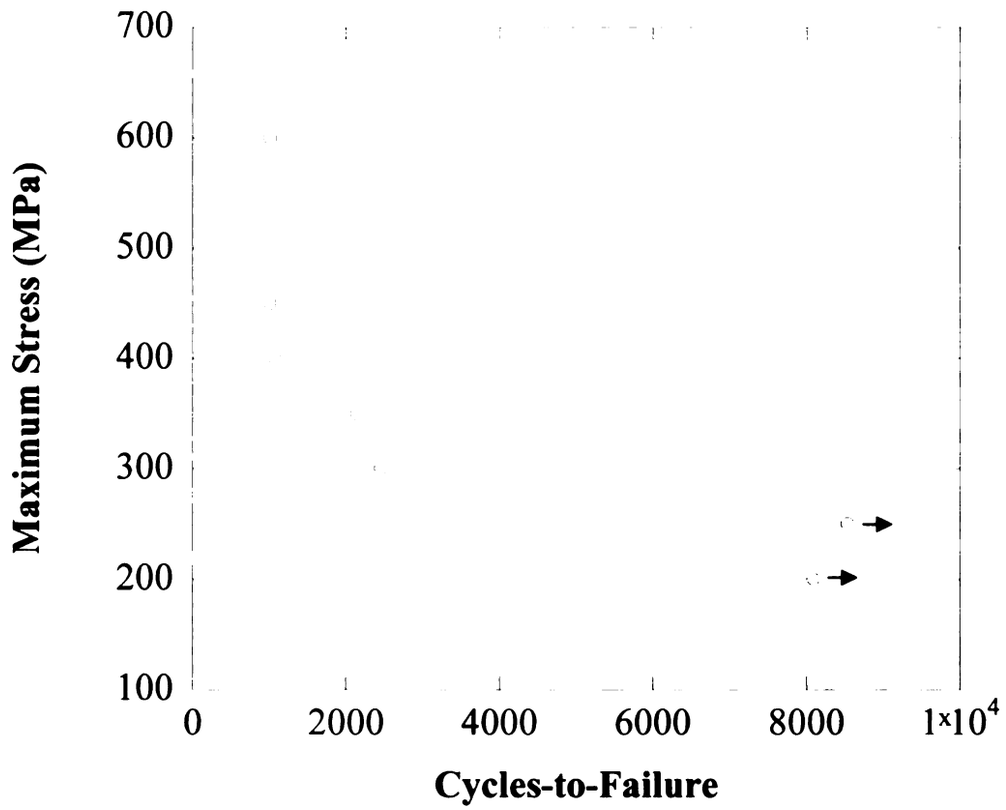

Figure 4.60 OOP TMF data for the Ti-24Al-17Nb-2.3Mo MMC tested with temperature cycling from 150°C to 450°C. Note that the arrows indicate run-out.

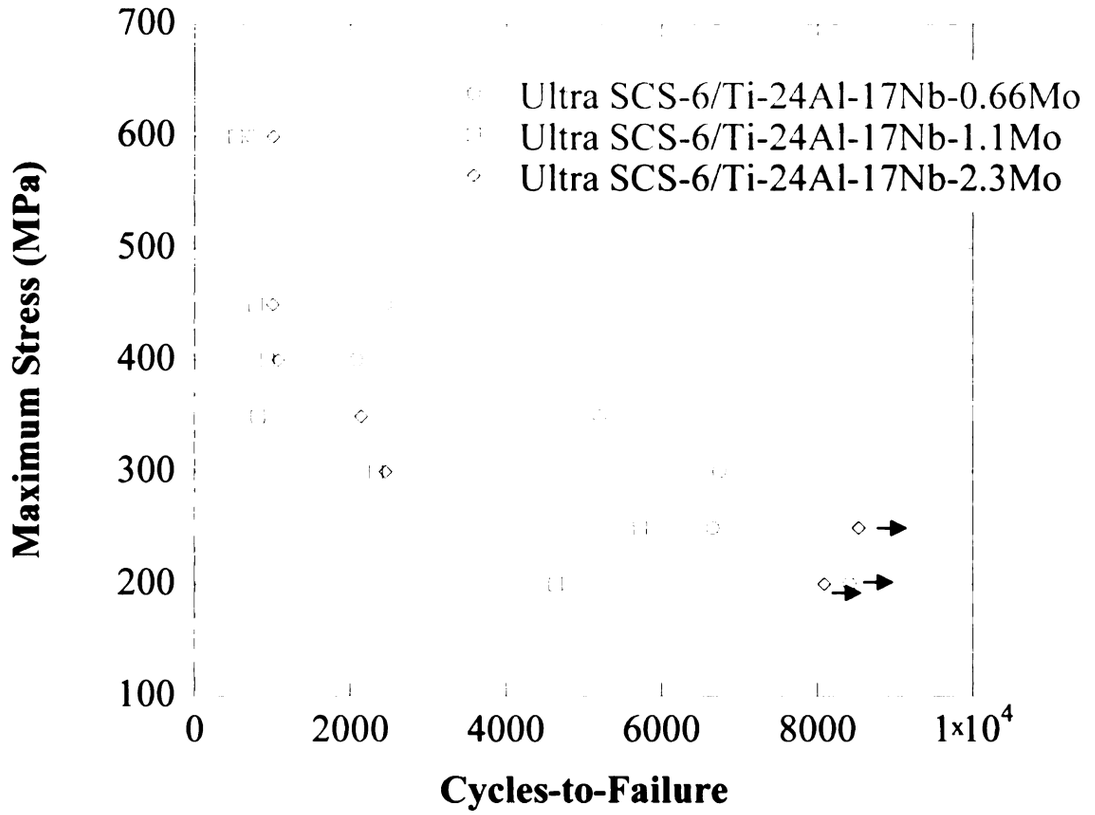

Figure 4.61 OOP TMF behavior of each MMC composition. Note the arrows indicate run-out.

Table 4.XVI OOP TMF test data

Material	Maximum Stress (MPa)	Cycles-to-Failure
Ultra SCS-6/Ti-24Al-17Nb-0.66Mo	600	736
	450	2443
	400	2076
	350	5207
	300	6742
	250	6659
	200	Run-out
Ultra SCS-6/Ti-24Al-17Nb-1.1Mo	600	529
	450	788
	400	936
	350	817
	300	2334
	250	5724
	200	4642
Ultra SCS-6/Ti-24Al-17Nb-2.3Mo	600	1017
	450	1007
	400	1075
	350	2138
	300	2457
	250	Run-out
	200	Run-out

The history of the strains at the maximum and minimum loading points throughout a fatigue test provide useful information about the damage mechanisms during a test. Figure 4.62, Figure 4.63, and Figure 4.64 show the typical strain versus time behavior for the Ultra SCS-6/Ti-24Al-17Nb-0.66Mo, Ultra SCS-6/Ti-24Al-17Nb-1.1Mo, and Ultra SCS-6/Ti-24Al-17Nb-2.3Mo MMCs, respectively. Each of these plots were constructed for tests performed at a maximum stress of 400 MPa, and each were representative of the behavior observed at all stress conditions. The difference between the two curves represents an indication of the stiffness of the material, where materials

with higher stiffness value have a smaller difference between curves than materials with lower stiffness values [Nicholas and Russ (1993), Russ *et al.* (1994)]. Observed in each figure, the strains at maximum and minimum loading tend to initially increase together and then converge near failure. The convergence is the result of a dramatic increase in the strain at maximum load. In the case of the Ultra SCS-6/Ti-24Al-17Nb-0.66Mo MMC, see Figure 5.62, the strain at maximum load overcomes that at minimum load.

The shapes of stress versus strain curves during fatigue provide insight into the deformation response of materials. Such plots of the Ultra SCS-6/Ti-24Al-17Nb-0.66Mo, Ultra SCS-6/Ti-24Al-17Nb-1.1Mo, and Ultra SCS-6/Ti-24Al-17Nb-2.3Mo MMCs tested at 400 MPa are presented in Figure 4.65 - Figure 4.67, respectively. On each plot, a cycle is completed when the sample is cooled from 450°C to 150°C while increasing to the maximum stress then reheated to 450°C and unloaded to the minimum stress. A hysteresis is observed as the cyclic stress-strain loops change with increasing number of cycles. At the beginning of the test (i.e. at lower cycle counts) greater strains were observed at higher temperatures. This is shown on the plots by the cyclic loops that are slanted to the left of vertical. As the test progressed, the ratio of the strain at the maximum stress to the strain at the minimum stress increased, as indicated by the cyclic loops slanted more to the right. This behavior agrees with the strain versus time plots shown in Figure 4.62 – Figure 4.64. In fact, Figure 4.65 Cycle 2059, which is just 17 cycles prior to failure, displayed a much greater strain at maximum load compared to that at minimum load. This agrees with Figure 4.62, where a crossover in strain at maximum stress and strain at minimum stress was observed.

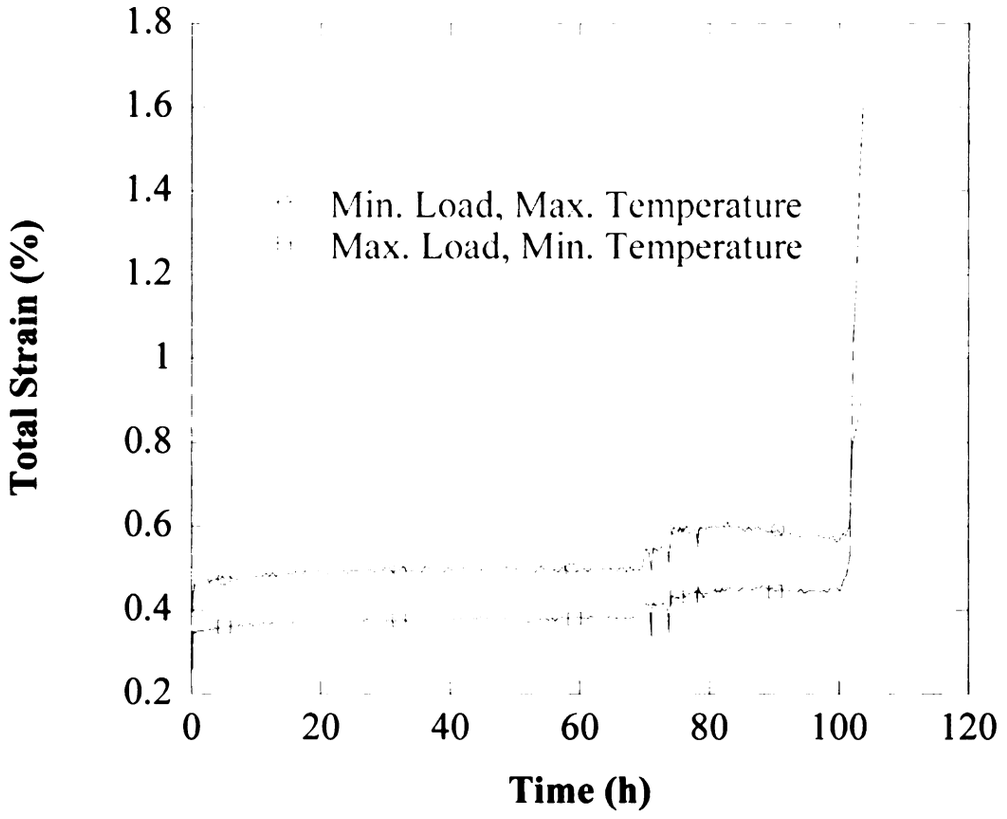

Figure 4.62 The total strain versus time plot for the peak and valley load data of a Ti-24Al-17Nb-0.66Mo MMC tested at a maximum stress of 400 MPa. Note that the symbols on the lines are provided to assist in identification of the cycle line.

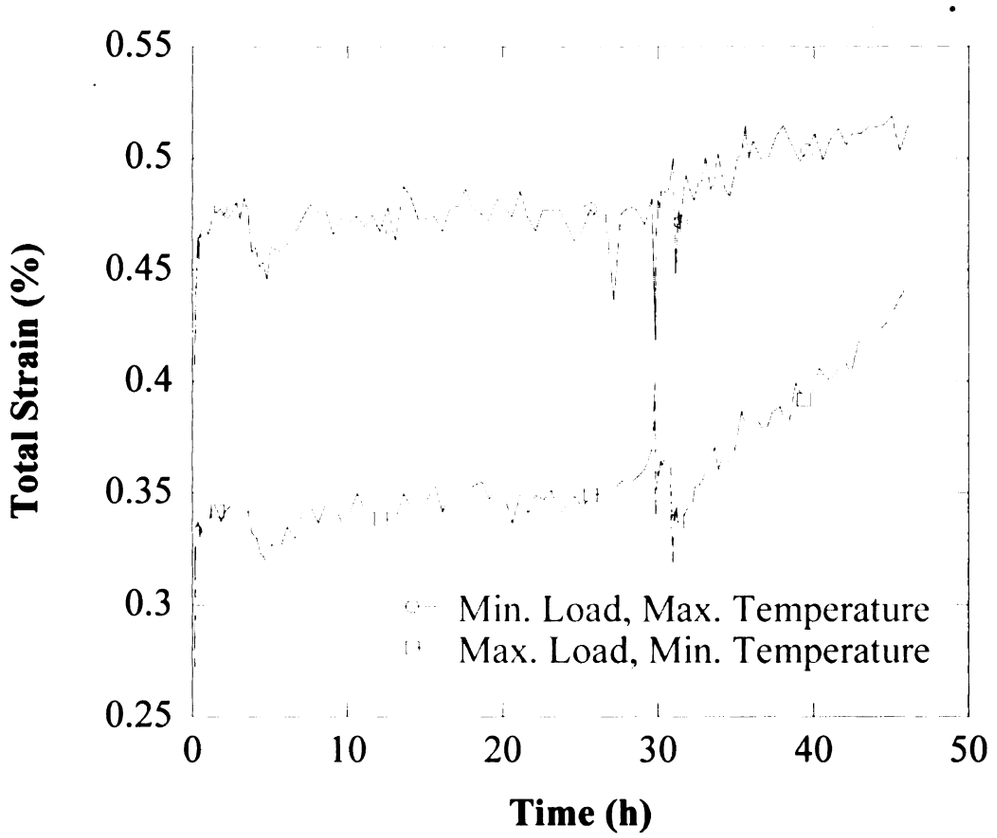

Figure 4.63 The total strain versus time plot for the peak and valley load data of a Ti-24Al-17Nb-1.1Mo MMC tested at a maximum stress of 400 MPa. Note that the symbols on the lines are provided to assist in identification of the cycle line.

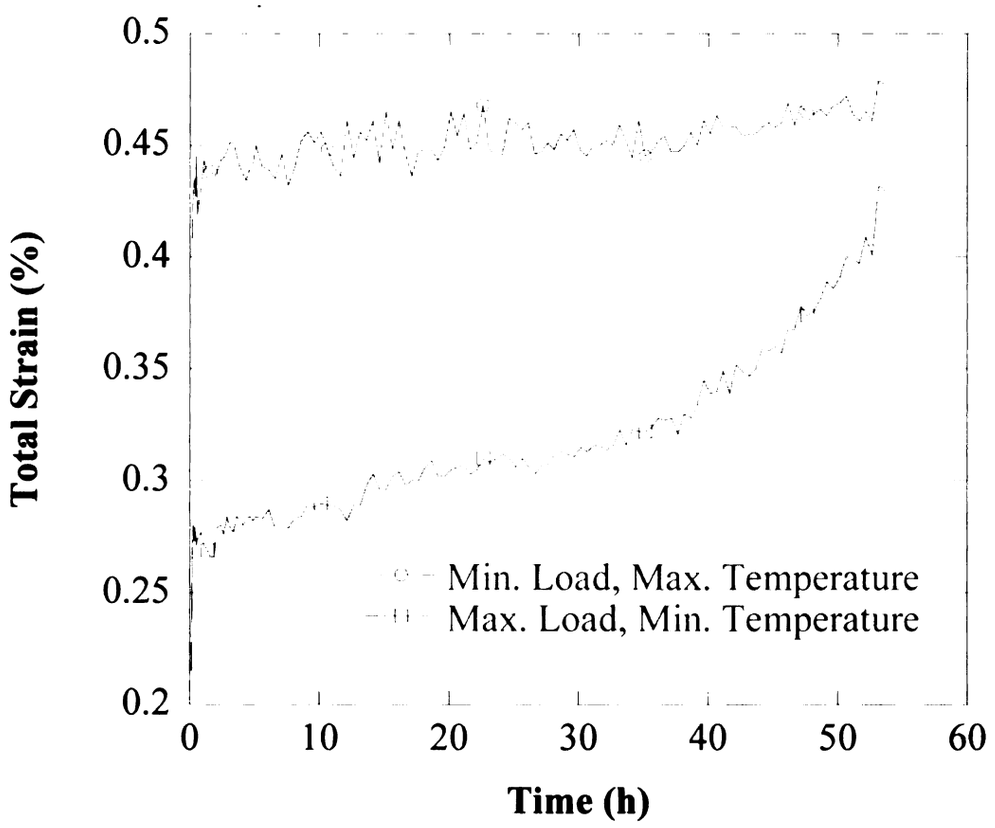

Figure 4.64 The total strain versus time plot for the peak and valley load data of a Ti-24Al-17Nb-2.3Mo MMC tested at a maximum stress of 400 MPa. Note that the symbols on the lines are provided to assist in identification of the cycle line.

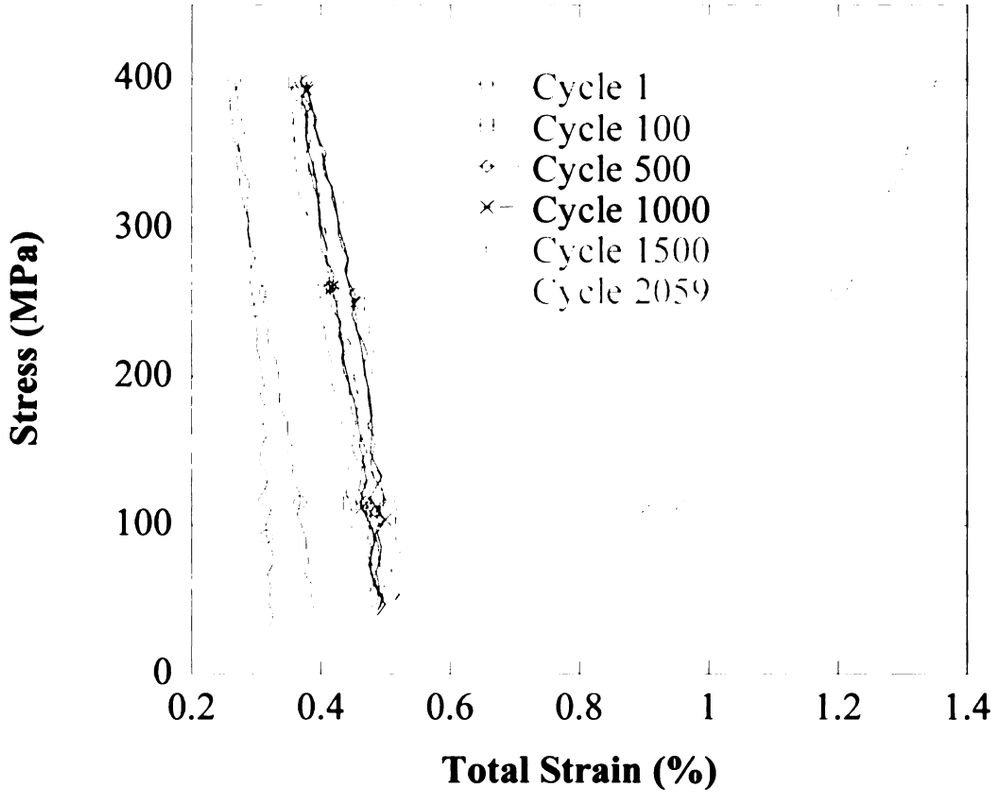

Figure 4.65 A hysteresis plot for the Ultra SCS-6/Ti-24Al-17Nb-0.66Mo MMC OOP TMF tested at a maximum stress of 400 MPa. Note that the symbols on the lines are provided to assist in identification of the cycle line.

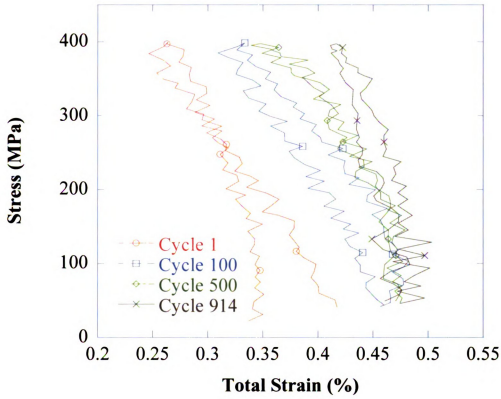

Figure 4.66 A hysteresis plot for the Ultra SCS-6/Ti-24Al-17Nb-1.1Mo MMC OOP TMF tested at a maximum stress of 400 MPa. Note that the symbols on the lines are provided to assist in identification of the cycle line.

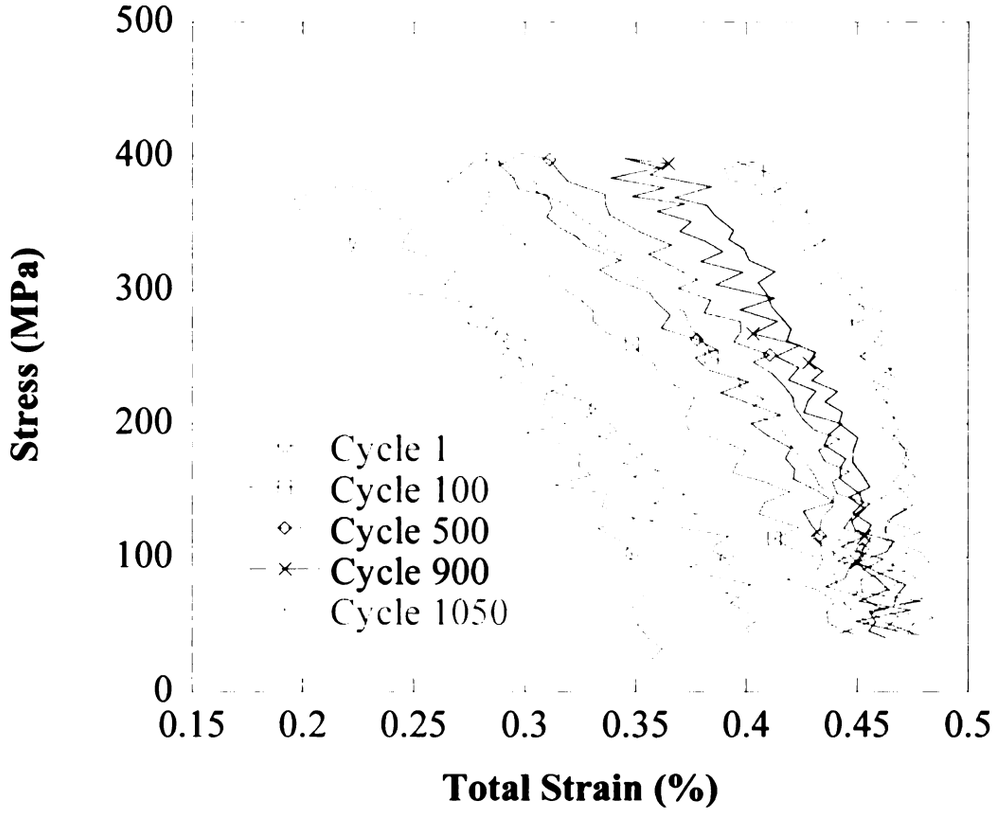

Figure 4.67 A hysteresis plot for the Ultra SCS-6/Ti-24Al-17Nb-2.3Mo MMC OOP TMF tested at a maximum stress of 400 MPa. Note that the symbols on the lines are provided to assist in identification of the cycle line.

2. Fracture Analysis of Thermomechanical Fatigue Samples

Fractography was conducted to provide insight into the deformation mechanisms and to highlight any differences for samples tested under different loading conditions. Secondary electron SEM images of samples tested at a maximum stress of 300 MPa are presented in Figure 4.68 - Figure 4.70 for the Ultra SCS-6/Ti-24Al-17Nb-0.66Mo, Ultra SCS-6/Ti-24Al-17Nb-1.1Mo, and Ultra SCS-6/Ti-24Al-17Nb-2.3Mo MMCs, respectively. For comparison, secondary electron SEM images of samples tested at a maximum stress of 600 MPa are presented in Figure 4.71- Figure 4.73 for the Ultra SCS-6/Ti-24Al-17Nb-0.66Mo, Ultra SCS-6/Ti-24Al-17Nb-1.1Mo, and Ultra SCS-6/Ti-24Al-17Nb-2.3Mo MMCs, respectively.

The fracture surfaces for each MMC composition did not vary greatly with stress. However, the Ultra SCS-6/Ti-24Al-17Nb-0.66Mo MMC fracture surfaces (Figure 4.68 and Figure 4.71) exhibited a greater amount of fiber pull-out than those of the Ultra SCS-6/Ti-24Al-17Nb-1.1Mo and Ultra SCS-6/Ti-24Al-17Nb-2.3Mo MMCs. Furthermore, the fracture plane of the Ultra SCS-6/Ti-24Al-17Nb-2.3Mo MMCs (Figure 4.70 and Figure 4.73) was more planar than that observed for the Ultra SCS-6/Ti-24Al-17Nb-0.66Mo and Ti-24Al-17Nb-1.1Mo MMCs. The matrix fracture appeared similar to that observed for the RT tensile tested specimens, which exhibited intergranular and cleavage failure. No clamshell markings were found on any of the fracture surfaces.

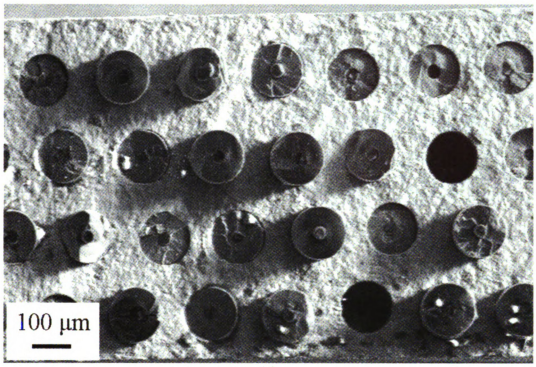

(a)

(b)

Figure 4.68 SE SEM images as (a) low magnification and (b) high magnification of the Ultra SCS-6/Ti-24Al-17Nb-0.66Mo MMC OOP TMF tested at a maximum stress of 300 MPa.

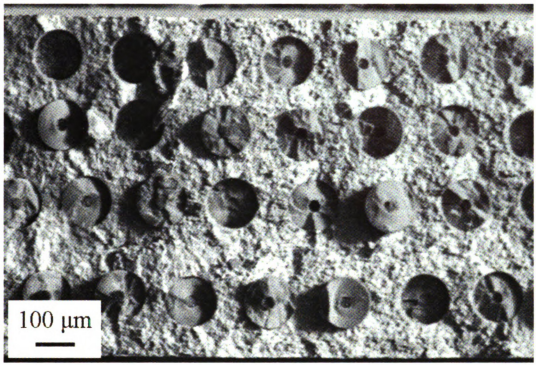

(a)

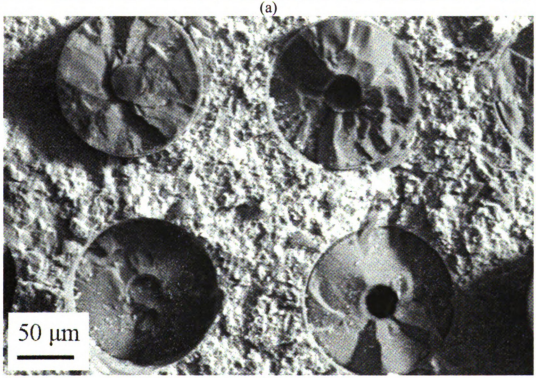

(b)

Figure 4.69 SE SEM images as (a) low magnification and (b) high magnification of the Ultra SCS-6/Ti-24Al-17Nb-1.1Mo MMC OOP TMF tested at a maximum stress of 300 MPa.

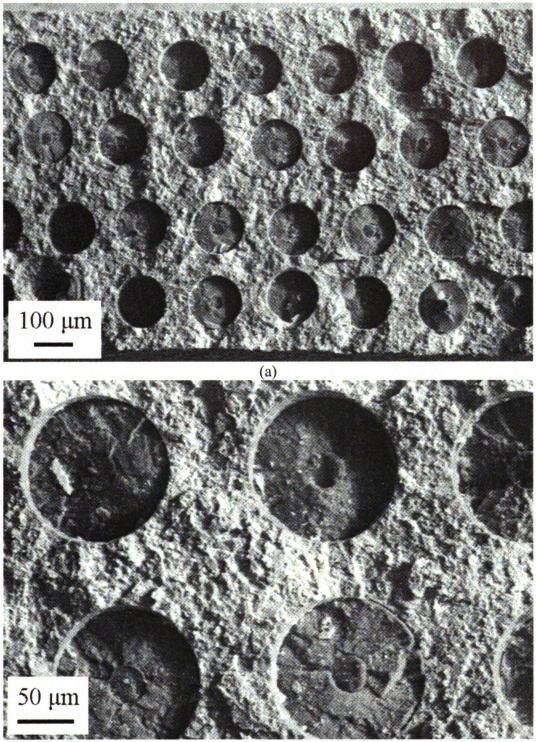

Figure 4.70 SE SEM images as (a) low magnification and (b) high magnification of the Ultra SCS-6/Ti-24Al-17Nb-2.3Mo MMC OOP TMF tested at a maximum stress of 300 MPa.

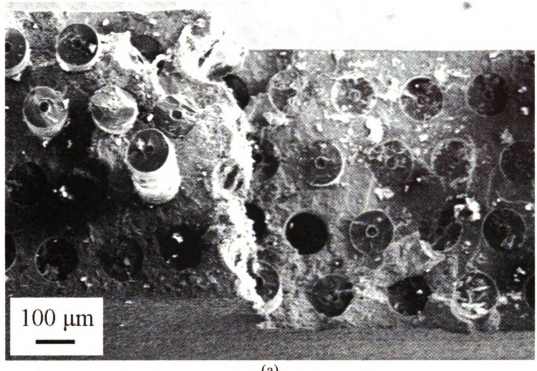

(a)

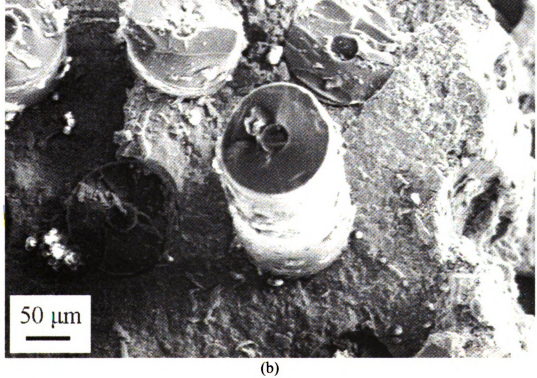

(b)

Figure 4.71 SE SEM images as (a) low magnification and (b) high magnification of the Ultra SCS-6/Ti-24Al-17Nb-0.66Mo MMC OOP TMF tested at a maximum stress of 600 MPa.

Figure
Ultra
MPa.

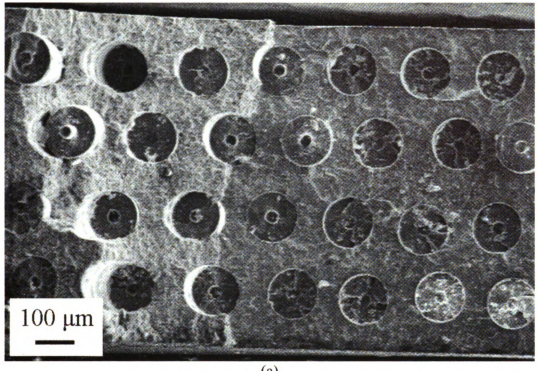

(a)

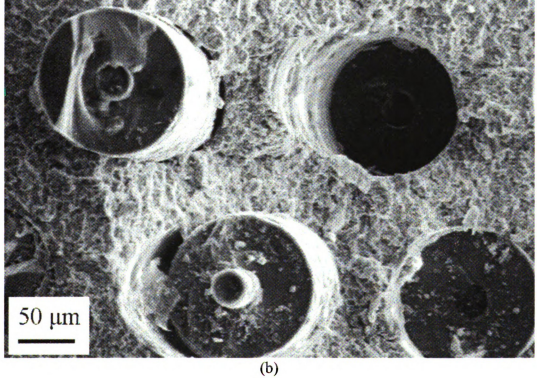

(b)

Figure 4.72 SE SEM images as (a) low magnification and (b) high magnification of the Ultra SCS-6/Ti-24Al-17Nb-2.3Mo MMC OOP TMF tested at a maximum stress of 600 MPa.

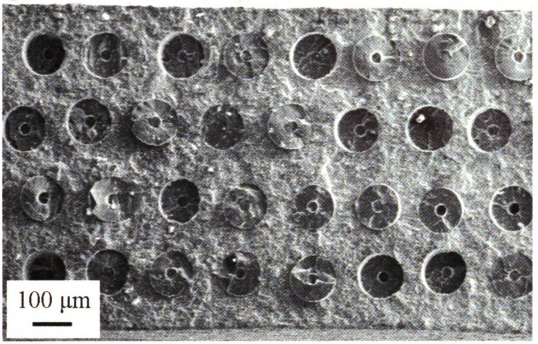

(a)

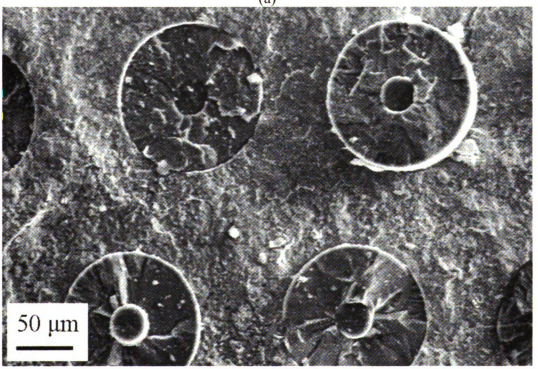

(b)

Figure 4.73 SE SEM images as (a) low magnification and (b) high magnification of the Ultra SCS-6/Ti-24Al-17Nb-2.3Mo MMC OOP TMF tested at a maximum stress of 600 MPa.

3. Microst

To h

adjacent to t

BSE SEM

17Nb-1.1M

where the m

4.74 – Figu

At

were obse

17Nb-1.1

Ultra SC

run-out c

cracking

450 MP

propaga

the bulk

never r

that cr

the O+

3. Microstructural Deformation Behavior

To help identify the microstructural deformation behavior of the MMCs a section adjacent to the fracture surface was metallographically prepared for imaging in the SEM. BSE SEM images of the Ultra SCS-6/Ti-24Al-17Nb-0.66Mo, Ultra SCS-6/Ti-24Al-17Nb-1.1Mo, and Ultra SCS-6/Ti-24Al-17Nb-2.3Mo MMC samples tested in OOP TMF where the maximum stress was 250 MPa, 450 MPa, and 600 MPa are presented in Figure 4.74 – Figure 4.82.

At a maximum stress of 250 MPa, only small cracks near the fracture surface were observed for the Ultra SCS-6/Ti-24Al-17Nb-0.66Mo and Ultra SCS-6/Ti-24Al-17Nb-1.1Mo MMCs, see Figure 4.72 and Figure 4.75. No cracking was observed in the Ultra SCS-6/Ti-24Al-17Nb-2.3Mo MMC, which did not fail and was stopped after the run-out condition of 8,000 cycles was achieved. A significantly greater amount of cracking was observed for each of the MMC compositions tested at maximum stresses of 450 MPa and 600 MPa. Cracks tended to emanate from the edge of the specimen and propagate perpendicular to the loading direction. However, crack initiation from within the bulk was also evident, see Figure 4.77, Figure 4.80, and Figure 4.82, as such cracks never reached the edges of the specimens. Higher magnification SEM images indicated that cracks primarily propagated transgranularly, passing through both the α_2 phase and the O+BCC colonies. However, some intergranular cracking was also observed.

Figure
Ultra S
MPa.

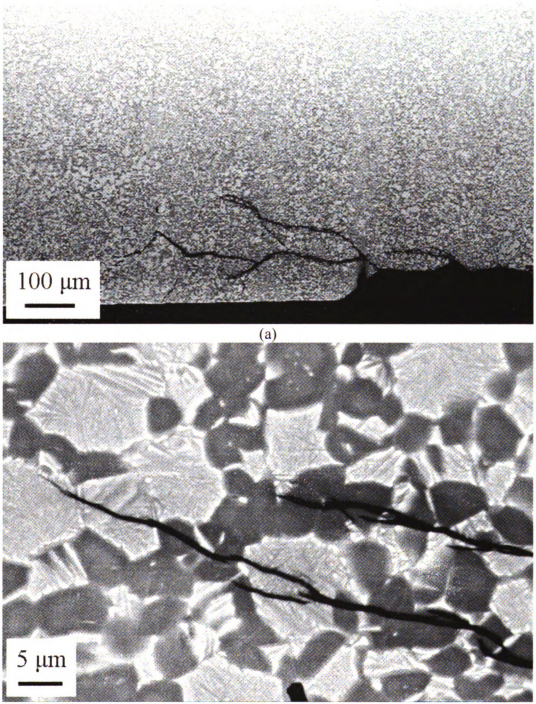

Figure 4.74 (a) Low-magnification and (b) high-magnification BSE SEM images of an Ultra SCS-6/Ti-24Al-17Nb-0.66Mo MMC OOP TMF tested at a maximum stress of 250 MPa. The loading direction is vertical.

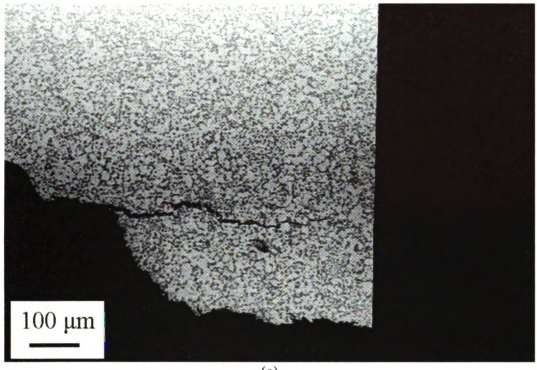

(a)

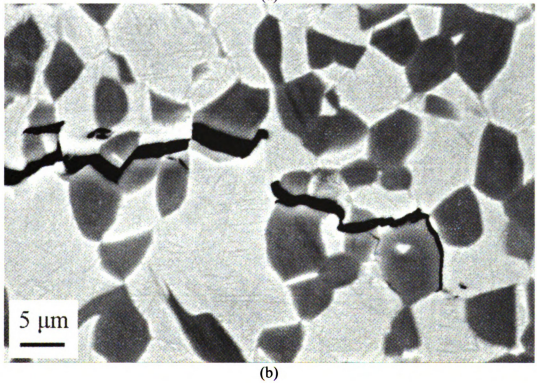

(b)

Figure 4.75 (a) Low-magnification and (b) high-magnification BSE SEM images of an Ultra SCS-6/Ti-24Al-17Nb-1.1Mo MMC OOP TMF tested at a maximum stress of 250 MPa. The loading direction is vertical.

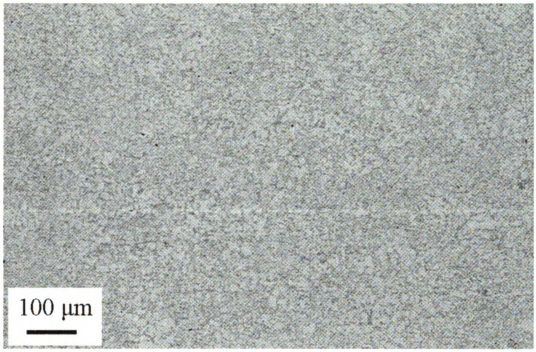

(a)

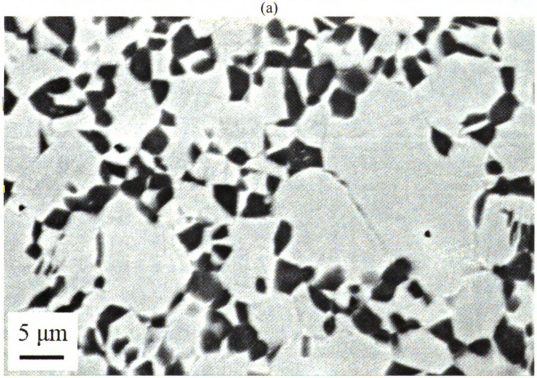

(b)

Figure 4.76 (a) Low-magnification and (b) high-magnification BSE SEM images of an Ultra SCS-6/Ti-24Al-17Nb-2.3Mo MMC OOP TMF tested at a maximum stress of 250 MPa. The loading direction is vertical.

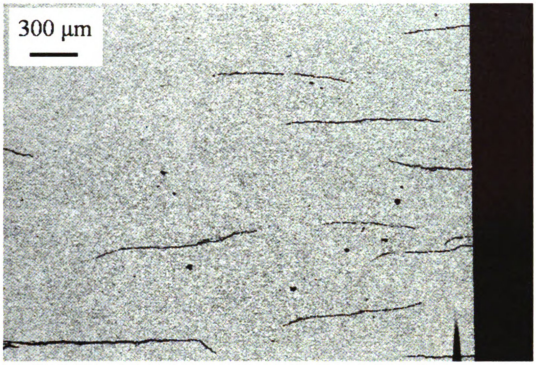

(a)

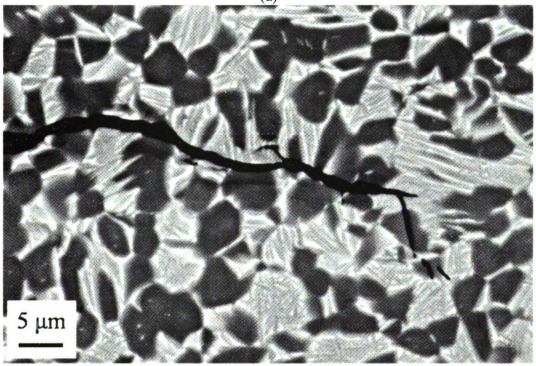

(b)

Figure 4.77 (a) Low-magnification and (b) high-magnification BSE SEM images of an Ultra SCS-6/Ti-24Al-17Nb-0.66Mo MMC OOP TMF tested at a maximum stress of 450 MPa. The loading direction is vertical.

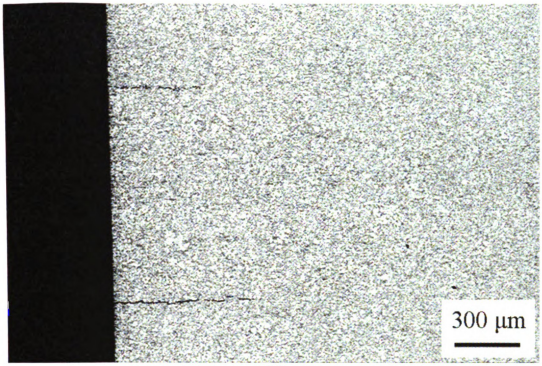

(a)

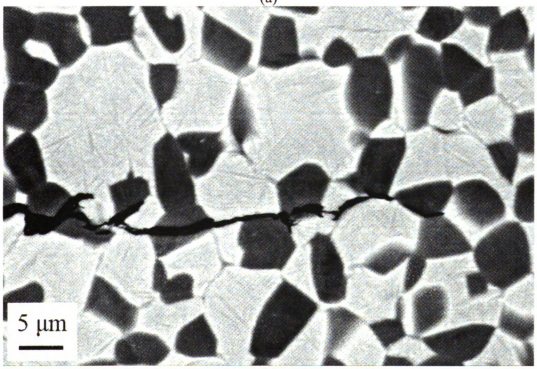

(b)

Figure 4.78 (a) Low-magnification and (b) high-magnification BSE SEM images of an Ultra SCS-6/Ti-24Al-17Nb-1.1Mo MMC OOP TMF tested at a maximum stress of 450 MPa. The loading direction is vertical.

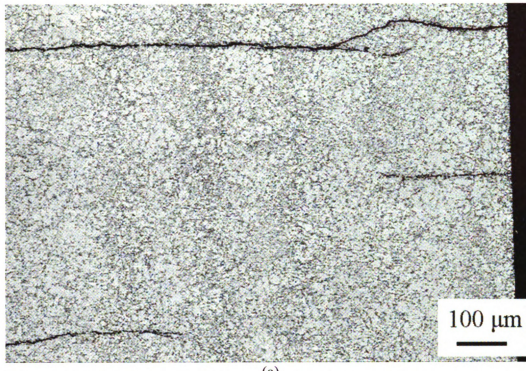

(a)

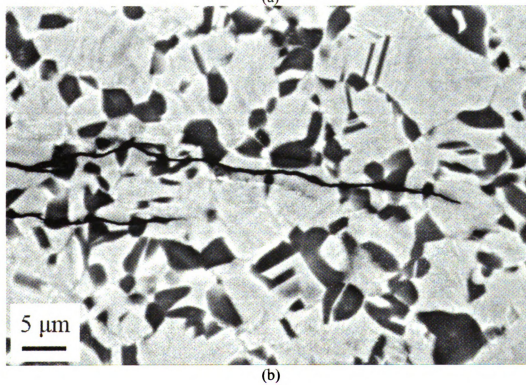

(b)

Figure 4.79 (a) Low-magnification and (b) high-magnification BSE SEM images of an Ultra SCS-6/Ti-24Al-17Nb-2.3Mo MMC OOP TMF tested at a maximum stress of 450 MPa. The loading direction is vertical.

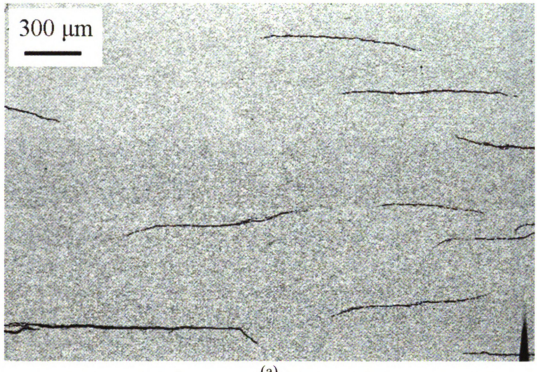

(a)

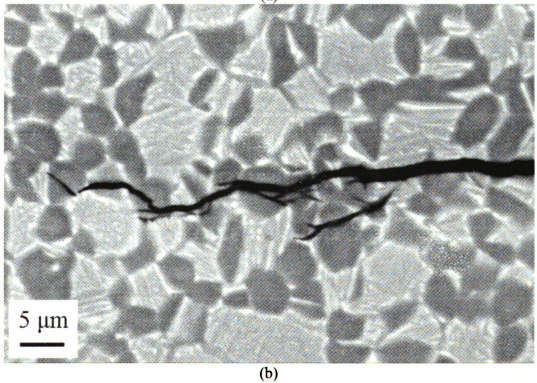

(b)

Figure 4.80 (a) Low-magnification and (b) high-magnification BSE SEM images of an Ultra SCS-6/Ti-24Al-17Nb-0.66Mo MMC OOP TMF tested at a maximum stress of 600 MPa. The loading direction is vertical.

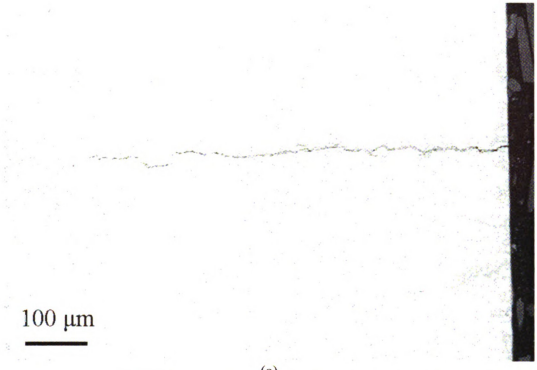

(a)

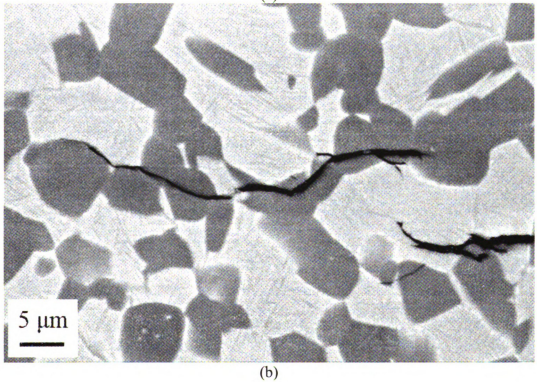

(b)

Figure 4.81 (a) Low-magnification and (b) high-magnification BSE SEM images of an Ultra SCS-6/Ti-24Al-17Nb-1.1Mo MMC OOP TMF tested at a maximum stress of 600 MPa. The loading direction is vertical.

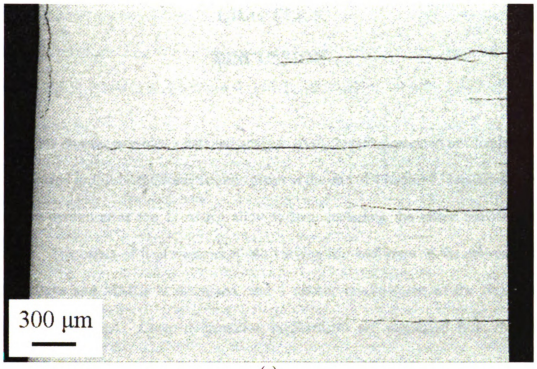

(a)

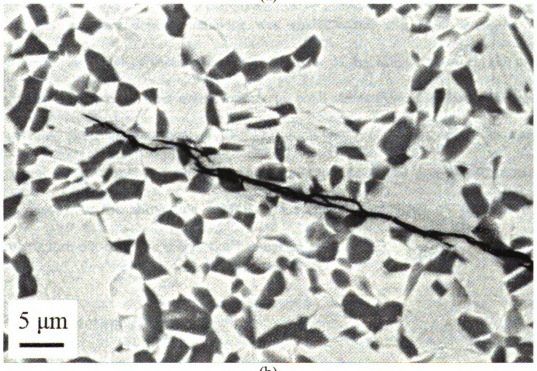

(b)

Figure 4.82 (a) Low-magnification and (b) high-magnification BSE SEM images of an Ultra SCS-6/Ti-24Al-17Nb-2.3Mo MMC OOP TMF tested at a maximum stress of 600 MPa. The loading direction is vertical.

CHAPTER 5

DISCUSSION

This chapter provides a detailed analysis of the results presented in Chapter 4, and it is organized to follow the specific aims given at the end of Chapter 1. Discussed first is the phase evolution of the Ti-Al-Nb alloy system, including the phase transformation behavior. The effect of heat treatments and varying Mo additions on the microstructure of the alloys and MMCs is discussed, and a further investigation of the fiber/matrix interface is provided. Creep deformation mechanisms are suggested from the stress exponents, activation energies, and microstructural deformation observations. The fiber/matrix interface debond behavior was characterized and bond strengths were determined. A model predicting the creep behavior of the MMCs based on the matrix alloy creep rates and the fiber-matrix interfacial bond strengths was applied. This model incorporated finite element analysis (FEA), which was used to determine the residual stresses at the fiber/matrix interface. The microstructure-tensile property relationships are discussed for the alloys and MMCs. This chapter ends with an analysis of the microstructure-out-of-phase thermomechanical fatigue results.

A. Microstructure Discussion

1. Apparent Phases

One motive for choosing the alloy compositions in this study was the improved creep resistance observed in a Ti-24Al-17Nb-1.0Mo alloy compared to that for a ternary Ti-24Al-17Nb alloy [Majumdar *et al.* (1995)]. While no phase diagram has been

developed for Ti-24Al-17Nb-xMo, a phase map of the Ti-25Al-xNb composition has been constructed, see Figure 5.1, and is applicable to the alloys in this study [Sagar *et al.* (1996)]. Based on the β-phase stabilizing ability of Mo, one atomic percent addition of Mo corresponds to the replacement of 4.25 atomic percent Nb [Ankem and Seagle (1983)]. Therefore, the Ti-24Al-17Nb-0.66Mo, Ti-24Al-17Nb-1.1Mo, and Ti-24Al-17Nb-2.3Mo alloys were expected to have phase equilibria similar to that of Ti-24Al-19.8Nb, Ti-24Al-21.7Nb, and Ti-24Al-26.8Nb, respectively.

The phase map was constructed through microstructural evaluations of Ti-25Al-xNb alloys heat-treated at various temperatures. While the apparent phases are indicated on the map, it is noted that this phase diagram violates the Gibbs phase rule, which states that the number of phases plus the degrees of freedom for a system is equal to the number of components plus two [Porter and Easterling (1992)]. A degree of freedom corresponds to a variable such as temperature, pressure, and component composition. When considering a system where pressure is held constant and the number of components is three, this rule simplifies to the number of phases plus degrees of freedom is equal to four. This means that for Ti-25Al-xNb containing one phase has three degrees of freedom. On this phase map, violations occur where a phase change transition is not separated by a change in the number of phases. For example, at high temperatures the phase map indicates there is a transition from the β phase to the B2 phase. To be in accordance with Gibbs phase rule, this should be transitioned by a β+B2 phase region. Similar occurrences can be found in other locations on the phase map. Despite these violations, the map provides an adequate look at the expected phases present within the microstructures of the alloys and matrices.

The microstructure of each alloy consisted of equiaxed α_2 grains and O-phase laths in a BCC-phase matrix. In accordance with the phase map, equilibrium cooling from the BCC-phase field of a Ti-25Al-xNb ($x \geq 17$) alloy passes through the α_2+BCC two-phase field, then to the α_2+BCC+O three-phase field, and lastly into the O or O+BCC field. The transformation from BCC to α_2+BCC is relatively slow and depends on the alloy composition and cooling rate [Banerjee *et al.* (1993), Muraleedharan *et al.* (1992a)]. The formation of the α_2 phase was entirely suppressed for a Ti-25Al-17Nb-1Mo alloy at a cooling rate of 12°C/min [Zhang *et al.* (1998)]. Also, increasing the content of BCC-phase stabilizer can reduce the temperature range of the α_2+BCC and the α_2+BCC+O phase fields [Zhang *et al.* (1998)]. Similar to the α_2-phase formation, the cooling rate has been shown to have a significant effect on the O-phase formation, where increased cooling rates resulted in less O phase and more BCC phase [Rowe (1993)]. In fact, a cooling rate of 30°C/min almost entirely suppressed the BCC → BCC+O transition for a Ti-23Al-27Nb-0.25Mo alloy, and it effectively shifted the transition to a temperature which was 100°C lower [Rowe (1993)]. Moderate cooling rates (approximately 2°C/min) were used in this study, thereby allowing for the α_2-phase and O-phase formation to occur.

The addition of Mo was expected to decrease the BCC → α_2+BCC transition temperature and also narrow the temperature range of the α_2+BCC and the α_2+BCC+O phase fields. Differential thermal analysis was conducted to determine the BCC phase transition temperature. The disappearing phase technique was used to verify the results. The results indicated that the BCC transus temperature lied between 1115°C – 1130°C for the Ti-24Al-17Nb-0.66Mo alloy and between 1130°C – 1145°C for the Ti-24Al-17Nb-

2.3Mo alloy. Although the Ti-24Al-17Nb-2.3Mo alloy was expected to exhibit a lower BCC-phase transformation temperature than the Ti-24Al-17Nb-0.66Mo alloy due to the increase in Mo (a beta phase-stabilizing element), the higher oxygen content in the Ti-24Al-17Nb-2.3Mo alloy may have negated the effect of the Mo content. According to the phase map the transitions for corresponding ternary alloy compositions of Ti-24Al-17Nb-0.66Mo (i.e. Ti-24Al-19.8Nb) and Ti-24Al-17Nb-2.3Mo (i.e. Ti-24Al-26.8Nb) are approximately 1080°C and 1050°C. Therefore, the predicted transition temperatures are significantly lower than those obtained experimentally. This increase in BCC transus temperature is believed to be due to the relatively high oxygen content (1830 ppm for the Ti-24Al-17Nb-0.66Mo alloy and 1670 ppm for the Ti-24Al-17Nb-2.3Mo alloy) along with the sluggish diffusion kinetics of Mo. Previous work on a Ti-24.5Al-17Nb-1Mo alloy observed a drop on the BCC transus temperature by approximate 20°C [Krishnamurthy *et al.* (1995)].

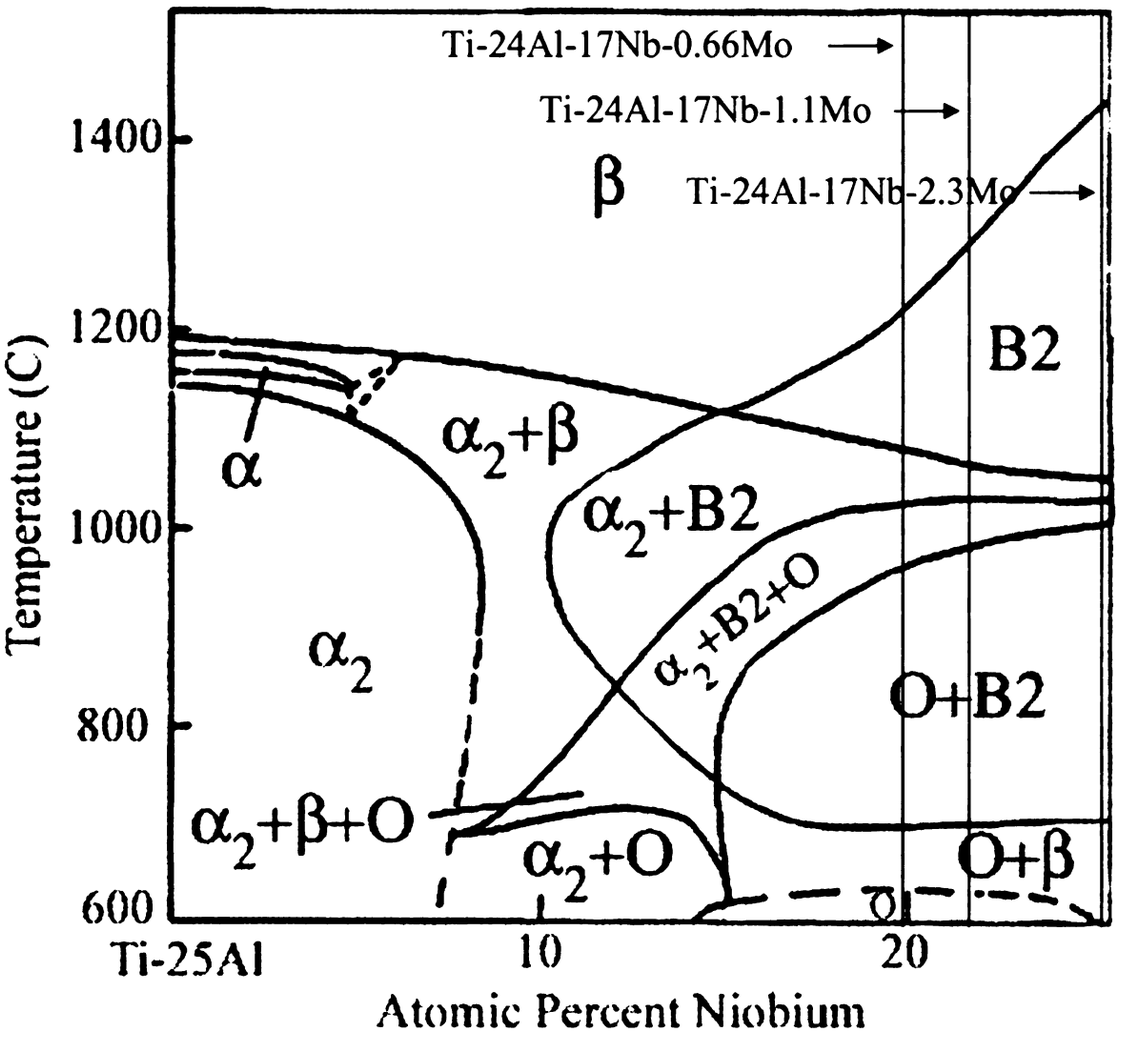

Figure 5.1 A phase map of the Ti-25Al-xNb system [Sagar *et al.* (1996)].

2. O Phase Formation

The O phase precipitated out of the BCC phase into a Widmanstatten lath morphology during the post-processing heat treatment. The O phase laths have a specific orientation relationship with the parent BCC phase: $[110]_O//[1\,\bar{1}\,1]_{B2}$ and $(001)_O//(011)_{B2}$ [Muraleedharan *et al.* (1992), Boehlert *et al.* (1997)]. While microstructural texturing of the α_2 and O+BCC phases was not observed (i.e. the microstructures appeared similar in all sectioned orientations), many of the O phase laths within a single BCC grain appeared to be oriented similarly. This tendency has been previously noted and was suggested to occur due to larger laths consuming the smaller laths of different orientation and also suggested to occur due to slow cooling resulting in grain boundary nucleation and growth-dominated behavior of one orientation relative to the others [Boehlert *et al.* (1997)]. The O phase was also sometimes observed surrounding the edges of the α_2 grains. Such previous observations have been termed rim O phase where the orientation relationship between the two phases, $[100]_O//[2\,\bar{1}\,\bar{1}\,0]_{\alpha 2}$ and $(001)_O//(0001)_{\alpha 2}$, is exhibited [Banerjee *et al.* (1988) and Muraleedharan *et al.* (1995)]. The volume fraction of rim O phase was small compared with the O phase in the BCC regions.

3. Alloy Microstructure

The Ti-24Al-17Nb-2.3Mo alloy contained a greater O+BCC phase volume percent compared to that of the Ti-24Al-17Nb-0.66Mo alloy. This was attributed to the increase in Mo, a strong BCC phase stabilizing element. For both alloys the heat treatment resulted in lower α_2-phase volume percents and corresponding increases in O+BCC phase volume percents. With the reduction in α_2-phase volume percent there

was a corresponding decrease in the equiaxed grain size of the α_2 phase and an increase in the O+BCC colony size. The heat treatment process involved a solutionizing step at 1050°C, which according to the DTA and disappearing-phase results was expected to fall within the α_2+BCC two-phase field. The aging temperature (850°C) for both alloy compositions fell within the expected O+BCC two-phase field, thereby rationalizing the increase in the O+BCC phase volume percent observed for the heat-treated alloys.

There was a semi-continuous network of α_2-phase observed throughout the Ti-24Al-17Nb-0.66Mo alloy even in the HT condition. The α_2-phase network in the Ti-24Al-17Nb-2.3Mo alloy was more dispersed, containing fewer α_2/α_2 grain boundaries. The Ti-24Al-17Nb-2.3Mo microstructure exhibited a finer O+BCC structure than the Ti-24Al-17Nb-0.66Mo microstructure. This was most likely the result of sluggish kinetics due to Mo being a slow-diffusing element [Smith *et al.* (1999)]. Previous microprobe work along with the work conducted in this dissertation has shown that the O+BCC phase regions are rich in Nb and lean in Al compared to the α_2 phase [Boehlert *et al.* (1997), Smith *et al.* (1999)]. This was also observed for Ti-24Al-17Nb-0.66Mo and Ti-24Al-17Nb-2.3Mo alloys, as shown in Figure 5.2. The Mo was also shown to preferably segregate to the O+B2 region, which is in agreement with previous work [Smith *et al.* (1999)]. Furthermore, the Mo tended to be dispersed among the Nb, which is evident in Figure 5.2 (d). Areas with solely Mo would appear red whereas areas with solely Nb would appear green. The areas colored yellow arise due to a mixture of red (Mo) and green (Nb).

A modest amount of porosity, less than 1%, was observed in each alloy. This porosity was most likely due to incomplete consolidation during the HIP cycle and was

expected to have had a detrimental effect on all mechanical properties, especially ε_f, due to the associated stress concentration at the pores.

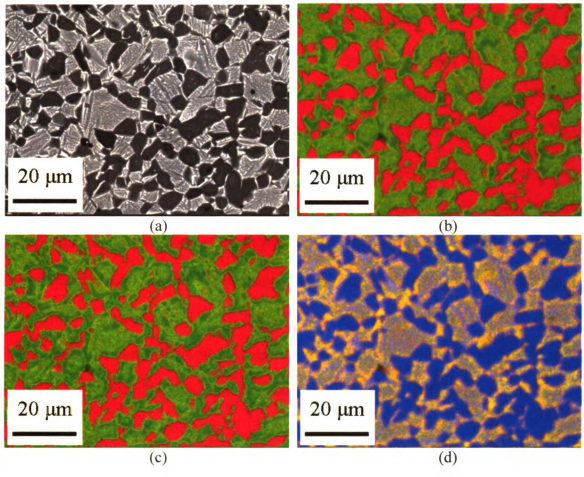

Figure 5.2 (a) A BSE SEM image of the HT Ti-24Al-17Nb-0.66Mo alloy. Color-coded micrographs, formed using EDS, show the distribution of Al, Nb, and Mo. (b) displays Al (red) and Nb (green), (c) displays Al (red) and Mo (green), and (d) displays Al (blue) and the combination of Nb and Mo (yellow – formed from the combination of red and green).

4. Elemental Analysis and BCC Phase Ordering

The chemical compositions of each phase were determined using a microprobe analysis. The average chemical composition of the α_2 phase was 61.8Ti-26.5Al-11.6Nb-0.1Mo and 60.9Ti-26.7Al-11.9Nb-0.5Mo for the Ti-24Al-17Nb-0.66Mo and Ti-24Al-17Nb-2.3Mo alloys, respectively. As stated in Chapter 2, the chemical make-up of α_2 is Ti_3Al. The Nb and Mo exist in a solid-state solution within the α_2 phase. For a Ti-26Al-17Nb alloy, the composition of the α_2 phase was measured to be Ti-27Al-10Nb, which is comparable to that observed in this alloy system [Banerjee (1995)]. A previous study has shown Nb contents as high as 19.7 at.% within the α_2 phase [Cowen (2006)]. The α_2 phase has now been shown to hold up to 0.5 at.% Mo in solid solution for a Ti-24Al-17Nb-2.3Mo alloy. To the author's knowledge this is the highest Mo content observed in titanium aluminides to date.

The average chemical composition of the O phase was 58.7Ti-24.5Al-16.3Nb-0.6Mo and 54.9Ti-25.5Al-17.3Nb-2.3Mo for the Ti-24Al-17Nb-0.66Mo and Ti-24Al-17Nb-2.3Mo alloys, respectively. The O-phase stoichiometry is Ti_2AlNb. With a 2:1:1 ratio of Ti:Al:Nb, Nb was the limiting element in the formation of the O phase. Therefore, the amount of O phase that can be formed within these alloys is strongly dependent on the Nb content. An increase in the nominal Nb content would therefore be expected to increase the O-phase volume fraction of the alloys. The O phase of the Ti-24Al-17Nb-2.3Mo alloy was shown to hold up to 2.3 at.% Mo. Given the similarity in atomic radii of Nb (2.080 Å) and Mo (2.010 Å), it is likely that the Mo substitutes at Nb atom sites within the crystal structure.

The chemical compositions of the BCC phase were 56.6Ti-17.6Al-24.2Nb-1.5Mo and 53.8Ti-18.3Al-25.3Nb-2.6Mo for the Ti-24Al-17Nb-0.66Mo and Ti-24Al-17Nb-2.3Mo alloys, respectively. The BCC phase is based on the CsCl structure with Ti atoms occupying the ½ ½ ½ position and either Al or Nb atoms at the 0 0 0 position. In this alloy system, the BCC phase is typically enriched in Nb, due mainly to the diffusion of Nb away from the α_2 phase (Ti_3Al). Therefore, the low Al contents observed in the BCC phase of these alloys were expected. The BCC-phase Mo content was always higher than the bulk alloy Mo content, while the α_2-phase Mo content was always lower than the bulk alloy content. The Mo content within the BCC phase was as high as 2.6 at.% for the Ti-24Al-17Nb-2.3Mo alloy.

A comparison of the microprobe data to those found for bulk chemical analysis was performed using a rule-of-mixtures calculation. The calculated bulk chemical composition was determined using:

$$\text{Bulk Composition} = V_{\alpha}X_{\alpha} + V_{(O+BCC)}X_{(O+BCC)} \qquad (5.1)$$

where V_{α} and V_{O+BCC} are the phase volume percentages of the α_2 phase and O+BCC colonies, respectively, and X_{α} and X_{O+BCC} are the element (Ti, Al, Nb, or Mo) contents in the α_2 phase and the O+BCC colonies, respectively. X_{O+BCC} was taken to be a weighted average of the elemental contents found within the O and BCC phase. The calculated results are presented in Table 5.I along with those determined from the bulk chemical analysis. The calculated phase compositions compare favorably to those found using bulk chemical analysis. The difference between the two sets of values is attributed to the missing phase volume percents of the individual O and BCC phases. The average

element content was used for the O+BCC colonies. This suggested that the alloys contained equal volume fractions of the O and BCC phases, which was unlikely.

Table 5.I A comparison of the rule-of-mixture calculations to bulk chemical analysis

Method	Material	Ti (at.%)	Al (at.%)	Nb (at.%)	Mo (at.%)
Rule-of-Mixtures	HT Ti-24Al-17Nb-0.66Mo	59.2	23.1	16.9	0.69
Rule-of-Mixtures	HT Ti-24Al-17Nb-2.3Mo	55.9	23.1	19.0	1.98
Bulk Chemical Analysis	HT Ti-24Al-17Nb-0.66Mo	60.8	22.2	16.3	0.66
Bulk Chemical Analysis	HT Ti-24Al-17Nb-2.3Mo	56.1	24.4	17.2	2.3

Previous studies have shown that the Al content within the BCC phase affects ordering, where higher Al contents favor the formation of the ordered BCC phase (B2) and lower Al contents favor the formation of the disordered BCC phase (β) [Bendersky (1991), Boehlert *et al.* (1991), Cowen (2006)]. It was shown that the BCC phase within a Ti-21Al-29Nb alloy with at least 18 at.% Nb tended to be ordered, while a Ti-15Al-33Nb alloy with at most 15 at.% Nb favored the formation of the disordered BCC phase [Cowen (2006)]. The BCC phase of the each alloy in this study contained approximately 18 at.% Nb, therefore suggesting the formation of the ordered BCC phase.

Verification of the ordered BCC phase was accomplished using XRD to look for superlattice reflections. These reflections only occur if lattice sites are occupied by specific atoms apparent in the ordered B2 phase. The disordered phase lacks superlattice reflections because the BCC structure factor is followed, which only allows a given reflection to appear (shown by a peak in the XRD scan) when the Miller indices (hkl) sum to an even number (i.e. h+k+l = even). However, for the ordered B2 phase the simple cubic structure factor is followed, allowing for a greater number of diffracting planes to appear in the scan, although at a weaker intensity. An XRD scan of the Ti-

24Al-17Nb-0.66Mo and Ti-24Al-17Nb-2.3Mo alloys both showed the (210) supperlattice reflection to be present (see Figure 4.16 on p. 119). Therefore, it is likely that the BCC phase within these alloys is ordered B2. However, the degree of order was not determined, and the microstructure likely consisted of both the ordered B2 phase and the disordered β phase, where only the ordered B2 phase would contribute to the superlattice reflection peak.

5. Metal Matrix Composite Microstructure

For the MMC panels, the fiber distribution was relatively uniform and in general the fiber-matrix interface was well consolidated. The microstructures within the matrices of the MMCs were similar to those within the alloys. However, the α_2 phase volume percent in the Ti-24Al-17Nb-0.66Mo matrix was greater than that in the alloy. The phase volume percents of the Ti-24Al-17Nb-2.3Mo alloy and MMC were similar. For the Ti-24Al-17Nb-1.1Mo matrix the phase volume percents of α_2 and O+BCC fell between the values obtained for the Ti-24Al-17Nb-0.66Mo and Ti-24Al-17Nb-2.3Mo matrices. The α_2 grain size of the Ti-24Al-17Nb-1.1Mo matrix was significantly greater than the α_2 grain size within the Ti-24Al-17Nb-0.66Mo and Ti-24Al-17Nb-2.3Mo matrices. This observation was justified by the variance in processing conditions, as discussed in Chapter 3.

6. Interface Microstructure

The matrix region near the fiber-matrix interface was depleted of the O+BCC phases and enriched in the α_2 phase. This is a result of the reaction between the fiber and

matrix during consolidation and subsequent heat treatment as when carbon diffuses across the interface it stabilizes a greater volume fraction of the α_2 phase [Krishnamurthy and Miracle (1997)]. The reaction zone between the matrix and the outer coating was between 1 – 2.5 μm thick.

For the MMCs, the diffusion of carbon from the fiber coating into the matrix, stabilizing the α_2 phase, poses a problem when selecting a heat treatment [Krishnamurthy and Miracle (1995)]. These reaction zones have also been observed in SCS-6/Ti-24Al-11Nb and SCS-6/Ti-24.5Al-17Nb MMCs [Smith *et al.* (1992), Krishnamurthy *et al.* (1994)]. Such reaction zones contain numerous α_2/α_2 grain boundaries that serve as potential sites for matrix cracks, which can significantly reduce elongation-to-failure. These reaction zones are affected by interstitial carbon, an α-phase stabilizer, which diffuses from the fiber coating during the consolidation of the MMC and the subsequent heat treatment. Interstitial carbon has been observed as far as 60 μm away from the interface for a SCS-6/Ti-6Al-4V (wt.%) MMC [Pickard and Miracle (1995)]. However, the amount of carbon diffusion within the alloys in this study was expected to be decreased due to the presence of Mo, as the addition of Mo has been shown to reduce diffusion controlled reactions [Porter *et al.* (1995)].

Carbides and silicides are reaction products that have been observed in a SCS-6/Ti-6Al-4V MMC [Martineau *et al.* (1985), Gundel and Miracle (1997)]. However, the addition of Nb and Al can produce more complicated reaction products, where Nb and Al can diffuse and react with TiC forming a complex carbide of (Ti, Al, Nb)C [Konitzer and Loretto (1989)]. The reaction zone of the MMCs in this study was expected to be composed of these complex carbides and silicides, similar to those seen in a SCS-6/Ti-

24Al-11Nb MMC [Yang and Jeng (1989)]. No experimental work was performed to determine the reaction products present between the fiber and matrix in this work.

B. Creep Discussion

1. Microstructure-Creep Relationships

The Ti-24Al-17Nb-2.3Mo and Ti-24Al-17Nb-1Mo alloys exhibited the lowest primary creep strains and minimum creep rates, while the baseline ternary alloy exhibited the worst primary and secondary creep resistance. The Ti-24Al-17Nb-2.3Mo alloy exhibited superior creep resistance compared with the Ti-24Al-17Nb-0.66Mo alloy. In fact, approximately one order of magnitude difference in minimum creep rate was observed at all stresses evaluated at 650°C. Thus, small increases in Mo content significantly increase the creep resistance of Ti-Al-Nb alloys. This was one of the major findings of this work. The reasons for the increased creep resistance of the Ti-24Al-17Nb-2.3Mo alloy compared to the Ti-24Al-17Nb-0.66Mo alloy are believed to be due to three microstructural differences: decreased number of α_2/α_2 grain boundaries, increased O+BCC colony size, and the solid solution strengthening effects of the Mo. However, the Ti-24Al-17Nb-1Mo alloy exhibited similar creep strain/time behavior as that for Ti-24Al-17Nb-2.3Mo. Consequently, Mo additions greater than 1 at.% may not be necessary to further enhance the creep resistance. The Ti-24Al-17Nb-0.66Mo alloy exhibited an average of 6.9% creep strain at failure, while the Ti-24Al-17Nb-2.3Mo alloy had an average creep strain of 1.7% at failure. Therefore, while increases in Mo contents resulted in greater creep resistance, such increases also led to lower creep failure strains.

Thus, the Mo content needs to be considered when both ε_f and time-to-rupture are important parameters.

Each of the microstructures contained a mixture of equiaxed α_2 and lath O+BCC regions. It is noted that the baseline ternary alloy underwent an identical subtransus heat treatment schedule as the alloys in the current study, while the Ti-24Al-17Nb-1Mo alloy also underwent a similar subtransus heat treatment. The baseline ternary alloy exhibited the greatest α_2-phase volume fraction (0.52), while the Ti-24Al-17Nb-1Mo and Ti-24Al-17Nb-2.3Mo alloys exhibited the lowest α_2-phase volume fractions; 0.21 and 0.24, respectively. Thus, the creep resistance increased with lower α_2-phase volume fractions and greater O phase volume fractions.

The size of the O+BCC colonies was expected to affect the creep resistance of each alloy. The average prior BCC grain diameter was measured to be 11.5±2.3 μm for the Ti-24Al-17Nb-0.66Mo alloy and 15.6±3.2 μm for the Ti-24Al-17Nb-2.3Mo alloy. The finer grain size of the Ti-24Al-17Nb-0.66Mo alloy may have contributed to its poorer creep resistance. The O-phase size and spacing has been shown to have a significant effect on creep rates. However, this observation is contrary to that observed for a Ti-25Al-17Nb-1Mo alloy, where a finer-lath microstructure possessed lower creep resistance than a coarse-lath microstructure [Zhang *et al.* (1998)]. Thus, the fine O+BCC phase regions may have also contributed to the greater creep resistance of the Ti-24Al-17Nb-2.3Mo alloy compared to the Ti-24Al-17Nb-0.66Mo alloy. A decrease in spacing between O-phase laths would be expected to increase the creep resistance of the alloys. The decreases in spacing would result in a lower mean free path slip plane within the BCC grains and would most likely result in the pileup of dislocations at the O-phase

grain boundaries. Observations of dislocation pileup at O-phase grain boundaries have been noted in other Ti-Al-Nb alloys [Boehlert and Miracle (1999), Boehlert (1999)]. Dislocation motion is important when the dominant secondary creep deformation mode is dislocation-controlled climb, where a steady-state creep rate is achieved when strain hardening is balanced by recovery. This was the suggested secondary-creep deformation mode for stresses above 170 MPa at 650°C. The piling up of dislocations at O-phase grain boundaries would increase the amount and rate of strain hardening, which would result in a lower minimum creep rate. The O-phase spacing for the heat treated Ti-24Al-17Nb-0.66Mo and Ti-24Al-17Nb-2.3Mo alloys were both submicron in size. However, the as-processed Ti-24Al-17Nb-0.66Mo and Ti-24Al-17Nb-2.3Mo alloys both had larger O-phase lath spacings suggesting that creep results of the as-processed alloys would exhibit poorer creep resistance than that of the heat-treated alloys. Furthermore, the BCC phase in the as processed alloys would have been transforming into the O phase during creep deformation at 650°C causing additional creep strain due to microstructural instability.

The addition of Mo may also have had a beneficial affect by solid-solution strengthening of the BCC phase and decreasing the creep diffusion rates. In this study identical microstructures of each alloy were not obtained through heat treatment. Thus, the sole effect of Mo content on the creep behavior was not determined. Therefore the above statements must be combined to summarize the creep data as there existed both a microstructural difference caused by Mo affecting the phase volume fractions and lath spacings as well as a solid-solution strengthening effect.

2. *In-Situ* Creep Observations

The *in-situ* creep experiments indicated that grain boundaries were the locus of deformation and cracking in each of the alloys investigated. Deformation in the form of cracking was observed within the α_2 phase and at the α_2 grain boundaries, which agrees with previous observations of a Ti-22Al-23Nb alloy creep tested at 650°C and 172 MPa [Smith *et al.* (1995), Smith and Porter (1997)]. With increased displacement, the α_2 grain boundary cracks grew in length and width. There is little evidence of crack initiation at the interface between the O phase and BCC phase. Therefore, it is expected that a decrease in the α_2 phase volume percent and correspondingly, an increase in the O+BCC phase volume percent would increase the creep resistance of the alloy. Previous studies on Ti-25Al-17Nb and Ti-22Al-23Nb alloys demonstrated that increased volume fractions of high aspect ratio O phase and corresponding decreases in equiaxed α_2 result in improved creep performance [Boehlert *et al.* (1995), Krishnamurthy *et al.* (1995), Smith *et al.* (1995), Smith and Porter (1997)]. These results have been attributed to the inherent improvement in creep resistance of lath structures over that of equiaxed structures and also to the lower creep strain rates obtained for the O phase over that of the α_2 phase [Albert and Thompson (1992), Cho *et al.* (1990), Hayes (1991), Banerjee *et al.* (1993)]. Thus, reducing the continuity and size of the α_2 phase through the addition of small amounts of Mo can have a significant effect on the creep behavior.

The amount of grain boundary cracking observed on the sample surface was greater than that observed within the bulk of the samples tested in air. This was due to a lack of constraint on the sample surface and the presence of higher stress states at the edges (due to sample geometry) than in the bulk of the sample, which resulted in a

greater extent of cracking and grain boundary sliding occurring on the surface. For the samples tested *in-situ* in a vacuum, environmentally-assisted cracking did not occur as readily as that for samples tested in air. Therefore, the effect of the environment on the stability of the alloys at high temperatures is of great concern. Thermal barrier coatings are being developed for Ti alloys and Ni-based superalloys to help prevent environmentally-assisted cracking and thereby improve creep resistance.

A BSE SEM image of the Ti-24Al-17Nb-0.66Mo alloy *in-situ* creep tested at 180 MPa and 650°C (previously presented in Chapter 4) is shown in higher magnification in Figure 5.3. This applied stress was chosen because it sits at the upper end of the stress range where grain boundary sliding is suggested to be the dominant creep deformation mechanism for the Ti-24Al-17Nb-0.66Mo alloy. Within Figure 5.3 (b) grain boundary cracking is apparent, and it is observed that the grain boundary displacement between individual grains varies. The grain boundary sliding was expected to be accommodated by grain boundary cracking. The amount of displacement between the grain boundaries was dependent on the amount of grain boundary sliding and grain boundary migration. Grain boundary migration is the process in which atoms diffuse across a grain boundary in an attempt to bring it back to a lower energy configuration [Garafalo (1965)]. When observed in polycrystalline structures, grain boundary migration has been associated with a recovery process involving subgrain formation and strain-induced migration [Garafalo (1965)]. Since not all portions of the grain boundaries behave similarly, grain boundary migration can lead to the development of serrations or corrugations at the boundaries of polycrystalline metals [Garafalo (1965)]. Serrations are evident along the O+BCC colonies that have slid away from α_2 grains in Figure 5.3 (b). Low-angle (1.5° or less) tilt

boundaries and high-angle (greater than 15°) boundaries tend to migrate faster than those with intermediate misorientation angles [Garafalo (1965)]. Therefore, the difference in grain boundary displacement may be attributed to the orientation of each grain with respect to its neighboring grains.

(a)

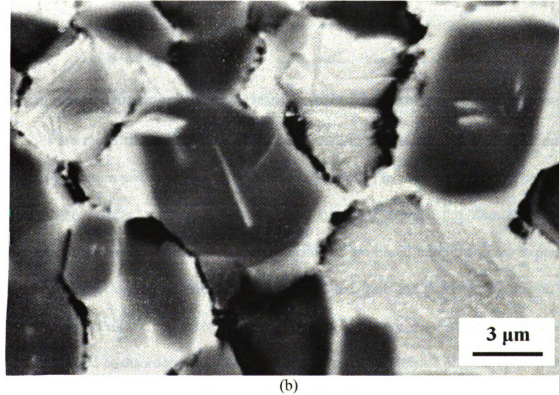

(b)

Figure 5.3 BSE SEM photomicrographs of the Ti-24Al-17Nb-0.66Mo alloy *in-situ* creep tested at 180 MPa and 650°C (a) prior to loading and (b) at a total displacement of 0.63 mm. The loading direction is horizontal.

During creep testing multiple deformation mechanisms can be present. The total creep strain observed is made up of intragranular deformation and grain boundary sliding. Therefore, the dominance of grain boundary sliding is dependent on the proportion of creep strain achieved due to sliding. However, if grain boundary sliding is dependent upon prior intragranular deformation then it is only an accommodating process and not a controlling process [Garafalo (1965)]. In comparing Figure 4.30 (a) – (f) (pp. 140-142) and Figure 5.3 (a) and (b), it is clear that little or no deformation was observed within the α_2 grains or O+BCC colonies, where the individual grains appeared the same prior to deformation and post deformation suggesting that grain boundary deformation was not accommodating intragranular deformation. Therefore, grain boundary cracking and sliding were considered to be the rate controlling creep deformation process for these test conditions.

3. Suggested Dominant Creep Deformation Mechanisms of the Alloys

Pure metal theory has been extensively used to suggest the dominant secondary creep deformation mechanisms of the O-phase alloys cited in this dissertation. Therefore, to compare results, pure metal theory was used to explain the dominant creep mechanisms in this dissertation. These mechanisms are based upon the creep exponent (n) and apparent activation energies (Q_{app}) calculated from the power-law equation for the creep strain rate. It is noted that the alloys in this study were not pure metals, but were composed of disordered solid solution phases and intermetallic phases.

The Ti-Al-Nb-Mo alloys investigated in this study contained the α_2, β/B2, and O phases. To the author's knowledge no self-diffusion data is available in the literature for

the O or β/B2 phases. The self diffusion data for α_2 was presented in Table 2.II. The activation energies for Ti, Al, and Nb in Ti_3Al (α_2 phase) are 288, 374, and 312 kJ/mol, respectively [Rusing and Herzig (1996)]. The activation energies of other α_2 alloys creep tested in a high stress regime (n greater than 4) range from 206 – 285 kJ/mol [Mendiratta and Lipsitt (1980), Malakondaiah and Rao (1981), Mishra and Banerjee (1990)]. These values are in close agreement with those found for lattice self diffusion of Ti, Al, and Nb in Ti_3Al. For alloys and pure metals activation energies approximately half that of lattice self diffusion typically correspond to grain boundary diffusion [Evans and Wilshire (1985)].

Using the creep exponents and apparent activation energies measured in this work, dominant deformation mechanisms of the Ti-24Al-17Nb-0.66Mo and Ti-24Al-17Nb-2.3Mo alloys were proposed. Each alloy displayed a transition in creep exponents, where a constant n value could be fit to each regime. The Ti-24Al-17Nb-0.66Mo alloy had an n value of 1.8 from 29 MPa to 172 MPa and an n value of 4.6 from 172 MPa to 225 MPa. The n values suggest grain-boundary sliding was the main deformation mechanism in the lower stress regime with a transition to dislocation climb at stresses greater than 172 MPa. A change in apparent activation energy was also observed in each stress regime. At 29 MPa, an apparent activation energy of 129 kJ/mol was calculated at temperatures ranging from 650°C to 710°C, while an apparent activation energy of 249 kJ/mol was calculated at 150 MPa over the same temperature range. The lower activation energy value (129 kJ/mol) was suggested to be representative of grain boundary diffusion, while the higher activation energy value (249 kJ/mol) was suggested to be representative of lattice self diffusion. The Ti-24Al-17Nb-2.3Mo alloy displayed a

similar shift in n value at 650°C, going from 2.0 in a stress regime ranging from 50 MPa to 225 MPa to 4.8 in a stress regime ranging from 225 MPa to 275 MPa. These n values suggested grain-boundary sliding and dislocation climb to be the dominant deformation mechanisms in the lower and higher stress ranges, respectively. An activation energy of 293 kJ/mol at 150 MPa obtained over a temperature range of 650°C – 670°C was suggested to be representative of lattice self diffusion. This value is within the range of those measured for Ti_3Al alloys mentioned on the previous page. *In-situ* testing verified that the majority of creep deformation that occurred in the lower stress regime occurred through grain boundary cracking and sliding.

4. Metal Matrix Composite Creep

MMC creep testing was conducted with specimens containing fibers oriented perpendicular to the loading direction. The greatest creep resistance was exhibited by the Ultra SCS-6/Ti-24Al-17Nb-2.3Mo MMC, while the Ultra SCS-6/Ti-24Al-17Nb-0.66Mo MMC exhibited the poorest creep resistance. This result was expected based on the poorer creep resistance of the Ti-24Al-17Nb-0.66Mo alloy compared with the Ti-24Al-17Nb-2.3Mo alloy and the fact that the 90°-oriented MMC creep response is strongly dependent on the matrix alloy's creep behavior. The alloys exhibited significantly lower secondary creep rates and greater creep resistance than their respective MMCs. The modified Crossman model suggests that such a condition arises when the applied creep stress is greater than the fiber/matrix interfacial strength [Majumdar (1997)]. In this case the MMC is expected to behave similarly to the matrix alloy tested with holes where the fibers lie. This will be further analyzed with respect to the interface strength

measurements later in this chapter. In comparing all the alloys and MMCs tested in this study, the Ti-24Al-17Nb-2.3Mo alloy exhibited the lowest secondary creep rates and greatest creep resistance. The secondary creep rates for the Ultra SCS-6/Ti-24Al-17Nb-1.1Mo MMC and Ultra SCS-6/Ti-24Al-17Nb-2.3Mo MMC were similar to those for the Ti-24Al-17Nb-0.66Mo alloy. However, each of these remained approximately one order of magnitude greater than those for the Ti-24Al-17Nb-2.3Mo alloy. The Ultra SCS-6/Ti-24Al-17Nb-1.1Mo MMC experienced similar creep rates to those for the Ultra SCS-6/Ti-24Al-17Nb-2.3Mo MMC, as was similarly observed for their respective alloys. The average creep failure strains for the Ultra SCS-6/Ti-24Al-17Nb-0.66Mo, Ultra SCS-6/Ti-24Al-17Nb-1.1Mo, and Ultra SCS-6/Ti-24Al-17Nb-2.3Mo were 2.6%, 1.5%, and 1.1%, respectively. These values are lower than those obtained for the corresponding alloy compositions (6.9% for the Ti-24Al-17Nb-0.66Mo alloy and 1.7% for the Ti-24Al-17Nb-2.3Mo alloy). The difference in values between the MMCs and alloys is likely due to the variance in creep failure modes observed.

SEM images revealed that transgranular cracking was apparent for each MMC creep tested (Figure 4.40 on p.157). These cracks tended to initiate at the fiber/matrix interfaces and at multiple sites along the specimen surface. Flaws resulting from a cut fiber, embrittled matrix, exposed fiber edge, and surface defects have been attributed to assist in surface crack initiation [Das *et al.* (1992)]. Cracks initiating at fiber/matrix interfaces could link with other fiber/matrix interface cracks or a surface crack forming a dominant crack. Propagation of the dominant crack eventually resulted in failure of the MMC. As the cracks propagated, stress-assisted environmental degradation occurred. A previous study of a SiC/Ti-24Al-11Nb MMC found that dislocations tended to pile up

against the reaction zone during creep, but because no dislocations were observed in the reaction zone is was suggested that this zone served as a barrier to dislocation motion [Das *et al.* (1992)]. The reaction zone of the Ti-24Al-17Nb-0.66Mo, Ti-24Al-17Nb-1.1Mo and Ti-24Al-17Nb-2.3Mo MMCs was likely to behave in a similar manner. It was therefore expected that the pileup of dislocations resulted in a stress concentration, which accounted for the cracking observed at the fiber/matrix interface of each MMC.

A constant n value was associated with each MMC composition. The Ultra SCS-6/Ti-24Al-17Nb-0.66Mo, Ultra SCS-6/Ti-24Al-17Nb-1.1Mo, and Ultra SCS-6/Ti-24Al-17Nb-2.3Mo MMCs exhibited creep exponent values of 1.5, 1.4, and 1.5, respectively. The applied stress ranged from 10 MPa – 75 MPa, depending on the MMC composition. These n values were lower than those obtained for the respective alloy compositions (n = 1.8 for the Ti-24Al-17Nb-0.66Mo alloy and n = 2.0 for the Ti-24Al-17Nb-2.3Mo alloy). An apparent activation energy of 80 kJ/mol was calculated for the Ultra SCS-6/Ti-24Al-17Nb-0.66Mo MMC over a temperature range of 670°C – 710°C and at a stress of 10 MPa. The apparent activation energy of the Ultra SCS-6/Ti-24Al-17Nb-1.1Mo MMC over a temperature range of 650°C – 710°C and at an applied stress of 30 MPa was 126 kJ/mol. The matrix of the MMCs was expected to deform in a manner similar to that observed for the respective alloy compositions, where in the lower stress regime grain boundary sliding was suggested to be dominant. However, SEM observations suggest that transgranular cracking was evident, which accounts for the higher creep strain rates observed for the MMCs over that of the alloys and hence, the poorer creep resistance. Therefore, by reducing the number of stress risers, which result in the formation of transgranular cracks, improvements in creep resistance can be expected.

5. Creep Modeling

5.1 The Modified Crossman Model

Analytical modeling provides a means to estimate the transverse MMC creep response from the creep behavior of the matrix alloy. In a finite element model, the stress that the matrix is subjected to in the 90°-oriented MMC can be represented by:

$$\sigma_{modified} = \sigma_{applied} \cdot \exp(-\eta \cdot V) \tag{5.2}$$

where V is the fiber volume fraction, $\sigma_{applied}$ is the applied stress on the MMC, and η is a bonding factor ranging from -2.0 (no bond strength or in the debonded condition) to 1.4 (infinite bond strength or in the bonded condition) [Crossman *et al.* (1974)]. Given that secondary creep can be represented by the power-law relationship between strain rate and stress:

$$\frac{d\varepsilon}{dt} = A\sigma^n \tag{5.3}$$

Majumdar has shown that substitution of the modified stress in equation (5.2) into equation (5.3) results in a representation of the MMC secondary creep rate:

$$\dot{\varepsilon}_{MMC} = \dot{\varepsilon}_{Matrix} \cdot \exp\left(-\eta \cdot V \cdot n\right) \tag{5.4}$$

where $\dot{\varepsilon}_{MMC}$ and $\dot{\varepsilon}_{Matrix}$ are the MMC and matrix alloy secondary creep strain rates, respectively [Majumdar (1997)]. This MMC creep model suggests that the MMC secondary creep rate is based on the matrix creep rate, fiber volume fraction, and bonding factor. An example of this model is provided in Figure 5.4, where n = 3 and V = 0.35. When η = 1.4, the MMC secondary creep strain rate is lower than that of the alloy. For η = -2.0, higher secondary creep strain rates are expected in the MMC compared to that

of the alloy. It is suggested that the transition between the infinite bond strength ($\eta = 1.4$) and zero bond strength ($\eta = -2.0$) conditions occurs at a finite bond strength. In Figure 5.4, this bond strength value is arbitrarily designated as 150 MPa, as shown with a solid line transition at $\sigma = 100$ MPa (assuming a stress concentration factor of 1.5). This model has been used to represent the transverse creep resistance of a SCS-6/Ti-6Al-4V (wt.%) MMC where for applied stresses below the fiber-matrix bond strength the MMC exhibited lower secondary creep rates than the matrix alloy, and for applied stresses greater than the bond strength the MMC exhibited greater secondary creep rates than the matrix alloy [Miracle and Majumdar (1999)].

Application of this modified Crossman model to the data in this study is given in Figures 5.5 (a) and 5.5 (b). Using the debonded condition, the model predicted the secondary creep rates of the MMC quite well. As discussed by Miracle and Majumdar [Miracle and Majumdar (1999)], the stress singularity at the free surface needs to be avoided in order to achieve MMC secondary creep rates lower than those for the matrix alloy. Previous studies have shown that when fibers intersect a free surface a tensile stress singularity arises at the fiber/matrix interface due to thermal loading (i.e. residual stresses) [Kurtz and Pagano (1991), Warrier *et al.* (1996a)].

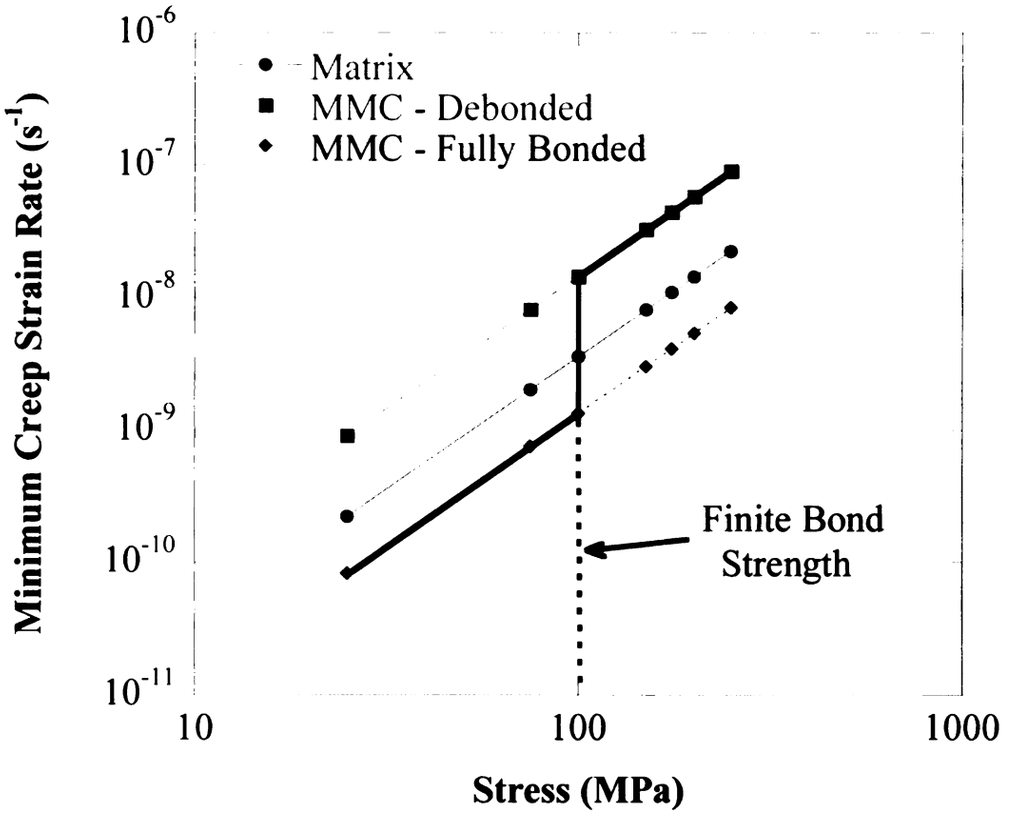

Figure 5.4 A depiction of the model designed by Majumdar [Majumdar (1997)] to describe the creep response of a MMC based upon the creep response of the matrix and the fiber/matrix bond strength.

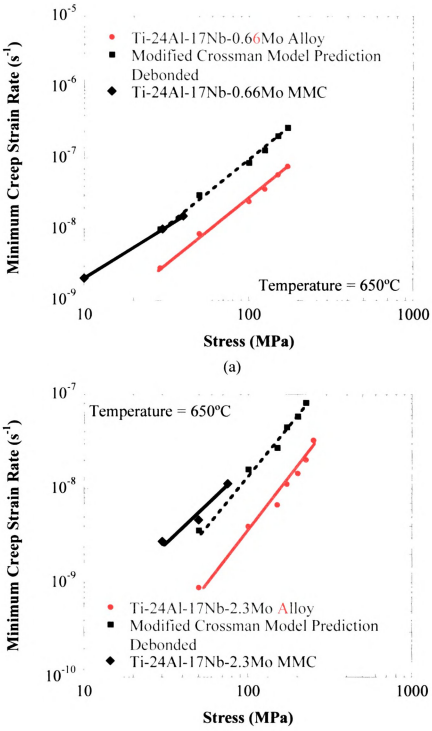

Figure 5.5 Creep Rate versus applied stress plot for the 90º MMCs and their alloys: (a) Ti-24Al-17Nb-0.66Mo and Ultra SCS-6/Ti-24Al-17Nb-0.66Mo and (b) Ti-24Al-17Nb-2.3Mo and Ultra SCS-6/Ti-24Al-17Nb-2.3Mo. The MMC data was in reasonable agreement with that predicted by the modified Crossman model [Majumdar (1997)] using the debonded assumptions.

The local interface stresses at the sample edges, due to residual stresses, are large enough to result in premature fiber/matrix separation. However, the radial residual stress at the interface changes from tensile at the edges to compressive away from the edge, and therefore damage to the interface integrity is not likely to extend much further than about one fiber radius into the sample [Miracle and Majumdar (1999)]. Upon loading though, a tensile stress concentration is also produced at exposed fiber ends. This creates a greater tensile singularity at the free edges, which in turn provides a driving force for crack propagation. Upon reaching stresses large enough to overcome the radial residual stress the singularity becomes unstable, extending the crack into the composite [Miracle and Majumdar (1999)]. It has been shown that debonding initiates at this stress singularity [Tandon *et al.* (1997)].

In the work performed by Miracle and Majumdar they avoided this stress singularity by embedding the fiber edges within the matrix, and this resulted in obtaining one data point where the secondary creep rate of the MMC was lower than that of the matrix alloy [Miracle and Majumdar (1999)]. No embedded fiber specimens were manufactured in the current work, and the MMC samples always exhibited secondary creep rates greater than the matrix alloys even at applied stresses as low as 10 MPa.

5.2 Bond Strength Determination

The fiber/matrix interfacial bond strength measurements were obtained through RT tensile testing of cruciform-geometry samples oriented with the fibers perpendicular to the loading direction. Previous work has shown that debonding events are correlated to the onset of nonlinearity in the stress-strain curves [Boehlert *et al.* (2001), Gundel *et*

al. (1995), Gundel and Miracle (1998), Gundel *et al.* (1997)]. This deviation in slope was shown in Figure 4.43 (p.161), where one experiment for each MMC composition is depicted. Through the use of an incremental slope method, which used the Pearson product moment correlation, the error in determining where a debond event occurs is minimized [Boehlert *et al.* (2001), Pearson (1896)]. The average local applied stress values at the onset of nonlinearity were 98.5 ± 12.0 MPa, 158.3 ± 32.3 MPa, and 105.8 ± 22.2 MPa for the Ultra SCS-6/Ti-24Al-17Nb-0.66Mo, Ultra SCS-6/Ti-24Al-17Nb-1.1Mo, and Ultra SCS-6/Ti-24Al-17Nb-2.3Mo MMCs, respectively. The higher local applied stress values for Ultra SCS-6/Ti-24Al-17Nb-1.1Mo may be partially attributed to the slightly different temperature and pressure used during the HIP procedure as mentioned in the experimental procedures section.

Finite element modeling was performed in ABAQUS to gain an understanding of the stress state in the cruciform geometry samples. The portion of the specimen modeled is shown in Figure 5.6. The modeled specimen was designed to have an applied stress of one. The resulting contour plots showing the von Mises stress distribution are given in Figure 5.7 for the horizontal axis (loading direction) and Figure 5.8 for the vertical axis (perpendicular to the loading direction). These plots show that the wings of the cruciform do not sustain significant stresses in either the horizontal axis or vertical axis. Therefore, the stress concentration at the edges of the samples due to fiber exposure was avoided. The highest stress concentration was observed along the gage of the specimen near the curve of the wings, which agreed well with the failure location observed during testing. The stress state within the cruciform in the loading direction is fairly uniform around the center of the cruciform. The maximum stress in this region is approximately

0.8 times that of the far-field stress. A previous study using a similar model found the maximum stress around the center of the cruciform to be 0.95 times that of the far-field stress [Boehlert *et al.* (2001)]. The difference in values between the two models was attributed to the different materials properties and to the use of a smaller radius of curvature for the model used in this work.

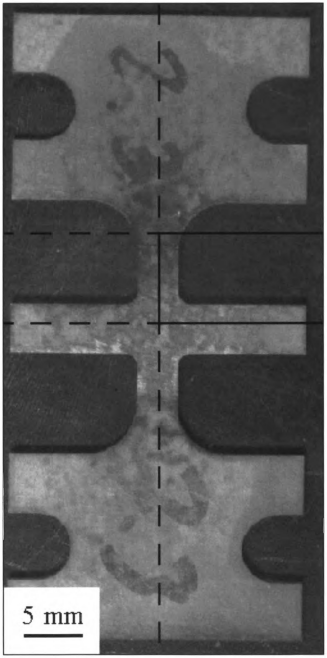

Figure 5.6 A photo of the cruciform specimen showing the section used (outlined in solid black lines) to develop the finite element model. Note that the fibers in this sample are horizontal.

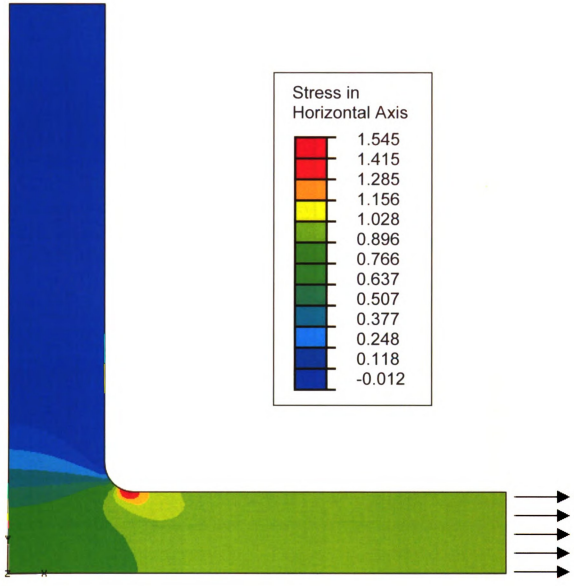

Figure 5.7 A contour plot of the cruciform sample showing the von Misses stress in the direction normal to the fiber alignment. The stress applied in the model (shown by the arrows) was equal to 1, and the corresponding concentration factors are listed based on color.

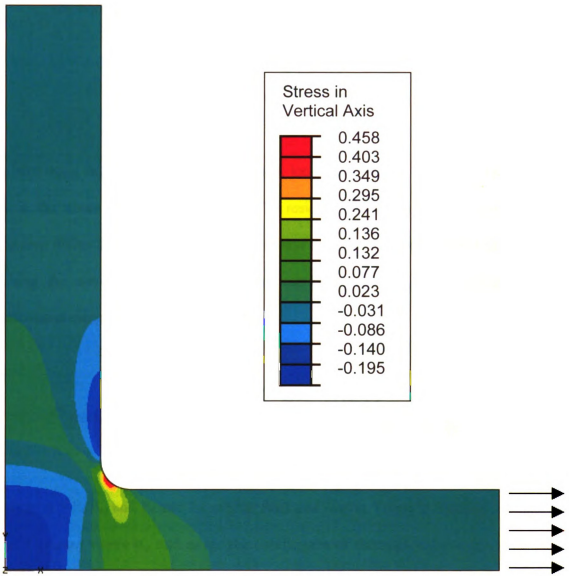

Figure 5.8 A contour plot of the cruciform sample showing the von Misses stress in the direction parallel to the fiber alignment. The stress applied in the model (shown by the arrows) was equal to 1, and the corresponding concentration factors are listed based on color.

The bond strength calculations were based on the following equation:

$$\sigma_{bond} = K\sigma_{local} + \sigma_{residual} \tag{5.5}$$

where σ_{bond}, σ_{local}, and $\sigma_{residual}$ are the bond, local, and residual stresses, respectively and K is the stress concentration factor. The residual stresses can be determined through neutron diffraction or etching experiments, and the also can be estimated using modeling. Using the concentric cylinder analysis described elsewhere, the residual stress was calculated using the following equation:

$$\sigma_{residual} = \frac{(1-V)\eta E_m \Delta\alpha\Delta T}{(1-V)(1-2\nu) - 2V\nu\eta + (1+V)\eta} \tag{5.6}$$

where $\eta = E_f/E_m$ and E_f and E_m are the fiber and matrix Young's modulus, respectively, $\Delta\alpha = (\alpha_m - \alpha_f)$ where α_m and α_f are the coefficients of thermals expansion for the matrix and fiber, respectively, ΔT is the stress free temperature minus the composite temperature, V is the fiber volume fraction, and ν is the Poisson's ratio (assumed to be identical for the fiber and matrix) [Boehlert *et al.* (2001), Hecker *et al.* (1970), Majumdar *et al.* (1998)]. The largest error in this calculation was expected to be the stress-free temperature [Boehlert *et al.* (2001)].

Equations (5.5) and (5.6) were applied to the data using a fiber volume fraction of 0.35, E_f of 390 GPa, and E_m of 110 GPa. Estimates for the remaining variables were:

$\nu = 0.25$, $\alpha_f = 4.65 \times 10^{-6}$ /°C and $\alpha_m = 10.0 \times 10^{-6}$ /°C, respectively, and $\Delta T = 800$°C. The resulting residual stress was -231.2 MPa.

The stress concentration factor (K) in Equation (5.5) was approximated using a finite element model developed in ABAQUS. A survey of the stress contour field at the fiber/matrix interface was developed. A BSE SEM image taken from a transverse cross-section of a MMC showing the area modeled is given in Figure 5.9. The stress contour plot resulting from cooling from 850°C (the aging temperature) to RT is shown in Figure 5.10. A fine mesh was used, particularly at the fiber/matrix interface. It was assumed that the fiber/matrix interface remained intact throughout the cooling process. The fiber axis (i.e. the bottom left corner) was constrained, providing a fixed origin. The x-axis (horizontal) was therefore constrained so that no displacement could occur in the y-direction, and similarly, the y-axis (vertical) was constrained so that no displacement could occur in the x-direction. The largest stress concentrations were observed near the fiber/matrix interface along the x and y axes. This was a result of the variance in coefficients of thermal expansion between the fiber and the matrix and also due to the boundary conditions established. The stress along the fiber matrix interface was integrated to determine an average stress. The radial and tangential stresses were then normalized with respect to that average stress along the interface and are presented in Figure 5.11. These stresses were determined from individual nodes at set points along the fiber matrix interface. The maximum stress concentration factor was found to be 1.23 times that of the average stress, which was comparable to that observed for other similar models [Boehlert *et al.* (2001), Gundel *et al.* (1999)].

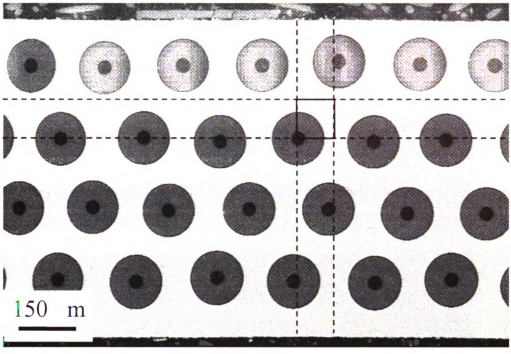

Figure 5.9 A BSE SEM photomicrograph of the MMC cross section. The square (outlined by solid black lines) depicts a typical area which the model was applied to.

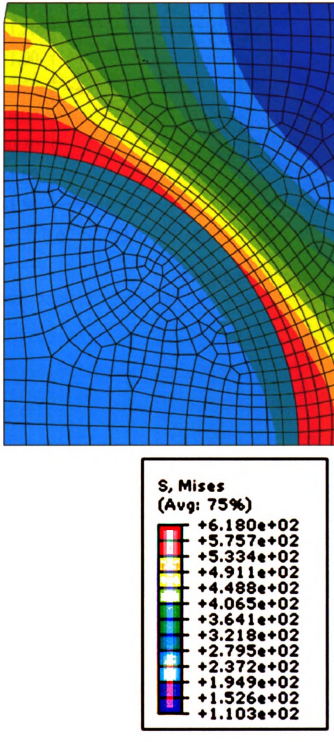

Figure 5.10 A contour stress plot showing the stress distribution resulting from heating a sample to 850ºC. The largest stress concentration occurred at the fiber-matrix interface. This suggests that debonding would preferentially occur within these regions when an applied tensile stress was imposed.

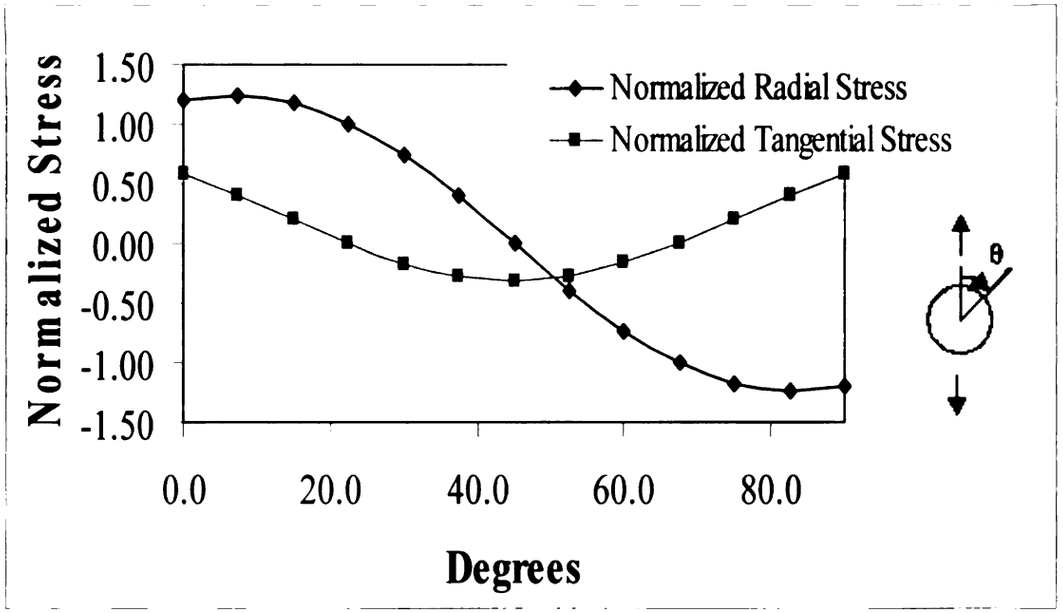

Figure 5.11 A plot of the tangential and normal stresses at the fiber/matrix interface occurring at various angles of the fiber. The largest normal stress was at 45° while the largest tangential stress was at approximately 83°.

The bond strengths were calculated and are provided in Table 5.II. Each of the MMCs exhibited a negative bond stress value. Although a negative bond strength does not have a physical meaning, the results suggest that each of the MMCs examined exhibited weak interfacial strengths. Thus, very low applied stresses would be expected to result in interfacial debonding. As shown, the bond strength for the Ultra SCS-6/Ti-24Al-17Nb-1.1Mo MMC was close to zero. This MMC exhibited the greatest stress at the onset of non-linearity for the cruciform tested samples. The greater bond strength of this MMC may have been partially related to the slightly different HIP pressure and temperature used as described in the experimental procedures section.

Table 5.II Interfacial bond strengths of the MMCs

MMC Composition	Interface bond Strengths (MPa)
Ultra SCS-6/Ti-24Al-17Nb-0.66Mo	-110.0
Ultra SCS-6/Ti-24Al-17Nb-1.1Mo	-36.5
Ultra SCS-6/Ti-24Al-17Nb-2.3Mo	-101.1

Debonding occurred within the multilayer carbon coating, which was common for each MMC. This was similar to that observed for a Sigma 1240/Ti-6Al-2Sn-4Zr-2Mo (wt.%) MMC [Boehlert *et al.* (2001)]. The carbon layer cracks propagated through the reaction layer and O+BCC depleted layer but were blunted by the BCC phase. The fracture always occurred in the uniform width section of the cruciform close to the fillet, due to the stress singularity, as similarly observed in the Sigma 1240/Ti-6Al-2Sn-4Zr-2Mo (wt.%) MMC, where the bond strength was also estimated to be low (22 MPa) [Boehlert *et al.* (2001)]. The low bond strength value also agrees well with that measured for the Sigma-1240/7040 glass ceramic matrix composite, $\sigma_{bond} \sim 5$ MPa [Chatterjee *et al.*

(1997)], which also debonded in the carbon-coating layers. In another ceramic matrix composite, SCS-6/Si_3N_4, the interfacial strength was between 5 – 18 MPa, and the 100 nm-thick pure turbostratic carbon layer between the two outermost carbon layers was the preferred failure site [Morscher *et al.* (1990)]. In addition, the interface strength of a Trimarc 1/Ti-6Al-4V (wt.%) MMC was estimated to be 40 MPa [Warrier *et al.* (1997)]. Failure within the carbon layers has also been observed for a transversely loaded SCS-6/Ti-6Al-4Zr-2Mo (wt.%) MMC containing 32 volume percent fibers and Sigma-1140/Ti-6Al-4V (wt.%) MMCs containing fiber volume percents of 8 percent and 21 percent [Hall and Ritter (1993), Wu *et at.* (2001), Wu *et al.* (2001a)]. Thus, the carbon-coating multi-layers appear to be the weakest link in the fiber-matrix interface for SiC fibers, and the low interfacial bond strengths estimated for the MMCs in this study are in good agreement with those for other SiC fiber-based MMCs. Due to the low fiber-matrix interface strength of this MMC system, a transition in the secondary creep rates of the MMC to values below those of the matrix alloy would not be expected even for any practical loading applications.

C. Tensile Behavior Discussion

1. Alloy Tensile Behavior

Previous studies have indicated that low ε_f values of the α_2 phase were due to the anisotropy of slip associated with DO_{19} crystal structure [Koss *et al.* (1990)]. While <a> slip occurs relatively easy on the prism plane, <c+a/2> slip is very difficult, and therefore large incompatibility stresses build up at α_2/α_2 interfaces [Smith *et al.* (1995)]. On the other hand, the O phase has displayed significantly more <c+a/2> slip than the α_2 phase [Koss *et al.* (1990)]. In this work, low ε_f values were exhibited for the alloys and MMCs.

The Young's moduli of the Ti-24Al-17Nb-0.66Mo AP and HT microstructures were 108 and 101 GPa, respectively. The moduli for the AP and HT Ti-24Al-17Nb-2.3Mo microstructures were 125 and 128 GPa, respectively. Thus, small Mo additions increase the Young's modulus. The RT ε_f values for the AP and HT alloys were less than 1.2%, as shown in Figure 4.48 (p.168). The Young's moduli for the HT Ti-24Al-17Nb-0.66Mo and Ti-24Al-17Nb-2.3Mo samples tested at 650°C were 80 GPa and 92 GPa, respectively. At 650°C, the ε_f values for Ti-24Al-17Nb-0.66Mo exceed 3.5%, while the ε_f value for the Ti-24Al-17Nb-2.3Mo remained less than 1%, as shown in Figure 4.48. Thus, the addition of 2.3Mo appears to embrittle the Ti-24Al-17Nb alloy. This is expected to be a large reason why the Ti-24Al-17Nb-0.66Mo alloy reached slightly greater tensile strengths than the Ti-24Al-17Nb-2.3Mo material. Thus, even though the Ti-24Al-17Nb-2.3Mo alloy exhibited lower α_2-phase volume fractions, the additional Mo in solid solution appears to embrittle the material, resulting in lower ε_f values than the Ti-24Al-17Nb-0.66Mo microstructures containing more α_2-phase volume fractions.

Deformation of the O phase has been observed to involve slip along both <a> (<110> and <100> type) and <c+a> (<114> type) directions [Banerjee *et al.* (1991)]. The existence of the <c+a> slip system along with the presence of ductile BCC phase adjacent to the O phase laths serve to help prevent cracking of the O phase. The dominant slip vector of the BCC phase, <111>, is parallel to one of the dominant slip vectors in the O-phase, <110> [Majumdar *et al.* (1995)]. This relationship alleviates the stress concentration effects allowing the transmission of planar slip in the O phase into the BCC phase where slip at the boundary interfaces can occur much more easily. Therefore, a microstructure consisting of lath O phase within a BCC matrix is capable of obtaining attractive RT fracture toughness and ductility.

At RT, there were no discernable differences among the fracture surfaces of the AP and HT Ti-24Al-17Nb-0.66Mo and AP and HT Ti-24Al-17Nb-2.3Mo alloys. Each of the fracture surfaces were flat and intergranular suggesting brittle failure, which corresponded well with the low ε_f values. At 650°C, some ductile dimpling was apparent in the HT Ti-24Al-17Nb-0.66Mo alloy fracture surface. The HT Ti-24Al-17Nb-2.3Mo alloy fracture surface appeared similar to those tested at RT. Therefore, this suggests that higher contents of Mo resulted in solid-solution strengthening and embrittled the alloy.

2. Metal Matrix Composite Tensile Behavior

Tensile testing of the Ti-24Al-17Nb-0.66Mo and Ti-24Al-17Nb-2.3Mo alloys showed that the ε_f at room temperature was quite low (less than 1.2%). Due to the coefficient of thermal expansion mismatch between the fiber and matrix, the matrix should have an ε_f value of 2.5% or higher in order to overcome the compressive residual

stress in the fiber and to effectively load the fiber [Amato and Pank (1992)]. Therefore, since the ε_f of the alloys is below this minimum value it was expected that incomplete loading of the fibers was observed prior to fracture of the MMC. Using the rule of mixtures, the expected Young's moduli and ultimate tensile strengths were calculated and compared to the experimentally obtained values in Table 5.III and Table 5.IV, respectively.

The Young's modulus was calculated using:

$$E_c = E_m(1-V_f) + V_fE_f \tag{5.7}$$

where E_c is the calculated composite Young's modulus, E_m and E_f are the Young's moduli of the matrix and fiber, respectively, and V_f is the fiber volume fraction. The composite UTS was calculated using:

$$\sigma_c = \sigma_m(1-V_f) + \sigma_fV_f \tag{5.8}$$

where σ_c is the calculated UTS and σ_m and σ_f are the UTS values of the matrix and the fiber. The values for E_m and σ_m were taken from the tensile data of the alloys tested, and the fiber volume fraction was considered to be 0.35, the fiber modulus was estimated to be 415 GPa, and the fiber strength was estimated to be 6,380 MPa at RT and 5,550 MPa at 650°C [Specialty Materials, Chaerjee *et al.* (1997)]. Temperature effects on the fiber modulus were not accounted for as the author was not able to find such effects in the literature. However, decreases in modulus and UTS were expected at higher temperatures.

Table 5.III Rule-of-mixtures comparison to experimental Young's modulus values

Material	Condition	Test Condition	R.O.M. E (GPa)	Experimental E (GPa)
Ultra SCS-6/Ti-24Al-17Nb-0.66Mo	AP	RT	216	211
Ultra SCS-6/Ti-24Al-17Nb-0.66Mo	HT	RT	211	205
Ultra SCS-6/Ti-24Al-17Nb-0.66Mo	HT	650°C	197	157
Ultra SCS-6/Ti-24Al-17Nb-2.3Mo	AP	RT	227	205
Ultra SCS-6/Ti-24Al-17Nb-2.3Mo	HT	RT	229	214
Ultra SCS-6/Ti-24Al-17Nb-2.3Mo	HT	650°C	205	147

Table 5.IV Rule-of-mixtures comparison to experimental UTS values

Material	Condition	Test Condition	R.O.M. UTS (MPa)	Experimental UTS (MPa)
Ultra SCS-6/Ti-24Al-17Nb-0.66Mo	AP	RT	2971	1332
Ultra SCS-6/Ti-24Al-17Nb-0.66Mo	HT	RT	2975	1483
Ultra SCS-6/Ti-24Al-17Nb-0.66Mo	HT	650°C	2529	1403
Ultra SCS-6/Ti-24Al-17Nb-2.3Mo	AP	RT	2855	775
Ultra SCS-6/Ti-24Al-17Nb-2.3Mo	HT	RT	2714	949
Ultra SCS-6/Ti-24Al-17Nb-2.3Mo	HT	650°C	2492	1214

The comparison of values indicates that the rule-of-mixture Young's modulus and UTS values were not met. The largest discrepancy of Young's modulus was observed for the samples tested at 650°C, where the difference between the rule-of-mixtures estimation and the achieved values were 40 GPa and 58 GPa for the HT Ti-24Al-17Nb-0.66Mo and HT Ti-24Al-17Nb-2.3Mo MMCs, respectively. All of the UTS values calculated using the rule-of-mixtures were significantly higher than those found experimentally. The experimental UTS values for the Ti-24Al-17Nb-0.66Mo alloy were approximately half that of the rule-of-mixture values, while an even greater disagreement was evident for the Ti-24Al-17Nb-2.3Mo alloy, where the experimentally determined UTS for the AP alloy tested at RT was less than three times that of the rule-of-mixtures approximation. The failure of the composites to reach the rule-of-mixture estimations was attributed to the

incomplete loading of the fibers, likely resulting from poor load sharing due to weak interfacial bond strengths, as discussed in the previous section of this chapter.

The fracture surfaces of the MMCs tested at RT were mostly planar. The matrix fracture surface appeared similar to that observed for the respective alloy tensile tests. The fiber fractures were localized near the fracture plane. This observation does not agree well with what is expected for load-sharing behavior, where fiber pull-out would be prevalent. Debonding of the fiber/matrix interface was apparent, but it was not certain whether the debonding occurred due to opening (i.e. mode I fracture) or due to sliding (i.e. mode II fracture). The fracture surfaces of the HT Ti-24Al-17Nb-2.3Mo MMCs tested at 650°C appeared similar to those tested at RT. However, the HT Ti-24Al-17Nb-0.66Mo MMC fracture surface was less planar, exhibiting greater amounts of fiber pull-out, which suggested that local load-sharing occurred. This observation is shown in Figure 5.12, comparing the HT Ti-24Al-17Nb-0.66Mo MMC fracture surface tested at 650°C to that of the Ti-24Al-17Nb-2.3Mo MMC. Furthermore, the matrix of the HT Ti-24Al-17Nb-0.66Mo MMC exhibited a greater amount of ductile dimpling that the fracture surface of the Ti-24Al-17Nb-0.66Mo alloy tested at 650°C.

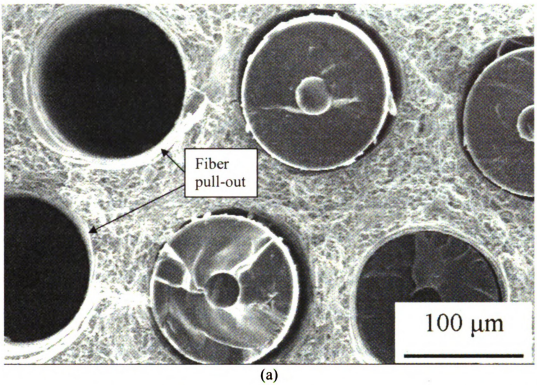

(a)

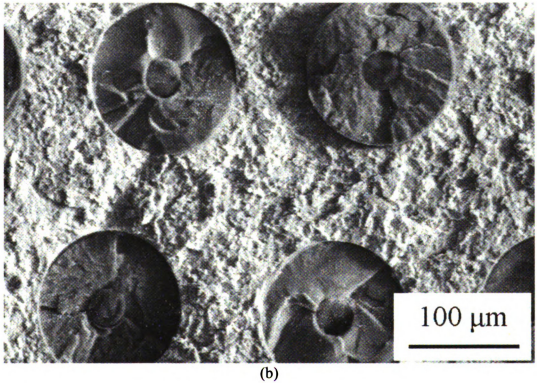

(b)

Figure 5.12 Fracture surface secondary electron SEM images of the (a) Ti-24Al-17Nb-0.66Mo and (b) Ti-24Al-17Nb-2.3Mo MMCs.

D. Out-of-Phase Thermomechanical Fatigue Discussion

The OOP TMF behavior of each MMC was analyzed. Overall, the Ultra SCS-6/Ti-24Al-17Nb-0.66Mo MMC exhibited longer fatigue lives than that of the Ultra SCS-6/Ti-24Al-17Nb-1.1Mo and Ultra SCS-6/Ti-24Al-17Nb-2.3Mo MMCs at most of the stress conditions examined. The total strain versus time plots (Figure 4.62 – Figure 4.64 on pp.191-193) from these OOP TMF experiments provided useful information about the MMC response and damage mechanisms. Similar to creep, these curves could be separated into three regimes. The primary regime consisted of the strain placed on the material during the first few cycles and is noted by a decreasing strain rate. The second regime was distinguished by a constant increase in strain over time. During this stage the strain at maximum stress (minimum temperature) increased at the same rate as the strain at minimum stress (maximum temperature), which has been suggested to imply inelastic deformation [Russ *et al.* (1994)]. This appeared to indicate accumulated creep strain in the matrix (assuming the fibers do not creep at these temperatures) [Russ *et al.* (1994)]. The start third regime is noted by an increase in the strain over time of the maximum load, minimum temperature curve, where this curve begins to converge upon the strain curve of minimum load, maximum temperature. At this point, the damage mechanism is suggested to transition from creep-dominated to fatigue-dominated. Therefore, the remaining cycles-to-failure are dependent on the fatigue resistance of the matrix.

For the MMCs in this work, it was expected that the Ultra SCS-6/Ti-24Al-17Nb-2.3Mo MMC would be able to sustain a greater number of cycles in the first and second regimes compared to that of the Ultra SCS-6/Ti-24Al-17Nb-0.66Mo and Ultra SCS-6/Ti-24Al-17Nb-1.1Mo MMCs based on the greater primary and secondary stage creep

resistance of the Ti-24Al-17Nb-2.3Mo alloy over that of the Ti-24Al-17Nb-0.66 and Ti-24Al-17Nb-1.1Mo alloys. However, based on the greater ε_f values of the Ti-24Al-17Nb-0.66Mo alloy compared to that of the Ti-24Al-17Nb-2.3Mo alloy, the resistance to crack propagation in the third regime was expected to be greater for the Ultra SCS-6/Ti-24Al-17Nb-0.66Mo MMC compared to that of the Ultra SCS-6/Ti-24Al-17Nb-1.1Mo and Ultra SCS-6/Ti-24Al-17Nb-2.3Mo MMCs. This is believed to be the reason for the increased number of cycles-to-failure for the Ultra SCS-6/Ti-24Al-17Nb-0.66Mo MMC within the intermediate applied stress range. This also can explain why the Ultra SCS-6/Ti-24Al-17Nb-2.3Mo MMC exhibited the greatest number of cycles in the lowest applied stress regime. These competing processes therefore justify the higher number of cycles-to-failure observed for the Ultra SCS-6/Ti-24Al-17Nb-0.66Mo and Ultra SCS-6/Ti-24Al-17Nb-2.3Mo MMCs over that of the Ultra SCS-6/Ti-24Al-17Nb-1.1Mo MMC. While no tensile testing was performed on the Ti-24Al-17Nb-1.1Mo alloy, the increase in average equiaxed grain size of this microstructure may suggest poorer ε_f than that observed for the Ti-24Al-17Nb-0.66Mo and Ti-24Al-17Nb-2.3Mo alloys.

Each of the fractured matrices within the failed MMCs exhibited a faceted/granular type fracture. Similar fracture surfaces were observed for a SCS-6/Ti-24Al-11Nb MMC OOP TMF tested at temperature ranging between 150°C – 650°C [Russ *et al.* (1991)]. These surface failures suggest that failure occurred at lower temperatures and higher loads, where the matrix was less ductile. Failure at low temperatures was more likely due to the higher tensile load on the matrix at low temperatures, as was described in Chapter 2. OOP TMF failures of Ti-Al-Nb-based MMCs have primarily involved extensive cracking initiating at the surface and edges of

specimens [Russ *et al.* (1991)]. Fracture surfaces of the matrix overload region tended to be smooth and granular, lacking ductile dimpling [Russ *et al.* (1991), Russ *et al.* (1995)]. In these studies, the lack of fiber pull-out observed in OOP TMF failures of Ti-Al-Nb-based MMCs indicated that fiber bridging did not occur and that the fibers broke in the crack plane as the crack tip progressed through the composite [Russ *et al.* (1991)].

The microstructures revealed that cracks initiated both along the edges of the sample and from within the cross-section of the sample. Both intergranular and transgranular crack propagation was observed, however the majority of cracks were transgranular. During creep deformation transgranular cracking was only apparent along the surface, where oxidation-assisted cracking was likely to affect the deformation. Therefore the crack formation during OOP TMF testing was likely affected by environmentally-assisted cracking occurring due to localized creep deformation. The evidence also suggested that the cracks were formed and propagated due to the thermal and mechanical loadings placed on the materials. Oxygen-related matrix embrittlement along with solid-solution embrittlement have been previously shown to have a detrimental effect on the fatigue lives of the alloys [Brindley *et al.* (1995), Brindley *et al.* (1995a), Cerchiara *et al.* (1995)].

CHAPTER 6

SUMMARY AND CONCLUSIONS

A. Summary

This dissertation comprised of a systematic study dealing with several aspects of the physical and mechanical metallurgy of Ti-Al-Nb-Mo alloys and MMCs intended for use in high temperature structural applications. Varying the Mo content, two different alloy compositions and three different MMC compositions were evaluated. The alloys and matrices in this study had a composition of Ti-24Al-17Nb-xMo (x = 0.66, 1.1, or 2.3). While previous studies have looked at Ti-Al-Nb-Mo alloys, no work had been done to determine the sole effect Mo has on the microstructure/mechanical property relationships. Of these studies, only two have evaluated at Ti-24Al-17Nb-xMo alloys, where Rowe investigated the tensile properties of Ti-24Al-17Nb-0.5Mo and Ti-24Al-17Nb-1Mo alloys [Rowe (1992)] and Kristnamurthy and coworkers evaluated the tensile and creep properties of a Ti-24.5Al-17Nb-1Mo alloy [Krishnamurthy *et al.* (1995)]. Through peer-edited scientific publications the work performed in this dissertation has been made available in the literature, presenting data that had been previously non-existent. The main focus of this work was on the microstructural characterization and the microstructure-creep property relationship of the alloys and MMCs, where an effort was made to establish a model used to predict the MMC creep response based on the alloy creep behavior and the bond strength between the fiber and the matrix. An evaluation of the tensile and OOP TMF behavior and the microstructural affect on these properties was also determined.

Ti-Al-Nb-Mo powders were tape cast and HIPed to produce the alloys and MMCs evaluated in this work. A subtransus heat treatment was used to produce microstructures consisting of the α_2 phase, O phase, and BCC phase. The heat treatment resulted in microstructures containing lower α_2-phase volume percents than that of the AP condition. Similarly, increasing amounts of Mo were shown to decrease the α_2-phase volume percents and correspondingly increase the O+BCC-phase volume percents for the alloys and MMCs. The varying Mo contents also affected the average equiaxed grain size of the α_2 phase and the O+BCC colony size, where larger Mo additions increased the O+BCC colony (prior BCC phase) size and resulted in a decrease in the α_2-phase grain size.

Microprobe data revealed that the highest Mo contents were present within the BCC phase, whereas the α_2 phase contained the smallest Mo contents, though increasing the bulk alloy Mo content resulted in increasing levels of Mo in the α_2 and BCC phases. An intermediate amount of Mo was observed in O phase. The BCC transus temperatures were found to be larger than that predicted from the phase diagram, which was attributed to the high amounts of oxygen present within the alloys.

Based on the creep exponents and apparent activation energies two dominant creep deformations were suggested for the alloys. At lower applied stress levels, n values ranged from 1.8 to 2.0, and Q_{app} ranged from 129 – 229 kJ/mol. At 650°C, grain boundary sliding was suggested to be the dominant deformation mechanism. *In-situ* tensile-creep testing conducted in this regime revealed that the equiaxed α_2 grain boundaries were the locus of deformation in the alloys. The interior of the grains showed little deformation, suggesting that the creep strain accumulation was caused by the sliding

of grains and crack opening. Observations of the sample interior revealed significantly less deformation than that on the sample surface. Comparison of creep data from tests conducted in air versus those tested in a vacuum revealed that environmental assisted cracking was present and attributed to increased creep rates. At higher stress levels, n values ranged from 4.6 to 4.8, suggesting dislocation climb to be the dominant deformation mechanism at 650°C.

Creep testing of the alloys revealed that the Ti-24Al-17Nb-2.3Mo alloy exhibited superior creep resistance compared with the Ti-24Al-17Nb-0.66Mo alloy. Approximately one order of magnitude difference in minimum creep rate was observed at all stresses evaluated at 650°C. Thus, small increases in Mo content significantly increased the creep behavior of Ti-Al-Nb alloys. However, a Ti-24Al-17Nb-1Mo alloy exhibited similar creep strain/time behavior as that for Ti-24Al-17Nb-2.3Mo. Thus, Mo additions greater than 1 at.% may not be necessary to further enhance the creep resistance.

The MMCs were creep tested with fibers perpendicular to the loading direction. In this orientation the failure mechanism was matrix dominated. Testing revealed the Ultra SCS-6/Ti-24Al-17Nb-2.3Mo MMC to posses greater creep resistance than the Ultra SCS-6/Ti-24Al-17Nb-0.66Mo and Ultra SCS-6/Ti-24Al-17Nb-1.1Mo MMCs. This result was attributed to the greater creep resistance of the Ti-24Al-17Nb-2.3Mo alloy compared to that of the Ti-24Al-17Nb-0.66Mo and Ti-24Al-17Nb-1.1Mo alloys. Deformation in the form of transgranular cracking was shown to dominate the failure mechanism. Cracks appeared to originate at surfaces or at fiber/matrix interfaces. These cracks propagated and were linked at fibers until one main crack overloaded and resulted

in failure. This variance in crack propagation compared to that observed for alloy creep testing resulted in lower creep lifetimes and higher creep strain rates observed for the MMCs compared with the respective alloy compositions.

A model was developed to predict the MMC creep behavior based on the alloy creep response and the bond strength between the fiber and the matrix. The model predicted the secondary creep rates of the MMCs well for a condition assuming no bond strength between the fiber and matrix. While the model was suggested to show a transition in secondary creep rates for the MMC from a higher strain rate than the alloy to a lower strain rate than the alloy, no such transition was observed in the experimental data. This transition was predicted to occur at an applied creep stress equal to the bond strength between the fiber and the matrix. Experimental bond strength determinations were made through the use of cruciform-shaped specimens tensile tested at RT to determine the localized bond strength along with a model developed in ABAQUS to predict the residual stresses at the fiber/matrix interface. The residual stresses developed during the cool down from high temperature processing due to the coefficient of thermal expansion mismatch between the fiber and the matrix. The calculations of the bond strength suggested that the fiber/matrix interfaces were weak. The weak interfaces were responsible for the lack of crossover in secondary creep rates to a condition in which the creep rate of the MMC is less than that of the alloy for practical loading conditions (i.e. greater than 10 MPa). The failure point at the fiber/matrix interface was found to be within the outermost carbon-containing layers of the fibers, suggesting these were the weakest link in the interface. This has been commonly observed elsewhere in the literature for MMCs.

RT tensile testing of the alloys revealed low ε_f values for both alloy compositions (less than 1.5%). At 650°C, the ε_f of the Ti-24Al-17Nb-0.66Mo alloy increased to greater than 3.5%, however this trend was not observed for the Ti-24Al-17Nb-2.3Mo alloy, which did not show any significantly increase in the ε_f. Ideally, the RT ε_f values would be greater than 2.5% so the matrix could overcome the residual stresses to effectively load the fibers. Since such ε_f values were not achieved, the rule-of-mixture calculations for the UTS and Young's moduli values of the MMCs predicted higher values than those obtained experimentally. The fracture surfaces of the alloys were granular, suggestive of a brittle failure. The tensile curves showed that addition of 2.3Mo to the Ti-Al-Nb alloys resulted in less plastic deformation, which indicates that the Mo addition served as an effective solid solution strengthener but also as an embrittling agent. The fracture surfaces of the MMCs were mostly planar, which signifies global load-sharing within the fibers was not fully achieved.

The OOP TMF results of the MMCs indicated that the Ultra SCS-6/Ti-24Al-17Nb-1.1Mo MMC exhibited the fewest cycles-to-failure at all stress conditions tested. The deformation within the microstructures was comprised of a creep-dominated mechanism followed by a fatigue-dominated mechanism. For the creep-dominated mechanism, the most cycles-to-failure were expected for the Ultra SCS-6/Ti-24Al-17Nb-2.3Mo MMC due to the exceptional creep resistance exhibited by this matrix alloy. For the fatigue dominated mechanism, the most cycles-to-failure were expected with the Ultra SCS-6/Ti-24Al-17Nb-0.66Mo MMC due to the matrix alloy exhibiting the greatest elongation-to-failure. The results showed that the Ultra SCS-6/Ti-24Al-17Nb-0.66Mo MMC achieved the greatest fatigue lives at the intermediate applied stress levels (fatigue

dominated) and Ultra SCS-6/Ti-24Al-17Nb-2.3Mo MMC achieved the greatest fatigue lives at the lowest applied stress levels (creep dominated).

B. Conclusions

1. Microstructure

1. The subtransus heat treatment produced microstructures containing the α_2, O, and BCC phases. The α_2 phase was equiaxed, while the O phase precipitated out in a lath morphology from prior equiaxed BCC grains. The differences in Mo contents resulted in variances in average equiaxed grain size of the α_2 phase and O+BCC colonies.

2. The addition of 2.3Mo to the Ti-Al-Nb alloys resulted in smaller O phase lath thicknesses compared to that observed with 0.66Mo additions, which was due to the slow diffusion kinetics of Mo.

3. The highest Mo content was found in the BCC phase, which was 1.5 at.% in the Ti-24Al-17Nb-0.66Mo alloy and 2.6 at.% in the Ti-24Al-17Nb-2.3Mo alloy. The lowest Mo content was found in the α_2 phase, having only 0.1 at.% in the Ti-24Al-17Nb-0.66Mo alloy and 0.5 at.% in the Ti-24Al-17Nb-2.3Mo alloy.

4. The bulk of the matrix microstructure in the MMCs appeared similar to the respective alloy microstructures. Near the fiber/matrix interface the microstructure was depleted of the O+BCC phases and enriched in α_2 phase due to carbon diffusion from the fiber during fabrication. The carbon diffusion also resulted in the formation of complex carbides in a reaction zone between the fiber and matrix.

2. Creep Behavior

1. The Ti-24Al-17Nb-2.3Mo alloy exhibited greater creep resistance than the Ti-24Al-17Nb-0.66Mo alloy. This was attributed to the decrease in the number of α_2/α_2 grain boundaries, increased O+BCC colony size, and Mo solid solution strengthening effects. However, the sole affect of Mo on the creep behavior was not determined as there existed both a microstructural difference caused by Mo affecting the phase volume fractions and grain sizes as well as a solid-solution strengthening effect.

2. Each alloy creep tested exhibit a transition in creep exponent, where grain-boundary sliding and dislocation climb were suggested to be the dominant deformation mechanisms for the lower stress and higher stress regimes, respectively.

3. *In-situ* tensile-creep testing revealed that grain boundaries were the locus of deformation accumulation, where the majority of cracking occurred at α_2/α_2 grain boundaries and α_2/O+BCC colonies.

4. Creep experiments conducted on the MMCs with the fibers oriented perpendicular to the loading direction revealed that the Ultra SCS-6/Ti-24Al-17Nb-2.3Mo MMC exhibited greater creep resistance than the Ultra SCS-6/Ti-24Al-17Nb-0.66Mo and Ultra SCS-6/Ti-24Al-17Nb-1.1Mo MMCs. However, the creep resistance of the MMCs was poorer than that of each respective alloy.

5. An attempt to model the creep behavior of the MMCs based on the creep response of the alloys and the bond strength between the fiber and the matrix was made. The model predicted the secondary creep rates of the MMCs well for a condition assuming no bond strength between the fiber and matrix.

6. Bond strength calculations revealed a low interfacial bond strength between the matrix and the fiber, suggesting that the MMC creep resistance would not be greater than the matrix alloy under practical loading applications. Failure at the fiber/matrix interface took place within the outer carbon-containing layers of the fiber.

3. Tensile Behavior

1. The Ti-24Al-17Nb-0.66Mo alloy exhibited higher RT ε_f values than the Ti-24Al - 17Nb-2.3Mo alloy, but neither had an ε_f greater than 1.2%. Little plastic deformation was observed for the Ti-24Al-17Nb-2.3Mo alloy, suggesting the solid solution strengthening effects of Mo in this alloy limit dislocation motion.

2. The low ε_f values of the matrices limited the ability of the MMCs to effectively load the fiber. As a result, experimental UTS and Young's moduli values fell below that predicted by the rule-of-mixtures.

3. At 650°C,the Ti-24Al-17Nb-0.66Mo alloy exhibited ε_f values greater than 3.5%, whereas the Ti-24Al-17Nb-2.3Mo alloy were less than 1%, similar to that observed for tests conducted at RT.

4. Out-of-Phase Thermomechanical Fatigue Behavior

1. In general, each of the MMCs exhibited similar fatigue responses at all the stress conditions examined. It was apparent that the Ultra SCS-6/Ti-24Al-17Nb-1.1Mo MMC displayed the poorest fatigue behavior. This was attributed to the combination of poorer creep resistance of the Ti-24Al-17Nb-1.1Mo alloy versus that that of the Ti-24Al-17Nb-

2.3Mo alloy and the likely lower ductility of the Ti-24Al-17Nb-1.1Mo alloy versus that of the Ti-24Al-17Nb-0.66Mo alloy.

2. The deformation consisted of a creep-dominated mechanism followed by a fatigue-dominated mechanism. The Ultra SCS-6/Ti-24Al-17Nb-0.66Mo MMC exhibited the greatest resistance to deformation within the fatigue-dominated regime, while the Ultra SCS-6/Ti-24Al-17Nb-2.3Mo MMC exhibited the greatest resistance to deformation within the creep-dominated regime.

3. Ultra SCS-6/Ti-Al-Nb MMCs containing matrices with greater Mo contents exhibited greater OOP TMF lives at the lowest applied stress levels, while the MMCs containing matrices with the lowest Mo content exhibited the greatest OOP TMF lives at the intermediate stress levels.

C. Recommendations for Future Work

1. No attempts to optimize the mechanical properties (tensile, creep, and fatigue) through microstructural modifications of the alloys and matrices were made. A heat treatment devised to further reduce the α_2 phase volume fraction may result in higher ε_f values and increase creep resistance.

2. The atomic coordinates of the Mo within the O phase and BCC phases of the alloys was not determined. Using neutron diffraction such information can be found.

3. Creep experiments on the alloys within the higher stress regime suggested dislocation climb to be the dominate deformation mechanism. The arrangement and interactions of dislocations within each phase would provide evidence and possibly verify the suggested deformation mechanisms.

4. Further analysis of the residual stresses at the fiber/matrix interface is warranted. In this study, the residual stress was estimated using a simple concentric cylinder model [Hecker *et al.* (1970), Majumdar *et al.* (1998)]. Experimental determination of the residual stresses would lead to a more accurate determination of the bond strength between the fiber and matrix. Ideally, a diffraction technique, such as x-ray or neutron diffraction, could be used to determine the amount of strain on a set of planes (noted by a shift in angle of a diffracted peak). Using elastic theory, the strain could be converted to a residual stress measurement.

5. To determine the factors causing the low interfacial bond strength, a deeper assessment of the cracking mechanisms is necessary. A special emphasis on the debond cracks within carbon layers of the fiber could provide insight on possible ways to improve the bond strength.

BIBLIOGRAPHY

Akkurt A.S., Liu G., and Bond G.M., *Mat. Res. Soc. Symp. Proc.*, **213** 455-460 (1991).

Albert D.E. and Thompson A.W., *Metall. Trans. A*, **23** 3035-3043 (1992).

Altan T., Oh S., and Gegel H.L., Metal Forming: Fundamentals and Applications, American Society for Metals, Metal Parks, OH (1983).

Amato R.A. and Pank D.R., *Titanium Matrix Composites*, WL-TR-92-4035, Wright-Patterson Air Force Base, OH 80-97 (1992).

Ankem S. and Seagle S.R., Beta Titanium Alloys in the 1980's, R.R. Boyer, H.W. Rosenberg (Eds.), Atlanta, 107-126 (1983).

Appel F., and Oehring M., *Titanium and Titanium Alloys*, Edited by Leyens C. and Peters M., Wiley-VCH Verlag, Weinheim, Germany, (2003).

Arsenault R.J., Composites, **25** 540-548 (1994).

Austin C.M., Dobbs J.R., Fraser H.L., Konitzer D.G., Miller D.J., Parks M.J., Schaeffer J.C., and Sears J.W., Technical Report WL-TR-93-4059, (1993).

D. Banerjee, T.K. Nandy, and A.K. Gogia, Scripta Metall. **21** 597-600 (1987).

Banerjee D., Gogia A.K., Nandy T.K., and Joshi V.A., *Acta Metall.*, **36** 871-882 (1988).

Banerjee D., Acta Metallurgica, **36** 871-882 (1989).

Banerjee D., Rowe R.G., and Hall E.L., Materials Research Society Symposium Proceedings, **213** 285-290 (1991).

Banerjee D., Gogia A.K., Nandy T.K., Muraleedharan K., and Mishra R.S., *Structural Intermetallics*, R. Daralia, J.J. Lewandowski, and C.T. Liu (Eds.), TMS, Warrendale, PA 19-33 (1993).

Banerjee D., *Intermetallic Compound*, Practice, J.H. Westbrook and R.L. Fieischer (Eds.), John Wiley & Sons Ltd., New York **2** 91-131 (1994).

Banerjee D., *Phil. Mag. A*, **72** 1559-1587 (1995).

Banerjee D., *Prog. Mater. Sci.*, **42** 135-158 (1997).

Bendersky L.A., Boettinger W.J., and Roytburd A., *Acta Metall. Mater.*, **39** 1959-1969 (1991).

Blackburn M.J. and Smith M.P., Technical Report AFML-TR-78-18 (1978).

Blackburn M.J., Ruckle D.L., and Bevan C.E., Research to Conduct an Exploratory Experimental and Analytical Investigation of Alloys, AFWAL, Wright Patterson AFB, OH, USA (1978).

Blackburn M.J. and Smith M.P., R&D on Composition and Processing of Titanium Aluminide Alloys for Turbine Engines, AFWAL, Wright-Patterson AFB, OH, USA (1982).

Blackburn M.J. and Smith M.P., Technical Report WRDC-TR-89-4095 (1989).

Boehlert C.J., Majumdar B.S., and Miracle D.B., Fatigue and Fracture of Ordered Intermetallic Alloys II, W.O. Soboyejo, T.S. Srivatsan, and R.O. Ritchie (Eds.), TMS, Warrendale, PA 135-153 (1995).

Boehlert C.J., Majumdar B.S., and Eylon D.. *Key Eng. Mater.*, **127-131** 843-850 (1997).

Boehlert C.J., Majumdar B.S., and Miracle D.B., *Metallurgical and Materials Transactions* **28A** 309-323 (1997a).

Boehlert C.J., Majumdar B.S., Krishnamurthy S., and Miracle D.B., *Metall. Trans. A,* **28A** 309-323 (1997b).

Boehlert C.J., *Mater. Sci. Eng. A*, **267** 82-98 (1999).

Boehlert C.J. and Miracle D.B., *Metall. Mater. Trans. A*, **30** 2349-2367 (1999).

Boehlert C.J., Majumdar B.S., Seetharaman V., and Miracle D.B., *Metall. Trans. A*, **30** 2305-23 (1999).

Boehlert C.J., Majumdar B.S., and Miracle D.B., *Metall. Mater. Trans. A*, **32** 3143-3155 (2001).

Bowen P., Chave R.A., and James A.W., *Mat. Sci. Eng.*, **A192/193** 443-456 (1995).

Brindley W.J., Smialek J.L., Smith J.W., and Brady M.P., Orthorhombic Titanium Matrix Composites Workshop, WL-TR-95-4068, Smith P.R. (Ed.), Wright-Patterson Air Force Base, OH 1-14 (1995).

Brindley W.J., Gabb T.P, and Smith J.W., Orthorhombic Titanium Matrix Composites Workshop, WL-TR-95-4068, Smith P.R. (Ed.), Wright-Patterson Air Force Base, OH 52-63 (1995a).

Burgers W.G., Physica, **1** 561-586 (1934).

Carrère N., Kruch S., Vassel A., and Chaboche J.-L., *International Journal of Damage Mechanics* **11** 41-63 (2002).

Cerchiara R.R., Meier G.H., and Pettit F.S., Orthorhombic Titanium Matrix Composites Workshop, WL-TR-95-4068, Smith P.R. (Ed.), Wright-Patterson Air Force Base, OH 15-40 (1995).

Chatterjee A., Roessler J.R., Brown L.E., Heitman P.W., and Richardson G.E., *Proceedings of the Second International Symposium on Structural Intermetallics*, TMS, M.V. Nathal, R. Darolia, C.T. Liu, P.L. Martin, D.B. Miracle, R. Wagner, and M. Yamaguchi (Eds.) 905-911 (1997).

Chawla K.K., Composite Materials Science and Engineering, Springer-Verlag, Inc., New York, (1998).

Cho W., Thompson A.W., and Williams J.C., *Metall. Trans. A*, **21** 641-651 (1990).

Clark D.S. and Varney W.R., Physical Metallurgy for Engineers, D. Van Nostrand Company, Inc., Princeton, NJ (1962).

Coble R.L., Journal of Applied Physics, **34** 1679-1682 (1963).

Conrad H., Doner M., and DeMeester B., Titanium Science and Technology, Edited by R.I. Jaffee and H.M. Burte, Plenum, New York, (1973).

Court S.A., Lofvander J.P., Loretto M., and Fraser H.L., Phil. Mag., **60** 109-139 (1990).

Cowen C.J. and Boehlert C.J., *Phil. Mag.*, **86** 99-124 (2006).

Cowen C.J., Ph.D. Thesis, Michigan State University (2006).

Cowen C.J. and Boehlert C.J., *Metall. Trans.* A, **39** 279-293 (2008).

Crossman F.W., Karlak R.F., and Barnett D.M., *Failure Modes in Composites – II*, AIME Symposium Proceedings, TMS, J.N. Fleck and R.L. Mehan (Eds.) 8-31 (1974).

Das G., Russ S.M., and Khobaib M., *Titanium '92, 7th World Congress on Titanium*, F.H. Froes and I.L. Caplan (Eds.) TMS-AIME, Warrendale, PA 2625-2632 (1993).

Dieter G.E., Mechanical Metallurgy, 3rd Edition, McGraw-Hill, Boston, MA, (1986).

Divecha A.P., Fishman S.G., and Karmarkar S.D., *J. Metals*, **9** 12-17 (1981).

Eggleston M.R. and Ritter A.M., *Metall. Trans. A*, **26** 2733-2744 (1995)

Evans R.W. and Wilshire B., *Creep of Metals and Alloys*, The Institute of Metals, New York, NY, (1985).

Evans R.W. and Wilshire B., Introduction to Creep, IOM Communications Ltd., London (1993) 32-35.

Feillard P., *Acta Metallurgica*, **44** 643-656 (1996).

Gambone M.L., *Fatigue and Fracture of Titanium Aluminides*, Technical Report WRDC-TR-89-4145, Wright-Patterson Air Force Base, OH (1989).

Garofalo F., *Fundamentals of Creep and Creep-Rupture in Metals*, The Macmillan Company, New York, NY, (1965).

Ghosh S., Ling Y., Majumdar B., and Kim R., *Mechanics of Materials* **32** 561-591 (2000).

Gogia A.K., Nandy T.K., Muraleedharan K., and Banerjee D., *Mater. Sci. Eng. A*, **159** 73-86 (1992).

Gogia A.K., Nandy T.K., Banerjee D., Carisey T., Strudel J.L., and Franchet J.M., *Intermetallics*, **6** 741-48 (1998).

Gundel D.B., Majumdar B.S., and Miracle D.B., Metal Matrix Composites, 2, Proc. Tenth International Conference on Composite Materials, A. Poursartip and K.N. Street, eds., Woodhead Publishing, Ltd., Cambridge, UK 703-710 (1995).

Gundel D.B., Majumdar B.S., and Miracle D.B., Scripta Metallurgica et Materialia **33** 2057-2065 (1995a).

Gundel D.B., Warrier S.G., and Miracle D.B., Acta Materialia **45** 1275-1284 (1997).

Gundel D.B. and Miracle D.B., *Proceedings from Orthorhombic Titanium Matrix Composite Workshop*, WL-TR-97-4082, Wright-Patterson Air Force Base, OH 34-46 (1997).

Gundel D.B., Warrier S.G., and Miracle D.B., *Acta Materialia*, **45** 1275-1284 (1997).

Gundel D.B. and Miracle D.B., Composites Science and Technology **58** 1571-1581 (1998).

Gundel D.B., Warrier S.G., and Miracle D.B., *Composites Sci. Technol.*, **5** 1087-1096 (1999).

Hall E.C. and Ritter A.M., *Journal of Materials Research*, **8** 1158-1168 (1993).

Harper J. and Dorn J.E., *Acta Metallurgica*, **5** 654-665 (1957).

Hartman G.A. and Russ S.M. *Metal Matrix Composites: Testing, Analysis and Failure Modes*, ed. W.S. Johnson, American Society for Testing and Materials, Philadelphia, PA, 43-53 (1989).

Hayes R.W., *Acta. Metall.*, **39** 569 (1991).

Hecker S.S., Hamilton C.H., and Ebert L.J., *J. Mater., JMLSA,* **5** 868-900 (1970).

Herring C., Journal of Applied Physics, **21** 437-445 (1950).

Hilliard J.E., *Metal Progress*, **78** 99-100 (1964).

Howatt G.N., Breckenridge R.G., and Brownlow J.M., J. Am. Ceram. Soc., **30** 237-42 (1947).

Huang S.C. and Siemers P.A., *Met. Trans. A*, **20** 1899-1906 (1989).

Hull D. and Bacon D.J., Introduction to Dislocations, 4th Ed., Elsevier Butterworth-Heinemann, Burlington, MA, (2004).

Jansson S., Dève H.E., and Evans A.G., *Metall. Trans. A,* **22** 2975-2984 (1991).

John R., Khobaib M., and Smith P.R., *Metall. Trans. A*, **27** 3074-3080 (1996).

Kerry S. and Winstone M.R., *Mater. Sci. Engin. A*, **192/193** 856-861 (1995).

Kestner-Weykamp H.T., Ward C.W., Broderick T.F., and Kaufman M.J. *Scripta Metall.*, **23** 1697-1702 (1989).

Konitzer D.G. and Loretto M.H., *Materials Science and Engineering A*, **107** 217-223 (1989).

Koss D.A., Banerjee D., Al Lukasak D., and Gogia A.K., Hihg Temperature Titanium Aluminides and Intermetallics, S.J. Whang *et al.*, (eds.), TMS-AIME, Warrendale, PA 175-196 (1990).

Krishnamurthy S., Smith P.R., and Miracle D.B., *Titanium Metal Matrix Composites II,* P.R. Smith and W.C. Reynolds (Eds.), WL-TR-93-4105, Wright-Patterson Air Force Base, OH 59-75 (1993).

Krishnamurthy S., Smith P.R., and Miracle D.B., *Scripta Metallurgica et Materialia*, **31** 653-658 (1994).

Krishnamurthy S., Smith P.R., and Miracle D.B., Proceedings Orthorhombic Titanium Matrix Composites Workshop, WL-TR-95-4068, Wright-Patterson Air Force Base, OH 83-105 (1995).

Krishnamurthy S., James M.R., Smith P.R., and Miracle D.B., Proceedings of the 10th International Conference on Composite Materials, Vol. II Metal Matrix Composites, A. Poursartip, K.N. Street (Eds.) Woodhead Publishing Ltd, Vancouver, BC 739-746 (1995a).

Krishnamurthy S., Smith P.R., and Miracle D.B., UES, Inc., Dayton, OH, Wright-Patterson Air Force Base, OH, Unpublished research, (1995b).

Krishnamurhty S. and Miracle D.B., Proceedings of the 11th International Conference on Composite Materials (ICCM-11), M.L. Scott, ed., Vol. 3, Woodhead Publishing, Cambridge, UK 399-408 (1997).

Krishnamurthy S., Smith P.R., and Miracle D.B., *Materials Science Engineering* **A243** 285-289 (1998).

Kurtz R.D. and Pagano N.J., *Composites Engineering*, **1** 13-27 (1991).

Larsen J.M., Russ S.M., and Jones J.W., *Metal. Mater. Trans. A*, **26** 3211-3223 (1995).

Leyens C., Hausmann J., and Kumpfert J., *Titanium and Titanium Alloys*, Edited by Leyens C. and Peters M., Wiley-VCH Verlag, Weinheim, Germany, (2003).

Majumdar B.S. and Newaz G.M.. Philosophical Magazine, **66** 187-212 (1992).

Majumdar B.S., Boehlert C.J., and Miracle D.B., WL-TR-95-4068, Wright-Patterson Air Force Base, OH 65-83 (1994).

Majumdar B.S., Boehlert C.J., and Miracle D.B., *Orthorhombic Titanium Matrix Composites*, Proc. Orthorhombic Titanium Matrix Composites Workshop, WL-TR-95-4068, Wright-Patterson Air Force Base, OH, 65-82 (1995).

Majumdar B.S., Interfaces in Metal Matrix Composites, Titanium Matrix Composites, S.Mall, T. Nicholas, eds., Technomic Publications, Lancaster, PA 113-168 (1997).

Majumdar B.S., Grundel D.B., Dutton R.E., Warrier S.G., and Pagano N.J., Journal of the American Ceramic Society, **81** 1600-1610 (1998).

Majumdar B.S., *Materials Science and Engineering A*, **259** 171-188 (1999).

Malakondaiah G. and Rao P.R., *Acta Metall.*, **29** 1263-1275 (1981).

Mall S. and Cunningham S.R., *Composite Structures*, **80** 65-72 (2007).

Marquardt B.J., Scarr G.K., Chesnutt J.C., Rhodes C.G., and Fraser H.L., Technical Report WRDC-TR-89-4133, (1989).

Martineau P., Pailler R., Lahaye M., and Naslain R., *Journal of Materials Science*, **19** 2749-2753 (1984).

Mendiratta M.G. and Lipsitt H.A., *J. Mater. Sci.*, **15** 2985-2990 (1980).

Meyers M.A. and Chawla K.K., Mechanical Behavior of Materials, Prentice-Hall Inc., Upper Saddle River, NJ 553-564 (1999).

Miller S., Advanced Materials Mean Advanced Engines, Materials World, **4** 446-449 (1996).

Miracle D.B. and Majumdar B.S., *Metal. Mater. Trans. A*, **30** 301-306 (1999).

Mishra R.S. and Banerjee D., *Mater. Sci. Eng. A.*, **130** 151-164 (1990).

Morscher G., Pirouz P., and Heuer H., *Journal of the American Ceramic Society*, **73** 713-720 (1990).

Mozer B., Bendersky L.A., Boettinger W.J., and Rowe R.G., *Scripta Met. Et Mater.* **24** 2363-2368 (1990).

Muraleedharan K., Nandy T.K., Banerjee S., and Lele S., *Metall. Trans. A*, **23** 417-431 (1992).

Muraleedharan K., Gogia A.K., Nandy T.K., Banerjee D., and Lele S., *Metall. Trans. A*, **23** 401-415 (1992a).

Muraleedharan K., Banerjee D., Banerjee S., and Lele S., *Phil. Mag.*, **71** 1011-1036 (1995).

Nabarro F.R.N., Report in Conference on Strength of Solids, The Physical Society, London (1948).

Nandy T.K., Mishra R.S., and Banerjee D., *Scr. Metall. Mater.*, **28** 569-574 (1993).

Nandy T.K., Mishra R.S., Gogia A.K., and Banerjee D., *Scr. Metall. Mater.*, **32** 851-856 (1995).

Nandy T.K. and Banerjee D. *Intermetallics*, **8** 915-928 (2000).

Nandy T.K. and Banerjee D., *Intermetallics*, **8** 1269-1282 (2000).

Neu R.W. and Sehitoglu H., *Metal. Trans. A*, **20** 1755-1767 (1989).

Neu R.W. and Roman I., *Composites Science and Technology*, **52** 1-8 (1994).

Nicholas T. and Russ S.M., *Proceedings of the Structural Testing Technology at High Temperature – II*, The Society for Experimental Mechanics, Bethel, CT 155-164 (1993).

Nicholas T., Russ S.M., Neu R.W. and Schehl N, Life Prediction Methodology for Titanium Matrix Composites, ASTM STP 1253, W.S. Johnson, J.M. Larsen and B.N. Cox (Eds.), American Society for Testing and Materials 595-617 (1996).

Niemann J.T. and Edd J.F., *Proceedings from Titanium Aluminide Composite Workshop*, WL-TR-91-4020, Wright-Patterson Air Force Base, OH, 300-314 (1991).

Owen D.M. and Langdon T.G., *Mater. Sci. Eng. A*, **216** 20-29 (1996).

Pearson K., *Phil. Trans. Royal Soc. London Ser.* A **187** 253-318 (1896).

Peters J.A., Baasi C., Scripta Metallurgica et Materialia, **24** 915-920 (1990).

Peters M., Hemptenmacher J., Kumpfert J., and Leyens C., *Titanium and Titanium Alloys*, Edited by Leyens C. and Peters M., Wiley-VCH Verlag, Weinheim, Germany, 2003.

Pickard S.M. and Miracle D.B., *Mater. Sci. Eng A.*, **203** 59-67 (1995).

Porter D.A. and Easterling K.E., Phase Transformations inMetals and Alloys, 2nd ed. Nelson Thornes Ltd., Cheltenham, United Kingdom (1992).

Porter J.R., Hall J.A., Chesnutt J.C., and Rhodes C.G., Advanced Ti-Based MMC Development, WL-TR-95-4034, Interim Rpt (1995).

Reed-Hill R.E. and Abbaschian R., Physical Metallurgy Principles, 3rd ed. PWS Publishing Company, Boston, MA (1994).

Rhodes C.G., Mater. Res. Soc. Symp. Proc. **273** 17-29 (1992).

Rhodes C.G., Graves J.A., Smith P.R., and James M.R. *Structural Intermetallics*, R. Darolia, J.J. Lewandowski, C.T. Liu, P.L. Martin, D.B. Miracle, and M.V. Nathal (Eds.), TMS, Warrendale, PA, 45-52 (1993).

Rhodes C.G., Technical Report, WL-TR-97-4082, P.R. Smith (Ed.), 83-100 (1997).

Rhodes C.G., Smith P.R., Hanusiak W.H., and Shephard M.J., *Metal. Mater. Trans. A*, **31** 2931-2941 (2000).

Rohatgi P.K., Asthana R., and Das S., *Intl. Met. Rev.* **31** 115-139 (1986).

Rosenberger A.H., Smith P.R., and Russ S.M., *Proceedings from Orthorhombic Titanium Matrix Composite Workshop*, WL-TR-97-4082, Wright-Patterson Air Force Base, OH 198-211 (1997).

Rowe R.G., C.T.L.S.H. Whang, D.P. Pope, and J.O. Stiegler (Eds.), TMS, AIME, Warrendale, OH, 375-401 (1990).

Rowe R.G., U.S. Patent Number 5,032,357 (1991).

Rowe R.G., Microstructure/Property Relationships in Titanium Aluminides and Alloys, Y-W. Kim and R.R. Boyer (Eds.), Warrendale, PA 387-398 (1991a).

Rowe R.G. and Hall E.L., *High Temperature Ordered Intermetallic Alloys-IV*, Symposia Proceeding of the Materials Research Society, L.A. Johnson, D.P. Pope, and J.O. Stiegler (Eds.), Materials Research Society, Pittsburgh, PA, **231**, 449-454 (1991).

Rowe R.G., Konitzer D.G., Woodfield A.P., and Chesnutt J.C., *High Temperature Ordered Intermetallic Alloys-IV*, L.A. Johnson, D.P. Pope, and J.O. Stiegler, Materials Research Society, Pittsburgh, PA, **231** 703-708 (1991a).

Rowe R.G., Proceedings for the Seventh World Conference on Titanium, TMS, F.H. Froes and I.L. Caplan (Eds.) Warrendale, PA 343-350 (1992).

Rowe R.G., Banerjee D., Muraleedharan K., Larsen M., Hall E.L., Konitzer D.G., and Woodfield A.P., Proceedings Seventh World Conference on Titanium, San Diego, CA June (1992), F.H. Froes and I. Caplan (Eds.), TMS-AIME, Warrendale, OH (1992).

Rowe R.G. and Larsen M. *Titanium 1995*, P.A. Blenkinsop, W.J. Evans, and H.M. Flowers (Eds.), The University Press, Cambridge, UK, **1** 364-371 (1996).

Ruano O.A., Wadsworth J., and Sherby O.D., *Acta Metall.*, **36** 1117-28 (1988).

Rusing J. and Herzig C., *Intermetallics*, **4** 647 (1996).

Russ S.M., Nicholas T., Bates M., and Mall S., *Failure Mechanisims in High Temperature Composite Materials*, ASME, **22/122** 37-43 (1991).

Russ S.M., Nicholas T., Hanson D.G., and Mall S., *Science and Engineering of Composite Materials*, **3** 177-189 (1994).

Russ S.M., Boehlert C.J., and Eylon D., *Materials Science and Engineering A*, **192/193** 483-489 (1995).

Russ S.M., Larsen J.M., and Smith P.R., *Proceedings from Orthorhombic Titanium Matrix Composite Workshop*,WL-TR-95-4068, Wright-Patterson Air Force Base, OH 162-183 (1995).

Sagar P.K., Banerjee D., Muraleedharan K., and Prasad Y.V.R.K., *Metall. Mater. Trans. A*, **27** 2593-2604 (1996).

Shastry S.M.L. and Lipsitt H.A., *Metall. Trans. A*, **8** 1543-1549 (1977).

Shultz U., Leyens C., Fritscher K., Peters M., Saruhan-Brings B., Lavigne O., Dorvaux J.-M., Poulain M., Mévrel R., Caliez M., Aero. Sci. Techn. **7** 73-80 (2003).

Sibum H., *Titanium and Titanium Alloys*, Edited by Leyens C. and Peters M., Wiley-VCH Verlag, Weinheim, Germany, 2003.

Smith P.R., Graves J.A., Rhodes C.G., James M.R., and Porter J.R., *Titanium Matrix Composites*, WL-TR-92-4035, Wright-Patterson Air Force Base, OH (1992).

P.R. Smith, J.A. Graves, and C.G. Rhodes, *Metal. Mater. Trans. A,* **25** 1267-1283 (1994).

Smith P.R., Porter W.J., Kralik W.J., and Graves J.A., *Metal Matrix Composites, Proceedings from the 10th International Conference of Composite Materials*, A. Poursartip and K.N. Street (Eds.), Woodhead Publishing, Ltd., Cambridge, UK, **2** 731-738 (1995).

Smith P.R. and Graves J.A., *Proceedings from the Orthorhombic Titanium Matrix Composite Workshop,* WL-TR-95-4068, Wright-Patterson Air Force Base, OH, 139-150 (1995).

Smith P.R., Gambone M.L., Williams D.S., and Garner D.I., Proceedings from Orthorhombic Titanium Matrix Composite Workshop, WL-TR-97-4082, Wright-Patterson Air Force Base, OH 1-28 (1997).

Smith P.R. and Porter W.J., *J. Mater. Sci.*, **32** 6215-6220 (1997).

Smith P.R., Rosenberger A., and Shepard M.J., *Scripta Metal.,* **41** 221-228 (1999).

Smith P.R., Rosenberger A., Shepard M.J., and Wheeler R., *J. Mater. Sci.* **35** 3169-3179 (2000).

Specialty Materials, Inc. http://www.specmaterials.com/silicarbsite.htm, May (2008)

Tandon G.P., Kim R.Y., Warrier S.G., and Majumdar B.S., *Proceedings of the American Society for Composites 12th Technical Conference*, Technomic Publishing Co., Lancaster, PA 1176-1185 (1997).

Tang F., Nakazawa S., Hagiwara M., *Scripta Mater.*, **43** 1065-1070 (2000).

Tang F., Nakazawa S., Hagiwara M., *Mater. Sci. Engin. A*, **329-331** 492-498 (2002).

Terlinde G., Witulski T., and Fischer G., *Titanium and Titanium Alloys*, Edited by Leyens C. and Peters M., Wiley-VCH Verlag, Weinheim, Germany, 2003.

Trent 800 courtesy Rolls-Royce Plc. Diagrams after Michael Cervenka, Rolls-Royce

von Mises R., *Göttin. Nachr. Math. Phys.*, **1**, 582-592 (1913).

Warrier S.G., Gundel D.B., Majumdar B.S., and Miracle D.B., *Metal. Mater. Trans. A*, **27** 2035-2043 (1996).

Warrier S.G., Gundel D.B., Majumdar B.S., and Miracle D.B., *Scripta Materialia*, **34** 293-299 (1996a).

Warrier S.G., Majumdar B.S., Gundel D.B., and Miracle D.B., *Acta Metallurgica*, **45** 3469-3480 (1997).

Weertman J., *Journal of Applied Physics*, **28** 362-364 (1957).

Wu X., Cooper C., and Bowen P., *Metal. Mater. Trans. A*, Vol. 32A 1841-1849 (2001).

Wu X., Cooper C., and Bowen P., *Metal. Mater. Trans. A*, Vol. 32A 1851-1860 (2001a).

Yang J.-M. and Jeng S.M., *Scripta Metallurgica*, **23** 1559-1564 (1989).

Zhang J.W., Lee C.S., Zou D.X., Li S.Q., Lai J.K.L., *Metal. Mater. Trans. A*, **29** 559-564 (1998).